Overview of measuring methods and equipment for calibration of instrument transformers

Dragana Naumović-Vuković, *Member, IEEE*

Abstract*— Instrument transformers are an important and inevitable element of AC current and voltage measurement techniques. They have been in use for more than a century. In parallel with the development of technical characteristics and improvement of instrument transformers measurements, the measurement methods and measuring equipment developed too. The significant parts of the development in this field are measuring methods, measuring devices, and systems for testing the accuracy of measuring transformers. The measurement accuracy is the most important characteristic of instrument transformers since that is the important factor in the accurate billing of electricity. The tradition in the field of testing instrument transformer's accuracy at the Electrical Engineering Institute Nikola Tesla is more than 60 years long. From the very beginning, the experts of the Institute have been active participants in the development of this field, both domestically and internationally. They have contributed to the development of measuring systems and standards for testing and calibration of instrument transformers, which have found application in laboratory calibration of the national metrology laboratories, as well as in industry. This paper provides an overview of the development of measuring methods for testing and calibration of instrument transformers, as well as a wide range of measuring devices and standards based on different measuring methods. The concrete application of measuring methods in the field of calibration in national institutes of metrology and research metrological laboratories is presented. The paper also presents the application of different measuring devices and systems in the industry, for intermediate and final control of measuring transformers as products in the instrument transformer manufacturers. A special review in this paper is dedicated to the contribution of the experts of the Electrical Engineering Institute Nikola Tesla in this field.

***Index Terms*—Instrument transformers, accuracy, measuring methods, calibration, standard transformers**

I. INTRODUCTION

Instrument transformers are unavoidable elements in the electric circuits and systems for measuring alternating voltage, current, power and energy. Their role is to adjust (transform) the real values of voltage and current (voltages of several hundred and thousands of volts and currents of several hundred to thousands of amperes) to the appropriate optimal levels of measuring, control and protection systems. Furthermore, galvanic separation of the working energy system from the metering and protection system achieves by them.

The electric voltage, current, power and energy measurement, as well as regulation and protection in power facilities, cannot be imagined without the use of instrument transformers.

According to their purpose instrument transformers are divided in two main groups: measuring instrument transformers and protective instrument transformers. In this paper emphasis is on instrument transformers for a measuring purpose.

Their role in the billing metering of electricity is especially important, where the overall accuracy of energy measurement directly depends on the accuracy of measuring transformers [1]. In the production - transmission - distribution chain, electricity is measured at least three times. Therefore, it is also financial interest, especially in the conditions of a deregulated market, to measure energy with the least possible error. Consequently, measuring transformers as well as electricity meters belong to legal metrology. Legal metrology regulations and domestic and international standards precisely define the conditions of application, calibration, as well as the deadlines for periodic review of these types of measuring instruments [2, 3, 4, 5, 6, 7].

The main direction of development of measuring transformers, in addition to improving their reliability, is to reduce the error of transformation of primary quantities into secondary ones. Improving the accuracy of instrument transformers is conditioned by the development of measuring methods and devices for measuring and determining its errors. Historically, the subject of measuring transformers dates back to the beginning of the twentieth century [8, 9]. The development of measuring methods and devices for errors measurement of measuring transformers depended primarily on the technical and technological capabilities of the time in which it took place. Consequently, the first methods and devices were based on a square electrometer [10, 11]. Modern devices have been developed on the most modern microprocessor technologies and virtual instrumentation [12, 13, 14, 15, 16].

The EEINT has the international reputation in the development and application of devices and systems for accuracy testing of instrument transformers for more than 60 years. Devices for accuracy testing of measuring transformers based on different measuring methods, developed at the EEINT, have been used in all manufactories for instrument transformers in the former Yugoslavia, as well as in many other testing laboratories of distribution companies and transmission networks. These devices have shown a number of advantages over other solutions, especially in the on-site

---

Dragana Naumović-Vuković is with the Electrical Engineering Institute Nikola Tesla, University of Belgrade, Koste Glavinića 8a, 11000 Belgrade Serbia (e-mail: dragananv@ieent.org), (https://orcid.org/0000-0002-8334-4452).

testing of measuring transformers, in factory serial quality control, as well as the most accurate measurements [17, 18].

New generations of devices for accuracy testing of the instrument transformers, developed at the EEINT in the last ten years, have been used at the following manufacturers: MINEL -FEPO Zrenjanin (Serbia), FMT - Factory of instrument transformers Zajecar (Serbia), "Energoinvest" (Bosnia and Hercegovina), EMO-Ohrid (Macedonia), Končar – Instrument Transformers (Croatia), MBS - Instrument transformers (Germany). In the EEINT special attention is paid to the development of measuring devices for application in the most accurate measurement in this field. Such measuring systems have been developed and made for the National Research Council of Canada (NRC) and the Hydro Qebek High Voltage Testing Laboratory, also in Canada.

II. COMPLEX ERROR

Electric voltage and current are vector quantities. Therefore, their complex transformation error is defined by ratio (amplitude) error and phase displacement. Like any measurement transformation, this one is also followed by certain errors. In a case of vector quantities, discrepancy from the ideal transformation is characterized by a complex error $\underline{G}$. The complex error of measuring current and voltage transformers is defined as the fundamental harmonic of current, i.e., voltage. The complex error includes the ratio (amplitude) error, g, and the phase displacement, δ, expressed in mathematical form:

$$\underline{G} = g + j\delta \tag{1}$$

Ratio error of current transformer g in %, in accordance to standard [4] is defined as:

$$g = \frac{K_N \cdot I'' - I'}{I'} \cdot 100 \tag{2}$$

where K_N is the rated transformation ratio.

The phase displacement δ in min (1%=34.4min=1crad), is defined as the phase shift of the secondary current I'' in relation to the primary current I' [4].

The ratio error and phase displacement of the current transformer are defined by its:

- constructive and technological parameters: material, shape and dimensions of the magnetic circuit, number of ampere-turns, length and cross-section of the wire, geometry of the primary and secondary winding;
- operating parameters: secondary load, ratio of measured current to rated, frequency, distortion and shape of measured primary current;
- ambient conditions: temperature and pressure.

The ratio error of voltage transformer g in (%), in accordance to standard [5] is defined as:

$$g = \frac{K_N \cdot U'' - U'}{U'} \cdot 100 \tag{2}$$

where K_N is rated transformation ratio

The phase displacement δ in (min), of voltage transformers is defined as the phase shift of the secondary voltage U'' in relation to the primary voltage U'. The ratio error and phase displacement of the voltage transformer are also defined by its constructive, technological, operating parameters and ambient condition.

The main difference between current and voltage transformers is that the initial design parameter in current transformers is the magnetic excitation force, while in voltage transformers this is the magnetic induction. However, in the constructive, technological and physical sense, there are significant differences between current and voltage transformers, which results from different operating modes. The current transformer operates in the short-circuit mode, and the voltage transformer in the idling mode.

The functional connections between parameters and ratio error and phase displacement are known. Therefore, it is possible to analytically calculate their values for a given current or voltage transformer, which is usually done during design.

The main parameters in designing current and voltage transformers as well as in declaring their errors (accuracy classes) are secondary burden and reference currents and voltages. The limits of errors for declared classes by standard, for current measuring transformers are defined in accordance to percentage of rated currents (i.e., reference currents) and for secondary burden between ¼ and rated value [4]. In the same way, the limits of errors for declared classes for voltage measuring transformers are defined in accordance to percentage of rated voltage (i.e., reference voltage) and also for secondary burden between ¼ and rated value [5]. This method of errors declaring corresponds to their nonlinear character. The accuracy class of measuring transformer directly affects its application.

However, the true (more accurate) error values are obtained only by measuring the accuracy of the measuring transformer.

III. THE MEASURING METHODS AND DEVICES FOR ACCURACY TESTING

From the early beginning of the application of measuring transformers, back in 1892, [19], there was a need for their accuracy testing. The errors of these first current transformers were in the order of about 3% for ratio error and approximately 200 minutes for phase displacement [8]. In that time, these errors had been determined by direct measurement of primary and secondary currents and phase shift. In addition to the error of the measurement method, limitations have also appeared in the application of analog measuring instruments [20]. For example, the limits of current measurement with analog measuring instruments were 200A. Appropriate shunts and pre-resistors were used for currents higher than this value.

With the rapid technological development, the applications of precise standard measuring transformers [21] have begun. With the progress in the production and application of new magnetic materials, in the thirties of the last century, the errors of measuring transformers have been reduced to 0.1% and 5min [22].

A. *Classical methods and devices for accuracy testing of instrument transformers*

The first methods for accuracy testing of instrument transformers appeared at the beginning of the last century [23, 24, 25]. The most important methods, whose influences extend to the present days, are compensation, differential and current comparator methods.

The compensation method, Fig 1, is basically a direct comparison of two alternating voltages generated on precision reference shunts (for current transformer testing) or voltage dividers (for voltage transformers testing), one in the primary circuits and the other in the secondary circuits of the transformer under test, (T_X).

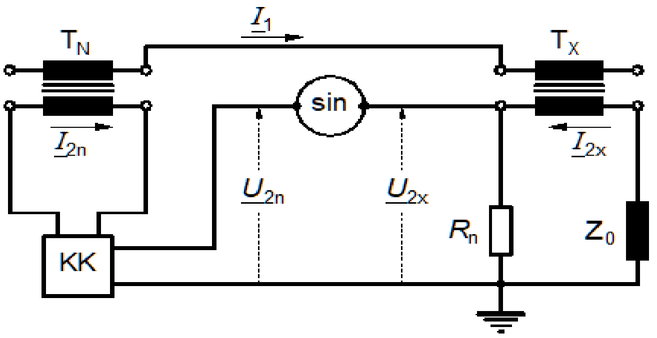

Fig.1. Compensation method for current transformer accuracy testing [17].

The compensating method was usually used in laboratory testing. The main reason for that is demand for satisfactory high accuracy of the elements that is incorporated in complex compensator (precise resistors and voltage dividers), and that are also temperature and time stable. In addition, there is also a problem of additional load in secondary circuits of transformer under test that is not negligible. The main advantage of this method is the ability to accuracy testing of the instrument transformers of non-standard transformation ratio.

The differential method is attributed to F. B. Silsbee and is related to 1917 [23]. This method was perfected by Hole (W. Hohle) in 1934 [26]. The essence of this method, Fig. 2, is to measure the differences between two quantities. In this method the secondary voltages (or currents) of the device under test (current or voltage transformer), (T_X) and of the standard transformer (T_N) of approximately equal transformation ratios are compared. In order to achieve comparison as accurate as possible, the standard current transformer should have a negligibly error.

The basic elements of the devices for accuracy testing based on differential and compensational methods are complex compensator (KK) and selective zero indicator (SIN), Fig. 1, and Fog. 2.

Around 1930, measuring devices based on the compensation method and the complex compensator [27, 28] appeared. The best accuracy of such early commercial devices was about 0.02% and 2 min. There are many solutions of complex compensators, but from the point of view of accuracy testing of instrument transformers, the most significant is certainly the work of scientists Schering and Alberti [24].

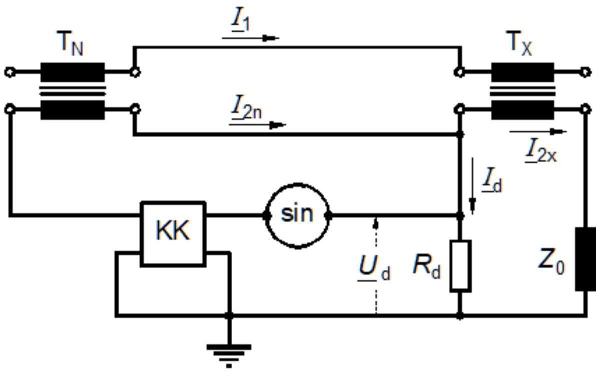

Fig.2. Differential method for current transformer accuracy testing [17].

Measuring device, so-called Hole's compensator based on differential method has also found wide practical application [29].

With the selective zero indicator, the equality of two voltages is determined at a certain (basic) frequency. This implies two requirements: indicator should be sufficiently sensitive to the basic measured voltage and also insensitive to parasitic (disturbing) voltages as well as to higher harmonics of the measured voltage. Two types of selective zero indicators have been used: a classic solution with a vibrating galvanometer and an electronic zero indicator.

Technological improvements and modifications of this compensator and selective indicators, made in the 1930s, especially in the late 1960s, made these instruments indispensable in the laboratories for testing and calibration of measuring transformers, for a long time during the last century.

The third, important measuring method that has remained until today is based on the application of a current comparator. The idea of the current comparator was first presented in 1917 by the American physicist Baker [25]. He suggested measurement of the difference between the two currents by using windings on a magnetic core. The current comparator with a compensating winding was first used in 1930 by the English scientist Bruges [30], and the German physicist Reihe used it as a test device for the accuracy testing of current transformers [31]. This, therefore, long-known but, then technically and technologically imperfect method, experienced its reaffirmation in several metrological laboratories in the 1950s. The current comparator was first used in the comparison of alternating currents, and later for accurate measurement of resistance, capacity, etc. The

Electrical Engineering Institute Nikola Tesla (EEINT), mostly thanks to Ilija Obradovic, Petar Miljanic and Srdjan Spiridonovic, is the pioneers in this field. The first device for measuring the accuracy of current transformers is being realized then. This work, which have been continued to these days, is marked by a series of successful results and articles The very name "current comparator", today is internationally accepted technical term, first appeared in the works of experts from the EEINT [32].

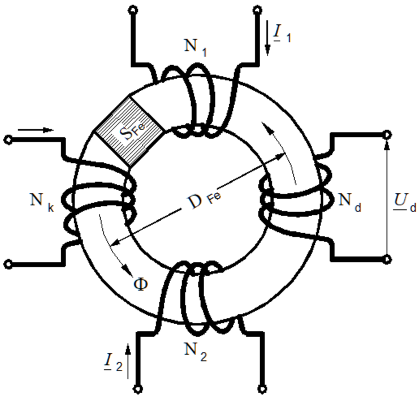

Fig.3. A simplified scheme of current comparator [35].

Significant progress in the construction and manufacture of current comparators has been achieved through the joint work of associates of the Canadian NRC (National Research Council) and the EEINT [33].

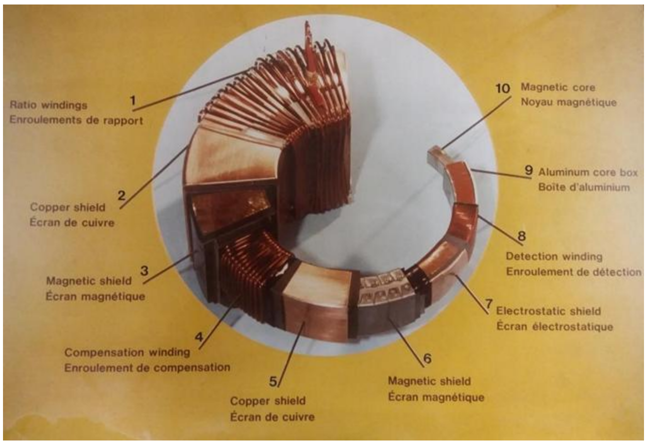

Fig.4 The structure of current comparator [17].

An ideal transformer is a transformer for which the equality of magnetomotive force applies [33]. In reality, a part of the primary magnetomotive force is spent on magnetizing of the core and losses in it. This is the main reason for the error of the current measuring transformer. If the magnetic flux in the core is artificially reduced to zero, then the current transformer becomes ideal. In that way the comparison of the currents reduces to the turn ratio of primary and secondary windings. This ratio is stable during the time and insensitive by temperature changes. This gives the possibility of a very accurate comparison of two alternating currents, which is the basic idea of the current comparator [34].

Fig. 3 shows simplified scheme of a current comparator. To measure the magnetic flux in the core of the current comparator, the detection coil N_d is used, and compensating coil N_k brings the magnetic flux to zero [35]. Practical realization of current comparator is more complex as shown in Fig. 4.

With carefully construction and realization of current comparators, it is possible to achieve its ratio error within the range from 10^{-6} to 10^{-7}, and the phase displacement in the order of 0.01 min.

B. The recent methods and devices for accuracy testing of instrument transformers

In the last years of the 20th century, with the application of modern electronic solutions and microcomputer techniques, measuring methods and devices for accuracy testing of instrument transformers have been significantly improved [36, 37]. Possibilities and advantages of PC hardware and software support are not only in the field of increasing efficiency, or reliability of work, but also in increasing measurement accuracy. Modern devices are based on the general tendency in electronics that the processing of the measuring signal is realized in digital form. The differences between the individual solutions of these devices are most often in the way of further digital processing of measuring signals [17, 38, 39, 40, 41].

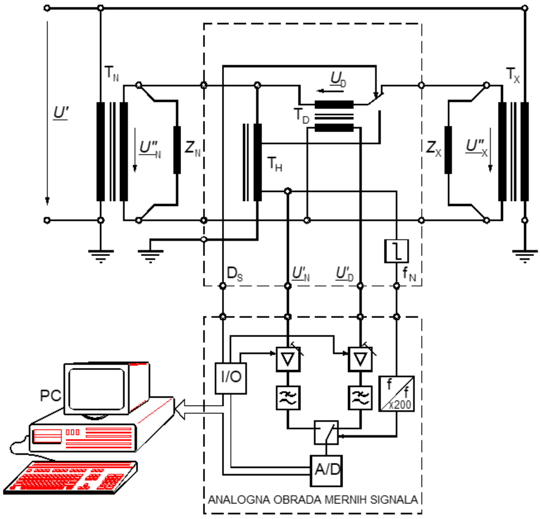

Fig. 5 The structure of DFT measuring method developed by PTB [46].

The application of the measuring method of discrete Fourier transformation (DFT) for the accuracy testing of measuring transformers originates from the laboratory for measuring transformers of the National Metrology Institute of Germany (PTB) which has a long tradition in the field of metrology, even from the early beginning in 1877 [42]. This laboratory has developed several important measuring devices for accuracy testing of the measuring transformers, known as: Schering-Alberti's [24], Hole's [26] and Keller's compensator [43]. PTB experts have significantly contributed to the development of measuring methods and measuring techniques in the field of measuring transformers. As a result of recent research in PTB, the method of discrete Fourier transform was applied, first for testing the accuracy of current measuring transformers [44], and later for testing voltage measuring transformers [45].

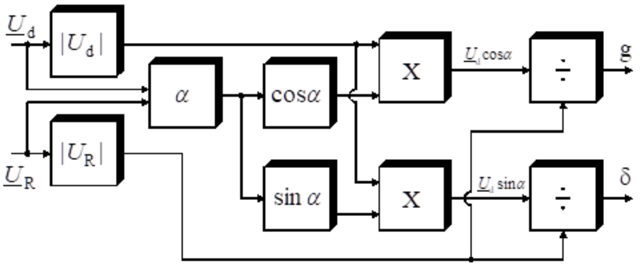

Fig. 6 The structure of measuring method based on orthogonal voltage components [48].

The structure of DFT measuring method developed by PTB experts is shown on Fig. 5 [46]. The device for accuracy testing of instrument transformers based this method, Fig. 5, have following characteristics: measurement range of ± 0,2 % and ± 2 % for ratio error, ± 0,2 crad and ± 2 crad for phase displacement; resolution of 0.000001%, accuracy ± 0,5 % of measuring value and ± 0,05 % of measuring range. This device was capable to measure in a full range from 1% to 200% of rated current, i.e., of rated voltage.

The structure of measuring method based on orthogonal voltage components is shown in Fig. 6

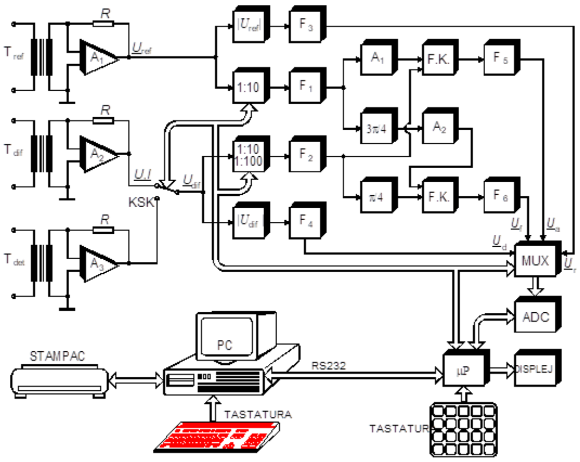

Fig. 7 Block scheme for device for instrument transformer accuracy testing, type INST-2A [47].

Basically, this is a differential method that enables measurement of fundamental harmonic of two voltages and its phase angle, but with some original solutions [47, 48]. The device based on this method is shown in Fig. 7. Novel solution of current-voltage transformer was applied for both differential and detection voltage, as well as for reference voltage. In this way, the adjustment of voltage measured signals to the optimal level was achieved, with minimal degradation of basic signals, and the conversion of current measuring signals into voltages. This initial level of analog processing of measuring signals is very important for the overall accuracy of the device. The second improvement is in electronic bloc that is applied phase regulated rectifier which makes phase shift between $\underline{U}_r$ and $\underline{U}_d$. The phase shift of π/2 by this phase rectifier is obtained as discrepancy between phase shift of 3π/4 for $\underline{U}_r$ and phase shift of 3π/4f or $\underline{U}_d$ [48]. Another recent improvement of differential measuring method is two phase conversion method [49]. The method is based on the measurement of phase angles between three relevant voltages, Fig. 8. The measured ratio error and phase displacement are than presented as a function of two angles. Structure scheme presented in Fig.8 consist of commercial dual channel power analyzer, electronic module and PC. The electronic module integrates: an amplifier, two summing circuits, circuits for π/2 phase shift and multiplexer. The input voltages U_R and U_d are subjected to relatively simple analog processing in the electronic module, and as such, are brought through multiplexer to a dual-channel power analyzer. The PC manages the operation of the electronic module and the dual power analyzer according to the given program [39, 49, 50].

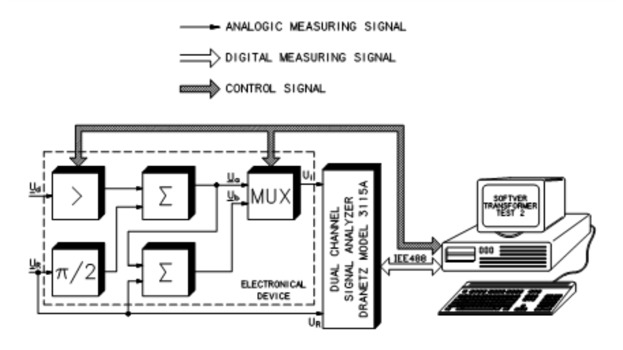

Fig. 8 The structure scheme of two phase conversion method realization [49]

IV. EEINT'S METHODS AND DEVICES

Measuring systems for accuracy testing instrument transformers based on measuring methods mentioned above usually consist of: standard current/voltage transformer, standard current/voltage burden, device for accuracy testing and measuring transformer under test.

In this field of measurement, methods that are used for testing and calibration purpose are basically the same. The difference is in the accuracy of the standard transformer and the device for accuracy testing which is applied [51].

The experts from EEINT continuously follow the development in this field. Devices for accuracy testing of instrument transformers based on different measuring methods as well as standard transformers developed at the EEINT, have been used for manufactory testing, on-site testing in the power and distribution facilities and for calibration in national metrology laboratories.

The first devices for current and voltage measuring transformer testing were developed in seventeens in last century, Fig. 9. These measuring systems are based on current comparator methods.

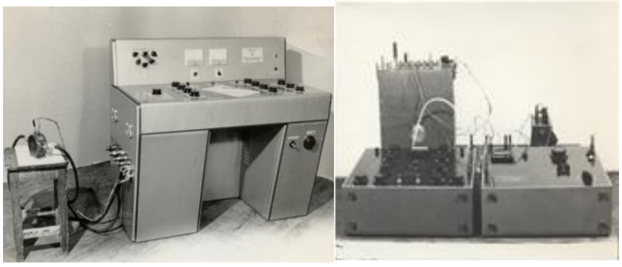

Fig. 9 Devices for current measuring transformer accuracy testing, type KSK-6 (1965) and KSK-7 (1968), respectively.

For accuracy testing of measuring voltage transformers EEINT experts developed measuring system type NIT-2p applied both for laboratory and on-site testing in distribution facilities, Fig 10. The system is based on classical differential method for accuracy testing of voltage transformers that assumed comparison between voltage transformer under test and standard voltage transformer. In that case transformer under test and standard transformer had to have the same transformation ratio.

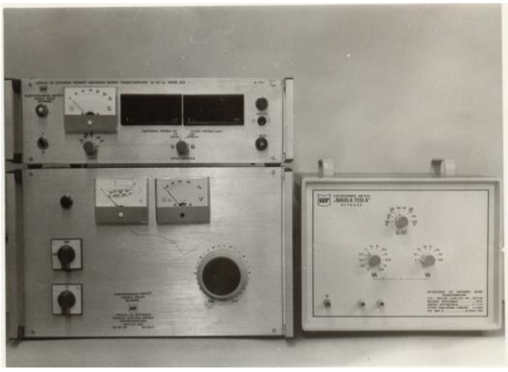

Fig. 10 System for voltage transformers accuracy testing, type NIT-2p (1981.)

With the development of instrument transformers industry in former Yugoslavia, the need for faster and more efficient routine accuracy testing appeared. This demand is satisfied with development of first automatic systems for accuracy testing of current transformers [52, 53], shown in Fig 11 and Fig 12.

Fig. 11 System for automatic accuracy testing of current measuring transformer, type ASK-1 [52]

Fig. 12 System for automatic accuracy testing of current measuring transformer, type ASK-2 [53]

Automatic systems for routine testing of measurement current transformers have been further developed together with new technological achievements. Together with ISKRA AMESI, Slovenia, in 2012, EEINT realized robotized system for routine testing of current transformer, Fig 13. Among the other routine tests according to standard [2], this system can perform accuracy testing of 7 current transformers synchronously. EEINT developed and manufacture the standard transformer, standard burden and device for accuracy testing based modified differential method and multiplexing concept [54].

Fig. 13 Robotized system for current transformers accuracy testing in MBS factory Germany (2012.) [54]

Three years later, for Instrument transformers factory FMT Zajecar, EEINT developed and made device for simultaneously testing of 3 current transformers [55], Fig. 14.

Fig. 14 Automatic device for accuracy testing of 3 current transformers simultaneously [55]

Based on the experience in the realization of different measuring devices in this field, in 2001, EEINT was designed and built a mobile laboratory for on-site accuracy testing of measuring transformers, Fig 15. This mobile laboratory was used by “Elektrostopanstvo”, Macedoni, for accuracy testing of measuring transformers in the distribution facilities [56].

Fig. 15 Mobile laboratory for accuracy testing of measuring transformers [56]

Experts from EEINT have made a special contribution to the development of standards and high-precision devices for use in national metrology laboratories. Standard current transformer with electronic compensation of errors type EST-3000 [57] was designed and made together with device for measuring transformers accuracy testing, type INST-2A [47] for Directorate for Measures and Precious Metals (DMDM). This system represents the national standard of Serbia in the field of measuring transformers.

In period from 2016 to 2019 in EEINT three high accuracy systems developed for the needs of National metrology institutes of Canada (NRC) and Singapore (A*Star), as well as for laboratory of power transmission system of Quebec (Hydro Quebec), Canada. In these measuring systems, a differential method with a special construction of a standard transformer and measuring device was applied [58]. The high accuracy of the standard transformer was achieved by an unconventional two stage design. The transformer's detection core is made of high permeability magnetic material, whereas the working core is made of a standard magnetic material for current transformers. The primary and secondary windings are evenly wound around the cores and magnetically and electrostatically shielded. The compensation winding is not connected to the secondary winding but instead to a separate differential transformer winding. This way, the N_{sc} winding of the Ts transformer is not burdened with a voltage created by the full secondary current I_{ss} and the N_{ds} winding impedance, but with a significantly smaller voltage created by a small compensation current I_{sc} and the N_{dc} winding impedance, Fig 16. This makes the impedance seen by the N_{sc} winding smaller and the compensation much thus more effective. This improvement leads to at least two to three times lower measurement errors [58]. The system is verified by simultaneously comparison with NRC system for current transformer accuracy testing – national standard of Canada. The obtained discrepancies in ratio and phase errors were within a few µA/A or µrad, respectively. Practical realization of mentioned measuring system is shown in Fig. 17. The method of simultaneously comparison is developed and firstly applied at EEINT [59].

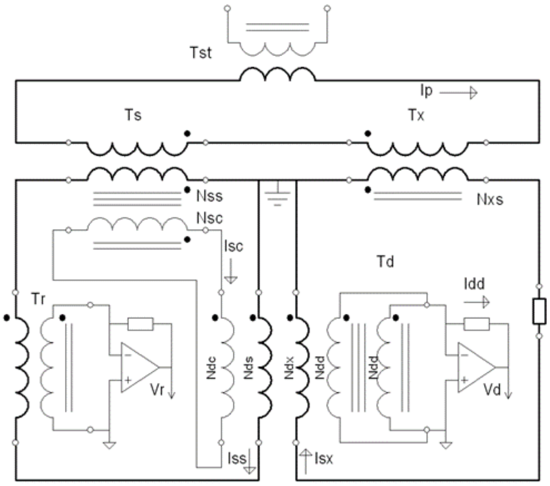

Fig. 16 Block diagram of the differential CT calibration system with special construction of two stage standard transformer T_s and differential T_d transformers [58]

V. NEW GENERATION OF MEASURING TRANSFORMERS

Digitalization of distribution and power facilities is the process that is part of much large movement, the Industrial Revolution 4.0 conventional transformers are no longer suitable for use in such systems. Therefore, new generations of current and voltage transformers and sensors have been developed that can be applied in digitized distribution and power facilities [60, 61, 62]. New types of measuring transformers and sensors require the development of new suitable measuring methods and devices for their testing. Some new proposals for accuracy testing of new generation of instrument transformers, so-cold low power instrument transformers are given in serial of EN/IEC standards [60]. It can be noted that these international standards recommend in the use of current comparators as a part of some proposed measuring systems for accuracy testing of low power instrument transformers.

Fig. 17 Practical realization of NRC measuring system for accuracy testing of current transformer

VI. CONCLUSION

The measurement accuracy is the most important characteristic of measuring transformers since that is the important factor in the accurate measurement of the high voltage and currents. The billing of electricity, as well as the power measurement at low power factors, is the explicit examples where accuracy of instrument transformers has very important role. The need for accurate measurement current and voltage by measuring transformers influenced both the improvement of their characteristics and the development of methods for determining their accuracy. The accuracy of measuring methods and measuring equipment for the accuracy testing of measuring transformers has improved along with technological progress.

This paper presents a historical overview of the development of measuring methods and devices in the field of measuring transformers. Also, the paper presents the most important trends in the development of measuring methods and devices for different applications. The systems for accuracy testing of measuring transformers in manufacturing process as well as high accuracy equipment for laboratory calibration of standard transformers are presented. Special attention was given to the contribution of EEINT experts in this field, both in the past and present.

ACKNOWLEDGMENT

Autor would like to thank dr. Slobodan Skundric for very useful discussion and suggestions regarding to topics that are presented in this paper.

REFERENCES

[1] S. Škundrić, D. Naumović-Vuković, D .Kovačević, “The Role and Importance of Instrument Transformers in Electrical Quantity measurements”, JUKO CIRED, Herceg Novi, 2004.

[2] Rule book of instrument transformers applied in the billing metering of electricity, "Official Journal RS", No. 66/15

[3] Instrument transformers – Part 1: General requirements, EN 61869-1: 2009

[4] Instrument transformers – Part 2: Additional requirements for current transformers, EN 61869-2:2012

[5] Instrument transformers – Part 3: Additional requirements for inductive voltage transformers, EN 61869-3: 2011

[6] Instrument transformers – Part 4: Additional requirements for combine transformers EN 61869-4: 2013

[7] Instrument transformers – Part 5: Additional requirements for capacitive voltage transformers EN 61869-5: 2011

[8] P. G. Agnew and T.T. Fitch, "The determination of the constants of instrument transformers", *Bull. Bureau Standards*, vol.6, pp.281-299, April 1909.

[9] H. B. Brooks and F.C. Holtz, "The two-stage current transformer", *Trans. Amer. Inst. Elect. Eng*., Vol. XLI, pp. 382-393, Jun, 1922.

[10] F. B. Silsbee, "A method for testing current transformers", *Bull. Bureau Standards*, vol.14, pp.317-329, July 1917.

[11] A. H. M. Amold, "Current transformer testing", *J. Inst. Elect. Eng*., vol. 74, No. 449, pp. 424-437, May 1934.

[12] G. Rietveld, L. Jol, H. E. van den Brom and E. So, "High-current CT calibration using a sampling current ratio bridge", *IEEE Trans. Instrum. Meas*. vol. 62, No. 6, pp. 1693-1698, Jun. 2013.

[13] E. Mohns, J. Meisner, G. Roeissle and M. Seckelmann, "A wideband current transformer bridge", *IEEE Trans. Instrum. Meas*. vol. 63, No. 10, pp. 2322-2329, Jun. 2013.

[14] E. Mohns, G. Roeissle, S. Fricke, F. Pauling, "An AC Current Transformer Standard Measuring System for Power Frequencies", IEEE Trans. on Instrumentation and Measurement, Vol. 66, Issue 6, pp. 1433-1440, 2017.

[15] E. Mohns, S Fricke, F. Pauling, "An AC power amplifier for testing instrument transformer test equipment", Conference on Precision Electromagnetic measurements, CPEM2016, 2016.

[16] S. Siegenthaler, C. Mester, "A Computer - Controlled Calibrator for Instrument transformer Test Sets", IEEE Trans. on Instrumentation and Measurement, Vol. 66, Issue 6, pp. 1184-1190, 2017.

[17] S.Škundrić, F. Smak, S. Spiridonović, N. Pandurović, D. Kovačević, "Modern methods and devices for testing of measuring transformers“ Study arranged for the United Electric Power Industry of Serbia, Electrical Engineering Institute „Nikola Tesla“, Belgrade, 1990.

[18] S. Škundrić, D. Kovačević, D. Naumović-Vuković, „The role and importance of Software Application in Instrument Transformers Accuracy Testing“, IMEKO XVIII World Congress, Rio de Janeiro, Brazil, September, 2006.

[19] S. Spiridonović, S. Škundrić, "Current measuring Transformers", Proceedings - Conference on instrument transformers in power engineering, 1996.

[20] G. Keinath, "Fehlergroben des Stromwandlers", ATM, (Z224-1), 1932.

[21] G. Keinath, "Stromwandler mit Hochter Genauigkeit, ATM, (Z20-4), 1932

[22] G. Keinath, "Hochmagnetische Legirungen", ATM, (Z913-3), 1932

[23] F. B. Silsbee, "A method for testing current transformers", *Bull. Bureau Standards*, vol.14, pp.317-329, July 1917.

[24] H. Schering, E. Alberti, Eine einfache Methode zur Prufung von Stromvandlern, Arch. Elektrotechn, Bd. 2, pp. 236-237, 1914.

[25] H.S. Baker, "Current Transformer Ratio and Phase Error by Test Ring Method", AIEE Proc., Vol. XXXVI, pp.1173, 1917

[26] W. Hohle, Neure Stromwandler - Prufeinrictungen, ATM, (Z224-4), 1934

[27] W. Geyger, "Wechelstrom - Kompensatoren", ATM, (J94-1), 1932.

[28] W. Geyger, "Wechelstrom - Kompensatoren", ATM, (J94-9), 1937.

[29] W. Hohle, "Messwandler - Prufeinrichtungen", Arch. Elektrotechn., Bd27, pp849, 1933.

[30] W.E. Bruges, "Method of Testing Current Transformers", Jurnal IEVE, Vol. 68, pp.305, 1930.

[31] W. Reiche, "Stromwoundler Hochster Genauikeit", VDE Fachberichte, 1935.

[32] I. Obradovic, P. Miljanic, S. Spiridonovic, "Prufung von Stromwandler mittls eines Stromkomparators und eines elektrischen Hilfssystems", *ETZ-A*, H.19, pp.699-701., 1957.

[33] P. N. Miljanic, N. L. Kusters and W. J. Moore, "The development of the current comparator, a high-accuracy A-C ratio measuring device", Trans. Amer. Inst. Elect. Eng. I, Commun. Electron., vol 81, no.5, pp.359-368, Nov. 1962.

[34] W.J.M. Moore and P.N. Miljanic, “The Current Comparator”, Peter Peregrines Ltd., ISBN 0 86341 112 6, 1988.

[35] S. Škundrić, D. Kovačević, D. Naumović-Vuković, S. Milosavljević, „ Application of current comparator for testing the accuracy of standards and conventional transformers in measuring groups“, „Power systems: operation, management, testing, measurement“, Monography, Electrical Engineering Institute „Nikola Tesla“, Belgrade, 2006. (ISBN 86-83349-06-3, ISBN 978-86-83349-06-07 a) Power Systems COBISS.SR-ID 136938252

[36] E. Mohns, J. Meisner, G. Roeissle and M. Seckelmann, "A wideband current transformer bridge", *IEEE Trans. Instrum. Meas*. vol. 63, No. 10, pp. 2322-2329, Jun. 2013.

[37] G. Rietveld, L. Jol, H. E. van den Brom and E. So, "High-current CT calibration using a sampling current ratio bridge", IEEE Trans. Instrum. Meas. vol. 62, No. 6, pp. 1693-1698, Jun. 2013.

[38] E. Mohns, G. Roeissle, S. Fricke, F. Pauling, "An AC Current Transformer Standard Measuring System for Power Frequencies", IEEE Trans. on Instrumentation and Measurement, Vol. 66, Issue 6, pp. 1433-1440, 2017

[39] S. Škundrić, V. Radenković, D. Kovačević, F. Smak, S. Mikičić, Testing of Instrument Transformers with non-standard rations, XXIV IMEKO World Congress, Tampere, 1997.

[40] S. Škundrić, F.Smak, D. Kovačević, S. Mikičić, The Testing of the Instrument Transformers Accuracy Calass in Power Plants, Universities Power Engineering Copnference, Crete, 1996.

[41] S. Škundrić, F. Smak, S. Vukovojac, D. Kovačević, “The Microprocessor based device for testing of measuring transformers”, Proceedings, 14. JUKEM, Sarajevo, 1990.

[42] www.ptb.de

[43] A. Keller, "Neuzeitliche Messwandler - Prufeinrictungen nach dem Differentialvervahren, ETZ-a, pp. 105-108, 1953

[44] A. Braun, "Elektronischer Vektormesser fur die Komplexe Wechselstrommesstechnik", TM50, H.10, pp. 372-377, 1985.

[45] A. Braun, H. Moser, "Rechnergesteuerter Massplatz yur Lakibrierung von Normalsoannungswandlern" PTB Miteilungen, pp. 298-302, 1989.

[46] G. Ramm, H. Moser, Eine neuartige, rechnergesteuerte und sebstkalibrierende Stromwandler-Messeinrichtung. PTB-Miteilungen Bd.105, H4, s.263-271, 1995

[47] F. Smak, S. Škundrić, S. Vukovojac, D. Kovačević, M. Korolija „The Modern device for testing of instrument transformers, type INST-2A“, Conference: Transformers in power engineering, Belgrade 1996.

[48] S. Škundrić, V. Radenković, „Electronic phase reversal of the measuring signal by π/2 in measuring transformer testing devices“, Conference ETRAN, Budva 1996.

[49] S. Škundrić, V. Radenković, Instrument Transformers Accuracy Testing by the Two-Phase Conversion Method, Electrical Engineering, H4, pp. 326-328, 1998.

[50] S. Škundrić, V. Radenković, Instrument Transformers in Contemporary Electronic Instruments, VI International SAUM Conference, Niš, 1995.

[51] E. Mohns, P. Rather, “Test equipment and its effect on the calibration of instrument transformers”, Journal of Sensors and Sensor Systems, No.7, pp339-347, 2018., https://doi.org/10.5194/jsss-7-339-2018

[52] N. Pandurović, D. Miličević, S. Škundrić, “A System for Automatoc Testing of Instrument Current Transformer Accuracy”, III Conference for Electricity Supply, London, 1977.

[53] S. Škundrić, D. Kovačević, F. Smak, S. Vukovojac, “”Computer-controlled system for automatic testing of accuracy of measuring current transformers, Proceedings of the Electrical Engineering Institute "Nikola Tesla", Vol. 9., Belgrade 1991.

[54] Dragana Naumovic - Vukovic, Slobodan Skundric, Aleksandar Zigic, The Device for Simultaneously Accuracy Testing of Current Transformers, Journal of Physics Conference Series 1065(5):052017, IOP Publishing, vol. 1065, pp. 1 - 4, issn: 1742-6596, Belfast, 3. - 6. Sep, 2018.

[55] D. Naumovic Vukovic, S. Skundric, A. Zigic, Three channels device for current transformers accuracy testing, Proceedings of 19th International Symposium on Power Electronics -Ee2017, Power Electronics Society, Faculty of Technical Science Novi Sad, Electrical Engineering Institute Nikola Tesla Belgrade, pp. 1 - 4, doi: 9781538635025/17/$31.00@2017IEEE, isbn: 978-86-7892-980-9, Novi Sad, 19. - 21. Oct, 2017.

[56] S. Skundric, D. Kovacevic, “Contribution to the teaching about measurement”, Conference MAKO-CIGRE, Ohrid 2005.

[57] F. Smak, S. Škundrić, D. Kovačević, M. Korolija, “Standard current transformer with electronic error compensation for primary currents up to 3000 A”, Conference on instrument transformers in power engineering, Belgrade 1996.

[58] B. Djokic, H. Parks, N. Wise, D. Naumovic Vukovic, S. Skundric, A. Zigic, V Poluzanski, A Comparison of Two Current Transformer Calibration Systems at NRC Canada, IEEE Transactions on Instrumentation and Measurement, IEEE Instrumentation and Measurement Society, vol. 66, no. 6, pp. 1628 - 1635, issn: 0018-9456, doi: 10.1109TIM.2017.2631739, 2017.

[59] D. Naumovic-Vukovic, “The Recent Contribution to Calibration of Current Transformers”, PhD Thesis, University of Novi Sad, Faculty of Technical Science, 2018.

[60] Instrument transformers – Part 6: Additional general requirements for low power instrument transformers EN 61869-6: 2016

[61] Instrument transformers – Part 10: Additional requirements for low-power passive current transformers EN 61869-10: 2018.

[62] Instrument transformers – Part 11: Additional general requirements for low-power passive voltage transformers EN 61869-11: 2018.

Effects of cryptocurrency mining rig operation on power quality in LV distribution network

Vladimir A. Katić, *Senior Member, IEEE,* Zoltan J. Čorba, *Member, IEEE,* Aleksandar M. Stanisavljević, *Member, IEEE*

***Abstract*—The paper presents the influence of power supply units of a cryptocurrency mining rig on the power quality in a standard low-voltage network. Measurement and monitoring of the power quality indices of one mining rig with an optimized power of 1000W were performed. For comparison, the results of power quality measurement of a group of desktop computers (PC cluster) from a computer centre are presented. It has been observed that the mining rig had a smaller impact on power quality (harmonics) than the PC cluster, but that they represent a significantly higher and almost constant power demand.**

***Index Terms*—Cryptocurrency mining rig; PC cluster; Power quality; Measurements.**

I. INTRODUCTION

Widespread use of computers, computer equipment, various digital electronic and mobile devices, consumer electronics, and household appliances, as well as other nonlinear systems based on energy electronic converters, has led to reports of distorted current waveforms in the network, i.e., occurrences of harmonics [1]. The consequence was a reduction in the power quality and the possibility of the appearance of some negative effects on other interconnected loads (linear), but also on the above-mentioned nonlinear ones. Computers and computer equipment are a special problem due to their frequent concentration in large groups (clusters) [2]. As individual loads, they draw pulse current waveforms from the network with a very high level of distortion, so the total harmonic distortion of this current (THDI) may reach more than 120% [1,2]. However, due to group work in different modes, with different individual parameters (diversity factor), as well as due to the phenomenon of harmonic cancellation and attenuation the THDI of a PC cluster is ranged between 30-40% [2,3]. Furthermore, as their power demand is low in relation to the short-circuit power at the connection point, these values are within the limits stipulated by the international standard IEC 61000-3-4 [1,4].

However, in recent years, the use of cryptocurrencies (Bitcoin, Ethereum, Tether, etc.) is growing, as well as the need to verify their transactions on a public digital ledger (public digital book) known as the blockchain. As this process will also create new cryptocurrency values it is called the Bitcoin, or more generally, the cryptocurrency mining [5]. Unlike individual PCs or their groups (PC clusters) where the power varies during operation, cryptocurrency mining is performed with almost constant power, i.e., with a constant engagement of microprocessor resources. In this case, two problems arise. One is the power demand or efficient operation of the device, i.e., its electricity consumption, and the other is the impact on the power quality in the connected network [6,7]. It should be noted that these devices are of low rated power, so they are connected to a low-voltage single-phase network, i.e., one cryptocurrency mining rig represents a set of 6 graphics cards, which are powered via one or two power supply units. The response to both mentioned problems depends on the quality of the rig, i.e., the optimization of its operation, as well as the construction of the power supply (AC/DC converter with PFC).

There are many papers in the scientific literature that treat the first problem, and a lot of articles and reviews on professional sites (blogs) and journalism are dedicated to that. For the sake of objectivity, only those papers that have been published in the reference scientific literature will be considered here [6-11]. The impact of increasing network losses as a result of the operation of these devices was mainly considered in [6], long-term trends related to changes in the amount of energy per transaction in [8], the cost-effectiveness of mining concerning electricity prices in certain countries and environmental factors in [9], and mining of other cryptocurrencies, beside of Bitcoin in [10]. The issue of the effects on the power quality was less prominent and not researched in more detail. Some results presented in [7] show that such a low interest was a consequence of the higher quality power supply unit applications than in standard PCs, so the recorded current distortion had been less than THDI<10% [7]. However, in the case of larger cryptocurrency mining operations, the distortion of electricity may be more significant, even beyond the standards' permissible limits. This was observed in [11], but more detailed measurements and analyses have not been performed.

This paper aims to present the impact of the cryptocurrency mining rigs, i.e., their power supply units, on the power quality in a low-voltage distribution network and to compare it with the effects of conventional desktop (PC) computers. To enable this, the results of multi-day measurements were used, as well as the appropriate analysis of the measured results in the time and frequency domain.

Vladimir A. Katić – Univerzitet u Novom Sadu, Fakultet tehničkih nauka, Trg Dositeja Obradovića 6 21000 Novi Sad, Srbija (e-mail: katav@uns.ac.rs), (https://orcid.org/0000-0002-0138-8807).

Zoltan J. Čorba – Univerzitet u Novom Sadu, Fakultet tehničkih nauka, Trg Dositeja Obradovića 6 21000 Novi Sad, Srbija (e-mail: zobos@uns.ac.rs)

Aleksandar M. Stanisavljević – Univerzitet u Novom Sadu, Fakultet tehničkih nauka, Trg Dositeja Obradovića 6 21000 Novi Sad, Srbija (e-mail: acas@uns.ac.rs), (https://orcid.org/0000-0002-7156-3869).

II. MEASUREMENTS OF POWER QUALITY INDICES

Professional device C.A. 8332 by Chauvin Arnoux [12] was used to measure electricity quality indices, which follow the European standard EN 50160 [1,4]. The measurements were performed over a period of seven days, continuously at the place of connection of the device, i.e., at the busbars of the distribution cabinet in the low voltage network. The power quality indices of a PC cluster placed in the computer centre and a cryptocurrency mining rig were measured. The measured values included the effective value of voltage and current, frequency, power, power factor (PF), flicker, harmonics of voltage and current, and k-factor. However, due to limited space, only the most significant measurement results will be presented here, namely, those related to work efficiency (active P, reactive Q, distortive D, and apparent power S, as well as PF), i.e., electricity consumption (kWh, kVAh), and the impact on the power quality (total harmonic distortion of voltage and current, THDU, THDI).

A. Measurement results for the computer centre

As part of the activities on the subject of master's academic studies "Quality of electricity", measurements of power quality indices are regularly conducted on the internal network of the Faculty of Technical Sciences. For the purposes of this paper, obtained measurement results at the distribution cabinet of the computer centre during November/December 2019 will be used. Fig. 1 shows the measuring point, and Fig. 2 shows the waveform of the voltage and current of the single-phase network. In the line shown, 42 computers are connected, which have different power supply units HP Lite-On PA 1181-7 and Fujitsu D12-250 P1A with powers of 180 W and 250W, respectively. During the measurement, not all of them were turned on, that is, 28 computers were working continuously. The operation of these computers is characterized by high current distortion (Fig. 2), so in addition to active and reactive power, there is also distortion power.

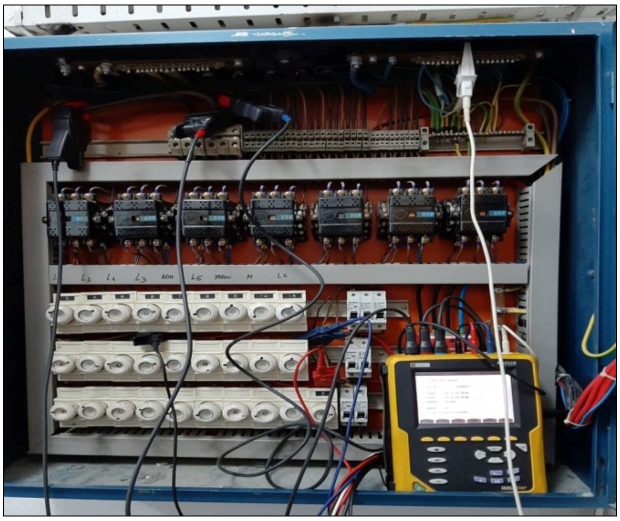

Fig. 1. Photo of measurement location during measurement at the computer centre

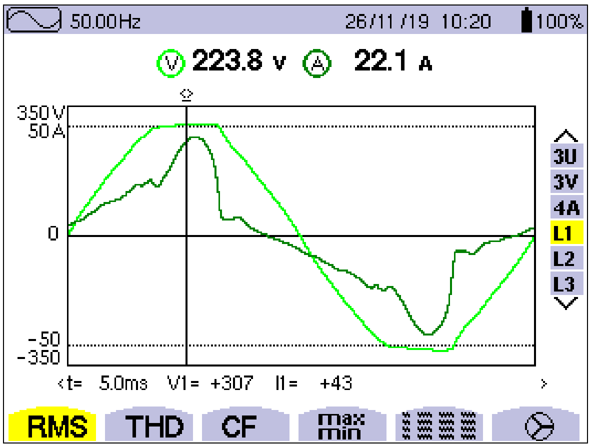

Fig. 2. Voltage and current waveforms of a single phase at the computer centre

Fig. 3 (up) shows the variation of the apparent (S), active (P), and reactive (Q) power, as well as distortion power (D) during a one-week measurement, while Fig. 3 (down) shows their statistical analysis. It can be seen that over 50% of the time computers work in standby (idle) mode, that they are capacitive as the reactive power is Q<0 (this can be also seen from Fig. 2, where the current waveform precedes the voltage one), and that the measured distortion power (D) is negligible. In addition, the measured power factor (PF) presented in Fig.4 indicates significant effects of the PC supply unit capacitance, but also the current harmonic distortion. Fig. 4 shows its variation during the one-week measurement and the statistical analysis. It can be seen that PF was below 0.95 all the time, which indicates a potential problem. In order to better understand all statistical values, Table I gives the most significant results of statistical analysis for all types of power (S, P, Q, and D), as well as for the power factor. It can be seen that power demand is much higher than average power, which shows variation in computers usage.

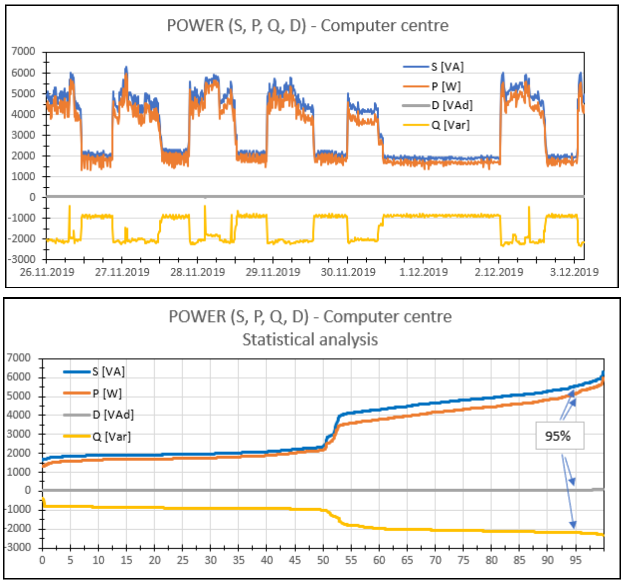

Fig. 3. Variation of the computer centre power demand during one-week measurements: time wave-form (up) and statistical analysis (down)

TABLE I
STATISTICS FOR POWER (S,P,Q,D) AND POWER FACTOR OF THE COMPUTER CENTRE

Power	Minimum	Median (50%)	Average	95% value	Maximum
S [kVA]	1657.3	2348.4	3373.1	5544.1	6290.9
P [kW]	1337.2	2180.7	3029.3	5157.8	5992.5
Q [kVAr]	-381.1	-995.6	-1448.4	-2195.3	-2328.4
D [kVAd]	39.2	50.9	58.6	73.7	75.7
PF	0.79	0,89	0,889	0,936	0,952

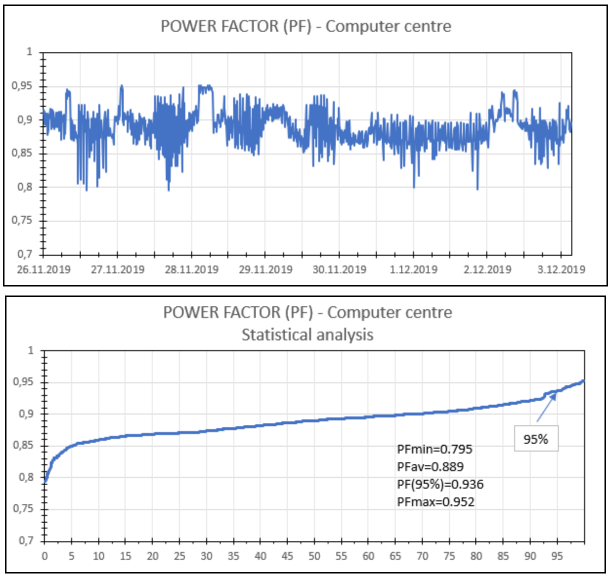

Fig. 4. Variation of the computer centre power factor during one-week measurements: time wave-form (up) and statistical analysis (down)

The observed waveforms of current and voltage (Fig. 2) indicate the existence of harmonic distortion, which is pronounced in the current pulsed waveshape, while in voltage it can be seen as a "flattened top" of the sinusoid. Both distortions are a consequence of the operation of power supply units (in PC and the monitor), which are usually realized as a diode bridge rectifier with a capacitive filtering (for "ironing" of the DC voltage) and additional DC/DC converter (for obtaining different voltage levels). Due to the parallel operation of a large number of computers, the mentioned phenomenon of harmonic cancellation and attenuation is present, so the values of THDI and individual harmonic distortion of the current (HDI) are less than in the case of individual computers. Figs. 5 and 6 show the variation of the THDU (Fig. 5) and THDI (Fig. 6) during one-week measurements. If the results are compared with Fig. 3, it can be seen that the distortions are smaller in the standby ("night" mode) (THDU≈2.2%; THDI≈22%), and that they increase during the working days when the PCs are in active use (THDU≈2.8%; THDI≈45%).

B. *Measurement results of cryptocurrency mining rig*

Cryptocurrency mining uses a dedicated computer assembly (rig) consisting of a power supply unit, mainboard, and graphics cards. Fig. 7 shows an illustrated block diagram of this device. A set of six graphic card units (GCU) were in operation during the measurement, which was powered by two high-quality power supplies: HPE model "ProLiant" DL580 G7 (1200W, Platinum, η=94%) and "Be Quiet!" model Straight Power 11 (650 W, Platinum, η=94%) connected to a single-phase network (230V, 50 Hz). The maximum power of both supplies is 1850W, but they are optimized to work on 1000W. Fig. 8 shows the photo of the treated rig and the location where C.A 8332 was connected.

The main characteristic of the rig´s operation is the constant engagement of the GCU processor, which leads to higher electricity consumption, but also significant thermal losses. For this reason, applied power supply units are of high efficiency (94% -95%), but also with a more complex schematic. They have an additional power factor correction (PFC) unit, which enables close to unity power factor, but also contributes to the significant reduction of harmonic distortion.

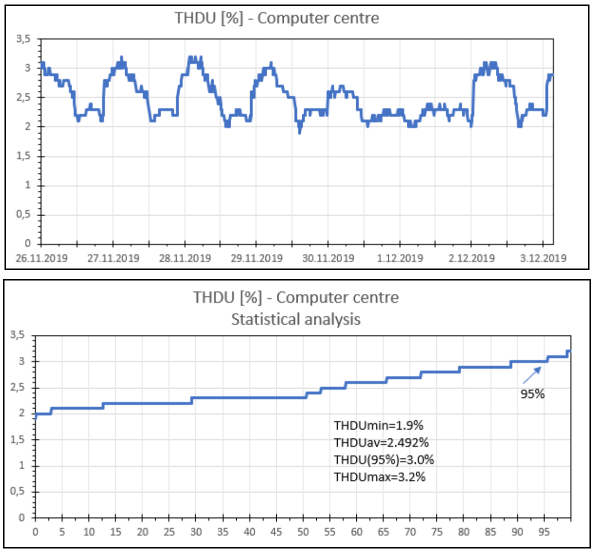

Fig. 5. Variation of the computer centre THDU during one-week measurements: time wave-form (up) and statistical analysis (down)

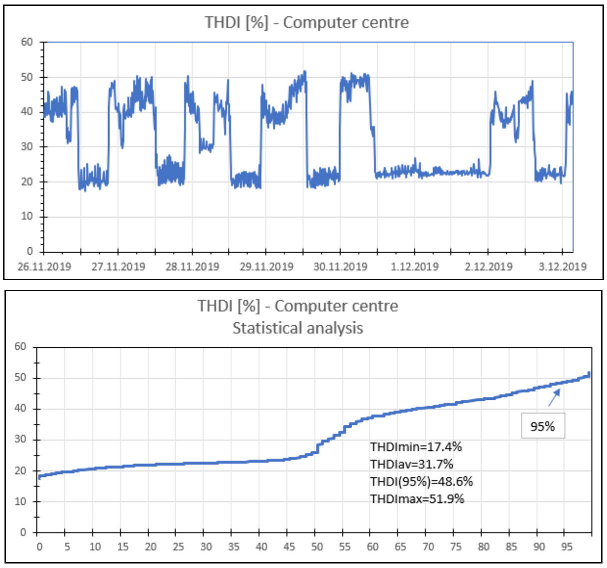

Fig. 6. Variation of the computer centre THDI during one-week measurements: time wave-form (up) and statistical analysis (down)

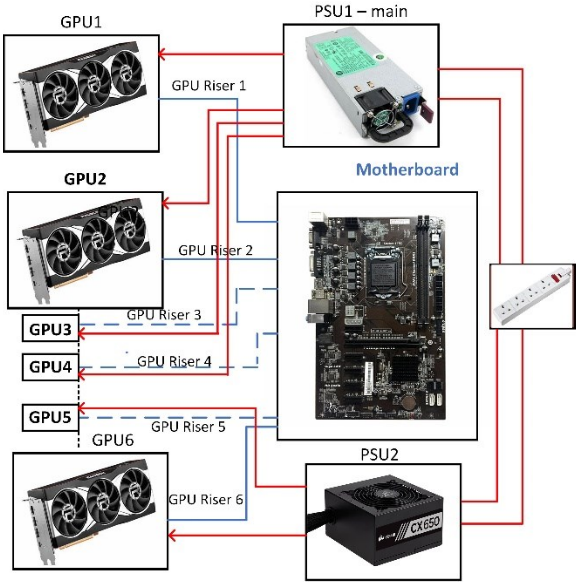

Fig. 7. Block scheme of the cryptocurrency mining rig

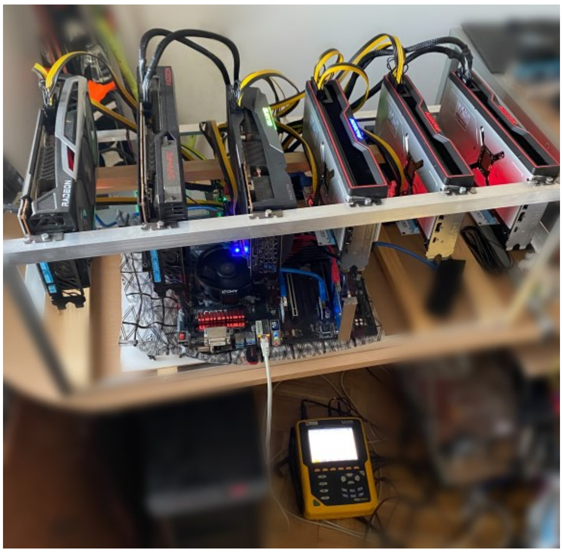

Fig. 8. Photo of measurement location during cryptocurrency mining rig measurement

The measurement results are shown in Figs. 9-14. Fig. 9 shows the waveforms of voltage and current, which are characterized by the flatness of the sinusoidal top and very low current distortion and displacement. Fig. 10 shows the measurement results for different types of power, while Fig. 11 the power factor. It can be seen that there were some short periods with lower power demand, which corresponds to some problems with the Internet and shutting down at the end of the measurement. In order to better understand the statistical values, Table II gives the most significant results of statistical analysis of measured power and power factors for the cryptocurrency mining rig. It can be noticed that the rig works with practically constant power and a close to unity power factor (0.988).

Figs. 12 and 13 show the results of the voltage and current harmonic distortion of the cryptocurrency mining rig. The variation of the THDU during one-week measurements is shown in Fig. 12, while the THDI is in Fig. 13. A low voltage and current distortion can be observed. However, significant increases in current distortion can be observed during the measurement and at the end (Fig.13). These are the periods when there was a significant reduction in processor activity of the GCU i.e., in the mining, when the system operates with lower power (see Fig. 10) and outside the optimal parameters. However, these periods do not significantly affect the overall assessment of current distortion.

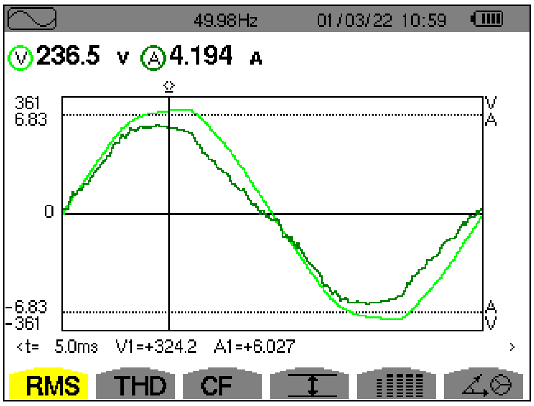

Fig. 9. Voltage and current waveforms of the cryptocurrency mining rig

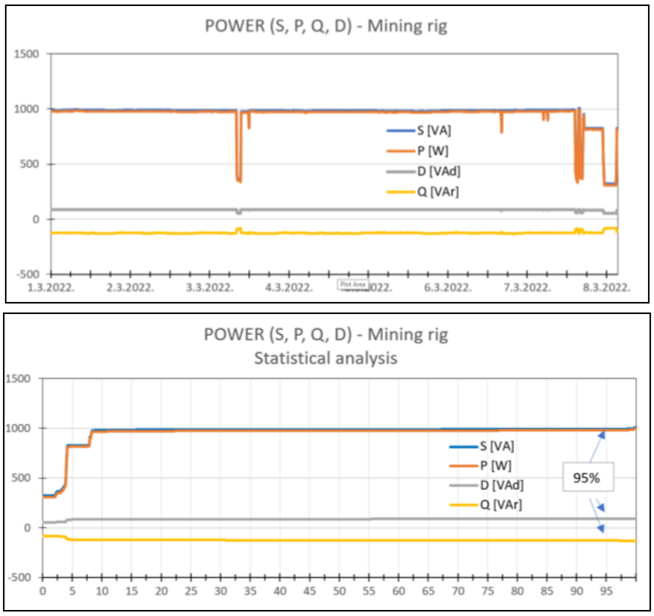

Fig. 10. Variation of the cryptocurrency mining rig power demand during one-week measurement: time wave-form (up) and statistical analysis (down)

III. DISCUSSION

A. *Comparison of PC cluster and Mining rig by distortion*

Commercial PCs, which are widespread and present in many locations are well-known as current and voltage distortion sources in low voltage distribution networks [1]. If they are clustered, the distortion is much less than if a single one is considered [2]. Yet, the current harmonic distortion limits stipulated by international standards are not surpassed.

Still, the voltage distortion is increased (depending on the power demand of the PC cluster) and may contribute to the appearance of some negative effects at other connected loads. The remaining problems are high and distorted current in the neutral conductor and poor power factor.

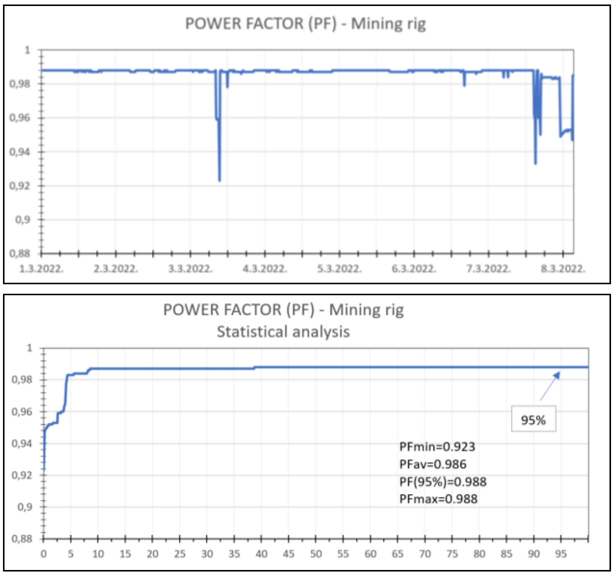

Fig. 11. Variation of the cryptocurrency mining rig power factor during one-week measurements: time wave-form (up) and statistical analysis (down)

TABLE II
STATISTICS OF POWERS (S,P,Q,D) AND POWER FACTOR OF THE CRYPTOCURRENCY MINING RIG

Power	Mini-mum	Median (50%)	Average	95% value	Maximum
S [VA]	323.8	987.8	956.1	992.7	1007.0
P [W]	308.4	975.7	943.9	980.9	994.9
Q [VAr]	-81.3	-125.4	-123.9	-128.6	-1431.3
D [VAd]	53.3	87.8	86.3	88.5	89.6
PF	0.923	0.988	0.986	0.988	0.988

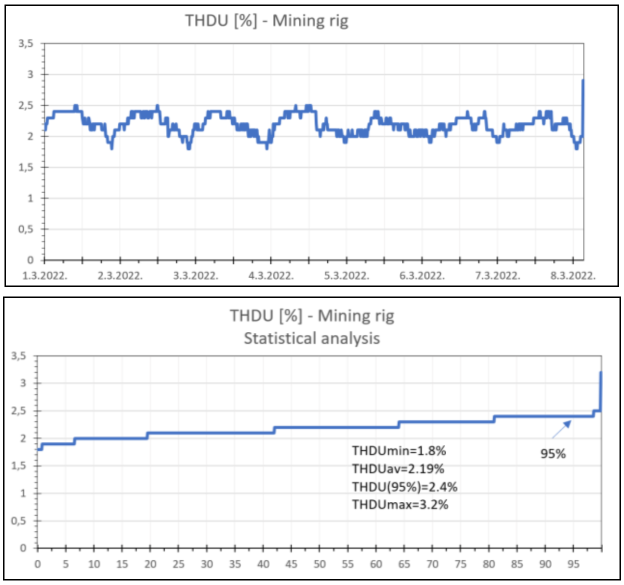

Fig. 12. Variation of the cryptocurrency mining rig THDU during one-week measurements: time wave-form (up) and statistical analysis (down)

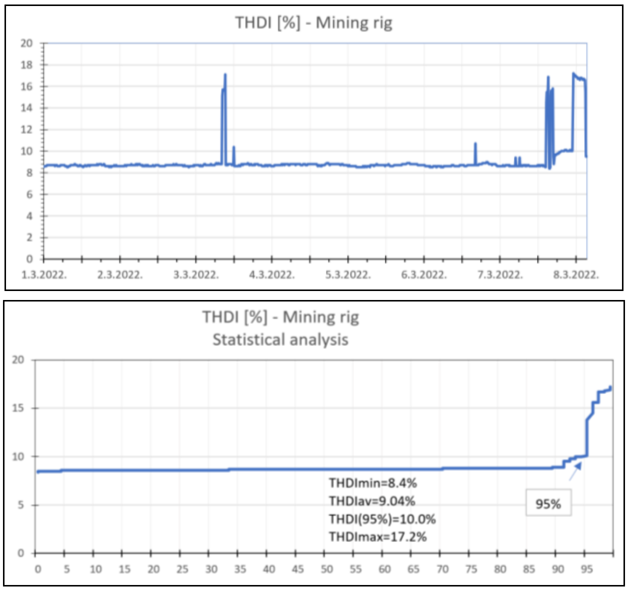

Fig. 13. Variation of the cryptocurrency mining rig THDI during one-week measurements: time wave-form (up) and statistical analysis (down)

In the case of the connection of the cryptocurrency mining rig to the low voltage distribution network the measured harmonic distortion factors and power factor are good and in accordance with international standards. It shows that the power supply units of the rig are carefully selected to enable optimum operation.

Table III shows a comparison of main power quality indicators recorded during measurements of the PC cluster and the cryptocurrency mining rig. It can be seen that the cryptocurrency mining rig has superior performance. Such a conclusion is not a surprise as the power supply units of the mining rig are of much higher quality than the ones of the PC in the cluster.

TABLE III
COMPARISON OF DISTORTION FACTORS AND POWER FACTORS OF THE PC CLUSTER AND THE MINING RIG

	THDU (95%)	THDU (Max.)	THDI (95%)	THDI (Max)	PF 95%	PF (Max)
PC cluster	3.0%	3.2%	48.6%	51.9%	0,936	0,952
Mining rig	2.4%	3.2%	10.0%	17.3%	0.988	0.988

B. *Comparison of PC cluster and Mining rig by power and electricity consumption*

The PC cluster and the cryptocurrency mining rig comparison by power demand and electricity consumption is more interesting. The measurement results show that the power demand of the cryptocurrency mining rig is much higher. Moreover, it is constant over time, so the low-voltage distribution network may see it as a high (~1000W) load of a resistive nature (like some heater).

Fig. 14 (up) shows a comparison of a PC cluster and the cryptocurrency mining rig's active power demand. The power demand of the PC cluster is downsized to the one comparable with the cryptocurrency mining rig (~1000 W). Fig.14 (down) shows the same comparison, but regarding the electricity consumption. It can be seen that the power demand of the cryptocurrency mining rig was in some periods much higher, while in others similar to the PC cluster. Regarding electricity, the consumption was much higher (almost twice).

C. Effects on voltage distortion (THDU)

Considering the above observations, it is rational to assume that the operation of the PC cluster, as well as the cryptocurrency mining rig, may have some effects on the low-voltage distribution network voltage harmonics. From Fig.5 it can be seen that there is a high difference between the voltage harmonic levels during the night (PCs are in idle mode) and during the day. It can be estimated that the PC cluster operation increase voltage harmonics from $THDU_{night}$=2.3% to $THDU_{day(95\%)}$=3.0%, i.e., for 30%, up to $THDU_{day(max)}$=3.2%, i.e., for almost 40%.

In the case of the cryptocurrency mining rig, there are no differences between night and day, so it is difficult to estimate the rig´s effect on voltage harmonics. Still, from Figs.10 and 14, it can be noticed some periods with low power operation (when the mining process has been ended and the rig had continued operation in an idle mode), i.e., with a reduced effect on voltage harmonics. Therefore, observing corresponding Fig.12 it can be estimated that the cryptocurrency mining rig operation increase voltage harmonics from $THDU_{min}$=1.8% to $THDU_{day(95\%)}$=2.4%, i.e., for around 33%, up to $THDU_{day(max)}$=3.2%, i.e., 78%!

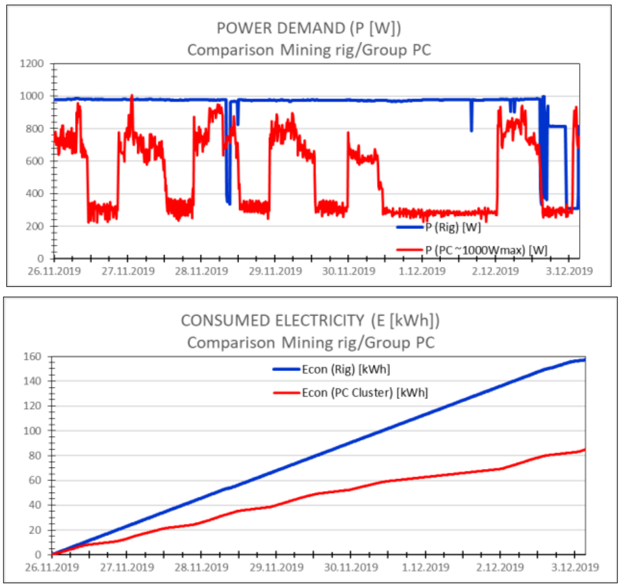

Fig.14. Comparison of the cryptocurrency mining rig and a PC cluster of the same size: of power demand (up) and consumed electricity (down)

IV. CONCLUSION

The paper presents research results of the cryptocurrency mining rig's effects on the power quality at the low-voltage distribution network. The most important power quality indices obtained during one-week measurements are recorded and discussed. For comparison, similar research has been worked out for a PC cluster.

The research results show that cryptocurrency mining rig has higher power demand and electricity consumption than the similar-sized PC cluster. The power factor is much better (close to unity) than the PC cluster has (below 0.95). It has a lower effect on current distortion (THDI), while the effects on voltage distortion (THDU) are similar to the PC cluster ones.

However, the THDU of the cryptocurrency mining rig might increase significantly if more rigs are connected at the same bus and endangered power (voltage) quality for other loads. Further research will be focused on this problem.

ACKNOWLEDGEMENT

This work was supported by the Republic of Serbia, Ministry of Education, Science, and Technological Development, through the Integrated and Interdisciplinary Research project entitled “Innovative Scientific and Artistic Research from the Faculty of Technical Sciences Activity Domain” under Grant No. 451-03-68/2022-14/200156.

REFERENCES

[1] V.A. Katić, *“Kvalitet električne energije – viši harmonici”*, Monografija, Br. 6, Fakultet tehničkih nauka, Novi Sad, Srbija, 2002.

[2] V.A. Katić, S.V. Mujović, V.M. Radulović, J.S. Radović, “The Impact of the Load Side Parameters on PC Cluster’s Harmonics Emission”, *Advances in Electrical and Computer Engineering*, Vol. 11, No. 1, 2011, pp.103-110. https://doi.org/10.4316/AECE.2011.01017

[3] L. Michalec, M. Jasinski, T. Sikorski, Z. Leonowicz, L. Jasinski and V. Suresh, „Impact of Harmonic Currents of Nonlinear Loads on Power Quality of a Low Voltage Network – Review and Case Study”, *Energies*, 2021 Vol. 14, Paper #3665, Open Access, https://doi.org/10.3390/en14123665

[4] V.A. Katic, „Network Harmonic Pollution - A Review and Discussion of International and National Standards and Recommendations”, 3rd Inter. Power Electronic Congress - CIEP '94, Puebla, Mexico, 21-25 Aug. 1994, https://doi.org/10.1109/CIEP.1994.494413

[5] U. Mukhopadhyay, A. Skjellum, O. Hambolu, J. Oakley, L. Yu, and R. Brooks, „A Brief Survey of Cryptocurrency Systems“, 2016 14th Conference on Privacy, Security and Trust (PST), Auckland, New Zealand, 12-14. Dec. 2016, https://doi.org/10.1109/PST.2016.7906988

[6] D. Stevanović, M. Andrejević Stošović, M. Dimitrijević, and P. Petković, “Utility losses due to cryptocurrency mining”, 10th Conf. on ICT Innovations, 2018, Web Proceedings, pp.27-36. https://proceedings.ictinnovations.org/attachment/paper/479/utility-losses-due-to-cryptocurrency-mining.pdf

[7] K.A. Wheeler, A.W. Bowers, C.H. Wong, J.Y. Palmer, and X. Wang, “A Power Quality and Load Analysis of a Cryptocurrency Mine”, 2018 IEEE Electrical Power and Energy Conference (EPEC), Toronto, Canada, 10-11 Oct. 2018, https://doi.org/10.1109/EPEC.2018.8598358

[8] Y-D. Song and T. Aste, “The Cost of Bitcoin Mining Has Never Really Increased”, *Frontiers in Blockchain*, 22 October 2020, Vol. 3, Article 565497, https://doi.org/10.3389/fbloc.2020.565497

[9] S.L.N. Alonso, J. Jorge-Vázquez, M.Á.E. Fernández, and R.F.R. Forradellas, “Cryptocurrency Mining from an Economic and Environmental Perspective. Analysis of the Most and Least Sustainable Countries”, *Energies*, 2021 Vol. 14, Paper #4254, Open Access, https://doi.org/10.3390/en14144254

[10] U. Gallersdorfer, L. Klaasen, and C. Stoll, “Energy Consumption of Cryptocurrencies Beyond Bitcoin”, *Joule*, Vol. 4, pp. 1839–1851, 2020, https://doi.org/10.1016/j.joule.2020.07.013

[11] I. Bitir-Istrate, C. Gheorghiu, and M. Gheorghiu, “The transition towards an environmental sustainability for Cryptocurrency mining”, E3S Web of Conferences, Vol. 294, 2021 6th Int. Conf. on Sustain. and Renewable Energy Eng., https://doi.org/10.1051/e3sconf/202129403004

[12] ***, “Qualistar+ C.A 8332”, Chauvin Arnoux, Datasheet, http://qualistar.chauvin-arnoux.com/en

Prediction of voltage dips characteristics in IEEE 13-bus test grid using harmonic footprint

Aleksandar M. Stanisavljević, *Member, IEEE,* and Vladimir A. Katić, *Senior Member, IEEE*

Abstract—**In this paper, the method of harmonic footprint (HF), as a significant feature of voltage dip is applied for a dip characterization. The dips are generated using an internationally verified test grid, the IEEE 13-bus test grid. First, the method of the HF is presented and described. Then, the IEEE 13-bus test grid modified by adding the distributed generators (wind or solar power) is described. Faults were simulated in the test network, and the values of the HF parameters were determined. The results were used for the voltage dips characteristics prediction. The results of simulation and prediction were compared and the mutual deviation (error) was determined. It is shown that the HF can be used for the early voltage dips characteristic prediction and further applied for training a deep-learning algorithm. Some limitations have been observed and their mitigation will be a topic of future research.**

Index Terms—**Electric power quality, Voltage Dips, Harmonic footprint, Test grids**

I. INTRODUCTION

In recent years, power quality issues have become more relevant, and significant attention had been paid to the related topics. In addition to the quality of delivery, the quality of delivered electrical energy is also important, which is often recognized as the quality of voltage. Voltage dips or sags are a consequence of disturbances in the operation of the power system and may have serious negative effects on industrial loads and connected distributed generation (DG) [1]. Particularly inconvenient are outages of industrial plants or the shutdown of small power plants in the distribution network, which can have major financial consequences. For these reasons, great research efforts are focused on the rapid detection and successful characterization of voltage dips [2, 3] and techniques of its compensation [4].

One of the successful methods for the dip's characterization is the application of harmonic footprint [5]. It provides the possibility for early characterization of a voltage dip so that in the first phase of fault its characteristics can be predicted with high probability [5, 6, 7]. For the sake of more accurate categorization and faster response, it is convenient to apply some of the methods of artificial intelligence, i.e., machine learning or deep learning [8, 9]. However, the main problem is the training, i.e., providing a huge number of adequate and different cases of voltage dips. Voltage dips occurrence in real grids is relatively rare, so long-term measurements are needed, which is costly and requires specialized equipment. Therefore, the use of synthetic dips based on mathematical calculations or simulated ones, based on the response from the grid simulation model are possible solutions.

This paper aims to test the application of the harmonic footprint method for the prediction of the voltage dip characteristics and to discuss such an approach for training a deep learning algorithm. The testing is based on recognizable and internationally verified references or test grids [10]. First, the method of harmonic imprinting is presented and described. Then, the IEEE 13-bus test grid is described, which is modified by additional distributed generators (wind and solar power plants). Faults were simulated in the test grid, and the values of the harmonic footprint parameters were determined for the various types of voltage dips thus obtained. The results of modeling and prediction of the voltage dips characteristics were compared and the mutual deviation (error) was determined.

II. HARMONIC FOOTPRINT

It is generally known that voltage dips are a consequence of faults in the network, high-power motor drive starting, or power transformer energizing [1]. During these events, a sudden rise of current may be observed, which distorts the voltage waveform all over a huge area of the grid. If the Fourier transformation is performed, the second and several other low-order harmonics may be noticed [1, 5]. If they are traced as a group, which consists of the 2nd, the 3rd, then 5th, and the 7th harmonics, and monitored throughout a voltage dip, a specific waveform may be observed [5]. It was named harmonic footprint (HF) [5]. Its mathematical representation is:

$$HF = \frac{\sqrt{\sum_{n=2,3,5,7} U_n^2}}{U_1^2} \cdot 100 \quad [\%] \tag{1}$$

where n is harmonic order, and U_n is r.m.s. value of the *n-th* harmonic.

The harmonic footprint is an important feature of a voltage dip. It appears at each voltage dip transition state, i.e., at the start of the dip and its end. Additionally, the HF may be recorded if the dip progresses from single-ground one to two-phase to ground or if some other voltage transition occurs. It

---

Aleksandar M. Stanisavljević with the University of Novi Sad, Faculty of Technical Sciences, Trg Dositeja Obradovića 6, 21000 Novi Sad, Serbia (e-mail: acas@uns.ac.rs).

Vladimir A. Katić is with the University of Novi Sad, Faculty of Technical Sciences, Trg Dositeja Obradovića 6, 21000 Novi Sad, Serbia (e-mail: katav@uns.ac.rs).

can be obtained in a few milliseconds, so the HF method represents one of the fastest tools [11].

The main parameters of an HF are its initialization (start-up), maximum value (MHF), and width (wHF). They may be used for voltage dip detection (start-up moment) and prediction of voltage dip magnitude (depth), and duration, i.e., for fast and accurate characterization [5, 6, 7]. The HF and its parameters are presented graphically in Fig.1.

The HF method was tested with voltage dips recorded in various real distribution grids, and the configurations of the different distribution grids did not significantly affect the accuracy of the algorithm [5, 6, 7]. Furthermore, it can be noted that stochastic quantities, like fault resistance and fault inception angle, have some influences on the HF, but their effects are combined with the distance from the fault (line impedance between the fault location and voltage dip recording point). Generally, the total impedance has an inversely proportional effect, i.e., if it is higher, the HF is usually of a smaller value. The fault inception angle does not influence the precision of the method, as it is tested with real faults, which had different fault inception angles.

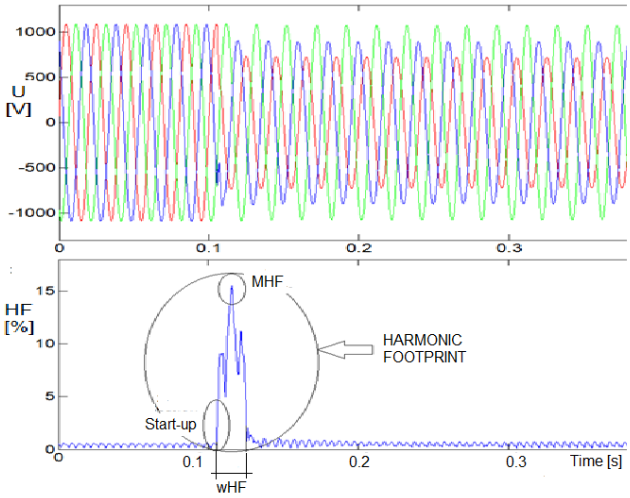

Fig.1.Harmonic footprint characteristics

III. MODIFIED IEEE 13-BUS TEST GRID

There are several different test grids available for the simulations of voltage disturbances in a grid [10]. In this paper, the IEEE 13-bus test grid will be used. It represents a sample of the North American distribution grid consisting of three-phase lines, with two-phase and single-phase ones close to the ends of feeder laterals (load side). The supply voltage is 155 kV, while the distribution voltage is 4.16 kV. The grid is loaded with constant current, constant impedance, and constant power consumers, so that the total load is 3.466 MW. Unity power factor is assumed.

The test grid was modified with the addition of DGs, to make a better representation of a modern distribution grid. The optimal DG size is 2.5 MW connected at bus #633 [12], but in this paper, it will not be concentrated. A 2 MW wind plant was added at bus #633, and a 0.5 MW solar PV system at bus #652. The wind plant consists of four wind generators of 0.5 MW each interconnected with the grid via a power transformer and a one-kilometer-long power line. The solar PV plant is an on-grid solar PV system of 0.5 MW connected to the grid at bus #652 via a power transformer, which is further connected to the mainline at bus #648 via a 2 km line. These plants are dispatchable, but also comply with low-voltage ride-through (LVRT) requirements [13]. Therefore, they can support the grid during the duration of a voltage dip.

The IEEE 13-bus test grid is available as the Matlab/Simulink simulation model in [14]. Its modification is also done in Matlab/Simulink and its one-line diagram is presented in Fig.2.

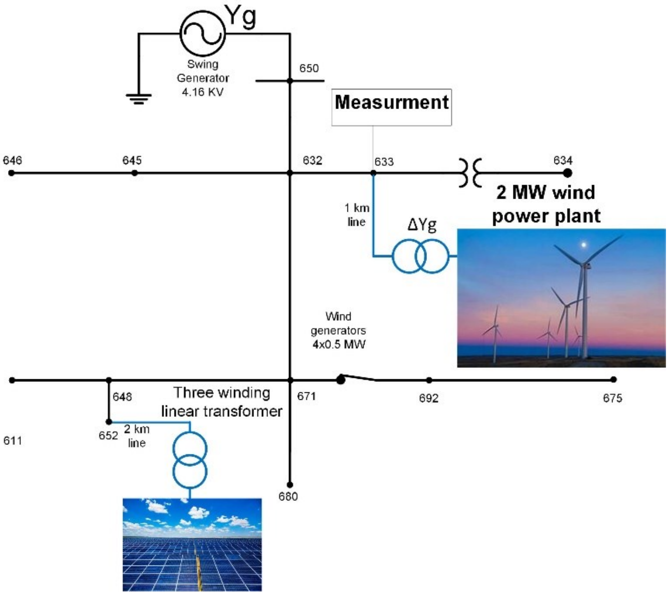

Fig.2. Modified IEEE 13-bus test grid with added DGs

IV. VOLTAGE DIPS SIMULATIONS

The simulated voltage dips are the result of hypothetical faults in the test grid. The faults are generated at buses #692, #633, and #671 with a rated voltage of 4.16 kV. Different faults are simulated: single-phase to the ground (line-to-ground), two-phase faults (line-to-line), and a three-phase to the ground.

The voltage dips are measured (recorded) at bus #633. Two main features are monitored, the magnitude of voltage dip (MoVD) and duration.

The magnitude of a voltage dip represents the voltage during the dip as a percentage of the rated voltage, i.e., it is defined as:

$$MoVD = \frac{U_{rem.}}{U_r} \cdot 100 \ [\%] \qquad (2)$$

where U_{rem} is the remaining voltage during the voltage dip at the observing bus and U_r is the rated voltage.

The duration of a voltage dip is defined as a period when the voltage at the observing bus is lower than $0.9U_r$.

Fig. 3 shows an example of the single-phase (line-to-ground) voltage dip recorded at bus #633. The fault occurred on line 1 (L1, the blue line) at bus #671. As the result, the voltage at observing bus #633 suddenly decreases from the rated to 5% of the rated, i.e., the MoVD=5%. The voltages of the other two lines (L2, the red one, and L3, the green one) experience voltage swells, i.e., increased by around 15%. The duration of the voltage dip was 0.16 seconds. After that, the fault was cleared and all voltages returned to the rated values. It can be easily observed that significant voltage distortion occurred during the voltage transient states, i.e., when a fault and corresponding voltage dip initiated (started) and when it ended. In these periods the HF appears, and it can be calculated and recorded.

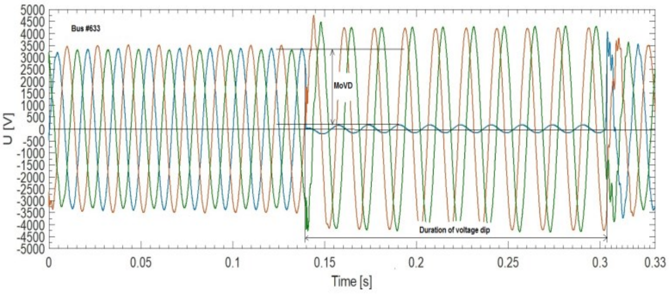

Fig. 3. Single-phase voltage dip recorded at bus #633.

Beside the single-phase to the ground (line-to-ground) fault and corresponding voltage dip presented in Fig. 3, six more cases of different faults were simulated. They are presented in Table I. It can be seen that three single-phase to the ground faults which occurred on the busses #692, #671, and #648 were simulated, together with the additional three phase-to-phase (line-to-line) faults on the same busses and one three-phase to the ground on bus #643. In total, seven faults were tested.

The recorded voltage dips on bus #633 were also summarized in Table I. It shows the main characteristics of the simulated voltage dips, their magnitude (given by MoVD), and their duration. It can be seen that for single-phase to the ground faults the MoVDs are very small, as well as for the three-phase to the ground fault, while in cases of phase-to-phase faults the MoVD values are around 50%.

V. HARMONIC FOOTPRINT PARAMETERS DETERMINATION

The harmonic analysis of the tested voltage dips resulting in their harmonic footprint was performed. An example of the HF for the case of the voltage dip presented in Fig. 3 (fault No.2 in Table I) is shown in Fig. 4. It can be seen that there are two HFs, one at the beginning of the dip and the other at its end. For further analysis, the first one will be considered. Specific parameters of the harmonic footprint can be distinguished, its MHF and wHF. For the voltage dip characterization, the MHF is important. It can be seen that the MHF value in this case (single-phase to the ground fault) is 36%.

A similar analysis is done for all other recorded voltage dips cases. Due to limited space, the HF diagrams for the other cases will not be shown here. The results for the MHF are presented in Table I (column to the right). It can be seen that in the cases of the low MoVD values (deep voltage dips) the MHF values are above 30%, while for the higher MoVDs the MHF is lower.

TABLE I
SIMULATED VOLTAGE DIPS CHARACTERISTICS

No.	Type of faults / Voltage dip characteristics	MoVD [%]	Duration [s]	MHF [%]
1	Single-phase to the ground at bus #692	7	0.18	37
2	Single phase to ground at bus #671	5	0.16	36
3	Single-phase to the ground at bus #648	8	0.20	35
4	Phase A and B at bus #692	48	0.30	24
5	Phase A and C at bus #671	49	0.33	25
6	Phase C and B at bus #648	62	0.50	18
7	Three-phase to ground at bus #643	9	0.80	32

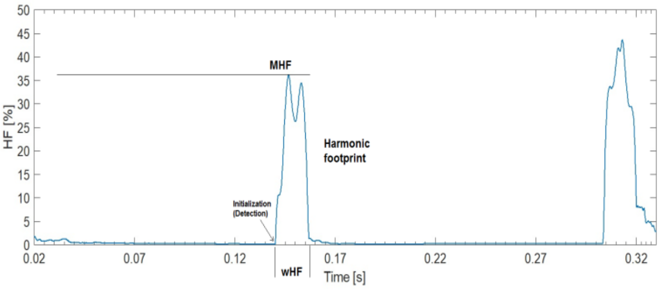

Fig. 4. The HF for the case of the single-phase voltage dip recorded at bus #633 for fault No. 2 in Table I

VI. ESTIMATION OF THE VOLTAGE DIPS CHARACTERISTICS

The obtained HF parameters can be used for the early prediction of the voltage dip characteristics, its magnitude (MoVD), and its duration. These characteristics can be predicted using the maximum value of the HF (MHF) according to the expressions given in [6, 7].

The prediction function calculates voltage magnitude as a function of the maximum value of the HF:

$$MoVD^{*} = f(MHF) \tag{3}$$

where $MoVD^{*}$ is the predicted value of the voltage dip magnitude, and MHF is a global maximum of the HF during the first transient stage. The voltage dip magnitude can be calculated using the following expression [6]:

$$\begin{aligned} \log_{10}(MoVD^{*}) &= 1.913 + 0.00284 \cdot MHF + \\ &+ 0.000036 \cdot MHF^{2} - 0.000024 \cdot MHF^{3} \end{aligned} \tag{4}$$

The results of the calculations are presented in Table II. For the generated faults (Table I) the values of the predicted MoVD* are presented in the second column of Table II. For comparison, the simulated (recorded) MoVD values are given in the third column (repeated from Table I). It can be seen that predicted values are close to the actual (simulated) ones. The absolute errors of prediction are given in the third column of Table II. It can be seen that these errors are below 9 percent. The average absolute error of the prediction is 4.2%, while r.m.s. error is 5.12%. It can be concluded that the prediction can be successfully performed with an acceptable error of prediction.

For prediction of the voltage dip duration, the method presented in [7] is used. The method uses the *MHF* values to calculate the probability function *f(MHF)* [7]:

$$f(MHF) = (1 + e^{9.15 - 0.23202MHF})^{-1} \tag{5}$$

The probability function determines the probability of the voltage dip duration being predicted as momentary or temporary. It is a sigmoid function, so two zones (momentary or temporary) can be distinguished easily. If the *f(MHF)* is less than 0.4, which corresponds to MHF<37.7% the voltage dip is momentary, i.e., less than 3 seconds. If the *f(MHF)* is above 0.6 (MHF>41.2%) then the voltage dip is temporary, i.e., longer than 3 s. In between is uncertainty or border zone, where both solutions are possible.

The probability function is calculated for the obtained MHF values and presented in Table III. It can be seen that for all observed cases of the voltage dips predicted duration was "momentary", i.e., less than 3 s, which is in accordance with the actual duration. Therefore, the prediction was true.

TABLE II
VOLTAGE DIPS MAGNITUDE PREDICTION AND PREDICTION ERROR

Fault No.	Predicted MoVD* [%]	Simulated MoVD [%]	Absolute Error [%]
1	7.11	7	0.11
2	8.75	5	3.75
3	10.65	8	2.65
4	46.79	48	1.21
5	42.81	49	6.19
6	68.52	62	6.52
7	17.96	9	8.96
The average absolute error of prediction			4.20
Root mean squared error			5.12

TABLE III
VOLTAGE DIPS DURATION PREDICTION AND PREDICTION ACCURACY

Fault No.	Probability function *f(MHF)*	Predicted VD DURATION [S]	Simulated VD DURATION [S]	Prediction accuracy
1	0.362	Momentary (<3s)	0.18	TRUE
2	0.311	Momentary (<3s)	0.16	TRUE
3	0.263	Momentary (<3s)	0.20	TRUE
4	0.027	Momentary (<3s)	0.30	TRUE
5	0.034	Momentary (<3s)	0.33	TRUE
6	0.001	Momentary (<3s)	0.50	TRUE
7	0.101	Momentary (<3s)	0.80	TRUE

VII. DISCUSSION

The harmonic footprint presents a unique feature of a voltage dip, which may be used for the prediction of its characteristics. Moreover, it offers the possibility of dip detection and obtaining its early characterization. The presented results show that the simulated voltage dips have been analyzed adequately and that the predicted characteristics are true and acceptable regarding prediction error.

The predicted dip magnitudes correspond to the simulated ones with the r.m.s. error of 5.12%, which is acceptable in engineering practice. The predicted dip durations were true, but the prediction was limited to only two options – momentary (less than 3 s) and temporary (more than 3 s). Additional problem is that the HF is not able to predict the exact duration of voltage sag, so the whole period of voltage sag should be recorded. In that case, the two HFs should be calculated (at the beginning and the end of a voltage dip) and their detection times compared (see Fig.4). Other possible solutions will be sawn in future research.

The results also show that simulated voltage dips may be used for creating a database for the training of a deep learning algorithm. Available reference or test grids (IEEE or others) are adequate and suitable, so many different cases may be simulated.

Still, the number of simulated cases is limited, as for the deep-learning algorithm or any other machine learning one high number of input data is needed. One solution is to use the test grids with more buses (feeders) where there are more options to generate the faults and obtain voltage dips. There are other options and they will be the topic of future research.

VIII. CONCLUSION

The voltage dips characterization is an important task for modern industrial or other loads, as well as for distributed generation and protection of the distribution network. The use of artificial intelligence and deep-learning algorithms for solving this task proved a good solution but require a huge database for the algorithm training process.

In previous papers, the authors have presented that the harmonic footprint, as a voltage dip feature, can be successfully implemented for the prediction of voltage dip characteristics. These results were based on the measurement results obtained in the real grid.

The result of this paper shows that simulation in the referenced test grids can be also used for that purpose. The harmonic footprint has been successfully applied for a voltage dip early characterization. It proves that such an approach can be also applied for the generation of an artificial (simulated) set of voltage dip cases (characteristics) and used for deep-learning algorithm training. Some limitations of this method have been observed, so future work will focus on their mitigation.

ACKNOWLEDGMENT

This work was supported by the Republic of Serbia, Ministry of Education, Science, and Technological Development, through the Integrated and Interdisciplinary Research project entitled "Innovative Scientific and Artistic Research from the Faculty of Technical Sciences Activity

Domain” under Grant No. 451-03-68/2022-14/200156.

REFERENCES

[1] M.H.J. Bollen, *Understanding Power Quality Problems – Voltage Sags and Interruptions*, IEEE Press - Series on Power Engineering, New York, USA., 2000.

[2] P. Khetarpal and M.M. Tripathi, “A critical and comprehensive review on power quality disturbance detection and classification, “*Sustainable Computing: Informatics and Systems*, Vol.28, Paper #100417,2020.

[3] A.E.L. Rivas and T. Abrao, “Faults in smart grid systems: Monitoring, detection, and classification,” *Electric Power Systems Research*, Vol.189, Paper #106602, pp.1-26, 2020.

[4] A.H. Soomro, A.S. Larik, M.A. Mahar, A.A. Sahito, A.M. Soomro, and G.S. Kaloi, “Dynamic Voltage Restorer - A comprehensive review”, *Energy Reports*, Vol. 7, pp. 6786-68905, 2021.

[5] V.A. Katić and A.M. Stanisavljević, “Smart Detection of Voltage Dips Using Voltage Harmonics Footprint,” *IEEE Trans. Ind. Applications,* vol. 54, no. 5, pp. 5331–5342, 2018.

[6] A.M. Stanisavljević and V.A. Katić, “Magnitude of Voltage Sags Prediction Based on the Harmonic Footprint for Application in DG Control System,” *IEEE Trans. Ind. Electronics*, vol. 66, no. 11, pp.8902–8912, 2019.

[7] A.M. Stanisavljević, V.A. Katić, and S.Lj. Milićević, “A method for real-time prediction of the probability of voltage sag duration based on harmonic footprint,” *IEEE Access*, Vol.10, pp.23757-23774, 2022.

[8] A.K. Ozcanli, F. Yaprakdal, and M. Baysal, “Deep learning methods and applications for electrical power systems: A comprehensive review,” *Int. Journal of Energy Research*, Vol.44, pp.7136-7157, 2020.

[9] R. Turović, D. Dragan, G. Gojić, V.B. Petrović, D.B. Gajić, A.M. Stanisavljević, and V.A. Katić, “An End-to-end Deep Learning Method for Voltage Sag Classification,” *Energies*, Vol.15, Paper #2898, pp.1-22, 2022.

[10] A.M. Stanisavljević, V.A. Katić, B.P. Dumnić, and B.P. Popadić, “A brief overview of the distribution test grids with a distributed generation inclusion case study,” *Serbian Journal of Electrical Engineering*, Vol.15, No.1, pp.115-129, 2018.

[11] A. Usman and M.A. Choudhry, “An Efficient and High-Speed Disturbance Detection Algorithm Design with Emphasis on Operation of Static Transfer Switch,” *Advances in Electrical and Computer Engineering*, Vol. 21, No. 2, pp.87-98, 2021.

[12] M. Shaaban and J.O. Petinrin, “Sizing and sitting of distributed generation in distribution systems for voltage improvement and loss reduction,” *Intern. Journal of Smart Grid and Clean Energy*, Vol.2, No.3, pp.350-356, Oct. 2013.

[13] R. Hiremath and T. Moger, “Comprehensive review on low voltage ride-through capability of wind turbine generators,” *Int. Trans. on Electrical Energy Systems*, Vol.30, Paper #e12524, pp.1-26, 2020.

[14] https://www.mathworks.com/help/physmod/sps/ug/ieee-13-node-test-feeder.html;jsessionid=0abf70e84f19a1618f96de0a91e3

Optimal Power Dispatch in Distribution Networks with PV Generation and Battery Storage

Jordan Radosavljević, Miloš Milovanović, Nebojša Arsić, Andrijana Jovanović, Bojan Perović and Jovan Vukašinović

***Abstract*—Numerous researchers in the last two decades have intensively dealt with various aspects of the integration of renewable energy sources (RES) into distribution networks (DNs). It has been shown that optimal planning and operation of RES can achieve positive effects, both in terms of technical performance of the system, and from the environmental and economic aspects. However, the uncontrollability and stochastic nature of wind speed and solar irradiance as the primary sources of RES remained their main shortcomings. The energy crisis that has been present lately imposes the need for much more flexible use of RES. This means finding technically efficient and economically acceptable solutions for energy storage, in order to fully exploit the potential of RES integrated into the system. This paper deals with the issues of the optimal operation and management of rechargeable batteries for energy storage in DNs with PV generation.**

***Index Terms*—Distribution networks, Renewable energy sources, Battery energy storage, Optimal power flow**

I. INTRODUCTION

In the last twenty years, we have witnessed the expansion of renewable energy sources (RES), primarily wind and solar photovoltaic (PV) power plants. The development and application of these technologies have several causes. First of all, it is the constant growth of the electricity consumption and need for new generation capacities. Another, no less important cause, is the ultimative request to limit the use thermal power plants in order to reduce global warming due to CO_2 emissions. In addition, the deregulation and liberalization of electricity market and preferential prices for green energy have contributed rapid growth of RES in the last two decades [1].

Wind and solar technology is becoming cheaper year by year [2], which makes it widely available. There are wind and solar power plants with installed capacity of several hundred MW connected to the transmission network. In addition, there has long been a trend of building smaller so-called distributed energy sources from several kW to several MW, which are integrated into distribution networks (DNs).

A large number of papers have been written on the topic of the distributed energy sources. Various aspects in their planning, operation and control have been explored. It has been shown that optimal planning and control can maximize their positive effects, such as reducing power losses, improving voltage profiles, increasing the supply reliability in DNs, reducing greenhouse gas emissions, etc. However, the uncontrollability and stochastic nature of wind speed and solar irradiance as primary sources of RES remained their main shortcomings.

The energy crisis that has been present recently, imposes the need for much more flexible use of RES. This means finding (using) technically efficient and economically acceptable solutions for energy storage, in order to fully use the potential of RES integrated into the DN.

There is no way to directly store active electricity. There are more or less developed technologies and solutions for indirect storage of the electricity, i.e. converting the electricity into another type of the energy that can be stored in a certain medium. The energy stored in this way is, when necessary, converted back into the electricity, which is injected into the transmission or distribution system.

At the level of DNs, the battery energy storage systems (BESS) are imposed as a solution. For their application in DNs with significant penetration level of RES, type WT and PV, it is necessary to solve two questions beforehand. The first one refers to the optimal planning of the BESS, which includes the choice of capacity, rated power and location in the DN. The second one is the optimal exploitation, i.e. determination of the BESS operation mode in a given period of time, usually 24 h. This implies defining the charging/discharging regime, i.e. the time schedule and the charging/discharging power of the BESS in accordance with the adopted function that it should perform in the DN. These functions can be [3-7]: (i) providing energy management and optimal power flow for reducing the cost for electricity, minimizing power losses, and improving the power quality, (ii) enable/facilitate the

Jordan Radosavljević is with the Faculty of Technical Sciences, University of Priština in Kosovska Mitrovica, 7 Knjaza Miloša, 38220 Kosovska Mitrovica, Serbia (e-mail: jordan.radosavljevic@pr.ac.rs).

Miloš Milovanović is with the Faculty of Technical Sciences, University of Priština in Kosovska Mitrovica, 7 Knjaza Miloša, 38220 Kosovska Mitrovica, Serbia (e-mail: milos.milovanovic@pr.ac.rs).

Nebojša Arsić is with the Faculty of Technical Sciences, University of Priština in Kosovska Mitrovica, 7 Knjaza Miloša, 38220 Kosovska Mitrovica, Serbia (e-mail: nebojsa.arsic@pr.ac.rs).

Andrijana Jovanović is with the Faculty of Technical Sciences, University of Priština in Kosovska Mitrovica, 7 Knjaza Miloša, 38220 Kosovska Mitrovica, Serbia (e-mail: andrijana.jovanovic@pr.ac.rs).

Bojan Perović is with the Faculty of Technical Sciences, University of Priština in Kosovska Mitrovica, 7 Knjaza Miloša, 38220 Kosovska Mitrovica, Serbia (e-mail: bojan.perovic@pr.ac.rs).

Jovan Vukašinović is with the Faculty of Technical Sciences, University of Priština in Kosovska Mitrovica, 7 Knjaza Miloša, 38220 Kosovska Mitrovica, Serbia (e-mail: jovan.vukasinovic@pr.ac.rs).

realization of smart grids, (iii) meeting peak electrical load demands, (iv) increasing the reliability of power supply. The mode of operation of the BESS is determined taking into account variable load, as well as the variable and stochastic power of RES (PV and WT).

In essence, this is a problem of optimal power dispatch in DNs. Given the specificity of the BESS, i.e. the limitation related to the state of charge (SoC), which directly affects the battery status in the next time segment (charging/discharging and power level), the problem of optimal power dispatch must be observed in a certain (given) time horizon, usually a period of 24 hours. Therefore, the problem of optimal power dispatch becomes a dynamic problem on a certain time horizon. The solution of this problem is performed by time segments (e.g. from 1 to 24 h), where the solution in a given segment (t) is conditioned by the solution obtained for the previous segment (t-1).

This paper presents a two-stage procedure for optimal dispatch of active and reactive power in DNs with PV sources and BESS. In the first stage, the optimal active power dispatch in DN is determined, based on the classical model of dynamic economic dispatch with neglected power losses. The aim is minimizing costs for electricity from the source (upstream) grid. After that, the problem of optimal reactive power dispatch in DN is solved to minimize energy losses and voltage deviation.

II. MODELS OF PV, LOAD AND BATTERY STORAGE

A. PV Model

The power generated by a PV unit is dependent on the solar irradiance. Beta PDF is suitable to modeling the stochastic nature of the solar irradiance. The solar irradiance measurements are made available with the sampling time of 1-10 min. Therefore, the mean and standard deviation of the solar irradiance can be calculated from measured data which correspond to the certain time interval τ (e.g. 1 h). Based on the mean and standard deviation of the solar irradiance, the shape parameters of Beta PDF can be calculated [8].

To realize Beta PDF in discrete form, the time interval τ is divided into N_s states, where the corresponding solar irradiance and probability for each state ($g = 1 \div N_s$) can be calculated. The output power of PV is then estimated taking into account the probabilities of all solar irradiance states in the observed time interval, as explained in [8,9].

B. Load Model

It is assumed that the load diagram is the same for active and reactive power. The load is assumed to be a random variable following the same normal PDF within each hour of a given daily load diagram.

To realize the normal PDF load function, the hour t is divided into N_L states, and the corresponding loads and probabilities for each state ($g = 1{:}\ N_L$) are calculated.

The level of the load in the certain time segment t is determined based on the probability of all possible conditions within that hour [9].

C. BESS Model

The BESS model is conditioned by a continuous change in the state of charge (SoC). This means that the value of the SoC at a given time-hour (t) depends on its value in the previous time segment (t-Δt or t-1). Mathematically, this can be expressed as follows [10]:

$$SoC(t) = SoC(t - \Delta t) + \Delta SoC\,, \tag{1}$$

$$\Delta SoC = \frac{P_{bat}(t-1)\cdot \Delta t}{C_B}\,, \tag{2}$$

where C_B is the total capacity of the battery, Δt is the time segment (1 h), and P_{bat} is the power of the battery.

BESS mode means the time schedule and dynamics of charging/discharging of the battery during the considered time period (e.g. 24 h). The mode of the operation of the BESS in each time segment of the observed period is determined in accordance with the adopted function of the BESS in the DN. This can be, for example, minimizing the cost for electricity from the source grid, reducing peak loads, maximizing the use of the energy from RES to supply local loads in the DN, etc. The power of the BESS at time t depends on the adopted battery mode operation. At the same time, the following limits must be met:

$$-P_{bat,n} \le P_{bat}(t) \le P_{bat,n}\,, \tag{3}$$

$$SoC^{\min} \le SoC(t) \le SoC^{\max}\,, \tag{4}$$

where $SoC^{\min}$ and $SoC^{\max}$ are the predefined minimum and maximum charge levels, respectively, and $P_{bat,n}$ is the rated power of the BESS.

III. OPTIMAL ACTIVE POWER DISPATCH

It seems that the minimization of the cost for electricity from the source grid is most appropriate function of BESS in the DN:

$$Cost = \sum_{t=1}^{24} P_g(t)\cdot C_{en}(t)\,, \tag{5}$$

where $P_g(t)$ is the active power from/to the source grid at the hour t, $C_{en}(t)$ is the electricity price in the hour t.

This means that during periods of the day when the electricity price is low, the BESS is used to store the energy from RES and the source grid, working in the charging mode. During periods of the day with a high price of the energy from the source grid, the BESS is used as an additional power source, i.e. it operates in the discharge mode. It is assumed that the electricity price from the source grid changes during the day according to a predetermined diagram, i.e. the electricity price is known in each time segment (hour) of the considered time period.

It is clear that in the charging mode BESS behaves as a load, and that according to the adopted reference directions the battery power is positive, and in the discharge mode BESS acts as a generator in the DN and the power P_{bat} is negative. In order to define the terms “high price” and “low price”, it is assumed that the electricity price at a given time t is high if it is higher than the mean price in the observed time period (day), and that the electricity price at the given time t is small if it is less than the mean value of the electricity price in the considered period.

In order to define the charging/discharging power of the BESS, i.e. to define the value of $P_{bat}(t)$, the principle was adopted is that the greater difference in the energy price at a given moment t, $C_{en}(t)$, in relation to the mean electricity price during the day, it is also the higher power of the battery $P_{bat}(t)$ in relation to the rated power of the battery $P_{bat,n}$. Therefore, the BESS mode at the time t can be defined as follows:

$$P_{bat}(t)=\begin{cases} 0 & \text{if} \quad SoC(t)=SoC_{\max} \\ & \text{and} \quad SoC(t)=SoC_{\max} \\ a_f(t)\cdot P_{bat,n} & \text{if} \quad C_{en}(t)\le C_{en,sr} \\ & \text{and} \quad SoC_{\min}\le SoC(t)<SoC_{\max} \\ 0 & \text{if} \quad C_{en}(t)>C_{en,sr} \\ & \text{and} \quad SoC(t)=SoC_{\min} \\ -a_f(t)\cdot P_{bat,n} & \text{if} \quad C_{en}(t)>C_{en,sr} \\ & \text{and} \quad SoC_{\min}<SoC(t)\le SoC_{\max} \end{cases} \tag{6}$$

where the coefficient a_f shows the difference in the electricity price at the time t from the mean value during the observed day:

$$a_f(t)=\frac{\left|C_{en}(t)-C_{en,mean}\right|}{C_{en,\max}}, \tag{7}$$

$C_{en,mean}$ and $C_{en,\max}$ are mean and maximum electricity price during the day, respectively.

The constraint related to the power balance in the DN for each time interval t, without considering power losses, can be expressed as folows:

$$P_g(t)=P_{load}(t)-P_{PV}(t)+P_{bat}(t), \tag{8}$$

where $P_{load}(t)$ is the total power of loads in the DN at the hour t, $P_{PV}(t)$ is the total power generation of PV sources at the hour t, while $P_{bat}(t)$ is the power of the BESS at the hour t determined according to (6).

The DN operating conditions are defined through the predicted daily load curve and PV source generation profile. In this model, the power losses in the DN are not taken into account, nor the cost of the BESS operation, and the cost of the PV generation.

IV. OPTIMAL DISTRIBUTION OF REACTIVE POWERS

PV sources and BESS are connected to the DN through three-phase inverters. Inverters have the ability to control the reactive power. Assuming that the rated power of the corresponding inverter is slightly higher (e.g. 10%) than the rated power of the PV source and BESS, it means that inverters can be used as an additional control resource in the DN. It is clear that the range of the reactive power is determined by the rated apparent power of the inverter and the active power that is transmitted through the inverter at a given moment. This can be expressed by the following relation [10]:

$$Q_{inv}^{\max}(t)=\pm\sqrt{S_{inv,n}^2-P_{PV}^2(t)}, \tag{9}$$

where $Q_{inv}^{\max}(t)$ is the maximum (minimum) reactive power of the inverter at the time t, $S_{inv,n}$ is the rated power of the inverter, and $P_{PV}(t)$ is the active power of the PV source at the time t. Equation (9) also applies to the BESS.

The optimal reactive power dispatch can be considered as a problem of determining the optimal values of the reactive powers of inverters with a certain objective function, such as minimizing power loss and/or voltage deviation in DN. Mathematically, this can be formulated as follows:

$$\min\ F(\mathbf{x},\mathbf{u}), \tag{10}$$

with constraints:

$$g(\mathbf{x},\mathbf{u})=0, \tag{11}$$

$$h(\mathbf{x},\mathbf{u})\le 0, \tag{12}$$

$$\mathbf{u}\in\mathbf{U}, \tag{13}$$

where **x** is the vector of dependent variables, **u** is the vector of control variables, and F is the objective function.

The vector of dependent variables **x** consists of the slack bus power (P_0), load bus voltages (V_L), and line loadings (S_l). On the other hand, the vector of control variables **u** consists of the inverters reactive powers (Q_{inv}), and slack bus voltage (V_0). The equality constraints (11) are the typical nonlinear power flow equations. Inequality constraints (12) are the functional operating constraints, such as: slack bus active power limits, load bus voltage limits, and branch flow limits. Constraints (13) define the feasibility region of the problem control variables, i.e. inverter reactive power limits, and slack bus voltage limits.

It is worth mentioning that the control variables are self-constrained. The inequality constraints of dependent variables are incorporated in the objective function (10) as quadratic penalty terms [11].

To solve this nonlinear optimization problem with constraints, a large number of classical and metaheuristic methods are available. In this paper, the hybrid metaheuristic method PSOS-CGSA was applied [12].

V. SIMULATION RESULTS

The proposed procedure was applied to a modified IEEE 69-bus test system [13]. Modification of the original IEEE 69-bus system is reflected in the fact that in buses 16 and 61, according to the results in [1], are connected PV sources, as shown in Fig. 1. Both PV sources have the same rated power of 1.8 MW, and they are connected to the network through inverters whose apparent powers are 10% higher than the rated powers of the PV sources. In the bus 4 is connected a BESS, rated power of 2 MW, and capacity of 8 MWh. The apparent power of the BESS converter is also 10% higher than the rated power of the BESS.

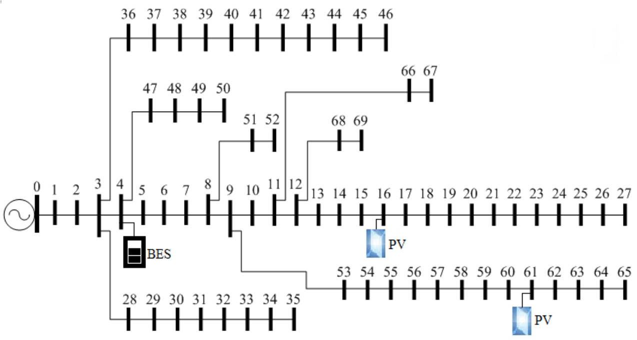

Fig. 1. Single-line diagram of the modified IEEE 69-bus test system.

It is assumed that all loads have the same daily load diagram, as shown in Fig. 2. The rated powers of loads are given in [13]. Also, it was adopted that the change of the solar irradiation is the same in the whole area of the DN, so that the powers of both PV sources change according to the same dynamics during the day, as in Fig. 2. The procedure for determining the optimal active power dispatch was carried out according to the algorithm described in Section III. The daily diagram of the change in the energy price from the source grid, expressed in p.u., is also shown in Fig. 2. The base energy price is 100 €/MWh [14]. It was adopted that $SoC_{\min}$ is 30%, $SoC_{\max}$ is 100%, and the initial state of charge is 30%.

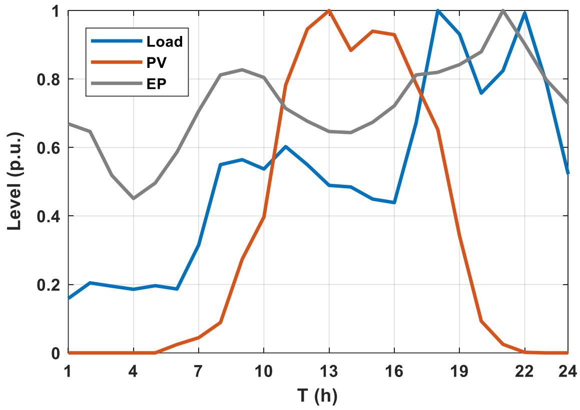

Fig. 2. Load, PV generation, and energy price (EP) profiles.

After determining the optimal active power dispatch, the procedure for determining the optimal reactive power dispatch was carried out for three types of the objective function, as follows:

- Case 1: Minimization of energy losses during the day
- Case 2: Minimization of load buses voltage deviation
- Case 3: Simultaneously minimization of energy losses and voltage deviation

It was adopted that the allowable voltage limits at load buses are from 0.95-1.05 p.u. The voltage magnitude at the slack bus is considered in the range 0.9 -1.1 p.u., whereas the reactive power limits of the inverters are changeable, according to (9).

A. *Optimal Active Power Dispatch*

In order to compare the results, the base case was adopted when PV sources are connected to the DN but there is no the BESS. Fig. 3 shows the costs for electricity from the source grid in the case when there is no the BESS and in the case when there is the BESS with the optimal active power dispatch obtained according to the algorithm described in Section III.

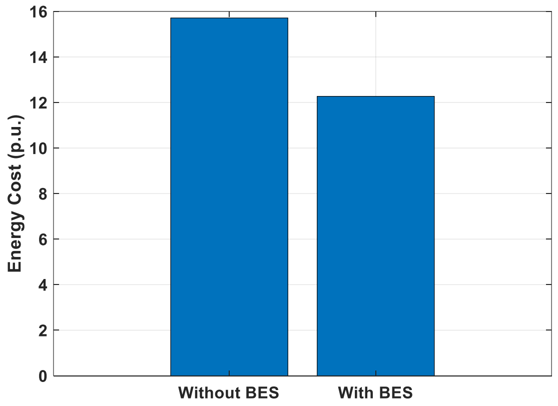

Fig. 3. Comparison of costs for energy purchased from the source grid.

As results of the optimal active power dispatch, daily diagrams of the active power and SoC of the BESS were obtained, as shown in Figs. 4 and 5, respectively.

Based on the results in Figure 3, it is clear that the integration of BESS and application of the proposed algorithm for optimal active power dispatch lead to a significant reduction in costs for electricity from the source grid. This conclusion is derived with the notation that the operating costs of the PV source and the BESS were not considered in this case.

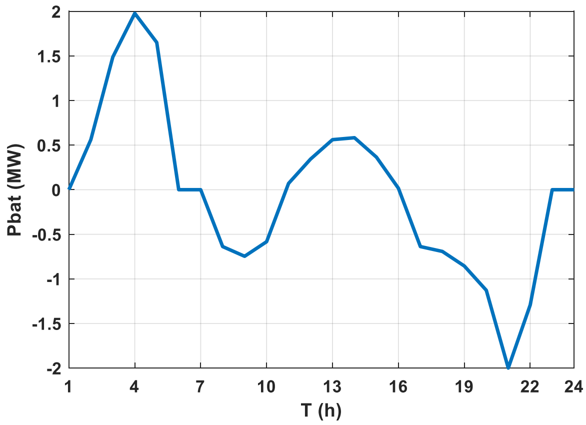

Fig. 4. The power change of the battery during the day.

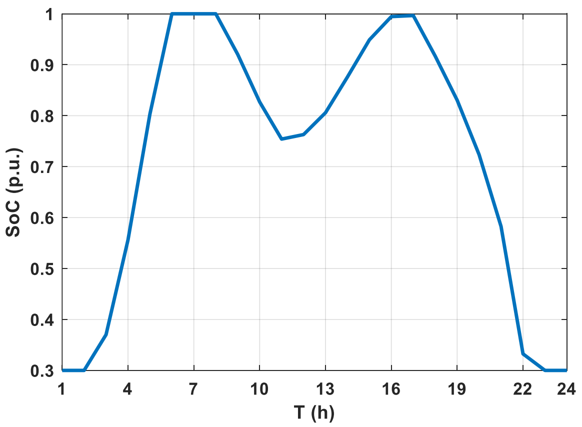

Fig. 5. The S_OC change of the battery during the day.

B. *Optimal Distribution of Reactive Powers*

The results of the optimal reactive power dispatch are given in Table I. The base case is taken when PV sources and BESS operate with unity power factor, and the slack bus voltage is equal to 1 p.u. The table shows the values of the active energy losses during the day (W_{loss}), the sum of voltage deviations at load buses during the day (ΔV_{pq}) and the maximum values of voltage deviations during the day in the whole DN. It is obvious that the proposed approach for the optimal reactive power dispatch in Case 1 achieves a significant reduction in energy losses, and in Case 2 a reduction in voltage deviations in the network. As expected, a compromise solution was obtained in Case 3. The optimal values of the control variables for Case 1 and Case 3 are shown in Figs. 6 and 7, respectively.

TABLE I
RESULTS OF THE OPTIMAL DISTRIBUTION OF REACTIVE POWERS

	Case			
	Base case	Case 1	Case 2	Case 3
W_{loss} (MWh)	2.33	2.04	2.93	2.15
sum(ΔV_{pq}) (p.u.)	22.60	57.19	16.88	19.78
max(ΔV_{pq}) (p.u.)	0.09	0.05	0.05	0.05

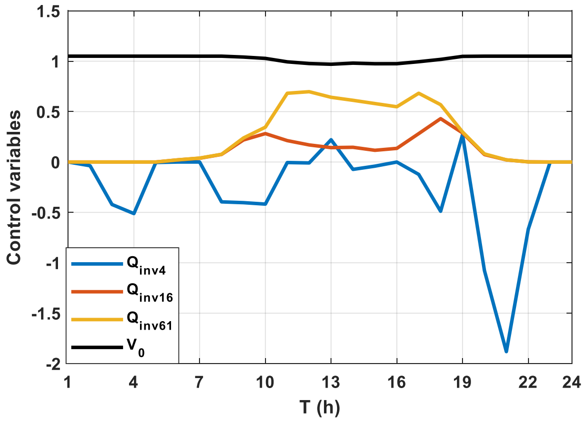

Fig. 6. Optimal values of control variables in Case 1.

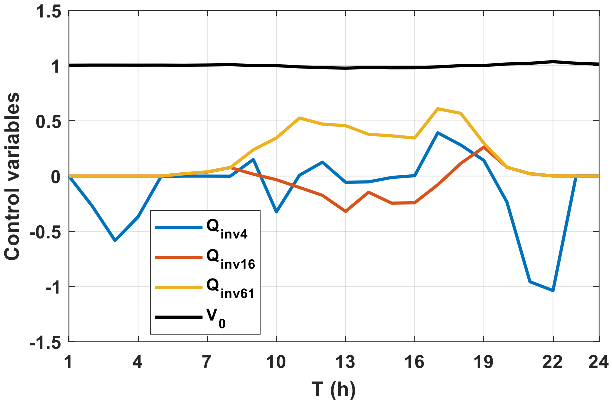

Fig. 7. Optimal values of control variables in Case 3.

The voltage profiles of the DN for the 24-hour period corresponding to the optimal active/reactive power dispatch for Cases 1-3 are shown in Figs. 8-10, respectively.

Based on these results, it can be seen a significant voltage deviation for Case 1 compared to the base case and Cases 2 and 3. This is a consequence of presenting loads with the constant power model; to minimizing the power losses in Case 1, control variables are optimized so that load voltages have higher values within the permissible limits to minimize branch currents, and thus power losses in the DN.

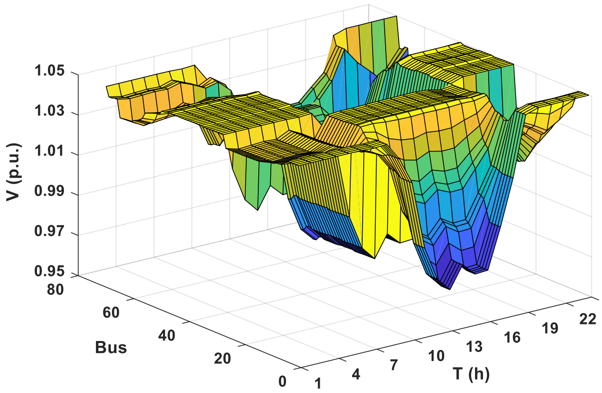

Fig. 8. Voltage profiles for Case 1.

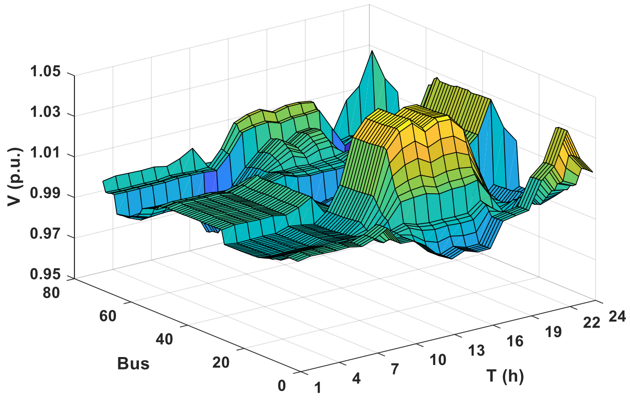

Fig. 9. Voltage profiles for Case 2.

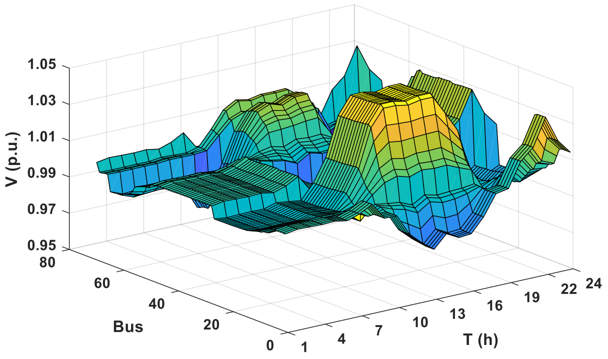

Fig. 10. Voltage profiles for Case 3.

VI. CONCLUSION

In this paper, a two-stage active/reactive power dispatch approach for DNs with high penetration of PV generation and BESS has been considered. The proposed procedure has been tested on the IEEE 69-bus test system with two PV sources and one BESS. The simulation results lead to conclusions that can be summarized as follows:

- Integration of BESS and application of proposed algorithm for optimal active power dispatch lead to a significant reduction in costs for electricity from the source grid. In this particular case, the results showed that it is possible to achieve a reduction in the energy cost by about 22%, compared with the base case without BESS.
- It has been shown that PV and BESS inverters can serve as additional control resources for reactive power. By applying the proposed algorithm for optimal reactive power dispatch, a significant reduction in active power losses and voltage deviations in DNs can be achieved. Specifically, in comparison with the base case, the solutions obtained by the proposed algorithm provide a reduction in energy losses of 12.45% for Case 1, and a reduction in voltage deviations of 25.31% for Case 2.

ACKNOWLEDGMENT

This work was supported by the Ministry of Education, Science and Technological Development of the Republic of Serbia under Grant TR 33046 and ERASMUS + project: “Knowledge triangle for a low carbon economy (KALCEA)”.

REFERENCES

[1] J. Radosavljević, N. Arsić, M. Milovanović, A. Ktena, “Optimal placement and sizing of renewable distributed generation using hybrid metaheuristic algorithm,” *Journal of Modern Power Systems and Clean Energy*, vol. 8, no. 3, pp. 499-510, 2020

[2] IRENA, “Renewable Power Generation Costs in 2020,” International Renewable Energy Agency, Abu Dhabi, 2021

[3] X. Luo, J. Wang, M. Donner, J. Clarke, “Overview of current development in electrical energy storage technologies and application potential in power system operation”, *Applied Energy*, vol. 137, pp. 511-536, 2015

[4] C. Tang, J. Xu, Y. Sun, S. Liao, F. Zhang, L. Ma, “Stochastic battery energy storage scheduling considering cell degradation and distributed energy resources,” *International Transactions on Electrical Energy Systems*, vol. 29, no. 7, e12028, 2019

[5] K. Das, A. L. T. P. Grapperon, P. E. Sorensen, A. D. Hansen, “Optimal battery operation for revenue maximization of wind-storage hybrid power plant,” *Electric Power System Research*, vol. 188, pp. 106-631, 2020

[6] M. Ahmadi, O. B. Adewuyi, M. Sayed, S. M. S. Danish, P. Mandal, A. Yona, T. Senjyu, “Optimum coordination of centralized and distributed renewable power generation incorporating battery storage system into the electric distribution network,” *Electrical Power and Energy Systems*, vol. 125, pp. 106-458, 2021

[7] J. Radosavljević, “Voltage regulation in LV distribution networks with PV generation and battery storage,” *Journal of Electrical Engineering*, vol. 72, no. 6, pp. 356-365, 2021

[8] J. Radosavljević, N. Arsić, S. Štatkić, “Dynamic Economic Dispatch Considering WT and PV Generation using Hybrid PSOS-CGSA Algorithm”, 2021 20th International Symposium INFOTEH-JAHORINA (INFOTEH), East Sarajevo, Bosnia and Herzegovina, vol. no, pp. 1-6, 17-19 March, 2021

[9] Z. Ullah, S. Wang, J. Radosavljević, J. Lai, A Solution to the Optimal Power Flow Problem Considering WT and PV Generation, IEEE Access, Vol. 7, 2019., pp. 46763-46772.

[10] A. Ali, K. Mahmoud, D. Raisz, and M. Lehtonen, “Probabilistic approach for hosting high PV penetration in distribution systems via optial oversized inverter with watt-var functions,” *IEEE Systems Journal*, vol. 15, no. 3, pp. 684-693, 2021

[11] J. Radosavljević, M. Jevtić, M. Milovanović, “A solution to the ORPD problem and critical analysis of the results,” *Electrical Engineering*, vol. 100, no. 1, pp. 253-265, 2018

[12] Z. Ullah, M. R. Elkadeem, S. Wang, J. Radosavljević, “A Novel PSOS-CGSA Method for State Estimation in Unbalanced DG-integrated Distribution Systems,” *IEEE Access*, vol. 8, pp. 113219-113229, 2020

[13] N. Ranjan, B. Venkatesh, D. Das, “Voltage stability analysis of radial distribution networks,” *Electric Power Components and Systems*, vol. 23, no. 2, pp. 129-135, 2001

[14] M. Giuntoli, M. Subasic, S. Schmitt, “Control of distribution grids with storage using nested Benders’ decomposition,” *Electric Power Systems Research*, vol. 190, pp. 1-6, 2021

Modeling of High-Voltage Induction Machines with Fallen-out Magnetic Slot Wedges

Milica Banović, Kristina Vujkov, *Student Member, IEEE*, Mladen Terzić, *Member, IEEE*, Dejan Jerkan, *Member, IEEE*

Abstract**—Electrical machines of medium to high voltage range are commonly fabricated with wide stator slot openings which often lead to the increase of noise, vibrations and power losses. The use of magnetic slot wedges is intended to minimize these effects. Exposure to high magnetic and mechanical forces may cause magnetic wedge fall-outs. In this paper, a dynamical model of an induction machine was developed in order to investigate the influence of stator slot magnetic wedge failures on the machine's performance. Through observation of the machine's terminal quantity disturbances, the model demonstrated remarkable differences in steady-state rated operation, regarding stator line currents, rotor loop currents and generated electromagnetic toque, in case of healthy and faulty machine.**

Index Terms**—induction machine; magnetic slot wedges; finite element analysis; MCCA; motor faults.**

I. INTRODUCTION

Induction machines (IMs) designed for use in modern drives and industry must cope with ever-growing demands for increased efficiency and high performance. Furthermore, there are strong requirements for the reduction of noise pollution and vibrations which represent one of the most common issues in today's motor drives. For high and medium voltage IMs, it is reported that wide open stator slots are the main cause of those issues [1-3]. A well-known means to mitigate suggested problems in medium and high voltage motors is to install magnetic stator slot wedges.

Most magnetic slot wedges are made from iron powder (~ 75%), glass fabric and epoxy resin binders, and therefore, have larger relative permeability (less than 10) compared to epoxy edges [4]. Their higher relative permeability compared to classical non-magnetic wedges reduces the flux fluctuations on the rotor core surface and decreases the effective air gap width. The smoothened flux [6] in the air gap reduces the surface core losses, acoustic noise and improves the torque characteristics [4, 5]. Therefore, magnetic slot wedges also improve motor efficiency, power factor and power density.

Since the iron powder in the magnetic wedges makes them mechanically weakened, they are more prone to failures (fall-outs) caused by exposure to high magnetic and mechanical forces. There are many cases of wedge failures in medium (high) voltage motors (above 3.3 kV) reported, where up to 50% of the wedges were lost within 3 years of service [4].

Magnetic wedge fall-outs impact the machine's performance and are observable through the IM terminal quantity disturbances. Numerical modeling of this phenomenon may be used as a starting point for the evaluation of this type of fault and investigation of reliable fault indicators.

For this purpose, a dynamical model of an IM, based on Multiple Coupled Circuit Approach (MCCA) and Finite Element Analysis (FEA) analysis [7-9] is developed in Section II. FEA calculations of IM inductances for the healthy and faulty machine are illustrated and discussed in Section III and then used for MCCA model inductance matrices formation. MCCA model simulation results, presented in Section IV clearly demonstrate the influence of magnetic slot wedge fall-outs through unbalanced stator line currents, distorted rotor bar currents and increased torque pulsation. Conclusion of this paper with further research topics suggestions is given in Section V.

II. MATHEMATICAL REPRESENTATION OF MCCA MODEL OF SQUIRREL-CAGE INDUCTION MOTOR

MCCA model of squirrel-cage IM is used to model energy conversion process in the machine, taking into account higher-order harmonic components in the magnetic field, induced voltages and currents. The nonsinusoidal electromagnetic field in the machine can be incorporated effectively by the rotor position-dependent variation of elements in MCCA model inductance matrices.

In this paper, the inductance matrix is reconstructed using series of linear 2-D FEA magneto-static simulations [7]. Discrete values of inductances obtained by this method are then represented via Fourier series, allowing the choice of harmonic components from the series which will be afterward used in the MCCA model.

The squirrel-cage rotor can be represented as identical and equally spaced rotor loops. Rotor loop consists of two neighboring rotors bars and adjacent end-ring segments. Fig. 1 shows three neighboring rotor loops (detail of rotor cage).

Milica Banović is with the School of Electrical Engineering, University of Belgrade, 73 Bulevar kralja Aleksandra, 11020 Belgrade, Serbia (e-mail: banovicmilicaa@gmail.com).

Kristina Vujkov is with the Faculty of Technical Sciences, University of Novi Sad, Trg Dositeja Obradovića 6, 21101 Novi Sad, Serbia (e-mail: kristina.vujkov@uns.ac.rs).

Dejan Jerkan is with the Faculty of Technical Sciences, University of Novi Sad, Trg Dositeja Obradovića 6, 21101 Novi Sad, Serbia (e-mail: dejan.jerkan@uns.ac.rs).

Mladen Terzić is with the School of Electrical Engineering, University of Belgrade, 73 Bulevar kralja Aleksandra, 11020 Belgrade, Serbia (e-mail: terzic@etf.bg.ac.rs).

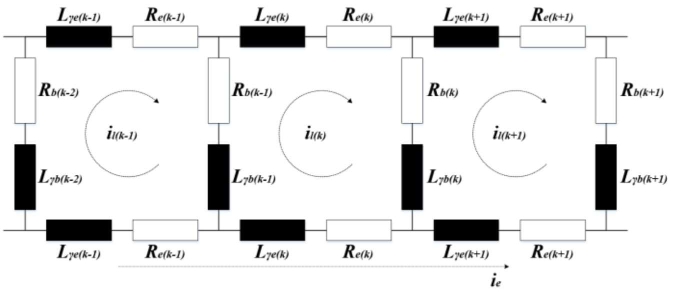

Fig. 1. Detail of squirrel-cage electrical circuit.

The mathematical model of the squirrel-cage IM can be formulated as:

$$\boldsymbol{V} = \boldsymbol{R}\boldsymbol{I} + \frac{d}{dt}(\boldsymbol{L}\boldsymbol{I}). \tag{1}$$

Voltage vector $\boldsymbol{V}$ consists of stator $(\boldsymbol{V_s})$ and rotor $(\boldsymbol{V_r})$ voltage vectors:

$$\begin{aligned} &\boldsymbol{V} = [\boldsymbol{V_s}\ \ \boldsymbol{V_r}]^T, \\ &\boldsymbol{V_s} = [v_a \quad v_b \quad v_c], \qquad , \\ &\boldsymbol{V_r} = [0 \quad 0 \dots 0 \quad 0]_{n_B+1.} \end{aligned} \tag{2}$$

where v_a, v_b, and v_c are three stator voltages and n_B is the number of rotor bars. There are $(n_B + 1)$ rotor voltages equal to zero for $(n_B + 1)$ independent current loops in the rotor cage which stand for n_B rotor bars and two end rings. Likewise voltage vector $\boldsymbol{V}$, current vector $\boldsymbol{I}$ in (1) consists of stator $(\boldsymbol{I_s})$ and rotor $(\boldsymbol{I_r})$ current vectors:

$$\begin{aligned} &\boldsymbol{I} = [\boldsymbol{I_s}\ \ \boldsymbol{I_r}]^T, \\ &\boldsymbol{I_s} = [i_a \quad i_b \quad i_c], \qquad . \\ &\boldsymbol{I_r} = [i_{l1} \quad i_{l2} \dots i_{ln_B} \quad i_e]_{n_B+1,} \end{aligned} \tag{3}$$

where $\boldsymbol{I_s}$ is the stator current vector for three stator phase windings i_a, i_b, and i_c. Rotor current vector $\boldsymbol{I_r}$ includes n_B rotor loops currents i_{r1}, i_{l2}, …, i_{ln_B} and one end-ring current i_e.

Diagonal 3x3 stator resistance matrix $\boldsymbol{R_s}$ and rotor resistance symmetrical matrix $\boldsymbol{R_r}$ comprise resistance matrix $\boldsymbol{R}$ from (1):

$$\begin{aligned} &\boldsymbol{R} = \begin{bmatrix} \boldsymbol{R_s} & \\ & \boldsymbol{R_r} \end{bmatrix}, \\ &\boldsymbol{R_s} = \begin{bmatrix} R_s & & \\ & R_s & \\ & & R_s \end{bmatrix}, \\ &\boldsymbol{R_r} = \begin{bmatrix} R_{l1} & -R_{b2} & \dots & -R_{bn_B} & -R_{e1} \\ -R_{b1} & R_{l2} & \dots & 0 & -R_{e2} \\ \vdots & \vdots & \dots & \vdots & \vdots \\ \vdots & \vdots & \dots & \vdots & \vdots \\ 0 & 0 & \dots & -R_{bn_B} & -R_{e(n_B-1)} \\ -R_{b1} & 0 & \dots & R_{ln_B} & -R_{en_B} \\ -R_{e1} & -R_{e2} & \dots & -R_{en_B} & \sum_{i=1}^{N_B} R_{ei} \end{bmatrix}_{(n_B+1)\mathrm{x}(n_B+1)} \end{aligned} \quad , \tag{4}$$

where R_{lk} represents resistance of rotor k loop, defined as $R_{lk} = R_{bk} + R_{b(k+1)} + 2R_{ek}$ with R_{bk} as k bar resistance and R_{ek} end-ring k segment resistance.

Interaction between neighboring rotor loops and end-ring segments shown in Fig. 1 are reflected in the resistance matrix $\boldsymbol{R_r}$. Voltage equation for arbitrarily k rotor loop $(1 < k \leq N_B)$ (Fig. 1) has the following form:

$$\begin{gathered} R_{ek} i_{rlk} + R_{bk}\big(i_{rlk} - i_{rl(k+1)}\big) + R_{ek}(i_{rlk} - i_e) - \\ R_{b(k-1)}\big(i_{rl(k-1)} - i_{rlk}\big) + \frac{d\Psi_{\mathrm{rlk}}}{dt} = 0, \end{gathered} \tag{5}$$

It can be noticed that negative elements in the matrix $\boldsymbol{R_r}$ (4) result from interactions between neighboring rotor loops and end ring.

Rotor bar current i_{bk} can be expressed through neighboring rotor loop currents as follows:

$$i_{bk} = i_{lk} - i_{l(k+1)}. \tag{7}$$

Inductance matrix $\boldsymbol{L}$ is a periodic function of rotor angular position θ, and it consists of four sub-matrices:

$$\boldsymbol{L}(\theta) = \begin{bmatrix} \boldsymbol{L_{ss}}(\theta) & \boldsymbol{L_{sr}}(\theta) \\ \boldsymbol{L_{rs}}(\theta) & \boldsymbol{L_{rr}}(\theta) \end{bmatrix}. \tag{8}$$

Stator inductance matrix $\boldsymbol{L_{ss}}$ is θ-dependent 3x3 matrix which defines magnetic coupling between stator phases:

$$\boldsymbol{L_{ss}}(\theta) = \begin{bmatrix} L_a & M_{ab} & M_{ac} \\ M_{ba} & L_b & M_{bc} \\ M_{ca} & M_{cb} & L_c \end{bmatrix}. \tag{9}$$

Rotor inductance matrix $\boldsymbol{L_{rr}}$ is a $(n_B + 1)\mathrm{x}(n_B + 1)$ position-varying matrix generated similarly to rotor resistance matrix with one major difference; any rotor loop is magnetically coupled with all the other loops and generally there are no zero elements in it:

$$\boldsymbol{L_{rr}}(\theta) = \begin{bmatrix} L_{l1} & \dots & M_{r1n_B} - L_{bn_B} & -L_{\gamma e1} \\ M_{r21} - L_{b1} & \dots & M_{r2n_B} & -L_{\gamma e2} \\ \vdots & \dots & \vdots & \vdots \\ \vdots & \dots & \vdots & \vdots \\ M_{r(n_B-1)1} & \dots & M_{r(n_B-1)n_B} - L_{bn_B} & -L_{\gamma e(n_B-1)} \\ M_{rn_B1} - L_{b1} & \dots & L_{ln_B} & -L_{en_B} \\ -L_{e1} & \dots & -L_{en_B} & \sum_{i=1}^{n_B} L_{ei} \end{bmatrix}. \tag{10}$$

Rotor k loop inductance L_{lk} $(1 \leq k \leq n_B)$ is defined as $L_{lk} = L_k + L_{\gamma bk} + L_{\gamma b(k+1)} + 2L_{\gamma ek}$, where L_k is k loop self-inductance, $L_{\gamma bk}$ is rotor k bar leakage inductance, and $L_{\gamma ek}$ is rotor end-ring k segment leakage inductance. Mutual inductances between arbitrary rotor loops m and n are labeled as M_{rmn} $(1 \leq m, n \leq n_B \wedge m \neq n)$.

Stator-rotor inductance matrix $\boldsymbol{L_{sr}}$ is defined as:

$$\boldsymbol{L_{sr}}(\theta)=\begin{bmatrix} M_{al1} & M_{al2} & \dots & M_{al n_B} & 0 \\ M_{bl1} & M_{bl2} & \dots & M_{bl n_B} & 0 \\ M_{cl1} & M_{cl2} & \dots & M_{cl n_B} & 0 \end{bmatrix}, \tag{11}$$

Mutual inductance between arbitrarily stator phase x and rotor loop k is labeled as M_{xlk}, where $x \in \{a,b,c\}, 1 \le k \le n_B$. Rotor-stator inductance matrix $\boldsymbol{L_{rs}}$ can be derived from (11), by transposition of stator-rotor inductance matrix $\boldsymbol{L_{rs}} = \boldsymbol{L_{sr}^T}$.

The calculation of torque T_e in the MCCA model is based on the virtual work principle (p is pole pairs number):

$$T_e = \frac{1}{2} p \begin{bmatrix} \boldsymbol{I_s} \\ \boldsymbol{I_r} \end{bmatrix}^T \frac{d}{d\theta}\left(\begin{bmatrix} \boldsymbol{L_{ss}} & \boldsymbol{L_{sr}} \\ \boldsymbol{L_{rs}} & \boldsymbol{L_{rr}} \end{bmatrix}\right)\begin{bmatrix} \boldsymbol{I_s} \\ \boldsymbol{I_r} \end{bmatrix}. \tag{12}$$

III. INDUCTANCE CALCULATION OF HEALTHY AND FAULTY IM

After derivation of MCCA model in Section II, inductance calculation method shall be presented in the following. Modeled induction machine is a 2-pole, 6 kV high voltage motor with rated output power of 1.03 MW (detailed machine data are given in Appendix). Magnetic slot wedges of relative permeability 5 are used to close stator slot openings.

Linear magneto-static 2-D FEA simulations are used to compute discrete values of machine's inductances relative to absolute rotor angular position. Saturation effect is neglected. In the calculated inductance waveforms, only harmonics provoked by geometry variations and presence/absence of the magnetic wedges are investigated. These harmonics are independent from saturation-induced harmonics and can be treated separately.

In order to obtain self- and mutual inductances of an arbitrary winding for a fixed rotor position, only the winding itself is supplied with 1 A direct current. After single magneto-static simulation is completed, flux linkages of all windings in the machine are determined and used for single discrete value inductance calculation. Next magneto-static simulation is performed in the same manner after fixed-valued angle increment of rotor position. The value of angle increment determines the precision of inductances waveforms.

One full revolution of rotor is necessary for complete inductance matric reconstruction. Derived discrete waveforms are then represented with Fourier series coefficients in the MATLAB&Simulink model.

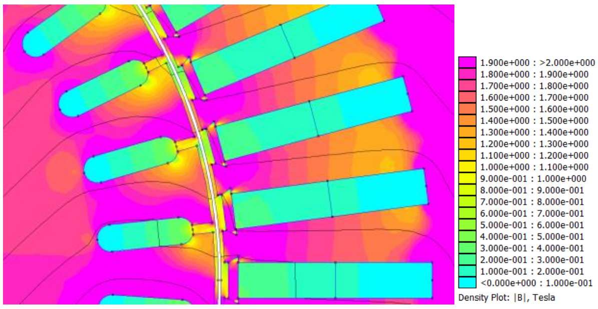

Fig. 2. Discrete magneto-static simulation of healthy IM

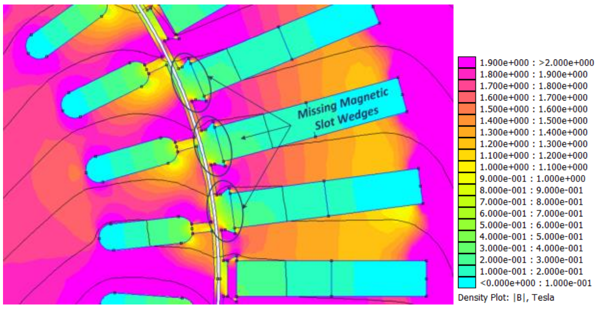

Fig. 3. Discrete magneto-static simulation of faulty IM (three consecutive fallen-out wedges)

Detail of magneto-static simulation for healthy and faulty IM is given in Fig. 2 and Fig. 3, respectively. The analyzed fault is modeled by three consecutive completely fallen-out wedges. As can be seen from the figures magnetic flux lines crossing the air gap from rotor to stator have significantly more homogeneous flow in the healthy motor compared to the one with missing wedges. Represented local distortion of flux lines will lead to deformation of machine inductances in case of fault occurrence.

Stator phase *A* self-inductance as a function of rotor angular position is shown in Fig. 4. Minor oscillations around the constant value of stator self-inductance are the result of air gap equivalent permeability variations caused by rotor slotting. Since analyzed IM has 36 rotor slots all three stator self-inductances have identical waveforms and their minor oscillations are in phase.

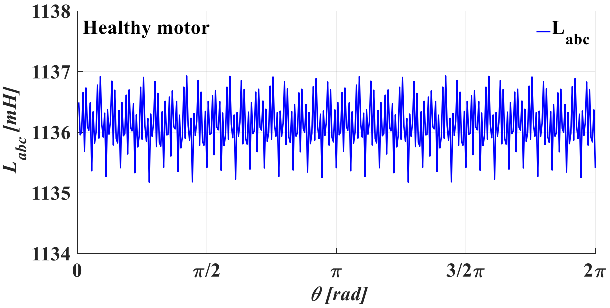

Fig. 4. Stator phase A self-inductance waveform – healthy motor

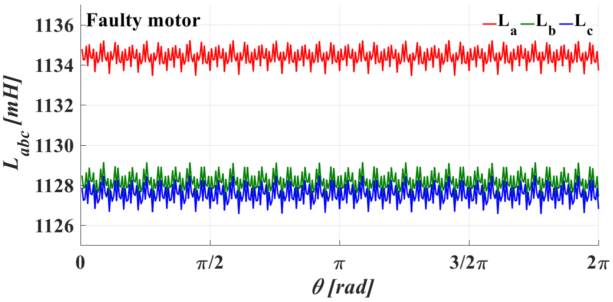

Fig. 5. Stator phases self-inductances waveform – faulty motor

In case of fallen-out wedges, the balance of stator windings is corrupted. This leads to different mean values of stator self inductances for phase *A*, *B*, and *C*. Modeled missing wedges are in close vicinity of phase *B* and *C* winding axes. Lack of ferromagnetic material caused by fallen-out magnetic wedges decreases inductances of most affected windings - Fig. 5.

Similar phenomena can be observed in stator mutual inductance waveforms. All stator mutual inductances are identical in case of healthy motor (Fig. 6), while in the event of fault (Fig. 7), all mutual inductances suffer in mean value reduction. Mutual inductances involving phase *A* are less influenced by the fault, as expected.

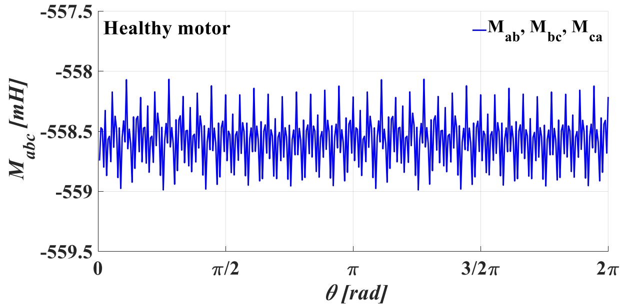

Fig. 6. Stator phases mutual inductances waveform – healthy motor

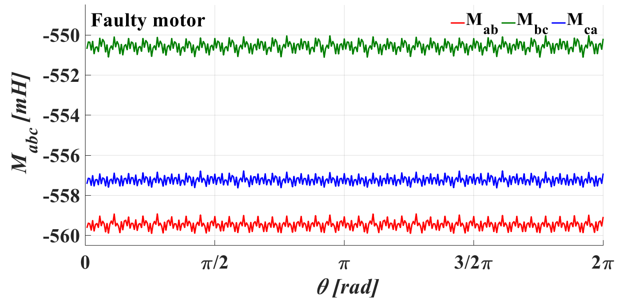

Fig. 7. Stator phases mutual inductances waveform – faulty motor

Stator-rotor inductances of IM are the main contributors to torque generation. For healthy motor, they are symmetrical, alternating, rotor angular position-dependent functions with characteristic trapezoidal shape (Fig. 8 – blue line). Therefore, spectrum of trapezoidal inductance signal contains only odd higher-order harmonics (Fig. 9 – blue bars). However, in the presence of slot wedge faults, a local dip in the waveform is formed each time specific rotor loop passes by stator slots with missing wedges (Fig. 8 – red line). As a result, new even harmonic components in the Fourier series appear (Fig. 9 – red bars). These additional components will further induce characteristic harmonics in flux linkages and consequently, in induced voltages and currents. This will affect torque production by causing unwanted pulsations.

The fallen-out magnetic slot wedges also have impact on rotor inductance matrix. Similar to stator inductances, rotor inductances in the healthy machine are fairly constant quantities with small oscillations around the mean value. These oscillations are the consequences of stator slotting. Slot wedges reduce these oscillations by making stator inner circumference more magnetically uniformed.

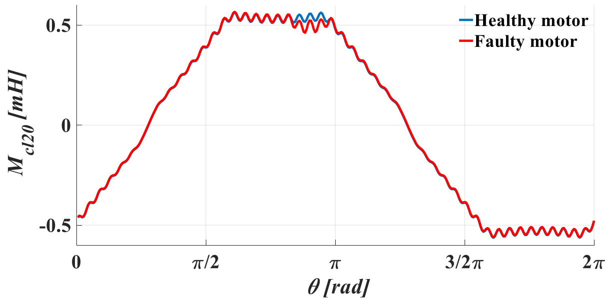

Fig. 8. Mutual inductance between stator phase C and rotor loop 20

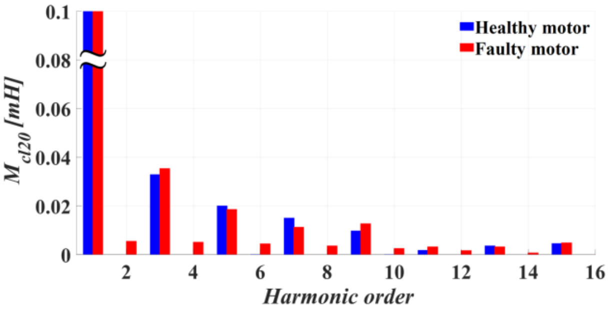

Fig. 9. Mutual inductance between stator phase C and rotor loop 20 - Fourier series coefficients

In Fig. 10 blue line illustrates rotor loop self-inductance waveform in healthy motor. There are exactly 48 oscillations in one rotor revolution due to the number of stator slots. When slot wedges are missing stator magnetic uniformity is lost which will locally diminish rotor self-inductance just as rotor loop passes by faulty slots. Since three neighboring slots are impacted by the fault, there will be three more prominent oscillations combined with lower mean value in the inductance waveform (Fig. 10 – red line).

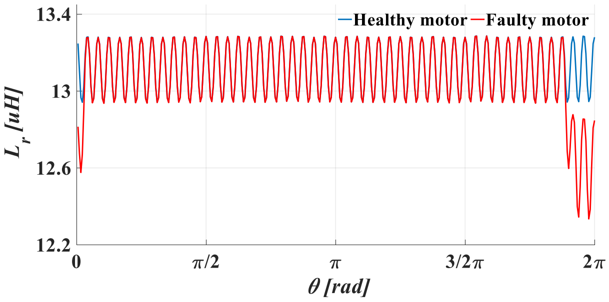

Fig. 10. Rotor loop self-inductance

A detail of rotor self-inductance spectrum, both for healthy and faulty motor, is shown in Fig. 11. In order to emphasize the emergence of additional spectral components, dominant mean value is excluded from the figure. Despite their small magnitudes, higher-order components have a significant impact on the energy conversion process which will be illustrated and discussed in the next Section.

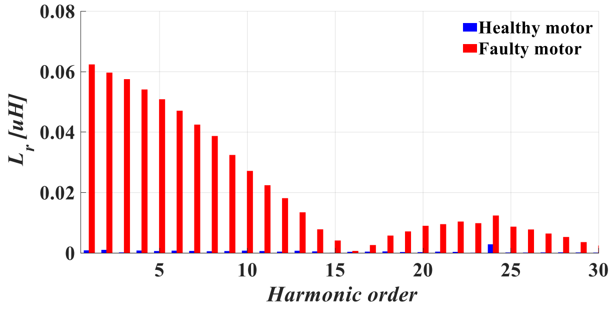

Fig. 11. Rotor loop self-inductance – spectrum with mean value excluded

As the last characteristic example of the magnetic wedge fall-outs impact on machine's inductances, mutual inductance between arbitrarily chosen rotor loops is shown in Fig. 11 (healthy machine in blue and faulty in red line). Magnetic coupling between two rotor loops subjects to complex mechanisms of flux lines formation and it is dependent on relative rotor position and the mutual position of the loops themselves. The situation grows even more puzzling when slot wedge fault is present, as observable in Fig. 11- red line.

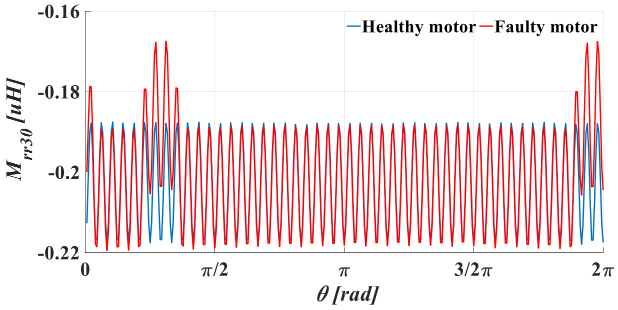

Fig. 12. Mutual inductance between first and 31st rotor loop

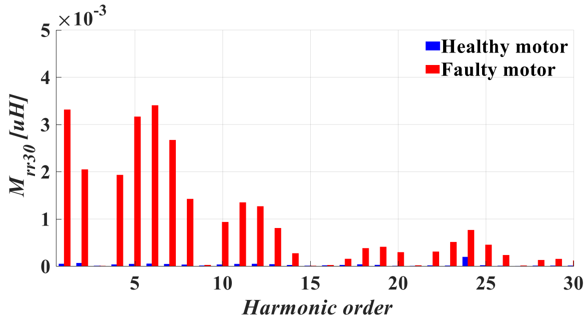

Fig. 13. Mutual inductance between first and 31st rotor loop – spectrum with mean value excluded

Singled out higher-order components of the mutual inductance between first and 31st rotor loop, shown in Fig. 13 are compliant with the expected increase in number and magnitude of additional components in the spectrum, similar to elaborated phenomena in Fig. 11.

IV. SIMULATION RESULTS

Based on FEA calculation of machine's inductances presented in Section III and MCCA model derived in Section II MATLAB&Simulink model of the machine under investigation (Appendix) was developed.

The output of FEA computations i.e. waveforms of machine inductances are firstly represented with Fourier series coefficients. These coefficients are then used for the formation of time and position varying inductance matrices of dynamic MCCA machine model. Inductances independent from geometry variations which cannot be calculated using 2-D representation of the machine: stator end-winding and rotor end-ring leakage inductances are added to the MCCA model inductance matrices as constant values. Their values are provided from separate simulations performed using commercial FEA software with such built-in options. MCCA model is able to simulate transient behavior of the machine under arbitrary supply and loading conditions, similar to conventional dq models, but with much more insight into construction-dependent properties of the specific machine.

Stator line currents during steady-state operation under the rated load of healthy machine are illustrated in Fig. 14. The machine was supplied from three-phase balanced voltage source of 6 kV at rated frequency of 50 Hz. Rated speed of the machine was 2985 rpm, rated torque 3.23 kNm and rated output power 1.03 MW. As expected, line currents are balanced in the case of healthy machine.

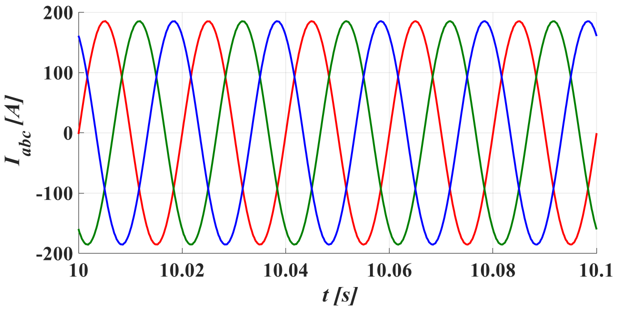

Fig. 14. Stator line currents under full load – healthy machine

Under the same supply and loading conditions, but with magnetic wedge fault present, unbalance in stator line currents is clearly visible in Fig. 15. Fallen-out magnetic wedges led to unbalanced inductances of stator phase windings (Fig. 5 and 7) which consequently caused noticeable imbalance in the currents as well.

Fig. 16 shows differences between arbitrary rotor loop current waveforms in case of the healthy and faulty machine. It is noticeable that, in the event of fault, rotor loop current waveform will contain more prominent oscillations which were expected as the result of emergence of additional components in the inductance spectrum of the faulty machine.

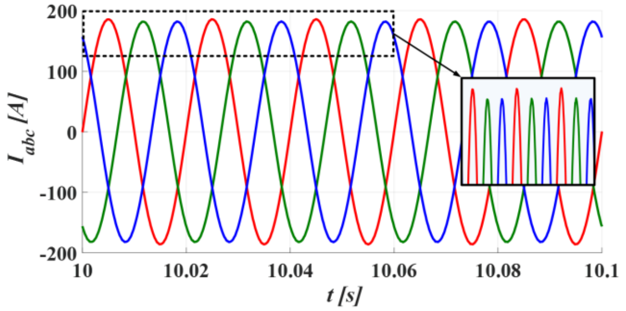

Fig. 15. Stator line currents under full load – faulty machine

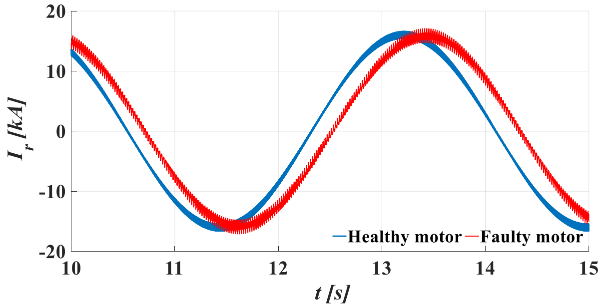

Fig. 16. Current waveform of arbitrary rotor loop under full load

Parasitic torque pulsations are direct outcome of increased oscillations in the machine inductances and currents. In the Fig. 17, the machine toque waveform is illustrated for rated operational mode with and without fault. Increased torque pulsations may provoke an unwanted mechanical response from the machine which could reflect on the level of noise and vibrations. Exceeding level of vibration can have great impact on bearing deterioration, may cause cracks in the winding insulation and tightness of the lamination stack.

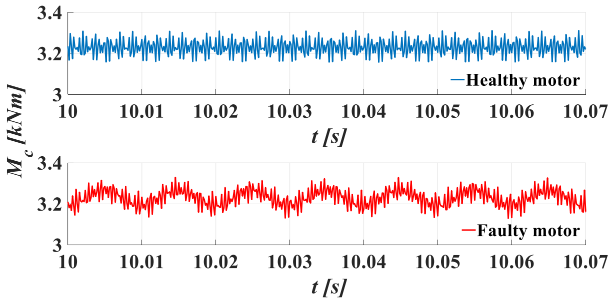

Fig. 17. Rated electromagnetic torque

V. CONCLUSION

In this paper MCCA model of high voltage squirrel-cage induction machine is used to investigate the influence of stator slot magnetic wedge failures on machine's performance. Series of magneto-static FEA simulations illustrated differences in waveforms of characteristic inductances of the machine in case of healthy machine and the machine with three consecutive fallen-out stator magnetic wedges. FEA results provided input data for MCCA inductance matrices formation, using the Fourier series coefficient. Through observation of the machine's terminal quantity disturbances, performed simulations in MATLAB&Simulink dynamic MCCA model of IM demonstrated remarkable differences in steady-state rated operation, regarding stator line currents, rotor loop currents and generated electromagnetic toque. Further research may include targeted thorough analysis of the terminal quantities in the interest of reliable and non-invasive detection of fallen-out wedges.

APPENDIX

TABLE I
MOTOR PARAMETERS

Rated Power	*1.03 MW*
Rated Speed	*2985 rpm*
Rated Torque	*3.23 kNm*
Rated Voltage	*6 kV*
Number of Stator Slots	*48*
Number of Rotor Slots	*36*
Stator Inner/Outer Diameter	*430/780 mm*
Air Gap Width	*4 mm*
Lamination Stack Length	*765 mm*

REFERENCES

[1] G. Stojicic, M. Vasak, N. Peric, G. Joksimovic and T. M. Wolbank, "Detection of partially fallen-out magnetic slot wedges in inverter fed AC machines under various load conditions," 2012 IEEE Energy Conversion Congress and Exposition (ECCE), 2012, pp. 4015-4020.

[2] G. Stojičić et al., "A method to detect missing magnetic slot wedges in AC machines without disassembling," IECON 2011 - 37th Annual Conference of the IEEE Industrial Electronics Society, 2011, pp. 1698-1703.

[3] G. Stojicic, M. Vasak, N. Peric, G. Joksimovic and T. M. Wolbank, "Detection of partially fallen-out magnetic slot wedges in inverter fed AC machines under various load conditions," 2012 IEEE Energy Conversion Congress and Exposition (ECCE), 2012, pp. 4015-4020.

[4] K. W. Lee et al., "Detection of Stator-Slot Magnetic Wedge Failures for Induction Motors Without Disassembly," in IEEE Trans. on Industry Applications, vol. 50, no. 4, pp. 2410-2419, July-Aug. 2014.

[5] Shuping Wang, Zhengming Zhao, Liqiang Yuan and Buyao Wang, "Investigation and analysis of the influence of magnetic wedges on high voltage motors performance," 2008 IEEE Vehicle Power and Propulsion Conference, 2008, pp. 1-6.

[6] H. Mikami, K. Ide, K. Arai, M. Takahashi and K. Kajiwara, "Dynamic harmonic field analysis of a cage type induction motor when magnetic slot wedges are applied," in IEEE Trans. on Energy Conversion, vol. 12, no. 4, pp. 337-343, Dec. 1997.

[7] D. G. Jerkan, D. D. Reljić and D. P. Marčetić, "Broken Rotor Bar Fault Detection of IM Based on the Counter-Current Braking Method," in IEEE Trans. on Energy Conversion, vol. 32, no. 4, pp. 1356-1366, Dec. 2017.

[8] Xiaogang Luo, Yuefeng Liao, H. A. Toliyat, A. El-Antably and T. A. Lipo, "Multiple coupled circuit modeling of induction machines," in IEEE Trans. on Industry Applications, vol. 31, no. 2, pp. 311-318, March-April 1995.

[9] M. Ojaghi, M. Sabouri and J. Faiz, "Performance Analysis of Squirrel-Cage Induction Motors Under Broken Rotor Bar and Stator Inter-Turn Fault Conditions Using Analytical Modeling," in IEEE Trans. on Magnetics, vol. 54, no. 11, pp. 1-5, Nov. 2018, Art no. 8203705.

Time-domain Simulation of Electric Circuit with Nonlinear Hysteretic Inductor

Srđan Divac and Branko Koprivica

***Abstract*—The aim of this paper is to present a method for simulation of electric circuits with nonlinear inductor with hysteresis in time domain. The method is based on solving equation derived from Kirchhoff's law of the considered electric circuit through a series of successive iterations. Electric circuit consisting of AC voltage source connected in series with linear resistor, linear inductor and nonlinear inductor with hysteresis has been considered. Simulations have been performed for four cases of the considered electric circuit – without linear elements, with one and both linear elements, for sinusoidal voltage source amplitudes from 2 V to 10 V with the step of 2 V. Detailed simulation procedure, measurement and simulation results, as well as adequate discussion, have been presented.**

***Index Terms*—Simulation method, electric circuit, nonlinear inductor, magnetic hysteresis, time domain.**

I. INTRODUCTION

SOLVING an electric circuit with nonlinear inductor with hysteresis is very challenging due to the appearance of higher harmonics in the electric current, due to distorted waveform of the magnetic field (strength) of considered inductor [1]. Methods used in power engineering are commonly obtained by substituting the inductor with an equivalent *RL* circuit (consisting of a single nonlinear inductor represented by magnetising curve in parallel with linear or nonlinear resistor to represent hysteresis power loss) and solving the circuit [2]. However, this method cannot accurately solve electric circuits in time domain. Better results in time domain can be obtained by varying the resistance and the inductance of the elements in time, as proposed by De Leon [3]. More complex solutions of the electric circuit implement the use of one of the hysteresis models to represent the inductor with hysteresis [4]. Some of the commonly used models are: Preisach [5], Jilles-Atherton [6], Neural Network based models [7] and others. This method gives better results in time domain but the mathematics behind the model itself can be quite complex and its parameters difficult to obtain.

Presented simulation method is based on solving equation derived from Kirchhoff's law for the considered electric circuit through series of successive iterations. Electric circuit consisting of AC voltage source connected in series with linear resistor, linear inductor and nonlinear inductor with hysteresis. Influence of the inductor with hysteresis has been accounted for by calculating circuit current from dynamic magnetic field waveform $H_{dyn}(t)$ of the inductor. Dynamic field $H_{dyn}(t)$ has been obtained by following the simulation method for dynamic hysteresis loops and rate-independent property of the quasistatic hysteresis loops [8, 9]. This has been done by considering three components of $H_{dyn}(t)$ - quasistatic field $H_{qs}(t)$, eddy current field $H_{eddy}(t)$ and excess field $H_{exc}(t)$ [10].

Measurements of the magnetic field waveform $H(t)$ and magnetic flux density waveform $B(t)$ have been made using the measurement method based on data acquisition with PC [1]. Waveforms have been measured at frequency of 1 Hz for amplitudes of sinusoidal $B(t)$ from 0.2 T to 1.6 T with measurement step of 0.2 T. Also, measurement has been made at frequency of 50 Hz for sinusoidal $B(t)$ with the amplitude of 1 T. This measurement has been used for calculation of phenomenological parameters of $H_{exc}(t)$ by fitting the calculated excess power loss to measured excess loss. Fitting has been performed using the criteria of least root mean square deviation (RMSD [11, 12]) between excess power loss.

Simulations have been made for four cases of the considered electric circuit - without linear elements, with one and both elements, for sinusoidal input voltage with amplitudes from 2 V to 10 V with the step of 2 V.

A description of the simulation procedure, presentation of measurement and simulation results, as well as adequate discussion have been given in the paper.

II. MEASUREMENT RESULTS

Measurements of magnetic field $H(t)$ and magnetic flux density $B(t)$ waveforms have been performed by using measurement method based on data acquisition and PC [1]. Measurements have been made with toroidal shaped sample made of electrical steel sheet 27PH100 (manufactured by POSCO). Parameters of used toroidal sample can be found in Table I. All measurements have been made with 1000 data points.

TABLE I
PARAMETERS OF THE TOROIDAL SAMPLE

N_1	175	r_1 [mm]	45
N_2	60	r_2 [mm]	52.5
l_c [m]	0,306	m [kg]	0.241
S [mm^2]	102,80	w [mm]	15

A set of quasistatic hysteresis loops has been measured at

Srđan Divac – Faculty of technical sciences Čačak, University of Kragujevac, Svetog Save 65, 32000 Čačak, Serbia, (e-mail: srdjan.divac@ftn.kg.ac.rs).

Branko Koprivica – Faculty of technical sciences Čačak, University of Kragujevac, Svetog Save 65, 32000 Čačak, Serbia, (e-mail: branko.koprivica@ftn.kg.ac.rs).

frequency of 1 Hz for controlled sinusoidal shape of $B(t)$ (voltage induced at the secondary winding). Measurements have been made for $B(t)$ amplitudes ranging from 0.2 T to 1.6 T with step of 0.2 T. The obtained hysteresis loops are presented in Fig. 1. Also, $H(t)$ and $B(\mathrm{t})$ have been measured at 50 Hz and 1 T to obtain a dynamic hysteresis loop needed for calculation of phenomenological parameters of $H_{exc}(t)$. This hysteresis loop is shown in Fig. 1 as dashed line.

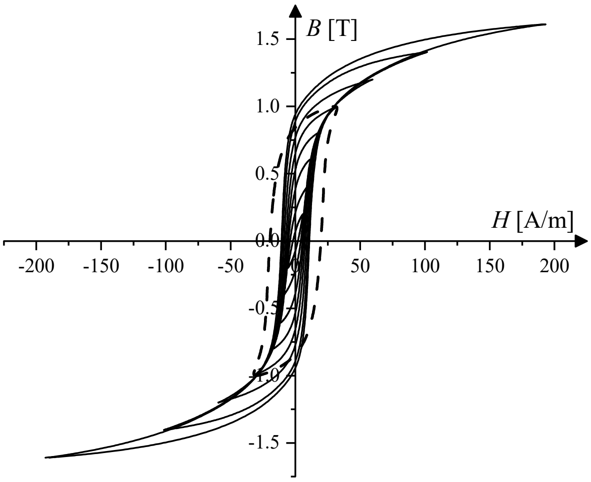

Fig. 1. Measured hysteresis loops for sinusoidal shape of $B(t)$.

III. SIMULATION PROCEDURE

Considered electric circuit consisting of voltage source $u(t)$ in series with linear resistor R, linear inductor L and nonlinear inductive element exhibiting hysteretic properties L_h is presented in Fig. 2.

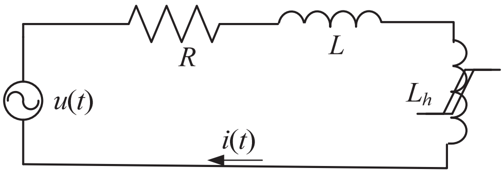

Fig. 2. Electric AC circuit with linear R and L elements and nonlinear L_h element with hysteresis.

Solving of this circuit means the calculation of its electric current $i(t)$, which depends on elements R, L and L_h and their characteristics. Obtaining dynamic solution is complicated due to the nonlinear and hysteretic characteristic of L_h. Its characteristic is usually represented with the dynamic hysteresis loops (the dynamic magnetic field $H_{dyn}(t)$ and magnetic flux density $B(t)$).

A. Calculation of dynamic magnetic field $H_{dyn}(t)$

Dynamic magnetic field $H_{dyn}(t)$ can be obtained by calculating its quasistatic $H_{qs}(t)$, eddy current $H_{eddy}(t)$ and excess $H_{exc}(t)$ components, and summing them up [10, 12]:

$$H_{dyn}(t) = H_{qs}(t) + H_{eddy}(t) + H_{exc}(t) \tag{1}$$

Calculation of $H_{qs}(t)$ requires two steps. First, quasistatic field $H_{int}(t)$ needs to be calculated for sinusoidal $B(t)$, $B_{int}(t)$, with the amplitude $B_{\max}$ of interest. So, N harmonic components (amplitudes and phases) of measured quasistatic $H(t)$ need to be calculated at particular amplitudes of $B(t)$ for each measured quasistatic loop, Fig. 1. For new $B_{\max}$ of interest, N new harmonics of $H_{int}(t)$ can be calculated by linear or higher order polynomial interpolation of previously calculated harmonics [8]. Further, $H_{int}(t)$ and a new quasistatic hysteresis loop formed by $H_{int}(t)$ and sinusoidal $B_{int}(t)$ can be obtained. In the second step, a general solution for $H_{qs}(t)$ for non-sinusoidal $B(t)$, $B_{Lh}(t)$, with the amplitude of $B_{\max}$, can be obtained by using inverted hysteresis loop $H_{int}(B_{int})$, which can be considered as rate-independent (having fixed shape) at the frequency of 1 Hz. The shape of that hysteresis loop is only determined by the amplitudes of $H(t)$ and $B(t)$ and not by the shape of their waveforms [9]. Thus, $H_{qs}(t)$ can be obtained by reconstructing data points for $B_{Lh}(t)$ over data points for $H_{int}(B_{int})$ [13]. This procedure is illustrated in Fig. 3.

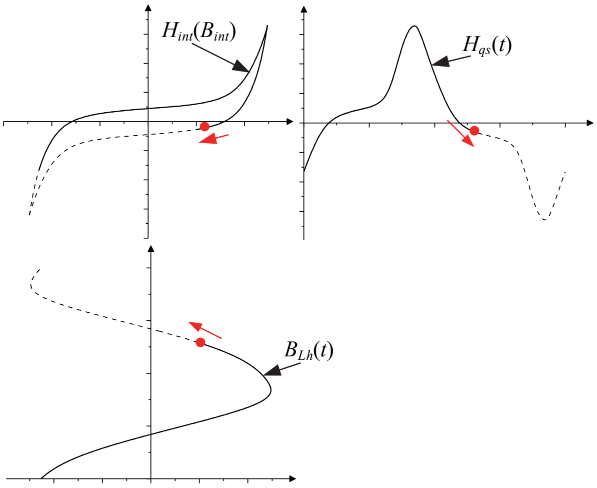

Fig. 3. Illustration of obtaining $H_{qs}(t)$ by reconstructing of non-sinusoidal $B_{Lh}(t)$ over the quasistatic hysteresis loop $H_{int}(B_{int})$.

Calculation errors may occur during this step due to the phase difference between $B_{Lh}(t)$ and $B_{int}(\mathrm{t})$. This phase difference can be taken into account by delaying $B_{Lh}(t)$ for the period of Δt, $B_{Lh}(t+\Delta t)$, and proceed further with the calculations. Delaying period should be chosen so that the minimum and maximum values of $B_{Lh}(t+\Delta t)$ occur at the same time as for $B_{int}(t)$. Resulting $H_{qs}(t+\Delta t)$ should be delayed for the period of $-\Delta t$ to obtain $H_{qs}(t)$.

Waveform of $H_{eddy}(t)$ can be calculated from well-known analytical expression [10]:

$$H_{eddy}(t) = \frac{\sigma d^2}{12} \frac{\mathrm{d}B_{Lh}(t)}{\mathrm{d}t}, \tag{2}$$

where σ is the conductivity of steel sheet and d is its thickness.

Calculation of $H_{exc}(t)$ can be made using the following expression [10]:

$$H_{exc}\left(t\right)=\frac{n_0V_0}{2}\left(\sqrt{1+\frac{4\sigma GS}{n_0{}^2V_0}\frac{\mathrm{d}B_{Lh}\left(t\right)}{\mathrm{d}t}}-1\right),\tag{3}$$

where G is equal to 0.1356 and n_0 and V_0 are phenomenological parameters of material.

Consideration of hysteresis loop measured at 1 Hz as rate-independent is not completely correct (accurate), as there would always exist some difference between such loop and true static loop due to the existence of the dynamic components of the field ($H_{eddy}(t)$ and $H_{exc}(t)$). Dynamic components at 1 Hz participate with several percent in the quasi-static field and power loss under sinusoidal and non-sinusoidal conditions [14]. However, these components are much smaller at 1 Hz than at 50 Hz, considered in the simulations. Accordingly, the accuracy of the simulation would not be significantly affected with such consideration (approximation).

It should be noted that all quantities measured and calculated (magnetic field and flux density) are averaged for the considered mean magnetic path length and cross-section area of the toroidal sample. Actually, these quantities vary with the radial distance from the sample longitudinal axis (over the radius). However, the variations are not too high when the outer to inner radius ratio ($r_2/\ r_1$) is low, as in the case of used sample (see Table I). The results of the simulation relate to the sample as a whole, as a part of the considered electric circuit, neglecting inhomogeneity of the magnetic field, which is acceptable in most of the practical applications. Accordingly, expressions (2) and (3) do not depend on the toroid dimensions (radiuses r_1 and r_2 and width w).

B. Iterative procedure

Proposed iterative algorithm for solving the circuit presented in Fig. 2 can be divided into the following steps:

1) calculating of the voltage at L_h for $(i+1)$-th iteration, $u_{Lh,i+1}(t)$, using II Kirchhoff's law [15]:

$$u_{Lh,i+1}(t)=u(t)-Ri_i(t)-L\frac{\mathrm{d}i_i(t)}{\mathrm{d}t},\tag{4}$$

where $i_i(t)$ is the current derived from i-th iteration, t is the time, R and L are the resistance and inductance of the considered linear elements,

2) calculation of $B_{Lh,i+1}(t)$ from $u_{Lh,i+1}(t)$ using Faraday's law [15], as follows:

$$B_{Lh,i+1}(t)=\frac{1}{N_1S}\int_0^t u_{Lh,i+1}(t)\mathrm{d}t,\tag{5}$$

where N_1 is the number of turns in the magnetising coil and S is the cross-section area of magnetic core of L_h,

3) calculation of $H_{dyn,i+1}(t)$ for non-sinusoidal $B_{Lh,i+1}(t)$ using the procedure explained in subsection A,
4) calculation of $i_{i+1}(t)$ using Ampere's law [15]:

$$i_{i+1}(t)=\frac{H_{dyn,i+1}(t)}{N_1}l_c,\tag{6}$$

where l_c is the mean magnetising path length of L_h,

5) steps 1-4 should be repeated until condition (7) is met:

$$\frac{\max\{|\,i_i(t)\,|\}-\max\{|\,i_{i+1}(t)\,|\}}{\max\{|\,i_{i+1}(t)\,|\}}100\%<\varepsilon,\tag{7}$$

where ε is predetermined limit, which is not so rigorous.

Iterative procedure starts with $i_0(t)=0$ A for each time sample of $t>0$ and amplitude of $u(t)$ factorised by $K>1$ to minimise the oscilations and time shifts between iterations, such that:

$$U_{m,k}=\frac{U_m}{K}k,\tag{8}$$

where $k=1, 2, 3,\ldots, K$. Solution of the k-th step is the new initial condition $i_k(t)$ for the $(k+1)$-th step. The value of K should be chosen high enough to allow for good convergence of the iterative procedure, but low enough to keep required computation time acceptable.

After finishing the iterative procedure, obtained waveforms of $H_{dyn}(t)$ and $B_{Lh}(t)$ can be used to plot dynamic hysteresis loop of L_h. Also, the specific power loss of L_h (corresponding to the area of the dynamic hysteresis loop), expressed in W/kg, can be calculated as:

$$P_s=\frac{1}{mT}\int_0^T u_{L_h}\left(t\right)i\left(t\right)\mathrm{d}t=\frac{S\,l_c}{mT}\int_0^T\frac{\mathrm{d}B_{L_h}\left(t\right)}{\mathrm{d}t}H_{dyn}\left(t\right)\mathrm{d}t,\tag{9}$$

where $T=1/f$ is the period and m is the mass.

IV. SIMULATION RESULTS

Four cases of the electric circuit presented in Fig. 2 have been considered:

I. with $R=0\ \Omega$ and $L=0$ H;
II. with $R=48\ \Omega$ and $L=0$ H;
III. with $R=0\ \Omega$ and $L=20$ mH and
IV. with $R=48\ \Omega$ and $L=20$ mH.

A sinusoidal voltage source with U_m from 2 V to 10 V with the step of 2 V and frequency of 50 Hz has been used for all performed simulations. All simulations have been made using 1000 data points.

Other, lower or higher frequencies can also be used in simulations. However, the frequency of 50 Hz is of particular importance, as it is used as the working frequency in most of the basic electric circuits, as considered one. Consideration of higher frequencies would also be interesting for some advanced applications of electric machines and drives, power electronics and other. However, that is beyond of the scope of this paper.

Total of N=35 harmonics of measured quasistatic $H(t)$ have been used during the 4th step of the simulation process. This number of harmonics has been found to be optimal in case of U_m=10 V, therefore, less harmonics could be used for lower U_m.

Parameters of the electrical steel σ and d, used to calculate the magnetic field of eddy currents in (2), have been provided by the manufacturer and amount 2083 kS/m and 0.27 mm, respectively. Other parameters of the material given by the producer are: density ρ=7650 kg/m^3, $B_{\max}$=1.90 T for $H_{\max}$=800 A/m, specific power loss at 50 Hz is 0.72 W/kg for 1.5 T and 0.95 for 1.7 T, maximum of the relative permeability is around 70000 for static fields, coercive field goes up to 10 A/m for static field and up to 25 A/m for field at 50 Hz under sinusoidal $B(t)$.

Parameters n_0=908 and V_0=0.08 A/m in (3) have been obtained by fitting the excess power loss caused by $H_{exc}(t)$ for sinusoidal shape of $B(t)$ at 1 T to the excess power loss calculated from measurements for the same $B(t)$ [12], taking into account both hysteresis and dynamic loss (given by the hysteresis loops measured at 1 Hz and 50 Hz) and eddy current loss calculated using $H_{eddy}(t)$ given by (2) at 50 Hz. Fitting has been performed using the criteria of RMSD between excess power loss produced by fitted and calculated excess magnetic field. Both parameters have been kept constant in all performed simulations.

Predetermined limit ε has been set to 0.5%. This value has been chosen in order to obtain best convergence of the simulation procedure. Parameter K has been set to 30 to obtain best solutions in case III for U_m=10 V and has been kept at this value for all simulations. It has been found that total number of iterations for K steps is 36, 30, 31 and 30, for each of the considered cases at U_m=10 V, respectively.

Results for $i(t)$ for case IV of electric circuit for all considered values of U_m are presented in Fig. 4.

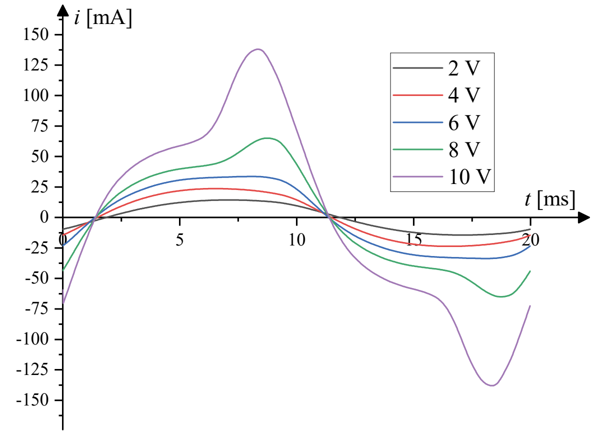

Fig. 4. Simulated $i(t)$ waveforms for the case of R=48 Ω and L=20 mH, for all considered values of U_m.

Influence of linear circuit elements R and L to the solution of the circuit for considered cases I-IV is better seen in observing the hysteresis loops of L_h than in observing $i(t)$. Therefore, a number of simulated hysteresis loops has been constructed and the loops have been compared to observe such influence.

Simulated hysteresis loops for each of the considered cases of circuit and all values of U_m are presented in Fig. 5-8, respectively. Scales are the same in all these figures for better illustration of R and L influence.

It can be seen that in all of the presented cases simulated hysteresis loops for lower U_m are fully encompassed by the hysteresis loops of higher U_m. This is in accordance with the hysteresis theory which states that hysteresis loops obtained for higher voltages, under same conditions, should encompass the ones at lower voltages [10].

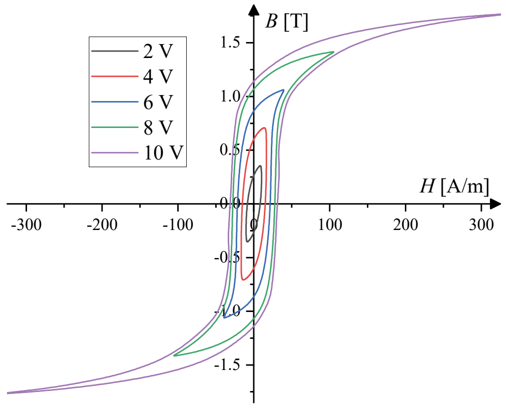

Fig. 5. Simulated hysteresis loops for the case of R=0 Ω and L=0 mH, for all considered values of U_m.

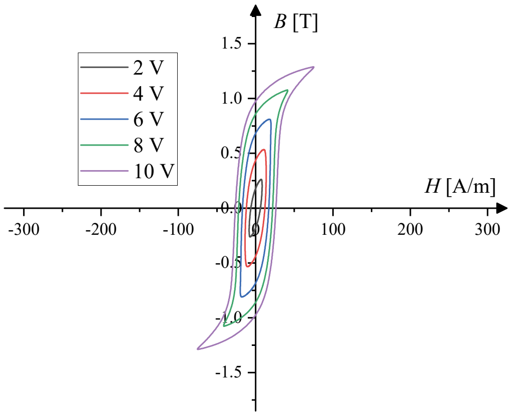

Fig. 6. Simulated hysteresis loops for the case of R=48 Ω and L=0 mH, for all considered values of U_m.

Hysteresis loops for all considered cases of electric circuit at particular values of U_m are presented in Fig. 9-13, respectively.

At lower voltages, Figs. 9 and 10, the used electrical steel exhibits almost linear behaviour, therefore resulting in almost elliptical loops and sinusoidal $i(t)$. This limits the influence of L in (4) since its voltage is proportion to the rate of change of $i(t)$. Also, adding R in the electric circuit results in lover voltage levels at L_h. Its influence is more noticeable than the L's, since the voltage over the resistor is proportional to the $i(t)$.

Simulations at higher voltages, Figs. 11-13, show greater influence of nonlinearity of the material, causing the significant peaks in the $i(t)$. Influence of L is more prominent under these conditions, resulting in smoother $i(t)$ in case III than in case I by effectively lowering its peaks. Choking of the current [15] is less prominent in case IV since in this case linear R causes lower voltage levels at L_h-lesser influence of nonlinearity on the shape of $i(t)$, making it smoother.

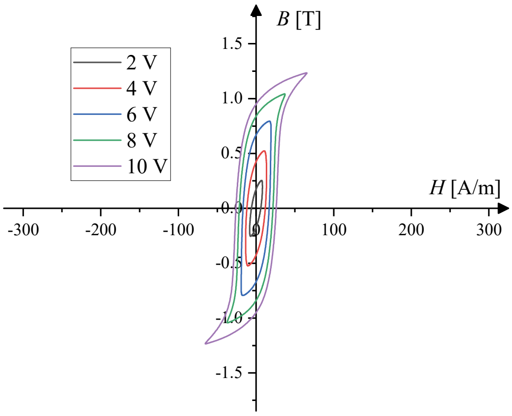

Fig. 7. Simulated hysteresis loops for the case of R=0 Ω and L=20 mH, for all considered values of U_m.

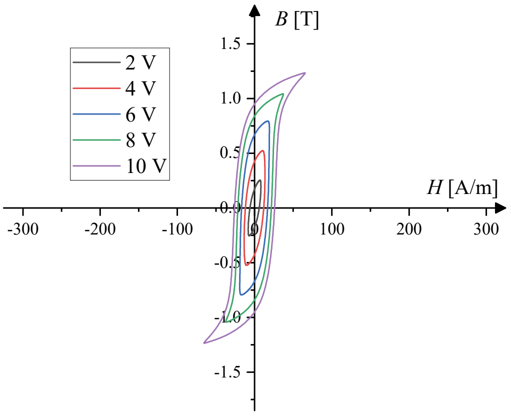

Fig. 8. Simulated hysteresis loops for the case of R=48 Ω and L=20 mH, for all considered values of U_m.

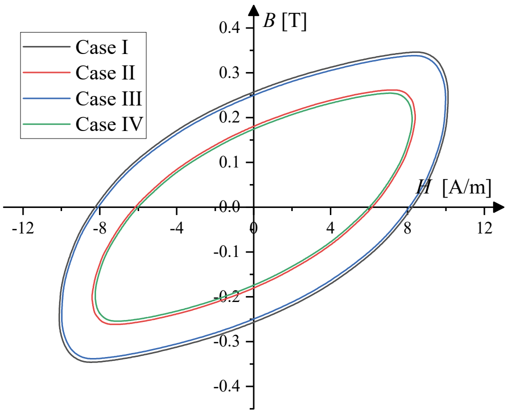

Fig. 9. Simulated hysteresis loops for U_m=2 V for all considered cases of electric circuit.

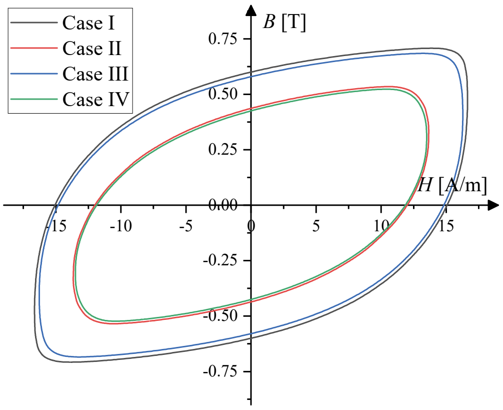

Fig. 10. Simulated hysteresis loops for U_m=4 V for all considered cases of electric circuit.

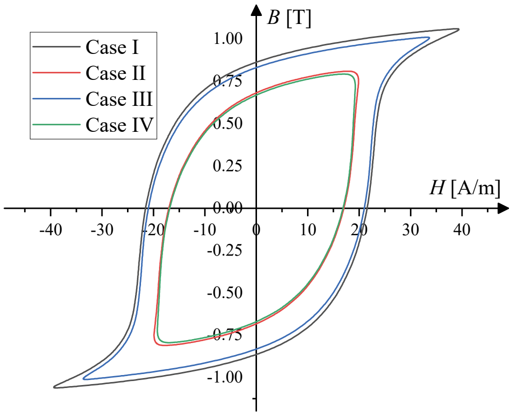

Fig. 11. Simulated hysteresis loops for U_m=6 V for all considered cases of electric circuit.

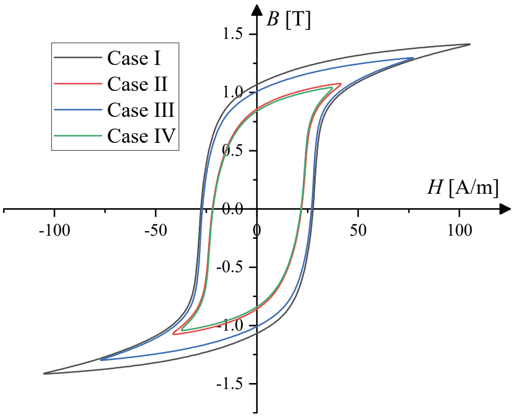

Fig. 12. Simulated hysteresis loops for U_m=8 V for all considered cases of electric circuit.

According to the results presented, simulation method presented could be suitable for solving electric circuits with L_h for sinusoidal $u(t)$ in the steady state time domain. The simulation method presented has not been tested in simulation of transient processes.

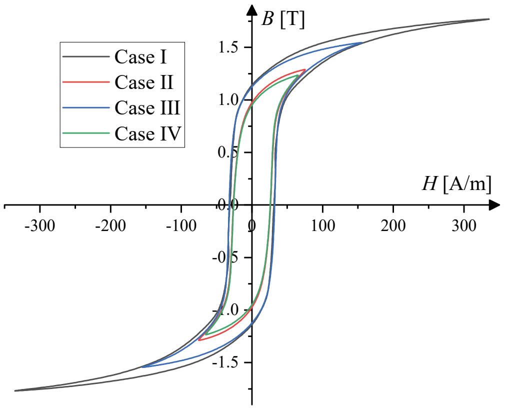

Fig. 13. Simulated hysteresis loops for U_m=10 V for all considered cases of electric circuit.

V. CONCLUSION

A simulation method for solving electric circuits with nonlinear inductor with hysteresis in time domain has been resented in this paper. The considered electric circuit consisted of AC voltage source connected in series with linear resistor, linear inductor and nonlinear inductor with hysteresis. Proposed calculation procedure has been based on solving an equation derived from Kirchhoff's law through series of successive iterations. Influence of the inductor with hysteresis has been accounted for by calculating current in the electric circuit from its $H_{dyn}(t)$ corresponding to the $B_{Lh}(t)$ from iteration. Waveform of $H_{dyn}(t)$ has been calculated as the sum of its quasistatic, eddy current and excess magnetic field components. Each component has been calculated separately for the considered $B_{Lh}(t)$.

Measurements have been made for $H(t)$ at low frequency of 1 Hz for sinusoidal shape of $B(t)$ for amplitude from 0.2 T to 1.6 T with the measurement step of 0.2 T. Also, measurements have been made at 50 Hz for the sinusoidal $B(t)$ of 1 T.

Simulations have been performed for sinusoidal voltage source with the amplitudes from 2 V to 10 V with the step of 2 V. Also, four cases of the electric circuit have been considered for each of the voltages-without, with one and with both linear elements. Based on the simulation result and their discussion, it can be concluded that the presented simulation method could be suitable for solving electric circuits with nonlinear inductors with hysteresis in steady state time domain.

ACKNOWLEDGMENT

This study was supported by the Ministry of Education, Science and Technological Development of the Republic of Serbia, and these results are parts of the Grant No. 451-03-68/2022-14/200132 with University of Kragujevac - Faculty of Technical Sciences Čačak.

REFERENCES

[1] B. Koprivica, A. Milovanović, M. Đekić, "Effects of Wound Toroidal Core Dimensional and Geometrical Parameters on Measured Magnetic Properties of Electrical Steel", Serbian Journal of Electrical Engineering, vol. 10, no. 3, pp. 459-471, Oct. 2013.

[2] A. Rezaei-Zare, R. Iravani, "On the Transformer Core Dynamic Behavior During Electromagnetic Transients", *IEEE Transactions on Power Delivery*, vol. *25*, no. *3*, pp. *1606-1619*, July 2010.

[3] F. G. Montoya, F. De Leon, F. Arrabal-Campos, A. Alcayde, "Determination of Instantaneous Powers from a Novel Time-Domain Parameter Identification Method of Non-Linear Single-Phase Circuits", *IEEE Transactions on Power Delivery* (Early Access), Dec. 2021.

[4] J. H. B. Deane, "Modelling the Dynamics of Nonlinear Inductor Circuits", *IEEE Transactions on Magnetics*, vol. *30*, n0. *5*, pp. *2795 – 2801*, Sept. 1994.

[5] I. D. Mayergoyz, "*Mathematical Models of Hysteresis and Their Applications*", Elsevier Science, New York, USA, 2003.

[6] A. R. P. J. Vijn, O.Baas, E. Leepelaars, "Parameter Estimation for the Jiles–Atherton Model in Weak Fields", *IEEE Transactions on Magnetics*, vol. *56*, no. *4*, April 2020.

[7] A. S. Q. Antonio, F. R. Fulginer, A. Laudani, A. Faba, E. Cardelli, "An Effective Neural Network Approach to Reproduce Magnetic Hysteresis in Electrical Steel Under Arbitrary Excitation Waveforms", *Journal of Magnetism and Magnetic Materials,* vol. *528*, June 2021.

[8] S. Divac, B. Koprivica, "Simulation of Dynamic Hysteresis Loops for Toroidal Sample for Sinusoidal Shape of Magnetic Flux Density", 21st International Symposium INFOTEH-JAHORINA, 16-18. March 2022.

[9] D. Makaveev, L. Dupre, M. De Wulf, J. Melkebeek, "Modelling of Rate-Independent Hysteresis with Feed-Forward Neural Networks", Conf. Proc. Neural Networks and Appl., Interlaken, Switzerland, pp. 3451-3456, Feb. 2002.

[10] G. Bertotti, "*Hysteresis in Magnetism for Physicists, Material Scientists and Engineers*", Academic Press, New York, USA, 1998.

[11] C. D. Schunn, D. Wallach, "Evaluating Goodness-of-Fit in Comparison of Models to Data", pp. *115-135*, 2005. In W. Tack (Ed.), Psychologie der Kognition: Reden and Vorträge anlässlich der Emeritierung von Werner Tack, Saarbrueken, Germany, University of Saarland Press.

[12] B. Koprivica, S. Divac, "Analysis and Modeling of Instantaneous Magnetizing Power of Ferromagnetic Core in Time Domain", *IEEE Magnetic Letters*, vol. *12*, p. *2103505*, Sept. 2021.

[13] J. Takacs, "Hysteresis Loop Reversing by Applying Langevin Approximation", *The International Journal for Computation and Mathematics in Electrical and Electronic Engineering*, vol. *36*, no. *4*, July 2017.

[14] M. De Wulf, L. Dupre, J. Melkebeek, "Quasistatic Measurements for Hysteresis Modeling", Journal of Applied Physics, vol. 87, no. 9, pp. 5239-5241, May 2000.

[15] K. L. Kaiser, "*Electromagnetic Compatibility Handbook*", CRC Press, New York, USA, 2004.

A Comparative Analysis of Three-Phase Phase-Locked Loops for Grid-Connected Systems

Filip Bakić, Lazar Stojanović, Katarina Obradović, Emilija Lukić

Abstract—**In renewable power generation system, synchronization of the inverter and the power grid is essential for the stable control of grid-connected inverters. Phase-Locked Loops (PLL) are widely used for grid synchronization due to simple implementation and robust performance against the grid disturbances. The main goal of this paper is to present a survey of the comparative performance evaluation among the synchronous reference frame PLL (SRF-PLL), Lag-PLL, stationary-frame based enhanced PLL (SF-EPLL) and double second-order generalized integrator PLL (DSOGI-PLL) under disturbances such as frequency changes, voltage sags and harmonic distortion. System structures and working principles are presented. Moreover, the parameters design for each algorithm are proposed. Dynamic analysis and experimental results of steady state performance of PLLs are observed and compared to verify and validate theoretical comparative analysis.**

Index Terms—**Phase-locked loop, grid synchronization, frequency estimation, three-phase**

I. INTRODUCTION

Over the past couple of decades, there is a clear trend of switching from fossil fuels to renewable energy sources (RES) in electricity production. Furthermore, distributed generation (DG) of RES and their wide prevalence created a possibility to work independently from the grid i.e. in islanded mode, but also as generating units that inject active or reactive power directly to the grid. Many such grid-tied solutions rely on the proper usage of DC-AC power converters in order to successfully connect to the power system. Hence, advancing both hardware and control solutions has become a great deal.

The process of connecting the inverter to the grid is called synchronization of the inverter. In order to achieve successful synchronization, it is important that amplitude, phase and the frequency of the inverter's and the grid's voltages are precisely determined. In case of small DG such as rooftop solar PV systems intended to connect to weak distribution grid, parameters and quality of grid's voltage can vary significantly due to constant change of load. Thus, robust, efficient and precise controlling scheme becomes even more important.

The research work for the most suitable way for synchronizing inverters with the grid has resulted in numerous solutions. In general, all these methods could be classified as either single phase or three-phase based methods. Some of them, such as open transition transfer, are less applicable due to reduced reliability of the power system. On the other side, others, such as passive synchronization, imply usage of synchoncheck relay for synchronization check of voltage, frequency and phase [1]. Although passive synchronization methods do not require control mechanism, using this type of synchronization results in longer reconnecting process. Nevertheless, the most commonly used synchronization method is active synchronization. With implementation of controlling mechanisms, synchronization can be done by controlling the frequency and voltage. The most acknowledged concepts nowadays are Frequency Locked Loop [2], Droop Control [3], [4] and Phase Locked Loop (PLL). Due to simplicity, robustness and effectiveness in various grid conditions, PLL is the most commonly used synchronization method. To improve PLL performances under various grid conditions, numerous modifications have been done, such as Synchronous Reference Frame PLL (SRF-PLL) [5], enhanced PLL (EPLL), fixed-reference frame PLL (FRF-PLL) [6], Lag-PLL, SF-EPLL and DSOGI-PLL [7] .

In this paper, multiple PLL solutions are introduced and discussed. In the third paragraph PLL algorithms Synchronous Reference Frame PLL (SRF-PLL), Lag-PLL, SF-EPLL and DSOGI-PLL are analyzed. Then, Paragraph IV The process of selection of the adequate parameters for each algorithm is explained. Finally, experimental results were conducted on real prototype of grid-connected inverter.

II. GENERALIZED STRUCTURE OF PLL

Basic structure of every PLL can be organized in three sections, Fig. 1:

1) Phase detector (PD): It compares generated signal with desired one and generates corresponding error. For three-phase systems, voltages u_{abc} in a stationary reference frame are transformed in a synchronous rotating frame, where sinusoidal voltages are represented as DC values u_{dq}.
2) Low-Pass filter (LPF): Some phase detectors generate undesired high frequency signals that need to be filtered. For three-phase systems, LPF is often designed as PI controller which input is q component of the voltage. The goal for PI controller is to bring q component to zero. This will ensure that phase is aligned with d axis.
3) Voltage controlled oscillator (VCO): After the angular frequency is estimated, it is integrated to get phase. This phase is then sent to phase detector to finish one iteration of PLL.

Filip Bakić is master student in School of Electrical Engineering, University of Belgrade (email: filip543bakic@gmail.com)

Lazar Stojanović is master student in School of Electrical Engineering, University of Belgrade (email: lazastojanovic99@gmail.com)

Katarina Obradović is master student in School of Electrical Engineering, University of Belgrade (email: obradovick15@gmail.com)

Emilija Lukić is master student in School of Electrical Engineering, University of Belgrade (email: emilija.lukic505@gmail.com)

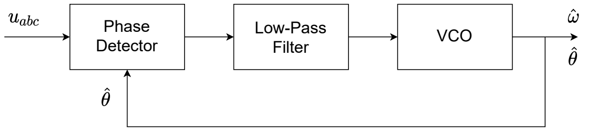

Fig. 1. Basic structure of PLL

III. OVERVIEW OF THE THREE-PHASE PLL ALGORITHMS

A. SRF-PLL

Synchronous Reference Frame PLL is one of most commonly used algorithm due to its low complexity and easy digital realization. Conventional scheme of the SRF-PLL is shown on Fig.2. Phase detector is cascade Clark (1) and Park (2) transformation. Angle used in Park transformation θ is one estimated from algorithm in previous cycle.

$$T_{abc/\alpha\beta} = \begin{bmatrix}\alpha \\ \beta\end{bmatrix} = \frac{2}{3}\begin{bmatrix}1 & -\frac{1}{2} & -\frac{1}{2} \\ 0 & \frac{\sqrt{3}}{2} & -\frac{\sqrt{3}}{2}\end{bmatrix}\begin{bmatrix}a \\ b \\ c\end{bmatrix} \tag{1}$$

$$T_{\alpha\beta/dq} = \begin{bmatrix}d \\ q\end{bmatrix} = \begin{bmatrix}\cos(\theta) & \sin(\theta) \\ -\sin(\theta) & \cos(\theta)\end{bmatrix}\begin{bmatrix}\alpha \\ \beta\end{bmatrix} \tag{2}$$

The goal of this PLL is to bring q component to zero and align the voltage vector with d axis. It is achieved by utilizing PI controller which output is angular frequency. A stationary value of frequency is added to ensure faster phase tracking. Frequency is then integrated to obtain phase, which is then used in PD.

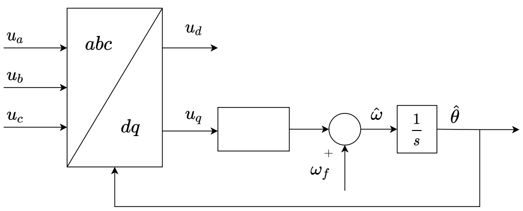

Fig. 2. Scheme of SRF-PLL

B. Lag-PLL

Another implementation of the PLL is shown in Fig.3 as proposed in [8] and referred as Lag-PLL, is derived from SRF-PLL by passing u_q through low-pass filter prior to the PI regulator. The intention of signal filtering is to improve PLL performance when sensing noise and higher harmonics are present in grid voltages.

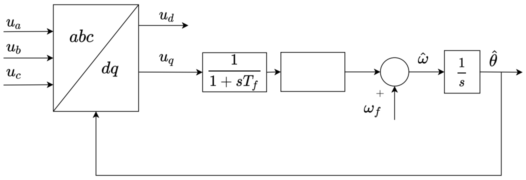

Fig. 3. Scheme of Lag-PLL

C. SF-EPLL

Since standard EPLL algorithm is implemented in a three-phase stationary it is relatively complex due to trigonometric and multiplying operations, the presented algorithm reduces complexity by transforming voltages in $\alpha\beta$ frame. Fig.4 shows the three-phase implementation of the enhanced PLL which was proposed in [9]. Besides estimating phase and frequency, EPLL add amplitude loop in PLL scheme. After the three-phase signals are transformed into u_α and u_β are subtracted by the estimated components y_α and y_β to obtain the estimated errors e_α and e_β. Amplitude and frequency error are defined as

$$e_v = e_\alpha sin(\tilde{\theta}) + e_\beta sin(\tilde{\theta} - 90°) \tag{3}$$

$$e_w = e_\alpha cos(\tilde{\theta}) - e_\beta cos(\tilde{\theta} - 90°) \tag{4}$$

They are, respectively, integrated to obtain amplitude and passed to the PI controller for frequency estimation. By integrating $\tilde{\omega}$ estimated angle is obtained.

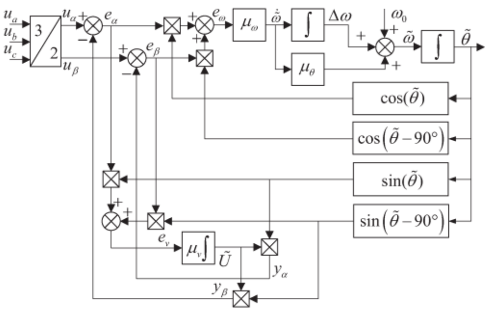

Fig. 4. Scheme of SF-EPLL [9]

D. DSOGI-PLL

Instead of filtering q component, DSOGI algorithm is designed in a way to prefilter $\alpha\beta$ components. Besides that, by dual integration, it is able to conserve information from positive sequenced harmonics by canceling negative sequenced harmonics in u'_α and u'_β by dividing with 2 voltage amplitude is preserved. Then u'_α and u'_β are transformed in dq components which further can be pass to standard SRF-PLL for frequency and phase estimation.

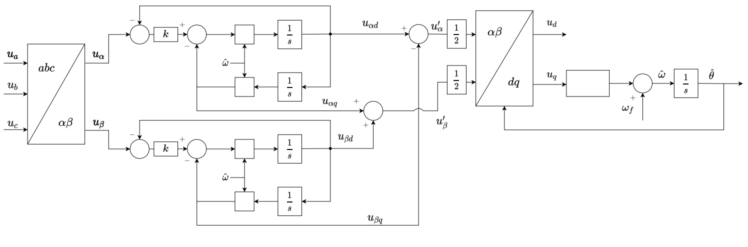

Fig. 5. Scheme of DSOGI-PLL

IV. SELECTION OF PARAMETERS

A. SRF-PLL

Because of nonlinear structure of phase detector analysis and parameters selection would be complicated so model is linearized Fig. 6. From the obtained linear model, we can select parameters of PI controller to achieve desired response. Open loop transfer function is equal to:

$$W_{open}(s) = \frac{\varphi_{PLL}}{\varphi_{grid}} = \frac{sK_pK_{pd} + K_iK_{pd}}{s^2} \tag{5}$$

from which closed loop function is equal to:

$$W_{close}(s) = \frac{sK_pK_{pd} + K_iK_{pd}}{s^2 + sK_pK_{pd} + K_iK_{pd}} \tag{6}$$

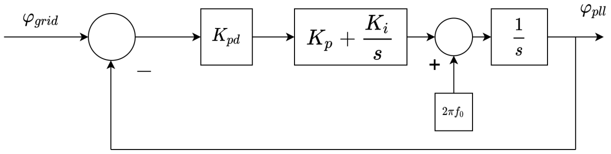

Fig. 6. Linearized model of SRF PLL

Where K_p, K_i are parameters of PI controller and Kpd represents amplitude of three-phase voltage. Selecting of parameters K_p and K_i is done to achieve desired bandwidth and damping by selecting coefficients to meet standard second order polynomial.

$$s^2 + 2\xi\omega_n s + \omega_n^2 = s^2 + sK_pK_{pd} + K_iK_{pd} \tag{7}$$

From where we can obtain parameters as:

$$K_i = \frac{\omega_n^2}{K_{pd}},\ K_p = \frac{2\xi\omega_n}{K_{pd}} \tag{8}$$

in this study, we chose $\xi = 1$ and $w_n = 37.7$ rad/s which corresponds with desired closed loop bandwidth of 6 Hz and absence of oscillations in response.

B. LAG-PLL

The idea of this PLL is to better filter higher harmonics than SRF. Since it only differs from SRF in added filter, we can use K_i and K_p used for SRF PLL. T_f is selected to minimize effect on system response. Open loop transfer function is equal to:

$$W_{open}(s) = \frac{\varphi_{PLL}}{\varphi_{grid}} = \frac{sK_pK_{pd} + K_iK_{pd}}{s^3T_f + s^2} \tag{9}$$

To find poles positions of closed loop in depending on T_f we used modified transfer function W_{mod}

$$W_{mod}(s) = \frac{T_f s^3}{s^2 + sK_pK_{pd} + K_iK_{pd}} \tag{10}$$

because closed loop poles for both transfer functions are the same. Poles position with respect to different value of T_f is shown in Fig. 7.T_f must be small enough to not interfere with system dynamics and large enough to filter higher harmonics. As a good compromise, T_f is selected to filter dynamics over 100Hz so $T_f = \frac{1}{200\pi}$.

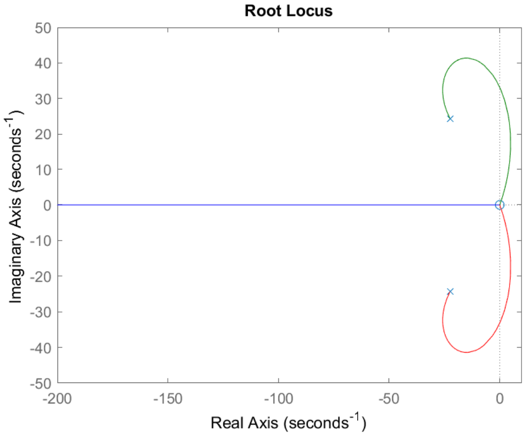

Fig. 7. Pole position for different values of T_f

C. DSOGI

Filtering power of dual integrator is determined by parameter, k which can we see in transfer functions from u_α to $u_{\alpha d}$ and u_α to $u_{\alpha q}$

$$G_d(s) = \frac{u_{\alpha d}}{u_\alpha} = \frac{k\omega_1 s}{s^2 + k\omega_1 s + \omega_1^2} \tag{11}$$

$$G_q(s) = \frac{u_{\alpha q}}{u_\alpha} = \frac{k\omega_1^2}{s^2 + k\omega_1 s + \omega_1^2} \tag{12}$$

transfer functions from u_β to $u_{\beta d}$ and u_β to $u_{\beta q}$ are the same.

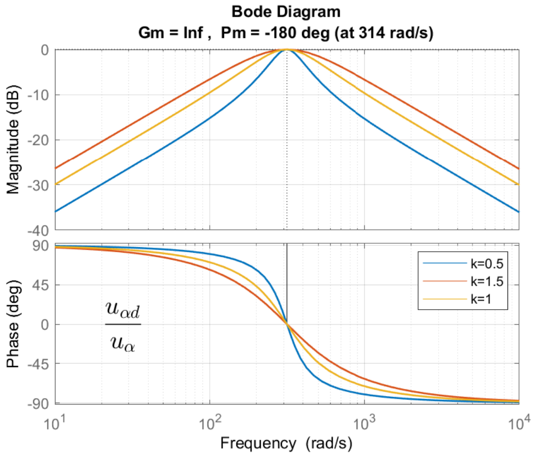

Fig. 8. Bode plot G_d in function of k

As it is shown on Fig. 8 and Fig. 9 increasing k give better attenuation of harmonics but also causes higher overshoot and greater settling time of estimation. For best trade-off $k = 1$ is selected. Parameters of PI controller K_i and K_p are same as in SRF and Lag-PLL.

D. SF-EPLL

For this PLL parameters for amplitude and frequency estimation can be chosen separately. For amplitude loop time

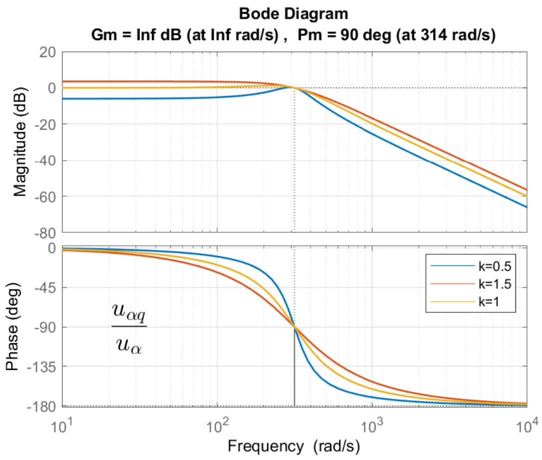

Fig. 9. Bode plot of G_q in function of k

constant of response is the same as $1/\mu_v$, from setting time of 50ms and $T_{sett} = 5/\mu_v$ we chose $\mu_v = 100$. Dynamic model of this PLL are provided in [9] from where $\mu_\theta = 2\xi/w_n$ and $\mu_\omega = w_n/\mu_\theta/U$ where U is estimate amplitude of grid voltage.

V. Simulation Results

Modeling of different PLLs and simulation is done by using Matlab and Simulink software.

Dynamic response of different PLLs is examined by step frequency change. As shown in Fig. 10 PLLs have similar rise time which means that regulation bandwidth is roughly the same. Despite, $\psi = 1$ overshoot is present due to the presence of dominant zero. Difference in overshoot is not crucial for performance of PLL.

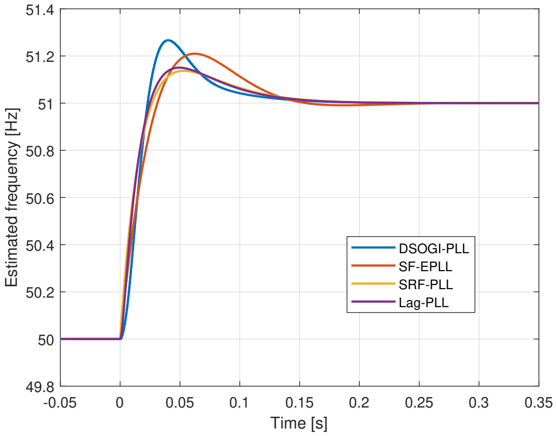

Fig. 10. Response on step frequency change

Unbalanced three-phase system is a problem for PLLs because it introduces ripple in frequency estimation. Unbalanced grid voltage used for simulation is shown in Fig. 11. Unbalanced grid conditions have the largest impact on SRF PLL. On the other hand, DSOGI is unaffected by distortions.

TABLE I
Performance comparison on step frequency change

PLL	Overshoot [%]	2% settling time [s]
SRF	13.70	0.143
Lag	15.05	0.140
SF-EPLL	20.95	0.138
DSOGI	26.65	0.130

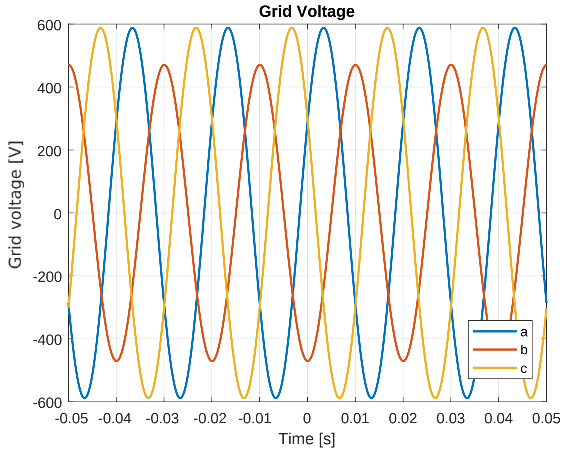

Fig. 11. Unbalanced grid voltage during simulation

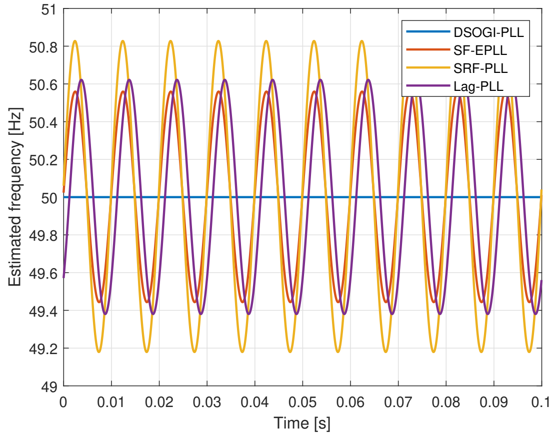

Fig. 12. Frequency estimation

TABLE II
Performance comparison in unbalanced conditions

PLL	Steady oscillation amplitude [Hz]
SRF	0.828
Lag	0.622
SF-EPLL	0.560
DSOGI	0

VI. Experimental Results

Experimental results were conducted of grid-connected inverter prototype. The prototype was designed for a grid with 208 V line voltage, so tests were conducted on that voltage. The algorithm is implemented on TMS320F28379D microcontroller. Experimental setup is shown on Fig. 13. The idea of this test is to show influence of real implementation and grid conditions on performance of PLL algorithms. Grid voltage with THD of 3.67% is shown on Fig. 14. Performance of different algorithms can be seen on Fig. 15 and Table III.

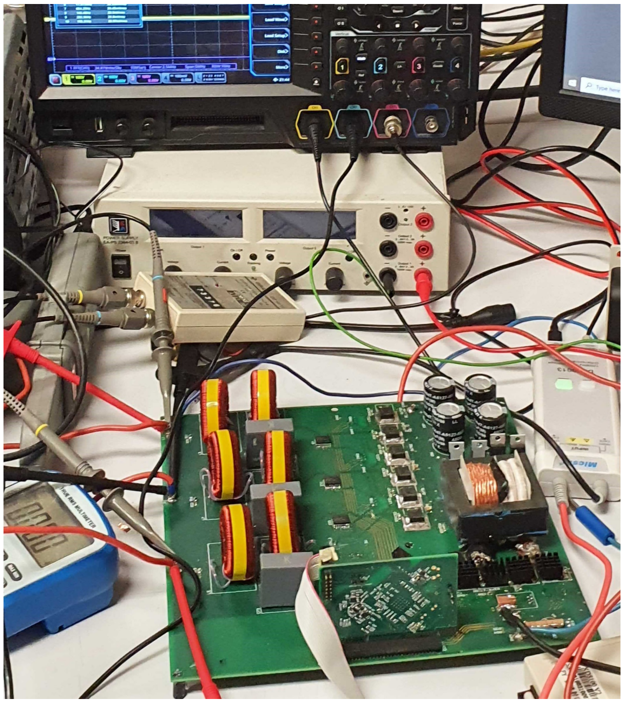

Fig. 13. Experimental setup

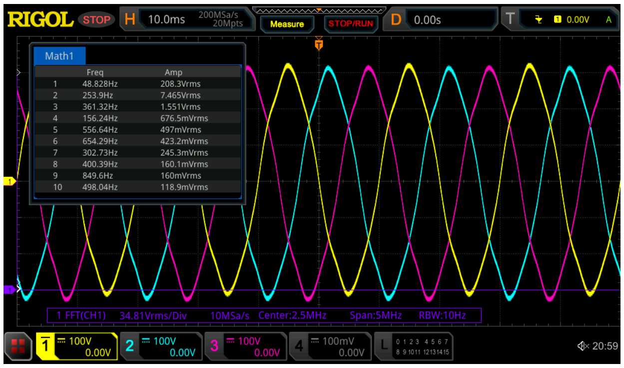

Math1

	Freq	Amp
1	48.828Hz	208.3Vrms
2	253.9Hz	7.465Vrms
3	361.32Hz	1.551Vrms
4	156.24Hz	676.5mVrms
5	556.64Hz	497mVrms
6	654.29Hz	423.2mVrms
7	302.73Hz	245.3mVrms
8	400.39Hz	160.1mVrms
9	849.6Hz	160mVrms
10	498.04Hz	118.9mVrms

Fig. 14. Grid voltage

TABLE III
PERFORMANCE COMPARISON IN EXPERIMENTAL CONDITIONS

PLL	Maximum error [Hz]	Mean error [Hz]
SRF	0.771	0.439
Lag	0.675	0.4153
SF-EPLL	0.509	0.2930
DSOGI	0.357	0.224

VII. CONCLUSION

Analysis and performance comparison of four three-phase PLL structures have been simulated and tested on real prototype. From the presented comparison, it is found that DSOGI-PLL has the best performance in all three scenarios, providing the most accurate frequency estimation. Worst results are obtained with SRF-PLL which was expected knowing that all other PLLs presents modification of this algorithm in desire to achieve better performance. Future analysis will focus on quality of current injected to grid by inverter knowing the dynamic and performance of frequency estimation, which is essential for accurate grid synchronization.

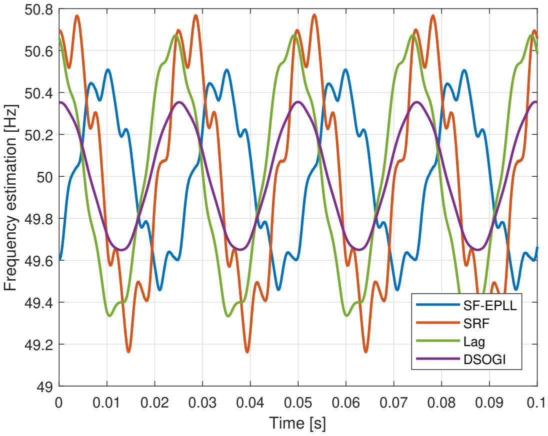

Fig. 15. Frequency estimation

ACKNOWLEDGMENT

We are grateful to Laboratory of the Digital Drive Control in the School of Electrical Engineering, University of Belgrade for testing equipment. Also, we are grateful to all H-Bridges team members for developing and implementation of this prototype.

REFERENCES

[1] N. Lidula and A. Rajapakse, "Voltage balancing and synchronization of microgrids with highly unbalanced loads," in *Renew. Sustain.Energy Rev.*, vol. 31, 2014, pp. 907–920.
[2] L. Widanagama Arachchige and A. Rajapakse, "Voltage balancing and synchronization of microgrids with highly unbalanced loads," *Renewable and Sustainable Energy Reviews*, vol. 31, pp. 907–920, 03 2014.
[3] C. Jin, M. Gao, X. Lv, and M. Chen, "A seamless transfer strategy of islanded and grid-connected mode switching for microgrid based on droop control," in *2012 IEEE Energy Conversion Congress and Exposition (ECCE)*, 2012, pp. 969–973.
[4] Y. Jia, D. Liu, and J. Liu, "A novel seamless transfer method for a microgrid based on droop characteristic adjustment," in *Proceedings of The 7th International Power Electronics and Motion Control Conference*, vol. 1, 2012, pp. 362–367.
[5] A. Bellini, S. Bifaretti, and F. Giannini, "A robust synchronization method for centralized microgrids," *IEEE Transactions on Industry Applications*, vol. 51, no. 2, pp. 1602–1609, 2015.
[6] M. Martinez-Montejano, G. Escobar, and R. Torres-Olguin, "Fixed reference frame phase-locked loop (frf-pll) for unbalanced line voltage conditions," in *2008 IEEE Power Electronics Specialists Conference*, 2008, pp. 4723–4728.
[7] X. Wang, "Optimization strategy of dsogi-pll precision under harmonic interference conditions," in *2020 IEEE Sustainable Power and Energy Conference (iSPEC)*, 2020, pp. 852–857.
[8] A. Ortega and F. Milano, "Comparison of different pll implementations for frequency estimation and control," in *2018 18th International Conference on Harmonics and Quality of Power (ICHQP)*, 2018, pp. 1–6.
[9] F. Wu, L. Zhang, and J. Duan, "A new two-phase stationary-frame-based enhanced pll for three-phase grid synchronization," *IEEE Transactions on Circuits and Systems II: Express Briefs*, vol. 62, no. 3, pp. 251–255, 2015.

Parameter estimation of induction motors using Wild Horse Optimizer

Jovan Vukašinović, Miloš Milovanović, Nebojša Arsić, Jordan Radosavljević, Saša Štatkić, Bojan Perović and Andrijana Jovanović

Abstract—**In this paper, a new metaheuristic algorithm called the Wild Horse Optimizer (WHO) is for the first time proposed for estimation of the equivalent circuit parameters of the single-cage induction motors. The parameters of the motors are found as a result of the error minimization function between the calculated and manufacturer data. Simulation results obtained using the WHO algorithm are compared to the results obtained using other optimization methods applied in solving the induction motor parameter estimation problem. The performances of the methods are evaluated using the motors of different powers (i.e. 5 HP and 40 HP), based on the statistical analysis of the results obtained in several independent runs of the methods. It is shown that the proposed WHO algorithm has better performance, i.e. it is able to provide quality solutions with faster convergence speed and better statistical indicators.**

Index Terms—**Induction motors, Parameter estimation, Optimization, Metaheuristic, Wild Horse Optimizer (WHO)**

I. INTRODUCTION

Induction motors are the most widespread electric motors in the world, and as such they represent one of the largest consumers of the electricity. Today, induction motors consume between 35% and 40% of the world's total electricity production. Knowing the parameters of the equivalent circuit of an induction motor is of great importance for drive control processes, as well as for fault diagnosis of the induction motor.

Classical methods for determining the parameters of the equivalent circuits of induction motors are based on no-load and short-circuit experiments. Because these tests are very difficult to perform in cases where the motor is already connected to a mechanical load, these methods are not always easily applicable in industry. For these reasons, in the recent years, many analytical and optimization methods have been proposed to estimate the parameters of induction motors. Some of the commonly used methods for estimation the parameters of induction motors that can be found in the literature are: Particle Swarm Optimization (PSO) [1], Genetic Algorithm (GA) [2], Charged System Search (CSS) [3], hybrid GA and PSO (HGAPSO) [4], Gravitational Search Algorithm (GSA) [5], hybrid Phasor Particle Swarm Optimization and Gravitational Search Algorithm (PPSOGSA) [6], and Shuffled Frog Leaping Algorithm (SFLA) [7].

In this paper, the Wild Horse Optimizer (WHO) [8] is for the first time proposed for estimating the single-cage induction motors parameters. It could be regarded as the main contribution of the paper. In the scientific literature, there is no research that deals with the direct application of the WHO algorithm for solving any problem of induction motor parameter estimation. The WHO algorithm has shown very good results in solving different complex benchmark functions, as pointed out in [8], and practical engineering problems, such as the problems of the parameter estimation of diode PV models [9], static/dynamic PV models [10], and damage identification in steel plates [11]. For this reason, the authors of this paper have decided to use the WHO algorithm.

II. PROBLEM FORMULATION

In order to optimize the values of the electrical parameters, the formulation of the objective function is required. In this case the objective function has the following form [7]:

$$OF = F_1^2 + F_2^2 + F_3^2 + F_4^2 , \tag{1}$$

where

$$F_1 = \frac{T_{fl.cal} - T_{fl.mf}}{T_{fl.mf}} , \tag{2}$$

$$F_2 = \frac{T_{st.cal} - T_{st.mf}}{T_{st.mf}} , \tag{3}$$

$$F_3 = \frac{T_{\max.cal} - T_{\max.mf}}{T_{\max.mf}} , \tag{4}$$

Jovan Vukašinović is with the Faculty of Technical Sciences, University of Priština in Kosovska Mitrovica, 7 Knjaza Miloša, 38220 Kosovska Mitrovica, Serbia (e-mail: jovan.vukasinovic@pr.ac.rs).

Miloš Milovanović is with the Faculty of Technical Sciences, University of Priština in Kosovska Mitrovica, 7 Knjaza Miloša, 38220 Kosovska Mitrovica, Serbia (e-mail: milos.milovanovic@pr.ac.rs).

Nebojša Arsić is with the Faculty of Technical Sciences, University of Priština in Kosovska Mitrovica, 7 Knjaza Miloša, 38220 Kosovska Mitrovica, Serbia (e-mail: nebojsa.arsic@pr.ac.rs).

Jordan Radosavljević is with the Faculty of Technical Sciences, University of Priština in Kosovska Mitrovica, 7 Knjaza Miloša, 38220 Kosovska Mitrovica, Serbia (e-mail: jordan.radosavljevic@pr.ac.rs).

Saša Štatkić is with the Faculty of Technical Sciences, University of Priština in Kosovska Mitrovica, 7 Knjaza Miloša, 38220 Kosovska Mitrovica, Serbia (e-mail: sasa.statkic@pr.ac.rs).

Bojan Perović is with the Faculty of Technical Sciences, University of Priština in Kosovska Mitrovica, 7 Knjaza Miloša, 38220 Kosovska Mitrovica, Serbia (e-mail: bojan.perovic@pr.ac.rs).

Andrijana Jovanović is with the Faculty of Technical Sciences, University of Priština in Kosovska Mitrovica, 7 Knjaza Miloša, 38220 Kosovska Mitrovica, Serbia (e-mail: andrijana.jovanovic@pr.ac.rs).

$$F_4 = \frac{pf_{fl.cal} - pf_{fl.mf}}{pf_{fl.mf}}. \tag{5}$$

In (1) – (5) variables have the following meaning: *OF* is the objective function, F_i ($i = 1,2,\ldots,4$) is the i-th component of the objective function (i.e., it is an error between the calculated and manufacturer value), T is a torque, I is a current, pf is a power factor, subscripts *st*, *fl* and max correspond to the start load, full load, and maximum load, respectively. Also, subscripts *cal* and *mf* are used for the calculated and manufacturer data.

According to Fig. 1, the stator ($\underline{I}_s$) and rotor ($\underline{I}_r$) currents in terms of slip (s) can be calculated using the following equations:

$$\underline{I}_s(s) = \frac{\underline{V}_{ph}}{R_s + jX_s + \underline{Z}_p(s)}, \tag{6}$$

$$\underline{I}_r(s) = \frac{\underline{Z}_p(s)\cdot \underline{I}_s(s)}{\frac{R_r}{s} + jX_r}, \tag{7}$$

where $\underline{V}_{ph}$ is the stator phase voltage, R_s is the stator resistance, R_r is the rotor resistance, X_s is the stator leakage reactance, X_r is the rotor leakage reactance, and X_m is the magnetizing leakage reactance.

The equivalent impedance ($\underline{Z}_p$) and Thevenin's equivalent impedance ($\underline{Z}_{Th}$) are:

$$\underline{Z}_p(s) = \frac{1}{\frac{1}{jX_m} + \frac{1}{\frac{R_r}{s} + jX_r}}, \tag{8}$$

$$\underline{Z}_{Th} = R_{Th} + jX_{Th} = \frac{1}{\frac{1}{R_s + jX_s} + \frac{1}{jX_m}}. \tag{9}$$

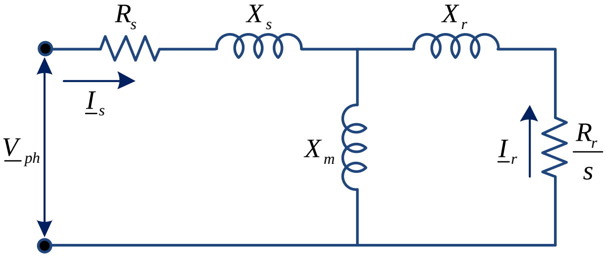

Fig. 1. One phase steady-state equivalent circuit of a single-cage three-phase induction motor.

The torque in terms of slip can be obtained by using the following equation:

$$T(s) = \frac{3p}{\omega_s}\left[I_r(s)\right]^2 \frac{R_r}{s}. \tag{10}$$

Thus, $T_{fl} = T(s_{fl})$, $T_{st} = T(1)$, and $T_{\max} = T(s_{\max})$, where the maximum torque slip ($s_{\max}$) is given by (11).

$$s_{\max} = \frac{R_r}{\sqrt{R_{Th}^2 + \left(X_{Th} + X_r\right)^2}}. \tag{11}$$

The apparent, active and reactive powers are:

$$\underline{S}(s_{fl}) = 3\cdot \underline{V}_{ph}\cdot\left[\underline{I}_s(s_{fl})\right]^*, \tag{12}$$

$$P_{fl} = \mathrm{Re}\left\{\underline{S}(s_{fl})\right\},\quad Q_{fl} = \mathrm{Im}\left\{\underline{S}(s_{fl})\right\}. \tag{13}$$

Finally, the power factor can be calculated:

$$pf_{fl} = \arctan\left(\frac{Q_{fl}}{P_{fl}}\right). \tag{14}$$

According to [6, 7], the following constraints are taken into account:

$$R_s, R_r, X_s, X_r, X_m > 0, \tag{15}$$

$$X_s = X_r. \tag{16}$$

III. SOLUTION METHOD

The WHO algorithm [8] is a recently proposed metaheuristic algorithm developed by Naruei and Keynia. This algorithm is inspired by the social life behavior of wild horses in the nature. Wild horses exhibit different group behaviors, such as grazing, chasing, mating, dominance and leadership.

The WHO algorithm consists of the following steps [8]:

A. *Creating an Initial Population and Forming Horse Groups, and Selecting Leaders*

The WHO begins with an initial population of N agents, $\mathbf{POP}(1) = \left[\mathbf{X}_1(1), \mathbf{X}_2(1), \ldots, \mathbf{X}_N(1)\right]^T \subseteq \mathbf{U}$. In the initial iteration, the i^{th} agent $\mathbf{X}_i(1)$ can be expressed as: $\mathbf{X}_i(1) = \left[X_i^1(1), \ldots, X_i^d(1), \ldots, X_i^n(1)\right]$, where X_i^d is the position of the i^{th} agent in the d^{th} dimension, n is the dimension of the problem, while $\mathbf{U}$ is the space of possible solutions. The initial population is divided into several groups. Each group has only one leader (stallion) and one or more mares and foals.

B. *Grazing of Horses*

The following equation is used to simulate the grazing:

$$\begin{aligned}\mathbf{X}_{i,G}^j(t+1) = {} & 2\cdot \mathbf{Z}(t)\cdot\cos\left(2\cdot\pi\cdot R\cdot \mathbf{Z}(t)\right)\times \\ & \times\left(\mathbf{Stallion}^j(t) - \mathbf{X}_{i,G}^j(t)\right) + \mathbf{Stallion}^j(t)\end{aligned} \tag{17}$$

where $\mathbf{X}_{i,G}^j(t)$ and $\mathbf{X}_{i,G}^j(t+1)$ are the current position and new position of the foal or mare, respectively; t is the current iteration; $t+1$ is the next iteration; $\mathbf{Stallion}^j(t)$ is the current position of the stallion; R is a uniform random number between [-2,2], and $\mathbf{Z}(t)$ is an adaptive mechanism described in [8].

C. *Horse Mating Behavior*

To simulate the departure and mating of horses, the following formula can be used:

$$\begin{gathered}\mathbf{X}_{G,k}^{p}=\text{crossover}\left(\mathbf{X}_{G,i}^{q},\mathbf{X}_{G,j}^{z}\right);\;\; i\neq j\neq k;\\ p=q=\text{end};\;\; \text{crossover}=\text{mean}\end{gathered} \tag{18}$$

where $\mathbf{X}_{G,k}^{p}$, $\mathbf{X}_{G,i}^{q}$ and $\mathbf{X}_{G,j}^{z}$ are the positions of horses *p*, *q* and *z* from groups *k*, *i* and *j*, respectively.

D. *Leadership and Leading the Group by the Leader*

The mathematical model of leading the group by the stallion can be described by (19).

E. *Exchange and Selection of Leaders*

In this step, the leaders of the groups – stallions are selected. Firstly, to preserve the stochastic nature of the algorithm, the leaders are selected randomly. In the later stages of the iteration process, the leaders are selected based on their fitness values using (20).

$$\mathbf{Stallion}_{G,i}(t+1)=\begin{cases}2\cdot\mathbf{Z}(t)\cdot\cos\left(2\cdot\pi\cdot R\cdot\mathbf{Z}(t)\right)\times\left(\mathbf{WH}(t)-\mathbf{Stallion}_{G,i}(t)\right)+\mathbf{WH}(t) & \text{if}\;\; R_2>0.5\\ 2\cdot\mathbf{Z}(t)\cdot\cos\left(2\cdot\pi\cdot R\cdot\mathbf{Z}(t)\right)\times\left(\mathbf{WH}(t)-\mathbf{Stallion}_{G,i}(t)\right)-\mathbf{WH}(t) & \text{if}\;\; R_2\leq 0.5\end{cases}, \tag{19}$$

$$\mathbf{Stallion}_{G,i}(t+1)=\begin{cases}\mathbf{X}_{G,i}(t+1) & \text{if}\;\; \text{cost}\left(\mathbf{X}_{G,i}(t+1)\right)<\text{cost}\left(\mathbf{Stallion}_{G,i}(t)\right)\\ \mathbf{Stallion}_{G,i}(t) & \text{if}\;\; \text{cost}\left(\mathbf{X}_{G,i}(t+1)\right)\geq\text{cost}\left(\mathbf{Stallion}_{G,i}(t)\right)\end{cases}. \tag{20}$$

In (19) and (20), **WH**(*t*) presents the position of the water hole (i.e. the global best position). More details about the WHO algorithm can be found in the paper [8].

As for any other optimization problem, a potential solution can be presented by a vector consisting of a combination of control variables, i.e., in this case, corresponding induction motor parameters. The electrical parameters of the single-cage motors are the following: R_s, R_r, X_s, X_r, and X_m. Generally, it is supposed that the stator and rotor leakage reactances are equal: $X_s = X_r$. Therefore, the position of the agent *i* can be defined as follows:

$$\mathbf{X}_i=\left[R_{s,i},R_{r,i},X_{s,i},X_{m,i}\right]. \tag{21}$$

The flowchart of the WHO algorithm is given in Fig. 2.

IV. SIMULATION RESULTS AND DISCUSSION

The proposed WHO method is tested on two three-phase single-cage induction motors. The manufacturer data of the test motors are shown in Table I.

TABLE I
MANUFACTURER DATA OF THE TEST MOTORS [6,7]

Parameters	Values	
Rated power P_n (HP)	5	40
Rated voltage U_n (V)	400	400
Rated frequency f_n (Hz)	50	50
Starting current I_{st} (A)	22	180
Full-load current I_{fl} (A)	8	45
Number of pole pairs *p*	2	2
Starting torque T_{st} (N·m)	15	260
Full-load torque T_{fl} (N·m)	25	190
Maximum torque $T_{\max}$ (N·m)	42	370
Full-load power factor pf_{fl}	0.8	0.8
Slip at full load s_{fl}	0.07	0.09

The following parameter ranges are considered:

- For the motor of 5 HP:

$$\begin{gathered}0.1\leq R_s\leq 5,\; 1\leq X_s\leq 15,\; 50\leq X_m\leq 150,\\ 0.5\leq R_r\leq 10,\; 1\leq X_r\leq 15\end{gathered}$$

- For the motor of 40 HP:

$$\begin{gathered}0.01\leq R_s\leq 0.5,\; 0.1\leq X_s\leq 2,\; 5\leq X_m\leq 15,\\ 0.05\leq R_r\leq 1,\; 0.1\leq X_r\leq 2\end{gathered}$$

The algorithm was developed in the MATLAB computing environment. To examine the effectiveness of the proposed WHO algorithm, the same problem was solved using the PPSOGSA algorithm [6] (which proved to be effective in solving problems in this area). The obtained results are compared with those obtained using the other methods reported in the literature.

The algorithms are implemented with the following control parameters: for the PPSOGSA [6], c_1 and c_2 are set to 2, α is set to 25, and G_0 is set to 1; for the WHO [8], the crossover process is carried out using the mean value of corresponding group members (mean crossover type), crossover percentage is set to 0.1, and the percentage of stallions in the total population (*PS*) is set to 0.2. For both algorithms, the population size (*N*) and the maximum number of iterations ($t_{\max}$) are set to 300 and 100, respectively.

The results of WHO and PPSOGSA are obtained after fifty consecutive test runs. The best results achieved over these runs are presented in Tables II and III. Also, the tables show the results obtained by other optimization methods. The corresponding steady-state equivalent circuit electrical parameters of the test motors are presented in Table IV.

By comparing the results from Tables II and III, it can be seen that the values of the objective function (*OF*) obtained with the WHO are lower than those obtained by other methods, except the MSFLA [7] for the motor of 5 HP. In [7], a larger range of control variables was taken into consideration, i.e. the optimal value of the stator resistance was 0.0037 Ω, which is far less than the value of 0.3 Ω obtained by the WHO, as presented in Table IV; that may be a possible reason why the *OF* value obtained using the MSFLA is less than the value obtained by the WHO.

The convergence profiles of the WHO and PPSOGSA for the motors of 5 HP and 40 HP are shown in Figs. 3 and 4, respectively. The figures indicate that the proposed WHO algorithm converges to the optimal solution in lower iterations in comparison to the PPSOGSA algorithm.

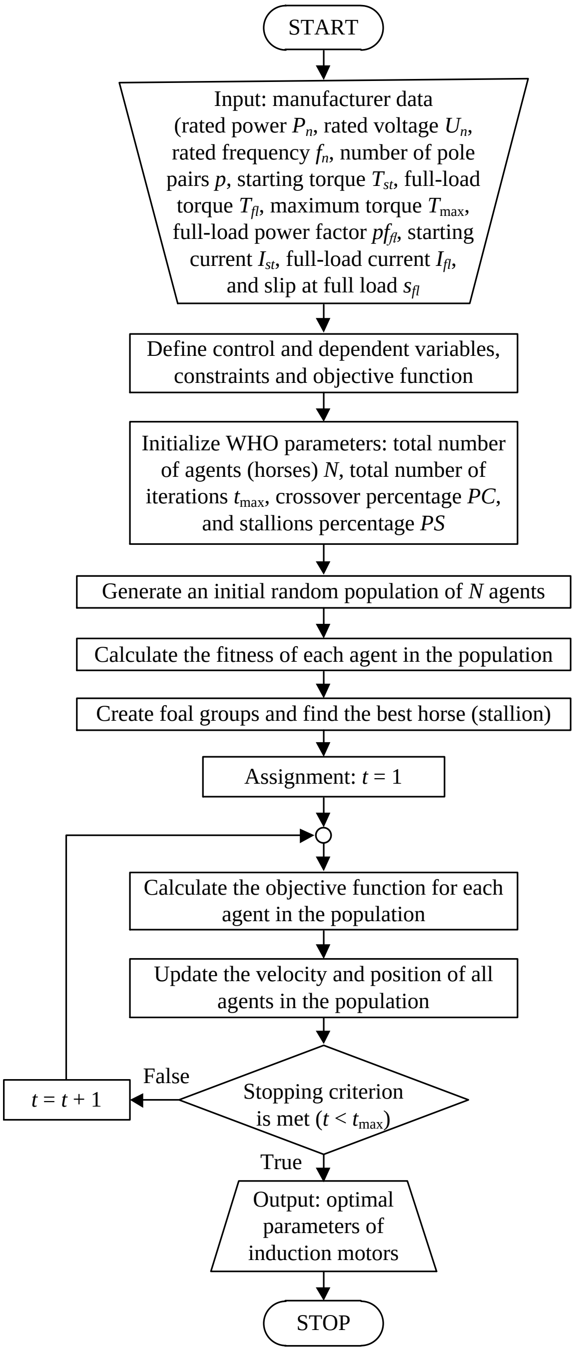

Fig. 2. The flowchart of the WHO algorithm in solving the induction motor parameter estimation problem.

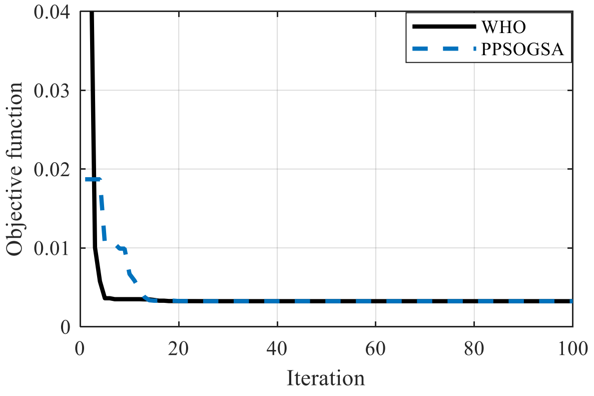

Fig. 3. Convergence profiles obtained for the motor of 5 HP.

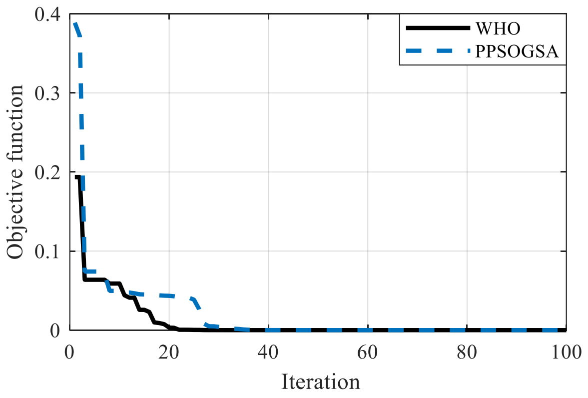

Fig. 4. Convergence profiles obtained for the motor of 40 HP.

Torque-slip characteristics of the motors of 5 HP and 40 HP obtained using the WHO algorithm are presented in Figs. 5 and 6, respectively. From these figures, it is evident that the results obtained by the WHO are in very good agreement with the manufacturer values.

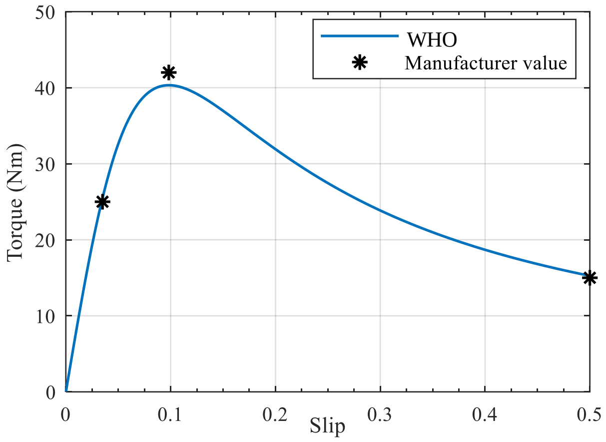

Fig. 5. Torque versus slip curve for the motor of 5 HP.

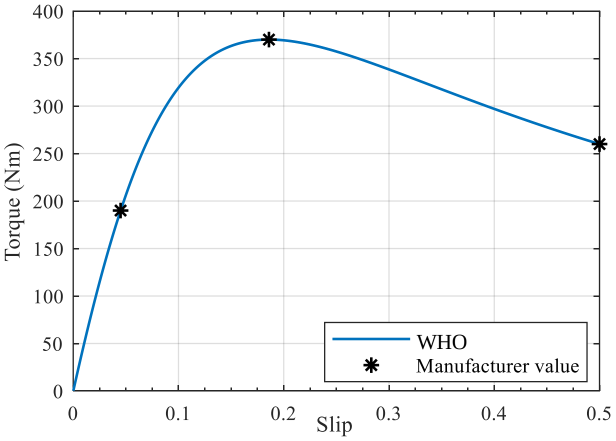

Fig. 6. Torque versus slip curve for the motor of 40 HP.

The statistical parameters of the results (i.e. minimum, maximum and mean values of the objective function, as well as the standard deviations) obtained by the WHO and PPSOGSA over fifty runs for the both test motors are presented in Table V. The results from Table V show that the proposed WHO algorithm is more robust compared to the PPSOGSA. From the aspect of running, the running time of the WHO is a little shorter than the time of the PPSOGSA.

TABLE II
A COMPARISON OF THE RESULTS OBTAINED BY THE PROPOSED METHOD AND OTHER METHODS FOR THE MOTOR OF 5 HP

Parameter	Manufacturer data	PSO [7]		SFLA [7]		MSFLA [7]		PPSOGSA		WHO	
		Reported result	Error (%)	Reported result	Error (%)	Reported result	Error (%)	Obtained result	Error (%)	Obtained result	Error (%)
T_{st} (Nm)	15	15.3465	2.31	15.4939	3.29	15.2725	1.82	15.3029	2.02	15.2987	1.99
T_{fl} (Nm)	25	25.5692	2.28	25.6484	2.59	25.5541	2.22	25.6067	2.43	25.5979	2.39
T_{max} (Nm)	42	39.0047	–7.13	40.7390	–3.00	40.3870	–3.84	39.9683	–4.84	40.0016	–4.76
pf_{fl}	0.8	0.7888	–1.40	0.7710	–3.63	0.7991	–0.11	0.8000	0.00	0.8000	0.00
OF	/	0.006334059*		0.003972333*		0.002297462*		0.003336732		0.003232706	

*Recalculated value

TABLE III
A COMPARISON OF THE RESULTS OBTAINED BY THE PROPOSED METHOD AND OTHER METHODS FOR THE MOTOR OF 40 HP

Parameter	Manufacturer data	PSO[7]		SFLA [7]		MSFLA [7]		PPSOGSA		WHO	
		Reported result	Error (%)	Reported result	Error (%)	Reported result	Error (%)	Obtained result	Error (%)	Obtained result	Error (%)
T_{st} (Nm)	260	261.1978	0.46	260.3347	0.13	259.5611	−0.17	259.9991	−0.00	260.00	0.00
T_{fl} (Nm)	190	188.9053	−0.58	193.5212	1.85	190.6352	0.33	189.9865	−0.01	190.00	0.00
T_{max} (Nm)	370	360.8307	−2.48	365.0454	−1.34	370.8140	0.22	370.0364	0.01	370.00	0.00
pf_{fl}	0.8	0.7883	−1.46	0.7860	−1.75	0.7995	−0.06	0.7999	−0.00	0.80	0.00
OF	/	0.000882452*		0.000830679*		$1.92569\times10^{-5*}$		3.03638×10^{-8}		0	

*Recalculated value

TABLE IV
ELECTRICAL PARAMETERS OF INDUCTION MOTORS OBTAINED BY THE PROPOSED METHOD AND OTHER METHODS

Parameter	Motor of 5 HP					Motor of 40 HP				
	PSO [7]	SFLA [7]	MSFLA [7]	PPSOGSA	WHO	PSO [7]	SFLA [7]	MSFLA [7]	PPSOGSA	WHO
R_s (Ω)	0.9872	0.0008	0.0037	0.3300	0.3000	0.3555	0.3437	0.2707	0.2694	0.2778
X_s (Ω)	5.3785	5.5847	5.7202	5.6667	5.6771	0.4353	0.4345	0.4773	0.4842	0.4797
X_m (Ω)	77.042	77.9101	94.1401	91.5892	91.9613	6.4223	6.2629	7.5432	7.7277	7.6037
R_r (Ω)	2.0322	2.1330	2.1818	2.1526	2.1574	0.3455	0.3360	0.3573	0.3631	0.3611
X_r (Ω)	5.3785	5.5847	5.7202	5.6667	5.6771	0.4353	0.4345	0.4773	0.4842	0.4797

TABLE V
STATISTICAL PARAMETERS AND EXECUTION TIMES OF WHO AND PPSOGSA METHODS

Power (HP)	Method	Minimum	Maximum	Mean	Standard deviation	Execution time [s]
5	PPSOGSA	0.00334	0.00348	0.00338	0.00024	1.89
	WHO	0.00323	0.00323	0.00323	0	1.73
40	PPSOGSA	3.0364×10^{-8}	0.04491	0.00389	0.01151	1.46
	WHO	0	0.00592	0.00041	0.00154	1.35

V. CONCLUSION

The main conclusions that can be drawn from the presented results and discussion of them are the follows:

- By comparing the results obtained using the WHO algorithm with those obtained using other algorithms (i.e. using the PSO, SFLA, MSFLA, and PPSOGSA algorithms), it is found that the WHO provides effective, robust and high-quality solutions.
- It is shown that the results obtained by the WHO algorithm are in very good agreement with the manufacturer data. The maximum relative deviations are less than 5%.
- The average running time of the WHO algorithm for both test motors was less than 2 s. This means that the calculation speed of the WHO algorithm is high.
- It is found that the WHO algorithm has better performance than the PPSOGSA algorithm in terms of the solution quality and convergence speed.

ACKNOWLEDGMENT

The research for this article was carried out with ERASMUS + project: “Knowledge triangle for a low carbon economy (KALCEA)” and with scientific project the TR 33016 – “Research, development and implementation of programs and procedures Energy efficiency of electric drives” funded by the Ministry of Education, Science and Technological Development of the Republic of Serbia.

REFERENCES

[1] V. P. Sakthivel, R. Bhuvaneswari, S. Subramanian, “Multi-objective parameter estimation of induction motor using particle swarm optimization,” *Engineering Applications of Artificial Intelligence*, vol. 23, iss. 3, pp. 302-312, 2010

[2] I. Kostov, V. Spasov, V. Rangelova, “Application of genetic algorithms for determining the parameters of induction motors,” *Technical Gazette*, vol. 16, no. 49, pp. 49–53, 2009

[3] A. I. Canakoglu, A. G. Yetgin, H. Temurtas, M. Turan, “Induction motor parameter estimation using metaheuristic methods,” *Turkish Journal of Electrical Engineering & Computer Sciences*, vol. 22, pp. 1177-1192, 2014

[4] H. R. Mohammadi, A. Akhavan, “Parameter estimation of three-phase induction motor using hybrid of genetic algorithm and particle swarm optimization,” *Journal of Engineering*, vol. 2014, pp. 198-204, 2014

[5] O. Avalos, E. Cuevas, E. Cuevas, “Induction Motor Parameter Identification Using a Gravitational Search Algorithm,” *Computers*, vol. 5, no. 6, 2016

[6] J. Vukasinović, M. Milovanović, N. Arsić, J. Radosavljević, S. Statkić, “Parameters estimation of double-cage induction motors using a hybrid metaheuristic algorithm,” 21st International Symposium INFOTEH-JAHORINA (INFOTEH) East Sarajevo, Bosnia and Herzegovina, pp. 1-6, March 16-18, 2022

[7] I. Perez, M. Gomez-Gonzalez, F. Jurado, “Estimation of induction motor parameters using shuffled frog-leaping algorithm,” *Electrical Engineering*, vol. 95, iss. 3, pp. 267-275, 2012

[8] I. Naruei, F. Keynia, “Wild horse optimizer: a new meta-heuristic algorithm for solving engineering optimization problems,” *Engineering with Computers*, vol. no, pp. no, 2021

[9] A. Ramadan, S. Kamel, I. B. M. Taha, M. Tostado-Véliz, “Parameter estimation of modified double-diode and triple-diode photovoltaic models based on wild horse optimizer,” *Electronics*, vol. 10, no.18, pp. 1-19, 2021

[10] A. Ramadan, S. Kamel, M. H. Hassan, M. Tostado-Véliz, “Parameter estimation of static/dynamic photovoltaic models using a developed version of eagle strategy gradient-based optimizer,” *Sustainability*, vol. 13, no. 23 pp. 1-29, 2021

[11] S. Khatir, M. A. Wahab, S. Tiachacht, C. L. Thanh, R. Capozucca, E. Magagnini, B. Benaissa, “Damage identification in steel plate using FRF and inverse analysis,” *Frattura ed Integrità Strutturale*, vol. 58, pp. 416-433, 2021

Damper Winding Inductances Calculation by Winding Function Approach

Aldin Kajević, Gojko Joksimović, *Senior Member, IEEE*

***Abstract*—The paper presents a procedure for dq model parameters calculation of a synchronous turbogenerator using winding function theory, with special emphasis on the damper winding. The advantage of this procedure is that the real spatial distribution of all windings in the machine is taken into account, therefore, taking into account all spatial harmonics simultaneously. A real synchronous turbogenerator of type TBB-200-2A was analyzed as a case study.**

***Index Terms*—Damper winding, Inductance, Synchronous machine, Turbo-generator, Winding function.**

I. INTRODUCTION

Mathematical model of synchronous machine projected on two mutually orthogonal axes, *dq* model, is the most common dynamic model of synchronous machine, [1], [2]. Although the model itself is often found in the literature, in rare cases attention is paid to determining the parameters that appear in the model itself. Additionally, model parameters are most often given in unit values. The key parameters of the model that are at the same time the most demanding to determine are the self and mutual inductances of the windings. Analytical expressions that assume an ideal, sinusoidal spatial distribution of windings are often used when determining these parameters, or, which is the same, only the fundamental harmonic of the real spatial winding distribution is taken into account, [3], [4]. In this paper, using the theory of the winding functions, [5], [6], [7], [8], all spatial harmonics of the magnetomotive force (mmf) of the real winding are taken into account simultaneously.

The generic synchronous machine is characterized by the existence of three symmetrical armature phase windings as well as the field and damper winding on the rotor.

The paper presents a methodology that allows direct and fairly intuitive determination of self and mutual inductances of windings, inductances that appear as parameters of the *dq* model of the machine. The first step in order to calculate inductances is to determine the winding functions of the stator windings and the damper windings of the machine in the natural frame of reference. However, the following convention should be introduced here: in order to avoid rugged constructions as "winding function of field winding" or "winding function of stator phase winding“, etc. a simpler sentence construction will be used – simply "field winding function" or "damper winding function" or "stator phase winding function". When the winding functions are known, then in the case of stator phase windings, their equivalent winding functions are determined in a rotating *dqn* reference frame fixed to the rotor. The role of these functions is twofold. Firstly, they enable obtaining self and mutual inductances of the stator windings directly in the *dqn* system. Secondly, their existence enables, in combination with the damper winding functions along the *d* and *q* axes, the direct calculation of its mutual inductances. The procedure for obtaining the damper winding functions along the *d* and *q* axes is also presented in this paper and these functions represent one of the main results of this paper.

The whole procedure is illustrated on the example of a synchronous turbogenerator of type TBB-200-2A. As a final result, all self and mutual inductances that appears as the parameters of the *dq* model are determined. A comparison of the obtained parameters concerning the stator windings with the factory data of the generator was performed and a high degree of agreement was observed.

II. DQ MODEL OF SYNCHRONOUS MACHINE

The voltage equations of a synchronous turbogenerator in matrix form are given below, [1]. The indexes *a*, *b* and *c* are associated with the values concerning the three phase windings of the stator, in the natural (*abc*) frame of reference. The indexes *d* and *q* are associated with the damper winding along the *d* and *q* axes, respectively. Index *f* refers to the field winding. The indexes *s* and *r* refer to the stator and rotor, respectively.

$$\left[U_{abcs}\right]=\left[R_s\right]\left[i_{abcs}\right]+\frac{d}{dt}\left[\psi_{abcs}\right] \tag{1}$$

$$\left[U_{dqfr}\right]=\left[R_r\right]\left[i_{dqfr}\right]+\frac{d}{dt}\left[\psi_{dqfr}\right] \tag{2}$$

The equations of magnetic coupling for the stator and rotor windings, in matrix form, are:

$$\left[\psi_{abcs}\right]=\left[L_{abcs}\right]\left[i_{abcs}\right]+\left[L_{abcsr}\right]\left[i_{dqfr}\right] \tag{3}$$

Aldin Kajević is with the Faculty of Electrical Engineering, University of Montenegro, Cetinjski put b.b, 81000 Podgorica, Montenegro (e-mail: Aldin.Kajevic@ucg.ac.me)

Gojko Joksimović is with the Faculty of Electrical Engineering, University of Montenegro, Cetinjski put b.b, 81000 Podgorica, Montenegro (e-mail: Gojko.Joksimovic@ucg.ac.me), (https://orcid.org/0000-0002-2764-1540)

$$\left[\psi_{dqfr}\right]=\left[L_{abcsr}\right]^T\left[i_{abcs}\right]+\left[L_{dqfr}\right]\left[i_{dqfr}\right] \qquad (4)$$

Vectors of voltages, currents and fluxes that appear in the previous expressions together with the matrices of inductance and resistance are given in the Appendix. The same will be done with the vectors and matrices in the continuation of the work.

It is now necessary to transform the previous equations from the natural (*abc*) frame of reference to the rotating *dqn* coordinate system. The transformation will be done using the transformation matrix [$T(\theta)$]. The angle θ in the transformation matrix is the angle that the rotating reference frame, fixed to the rotor, occupies at a certain point in time in relation to the reference, i.e. initial position. For a coordinate system that rotates with an arbitrary angular velocity ω, assuming that the initial angle is equal to zero, at time t=0, the following holds:

$$\theta=\omega t \qquad (5)$$

After the transformation of equations, procedure of which will not be presented in detail here, the following equations are obtained in the *dqn* system,

$$\left[U_{dqns}\right]=\left[R_s\right]\left[i_{dqns}\right]+\frac{d\left(\left[\psi_{dqns}\right]\right)}{dt}+\left[\omega\mathrm{x}\right]\left[\psi_{dqns}\right] \qquad (6)$$

$$\left[U_{dqfr}\right]=\left[R_r\right]\left[i_{dqfr}\right]+\frac{d}{dt}\left[\psi_{dqfr}\right] \qquad (7)$$

$$\left[\psi_{dqns}\right]=\left[L_{dqns}\right]\left[i_{dqns}\right]+\left[L_{dqnsr}\right]\left[i_{dqfr}\right] \qquad (8)$$

$$\left[\psi_{dqfr}\right]=\frac{3}{2}\left[L_{dqnsr}\right]^T\left[i_{dqns}\right]+\left[L_{dqfr}\right]\left[i_{dqfr}\right] \qquad (9)$$

where:

$$\left[L_{dqns}\right]=\left[T(\theta)\right]\left[L_{abcs}\right]\left[T(\theta)\right]^{-1} \qquad (10)$$

$$\left[L_{dqnsr}\right]=\left[T(\theta)\right]\left[L_{abcsr}\right] \qquad (11)$$

III. WINDING FUNCTIONS IN DQ SYSTEM, INDUCTANCES AND METHOD OF THEIR DETERMINATION

The stator winding functions in the *dqn* system are given in expression (12). There $N_a(\theta_m)$, $N_b(\theta_m)$ and $N_c(\theta_m)$ are the stator phase windings functions in the natural frame of reference, and θ_m is the mechanical angle.

In addition to the previously listed winding functions, it is necessary to determine the function of the field winding $N_{fr}(\theta_m)$, as well as the damper winding functions along the *d* and *q* axes, $N_{dr}(\theta_m)$ and $N_{qr}(\theta_m)$, respectively. All these functions will be determined in the following by applying the winding function theory on the example of a real synchronous turbogenerator of type TBB-200-2A.

When the winding functions for all windings are determined then self and mutual inductances in the model matrices can be obtained by numerical integration. Some of the inductances in the matrices [L_{dqns}], [L_{dqnsr}] and [L_{dqfr}] are given by expressions (15) - (20), just for illustration purposes.

$$N_{ds}=\frac{2}{3}\left(N_a(\theta_m)\sin(\theta)+N_b(\theta_m)\sin\left(\theta-\frac{2\pi}{3}\right)+N_c(\theta_m)\sin\left(\theta+\frac{2\pi}{3}\right)\right) \qquad (12)$$

$$N_{qs}=\frac{2}{3}\left(N_a(\theta_m)\cos(\theta)+N_b(\theta_m)\cos\left(\theta-\frac{2\pi}{3}\right)+N_c(\theta_m)\cos\left(\theta+\frac{2\pi}{3}\right)\right) \qquad (13)$$

$$N_{ns}=\frac{\sqrt{2}}{3}\left(N_a(\theta_m)+N_b(\theta_m)+N_c(\theta_m)\right) \qquad (14)$$

$$L_{dsds}=\frac{3\mu_0 rl}{2g}\int_0^{2\pi}N_{ds}^2(\theta_m,\theta)d\theta_m \qquad (15)$$

$$L_{dsqs}=\frac{3\mu_0 rl}{2g}\int_0^{2\pi}N_{ds}(\theta_m,\theta)N_{qs}(\theta_m,\theta)d\theta_m \qquad (16)$$

$$L_{dsdr}=\frac{\mu_0 rl}{g}\int_0^{2\pi}N_{ds}(\theta_m,\theta)N_{dr}(\theta_m,\theta_r)d\theta_m \qquad (17)$$

$$L_{dsqr}=\frac{\mu_0 rl}{g}\int_0^{2\pi}N_{ds}(\theta_m,\theta)N_{qr}(\theta_m,\theta_r)d\theta_m \qquad (18)$$

$$L_{drdr}=\frac{\mu_0 rl}{g}\int_0^{2\pi}N_{dr}^2(\theta_m,\theta)d\theta_m \qquad (19)$$

$$L_{drqr}=\frac{\mu_0 rl}{g}\int_0^{2\pi}N_{dr}(\theta_m,\theta)N_{qr}(\theta_m,\theta_r)d\theta_m \qquad (20)$$

etc.

IV. STATOR PHASE WINDING AND FIELD WINDING FUNCTIONS

The synchronous generator of type TBB-200-2A is a turbogenerator that is cooled by water and hydrogen. Its rated active power is 200 MW, rated voltage is 15.75 kV, rated frequency 50 Hz. It is a two-pole generator. On the stator of this generator, there exists 60 slots in which the stator winding is manufactured. The stator winding consists of three symmetrical phase windings. Each phase winding additionally consists of two half-windings connected in parallel. The phase windings are connected in star conection. Due to the existence of two parallel connected half-windings, this conection is also known as a double star conection. The three-phase stator winding consists of sixty coil groups with one coil, or twenty coils per phase - ten per half-winding. In Fig. 1 all slots and all coil groups on the stator and rotor are shown and numbered. On the stator, the shades of red represent the conductors of the phase A winding. More intense red color shows the first and lighter one the second half-winding. The other two phases are represented by shades of yellow and green - phase B in yellow and phase C in green. All slots, coil groups are clearly numbered and the adopted reference directions of currents and mechanical angle are shown. Based on the previous data, the functions of the phase windings can be determined, [5]-[8]. Thus, the winding function of phase A is given in Fig. 2.

Field and damper winding are mounted in 36 rotor slots. The rotor slot pitch is $\tau_r=2\pi/52$. The field winding consists of 18 coil groups, and each coil group consists of seven coils. Coil groups of the field winding are marked in green and red on the rotor, Fig. 1. Damper winding consists of conductive wedges made of aluminum alloy which close the slots in which the field winding is located. These bars are short-circuited on the front and back sides by a conductive tension rings. They are shown in blue in Fig. 1 The waveform of the field winding function is given on Fig. 3 – that is at the same time the waveform of the field winding mmf for a unit current, [1].

The functions of the fictive stator windings in the rotating frame of reference fixed to the rotor are obtained from the original functions of the phase windings using expresions (12)-(14). The winding functions obtained in this way, under the *d* and *q* axes, are given in Fig. 4 for the case $\theta=0^o$.

All of these functions will be used in the following paragraphs to calculate the inductances that appear in the *dq* model.

The function of the field winding that is located on the rotor does not need to be reduced because the rotating frame of reference is already fixed to the rotor. The magnetic axis of this winding is the *d* axis, Fig. 1.

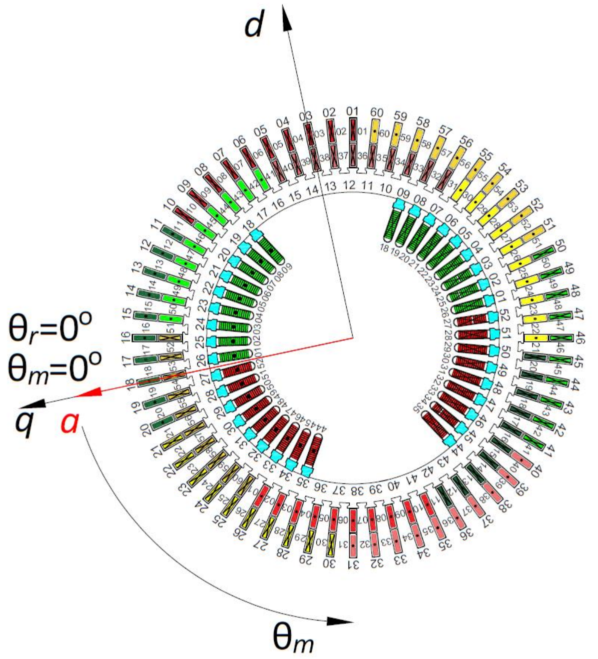

Fig.1. Design of phase, field and damper windings of the TBB-200-2A turbogenerator

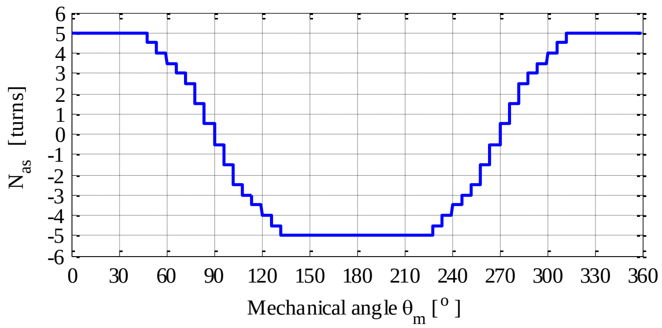

Fig.2. Stator phase A - winding function

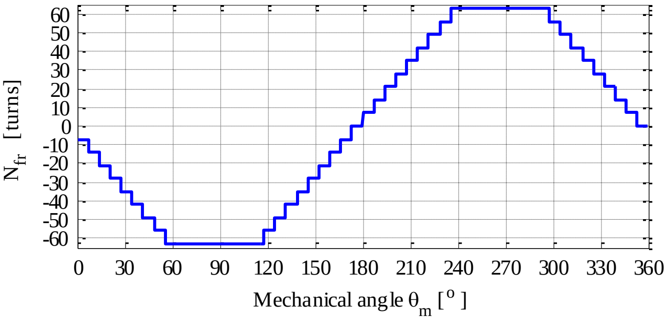

Fig.3. Field winding function

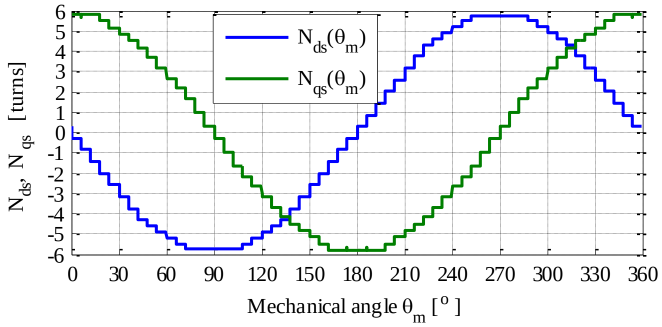

Fig.4. Fictive stator winding functions reduced to a rotating frame of reference, $\theta=0^o$

V. DAMPER WINDING FUNCTIONS

Structurally, the damper winding consists of conductive bars located in the top of the rotor slots. These bars are short-circuited on the front and back sides by the conductive tension rings. From the construction of the damper winding itself, it is clear that the same currents do not flow in short-circuited conducting bars, which, at first glance, makes this winding complicated for analysis using the concept of winding function. Namely, in order to be able to apply the definition of the winding function, it is necessary that one and the same current flows through that winding, [1]. This condition is met for armature phase windings and the field winding. This difficulty in determining the function of the damping winding can be overcome by taking into account some assumptions and neglections. As the bars on the rotor are short-circuited, currents in them are induced as a result of time-varying magnetic flux generated by currents in the phase windings of the stator. Due to the symmetry of the phase windings, it is sufficient to observe the case of induced currents resulting from the magnetic flux generated by one of the armature phase windings. The phase A winding will be observed here. Based on the currents induced in the bars as a consequence of the current in the phase winding, a usable damper winding function along the *d* and *q* axes can be obtained.

In order to determine the function of the damper winding along the *d* axis, Fig. 5 shows the developed scheme of the damper winding for the case when the *d* axis is in the same position as the axis of the phase A winding, i.e. the *d* axis is below the maximum value of fundamental harmonic of winding A mmf wave.

The N_{as} function shown in red in Fig. 5 represents the fundamental harmonic of the phase A winding function. Multiplying function $N_{as}(\theta_m)=N_m\cos(\theta_m)$ by the sinusoidal current in the winding, $I_a\sin(\omega_e t)$, gives a pulsating mmf. As the air-gap in the turbogenerator is uniform (ignoring the stator and rotor slots), the magnetic flux density wave created by the phase A winding will also be sinusoidal along the rotor circumference. Due to the existence of symmetry, the induced currents in bars 1 and 1' are the same but of opposite polarity, so these two bars can be considered as one fictious coil. The same situation is with 2-2', 3-3' pair of bars, etc. which are under same pole. The magnetic fluxes coupled by these fictitious coils are given by the following expressions,

$$\phi_{11'}=\frac{2\mu_0 N_m I_a r l\sin(9z/2)}{g}\sin(\omega_e t) \tag{21}$$

$$\phi_{22'}=\frac{2\mu_0 N_m I_a r l\sin(11z/2)}{g}\sin(\omega_e t) \tag{22}$$

etc.

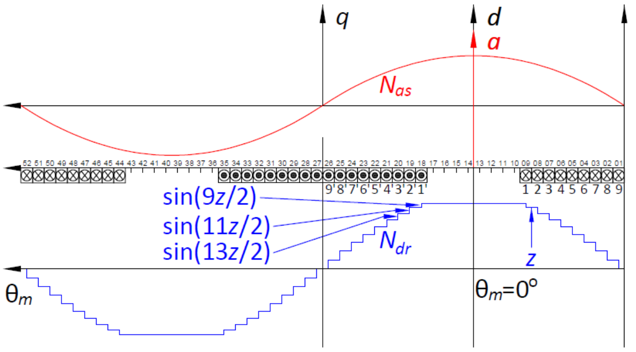

Fig.5. Damper winding function along the *d* axes

What can be seen from the previous expressions is the fact that the fluxes in the fictious coils differ only by the factors sin(9*z*/2), sin(11*z*/2), ... This difference is due to the difference in the area occupied by these coils, or differences in coil step. The induced electromotive forces in them differ for the same factors. The resistance and leakage inductance of each bar is the same. The resistance and leakage inductance of the ring segments connecting the two bars of the fictitious coil is different for each coil due to the difference in length. However, as the resistance and leakage inductance of the ring segments are usually very small, [1], around thousend times smaller than values for bars, they will not be considered here. As a consequence of the previously mentioned neglection, the currents in the fictitious windings will be the ratio of the induced electromotive force and the double impedance of the bar. Based on the above, it is concluded that the currents will differ only by the factors sin(9*z*/2), sin(11*z*/2), ..., too. Now the damper winding can be viewed as a fictive, concentrated winding through whose coils flows the same current. However, each coil has a number of conductors that differs by a factor of sin(9*z*/2), sin(11*z*/2), ... etc. In this way the mmf of the damper winding remains unchanged. The damper winding function obtained in this way is sketched in Fig. 5, in blue. Fig. 7 shows the exact shape of the damper winding function along the *d* axis, for the analysed machine, taking the position of the *q* axis as the starting position for the mechanical angle when it is in the same position as the phase A winding axis, $\theta_r=0^o$.

The procedure for obtaining the damper winding function along the *q* axis is similar to the previous procedure. Now, Fig. 6, *q* axis is placed in a position that coincides with the magnetic axis of the phase A winding. Due to the obvious symmetry the currents induced in bars 1 and 1' are the same in magnitude but opposite in direction, so these two bars can be viewed as a fictive coil. The situation is similar with other pairs of bars 2-2’, 3-3’, etc. The magnetic fluxes coupled by these fictive coils are:

$$\phi_{11'}=\frac{2\mu_0 N_m I_a r l\sin(z/2)}{g}\sin(\omega_e t) \tag{23}$$

$$\phi_{22'}=\frac{2\mu_0 N_m I_a r l\sin(3z/2)}{g}\sin(\omega_e t) \tag{24}$$

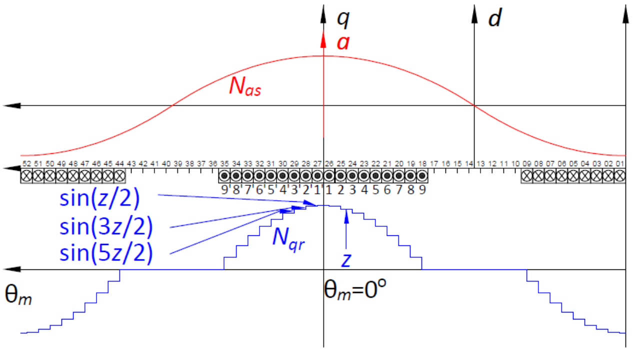

Fig.6. Damper winding function along the *q* axes

Now the factors are sin(*z*/2), sin(3*z*/2), etc. As before, ignoring the impedances of the ring segments that connect the corresponding bars, one can conclude that the currents will differ from each other only by the factors sin(*z*/2), sin(3*z*/2), etc. Now the damper winding along the *q* axis can be considered as fictitious concentrated winding through whose coils the same current flows, but each of the coils has different number of conductors. In this way the mmf of the damper winding remains unchanged. The function of the damper winding along the *q* axis is sketched in Fig. 7 in blue. Fig. 8 gives the exact waveform of the damper winding function along the *q* axis, for the analyzed machine and for the adopted reference directions from Fig. 1.

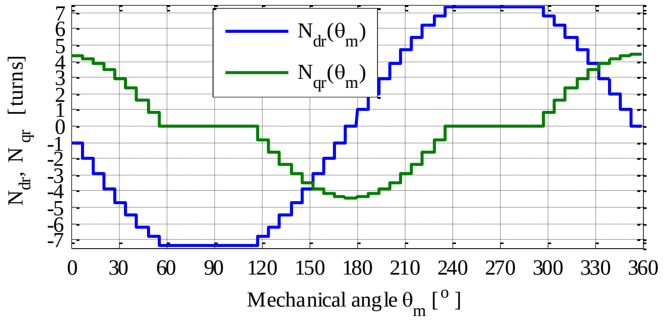

Fig.7. Damper winding functions along the *d* and *q* axes

VI. RESULTS

The winding functions defined in the previous paragraphs enable the determination of all inductances that appear in the equations of the *dq* model. As the rotating frame of reference is fixed to the rotor all the inductances of the model are constant valued. The values of inductances obtained on the example of the analyzed generator are given in Table I.

TABLE I

CALCULATED INDUCTANCES FOR ANALYSED MACHINE

L_{dsds}	L_{qsqs}	L_{dsqs}	L_{dsns}	L_{qsns}	L_{dsdr}	L_{qsqr}	L_{dsqr}
mH	mH	mH	mH	mH	mH	mH	mH
6.6	6.6	0.0017	0.0	0.0	5.9	2.65	0.16
L_{qsdr}	L_{dsfr}	L_{qsfr}	L_{drdr}	L_{qrqr}	L_{drqr}	L_{drfr}	L_{qrfr}
mH	mH	mH	mH	mH	mH	mH	mH
–0.36	48.8	–2.95	8.0	1.8	0.0	65.9	–0.0023

What can be noticed from the previous Table is that there is a certain magnetic coupling between those windings that are located on orthogonal axes (except on the fictitious *n* axis which is normal to the plane formed by the *d* and *q* axes). This magnetic coupling is, however, very weak, as illustrated by the obtained values of the mutual inductances of the windings along these axes: L_{dsqs}, L_{dsqr}, L_{qsdr}, L_{qsfr} and L_{qrfr}. The existence of these mutual inductances is a consequence of higher spatial harmonics which are taken into account by the winding functions.

By adding the leakage inductance of armature phase winding, which for this generator is 0.5 mH to the inductance L_{dsds}, synchronous inductance along the *d* axis is 7.1 mH. Multiplying this value by the electric angular frequency results in a synchronous reactance along the *d* axis of this generator: X_d =2.2305 Ω. By dividing this reactance with the base impedance of the generator, Z_b=1.0556 Ω, unit value of synchronous reactance along the *d* axis can be obtained: x_d=2.113. The unit value of synchronous reactance given in the "passport" of this generator is x_d =2.106. This very good match, testifies to the usefulness of this procedure in determining the parameters of the *dq* model.

VII. CONCLUSION

The method of determining the parameters of the *dq* model of a synchronous generator using winding function theory is presented in this paper. The procedure enables direct obtaining of parameters without the need for a large number of mathematical manipulations over matrix equations. The method of determining the functions of the damper winding along the *d* and *q* axes, which enables its modeling, is also presented. The procedure is illustrated on a real synchronous turbogenerator of type TBB-200-2A.

Plan for future research is to develop software that will enable obtaining electromagnetic torque, stator, field and damper windings curents in the time domain using the parameters obtained by the explained procedure.

APPENDIX

$$\left[U_{abcs}\right]=\left[U_{as} \quad U_{bs} \quad U_{cs}\right]^T$$

$$\left[U_{dqfr}\right]=\left[U_{dr} \quad U_{qr} \quad U_{fr}\right]^T$$

$$\left[i_{abcs}\right]=\left[i_{as} \quad i_{bs} \quad i_{cs}\right]^T$$

$$\left[i_{dqfr}\right]=\left[i_{dr} \quad i_{qr} \quad i_{fr}\right]^T$$

$$\left[R_s\right]=\begin{bmatrix} r_s & 0 & 0 \\ 0 & r_s & 0 \\ 0 & 0 & r_s \end{bmatrix}$$

$$\left[R_r\right]=\begin{bmatrix} r_{dr} & 0 & 0 \\ 0 & r_{qr} & 0 \\ 0 & 0 & r_{fr} \end{bmatrix}$$

$$\left[L_{abcs}\right]=\begin{bmatrix} L_{asas}+L_{ls} & L_{asbs} & L_{ascs} \\ L_{asbs} & L_{bsbs}+L_{ls} & L_{bscs} \\ L_{ascs} & L_{bscs} & L_{cscs}+L_{ls} \end{bmatrix}$$

$$\left[L_{abcsr}\right]=\begin{bmatrix} L_{asdr} & L_{asqr} & L_{asfr} \\ L_{bsdr} & L_{bsqr} & L_{bsfr} \\ L_{csdr} & L_{csqr} & L_{csfr} \end{bmatrix}$$

$$\left[L_{dqfr}\right]=\begin{bmatrix} L_{drdr} & L_{drqr} & L_{drfr} \\ L_{drqr} & L_{qrqr} & L_{qrfr} \\ L_{drfr} & L_{qrfr} & L_{frfr} \end{bmatrix}$$

$$\left[T(\theta)\right]=\frac{2}{3}\begin{bmatrix} \sin(\theta) & \sin\left(\theta-\frac{2\pi}{3}\right) & \sin\left(\theta+\frac{2\pi}{3}\right) \\ \cos(\theta) & \cos\left(\theta-\frac{2\pi}{3}\right) & \cos\left(\theta+\frac{2\pi}{3}\right) \\ \frac{1}{\sqrt{2}} & \frac{1}{\sqrt{2}} & \frac{1}{\sqrt{2}} \end{bmatrix}$$

$$\left[\omega x\right]=\begin{bmatrix} 0 & -\omega & 0 \\ \omega & 0 & 0 \\ 0 & 0 & 0 \end{bmatrix}$$

$$\left[U_{dqns}\right]=\left[T(\theta)\right]\left[U_{abcs}\right]$$

$$\left[i_{dqns}\right]=\left[T(\theta)\right]\left[i_{abcs}\right]$$

$$\left[\psi_{dqns}\right]=\left[T(\theta)\right]\left[\psi_{abcs}\right]$$

$$\left[L_{dqns}\right]=\begin{bmatrix} L_{dsds}+L_{ls} & L_{dsqs} & L_{dsns} \\ L_{dsqs} & L_{qsqs}+L_{ls} & L_{qsns} \\ L_{dsns} & L_{qsns} & L_{nsns}+L_{ls} \end{bmatrix}$$

$$\left[L_{dqnsr}\right]=\begin{bmatrix} L_{dsdr} & L_{dsqr} & L_{dsfr} \\ L_{qsdr} & L_{qsqr} & L_{qsfr} \\ L_{nsdr} & L_{nsqr} & L_{nsfr} \end{bmatrix}$$

REFERENCES

[1] T. A. Lipo, "Analysis of synchronous machines", CRC Press, 2012.

[2] I. Boldea, S. A. Nasar, "Synchronous generators", CRC Press, 2006.

[3] T. A. Lipo, "Introduction to ac machine design", IEEE Press, John Wiley & Sons, Hoboken, New Jersey, 2017.

[4] S. Vukosavić: "Električne mašine", Akademska misao, Beograd, 2010.

[5] G. Joksimović, M. Đurović, J. Penman, "Cage rotor mmf – winding function approach", IEEE Power Engineering Review, vol. 21, no. 4, pp. 64-66, April 2001.

[6] G. Joksimović, “AC winding analysis using winding function approach”, International Journal of Electrical Engineering Education, Manchester University Press, vol. 48, no. 1, pp. 34-52(19), January 2011.

[7] E. S. Obe, "Direct computation of ac machine inductances based on winding function theory", Energy Conversion Management, vol. 50, no. 3, pp. 539–542, 2009.

[8] G. Joksimović, E. Levi, A. Kajević, M. Mezzarobba, A. Tessarolo, "Optimal selection of rotor bar number for minimizing torque and current pulsations due to rotor slot harmonics in three-phase cage induction motors", *IEEE Access*, vol. 8, pp. 228572-228585, 2020.

Inteligentni DTC algoritam sa automatskom reorganizacijom u zavisnosti od ripla momenta

Marko Rosić

***Apstrakt* — Rad prezentuje karakteristike algoritma direktne kontrole momenta bazirane na diskretizovanim naponskim intenzitetima sa mogućnošću automatske modifikacije u cilju ograničenja ripla (pulsacija) momenta ispod njegove definisane maksimalno dozvoljene vrednosti u pogonu. Algoritam je baziran na konvencionalnoj prekidačkoj tabeli sa proizvoljnim brojem diskretizovanih naponskih intenziteta omogućavajući na taj način veću prostornu rezoluciju naponskih vektora u αβ ravni i rezultujući manjim intenzitetom ripla momenta. Broj raspoloživih naponskih intenziteta (vektora) može biti jednostavno definisan ili izmenjen bez potrebe za odgovarajućom izmenom prekidačke tabele. U zavisnosti od definisanog broja naponskih intenziteta odgovarajuće izmene upravljačke strukture algoritma su automatizovane, čineći ovaj algoritam jednostavnim, efikasnim i pogodnim za implementaciju u pametnim pogonima koje zahteva ubrzano dolazeća Industrija 4.0. Eksperimentalna verifikacija rezultata na digitalnoj platformi MSK28335, potvrđuje značajnu redukciju ripla momenta asinhrone mašine u zavisnosti od broja naponskih intenziteta istovremeno zadržavajući jednostavnost, efikasnosti i dobre dinamičke osobine DTC pogona sa asinhronom mašinom.**

***Ključne reči*—direktna kontrola momenta, asinhrona mašina, automatska modifikacija algoritma, pametni pogon, Industrija 4.0, ripl momenta, indukovana EMS, MSK28335.**

I. UVOD

Principi konvencionalne direktne kontrole momenta (cDTC) su dobro poznati i prezentovani u brojnoj naučnoj i stručnoj literaturi. Jednostavnost i dobre dinamičke osobine ovog vida kontrole čine ga i dalje aktuelnim u savremenim industrijskim pretvaračima. Kada se radi o metodama DTC zasnovane na prekidačkim tabelama, ripl momenta kao najveći nedostatak ove metode, pored ostalog, u najvećoj meri zavisi od broja raspoloživih naponskih vektora. Sa povećanjem broja raspoloživih naponskih vektora, korišćenjem invertora sa više nivoa ili kombinacije aktivnih naponskih vektora, DTC algoritmi zahtevaju definisanje nove, složenije prekidačke table koja zavisi od broja aktivnih naponskih vektora i brzine obrtanja motora [1, 2].

Sa druge strane, savremeni upravljački algoritmi, pored osnovnog dela, zahtevaju implementaciju i brojnih pratećih algoritamskih struktura kao što su estimacija parametara mašine u toku rada, self-tuning metode, napredni estimatori fluksa, opserveri stanja, kompenzacija efekta mrtvog vremena [3-5], itd. Iako ovi prateći algoritmi doprinose kvalitetu i stabilnosti pogona u širokom opsegu radnih brzina i režima rada, oni povećavaju ukupno proračunsko vreme algoritma (T_s ≈ 50-100 μs) smanjujući frekvenciju izvršavanja algoritma odnosno ograničavaju propusni opseg regulisane veličine. Iz tog razloga potrebno je da glavni deo algoritma bude što je moguće jednostavniji i manje vremenski zahtevan kako se ne bi umanjile dinamičke karakteristike sistema.

Industrija 4.0 takođe zahteva razvoj inteligentnih elektromotornih pogona sposobnih da izvrše samo evaluaciju, procenu stanja i životnog veka, autodetekciju kvara itd. [6-7]. Iz tog razloga upravljački algoritmi sa jedne strane treba da imaju sposobnost brze optimizacije i modifikacije u toku rada, a sa druge strane proračunsku jednostavnost i efikasnost koja ostavlja dovoljno prostora za implementaciju pomenutih pratećih kompenzacionih algoritamskih struktura.

Imajući u vidu navedeno, postoji potreba za robusnim, što jednostavnijim algoritmima, kao što je cDTC, sa visokim dinamičkim osobinama i malim riplom struje / momenta. Ovaj rad prezentuje karakteristike DTC algoritma baziranog na prekidačkoj tabeli sa mogućnošću njegove automatske adaptacije u cilju smanjenja ripla momenta, a u zavisnosti od broja raspoloživih diskretizovanih naponskih intenziteta (DVI). Definisanje broja naponskih intenziteta moguće je ručno (od strane korisnika) ili automatski, u zavisnosti od definisane maksimalne vrednosti ripla momenta u pogonu i ne zahteva izmene konvencionalne prekidačke tabele.

II. TEORIJSKA POZADINA DVI-DTC ALGORITMA

DVI-DTC metod baziran je na primeni više diskretizovanih naponskih intenziteta u svakom od šest osnovnih pravaca kod standardnog naponskog invertora kao što je prikazano na Sl.1.

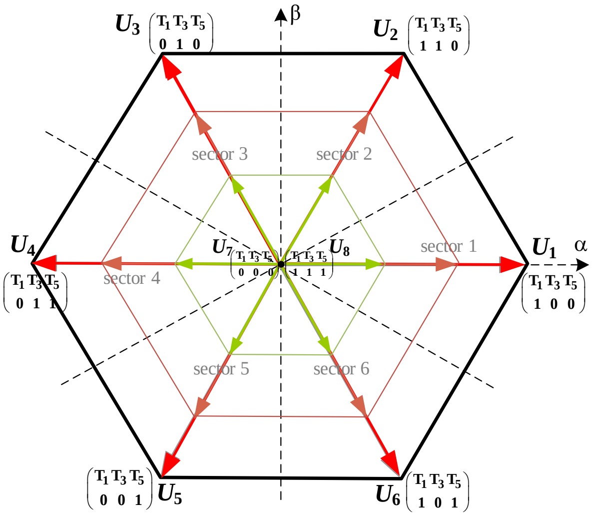

Sl. 1. Rezolucija naponskih vektora u αβ ravni sa definisana 3 naponska int.

Marko Rosić – Fakultet tehničkih nauka Čačak, Univerzitet u Kragujevcu, Sv. Save 65, 32000 Čačak, Srbija (e-mail: marko.rosic@ftn.kg.ac.rs).

U zavisnosti od definisanog broja naponskih intenziteta formira se odgovarajući komparator momenta. Komparator fluksa i prekidačka tabela (Tabela I) ostaju isti kao kod cDTC nezavisno od broja naponskih intenziteta . Ova osobina DVI-DTC omogućava da se broj naponskih vektora može jednostavno definisati ili promeniti bez potrebe za izmenom prekidačke tabele, kao što je to slučaj u [2, 8] gde je potrebno definisati novu prekidačku tabelu pri svakoj promeni broja raspoloživih naponskih intenziteta (vektora).

TABELA I – KONVENCIONALNA PREKIDAČKA TABELA

D_ψ	D_T		
	1	0	-1
1	U_{k+1}	U_7 or U_8	U_{k-1}
-1	U_{k+2}	U_7 or U_8	U_{k-2}

Izmene u broju naponskih intenziteta n kod DVI-DTC zahtevaju samo redefinisanje granica novog komparatora momenta T_{ba}, koja se može izvršiti prema (1).

$$T_{ba} = \frac{T_{ba\_c}}{3} \cdot i = \frac{T_{ba\_c}}{3} \cdot (2 \cdot n + 1) \tag{1}$$

Negativan efekat indukovane elektromotorne sile (EMS) na inkremente momenta pri visokim (dokumentovan u [9]) može se jednostavno kompenzovati prema (2).

$$\begin{aligned} \mathbf{u}_{s\,\text{new}} &= \mathbf{u}_s + \mathbf{u}_{\text{add.}} \\ &= \mathbf{u}_s + j\omega \boldsymbol{\psi}_s = u_{\alpha s} + ju_{\beta s} + j\omega\left(\psi_{\alpha s} + j\psi_{\beta s}\right) \\ &= \underbrace{u_{\alpha s} - \omega\psi_{\beta s}}_{\text{Re}(\mathbf{u}_{s\,\text{new}})} + j(\underbrace{u_{\beta s} + \omega\psi_{\alpha s}}_{\text{Im}(\mathbf{u}_{s\,\text{new}})}) \end{aligned} \tag{2}$$

Vrednost indukovane EMS potrebno je dodati prethodno izabranom naponskom vektoru odgovarajućeg intenziteta (kao izlaza iz komparatora momenta) formirajući rezultujući naponski vektor, kao što je to prikazano na slici 2. Blok dijagram DVI-DTC algoritma prikazan je na slici 3, gde su zelenom bojom obeleženi delovi koji su izmenjeni u odnosu na cDTC.

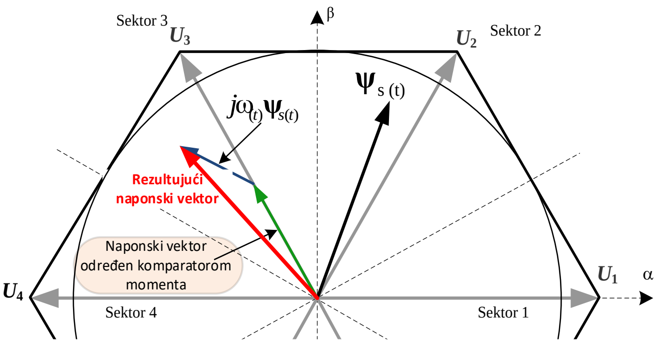

Sl. 2. Kompenzacija EMS i formiranje rezultujućeg naponskog vektora

Broj definisanih naponskih intenziteta teorijski može varirati od 2 pa do maksimalnog broja ograničenog brojačem DSP. Ipak, u [10] pokazano je da ripl momenta eksponencijalno opada sa povećanjem broja naponskih intenziteta i da je sa 6 naponskih intenziteta ripl smanjen 8 puta u poređenju sa riplom momenta koji se ima kod cDTC.

DVI-DT može biti dalje unapređen definisanjem više pravaca (8, 12, 16 ili više) naponskih vektora dalje povećavajući prostornu rezoluciju vektora statorskog napona. U tom slučaju bilo bi potrebno modifikovati prekidačku tabelu u zavisnosti od definisanog broja pravaca. Ipak, rezultati prezentovani u [11] pokazuju da stepen smanjenja ripla momenta kod DT algoritama baziranih na prekidačkim tabelama ne zavisi u velikoj meri od izabranog pravca naponskog vektora koliko od njegovog intenziteta. Stoga, zadržavanje konvencionalne prekidačke table sa 6 aktivnih naponskih vektora se čini opravdanim. Zahvaljujući odsustvu koordinatnih transformacija, složenih matematičkih operacija, PI regulatora itd., DVI-DTC algoritam ima veoma malo vreme izvršavanja i zadržava visoke dinamičke osobine karakteristične za cDTC. Navedene osobine promovišu DVI-DTC algoritam kao pogodnog kandidata za implementaciju u savremenim upravljačkim sistemima koji zahtevaju širok propusni opseg po momentu i kontrolu maksimalnog intenziteta ripla momenta u pogonu.

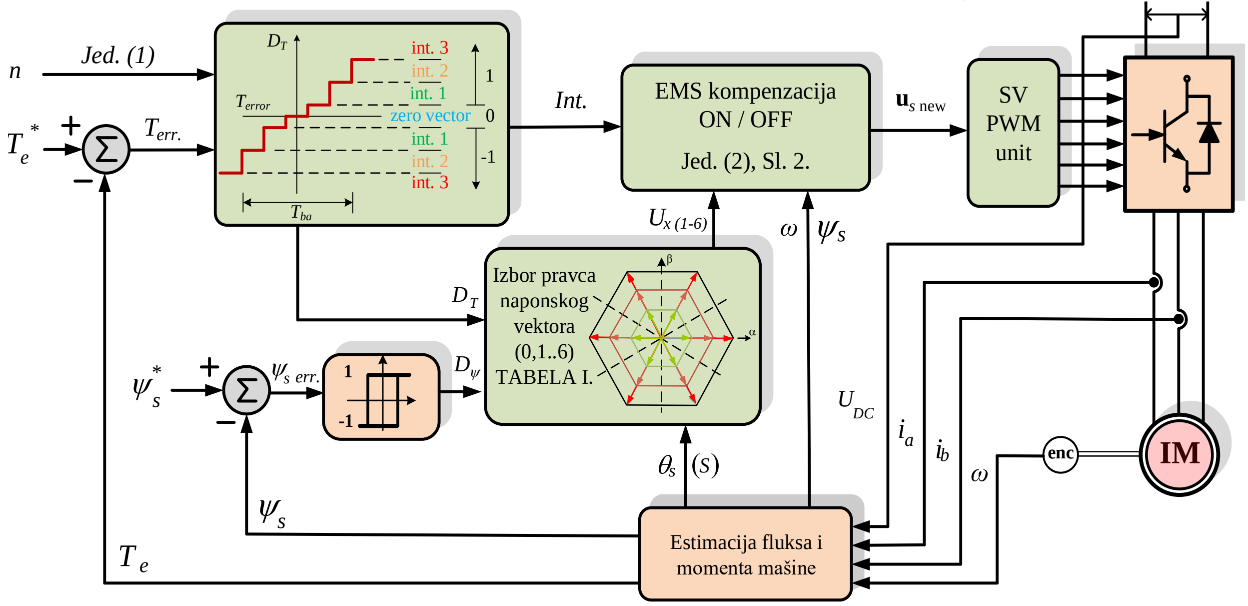

Sl. 2. Blok struktura DVI-DTC algoritma

III. AUTOMATSKA MODIFIKACIJA DVI-DTC ALGORITMA

U cilju adekvatnog smanjenja ripla momenta, broj diskretizovanih naponskih intenziteta može biti definisan na dva načina:

- Od strane korisnika (ručno) ili
- Automatski, od strane algoritma, bazirano na estimiranim vrednostima momenta i ripla.

Na početku algoritma korisnik definiše broj naponskih intenziteta *n*, na osnovu koga se DVI-DTC algoritam dalje modifikuje pre starta. Pored ovoga, potrebno je definisati i maksimalno dozvoljeni intenzitet ripla momenta u pogonu ΔT_{max}, kao i broj uzoraka estimiranog momenta *m* na osnovnu koga će biti određen trenutna vrednost ripla momenta. Ukoliko je ripl momenta veći od definisane vrednosti ΔT_{max}, broj naponskih intenziteta se uvećava za jedan i algoritam nanovo modifikuje pre sledećeg starta. Slika 3 daje prikaz kompletnog algoritma inteligentnog DVI-DTC algoritma.

Inteligentni DVI-DTC algoritam je podeljen na 5 sekcija. U sekciji I zahteva se definisanje inicijalnih karakteristika pogona kao što su početni broj naponskih intenziteta i opcija kompenzacije EMS (uključena ON ili isključena OFF) od strane korisnika. Takođe u sekciji I definišu se i vrednosti za ΔT_{max} i *m* potrebne za analizu ripla momenta u sekciji IV.

Kao što je rečeno, uvećanje broja naponskih intenziteta ne zahteva izmene u prekidačkoj tabeli. Dalja automatska modifikacija algoritma svodi se na sledeća dva koraka:

- predefinisanje odgovarajućih naponskih intenziteta u SVPWM jedinici i
- modifikacije granica komparatora momenta sa *n* nivoa.

Ova dva koraka, definisana u sekciji II, predstavljaju glavni deo automatske modifikacije DVI-DTC algoritma. Jednostavna automatizovana modifikacija u dva koraka omogućena je zahvaljujući raspregnutom izboru pravca i (prekidačka tabela) i intenziteta (komparator momenta sa *n* nivoa) kao glavnoj prednosti DVI-DTC algoritma.

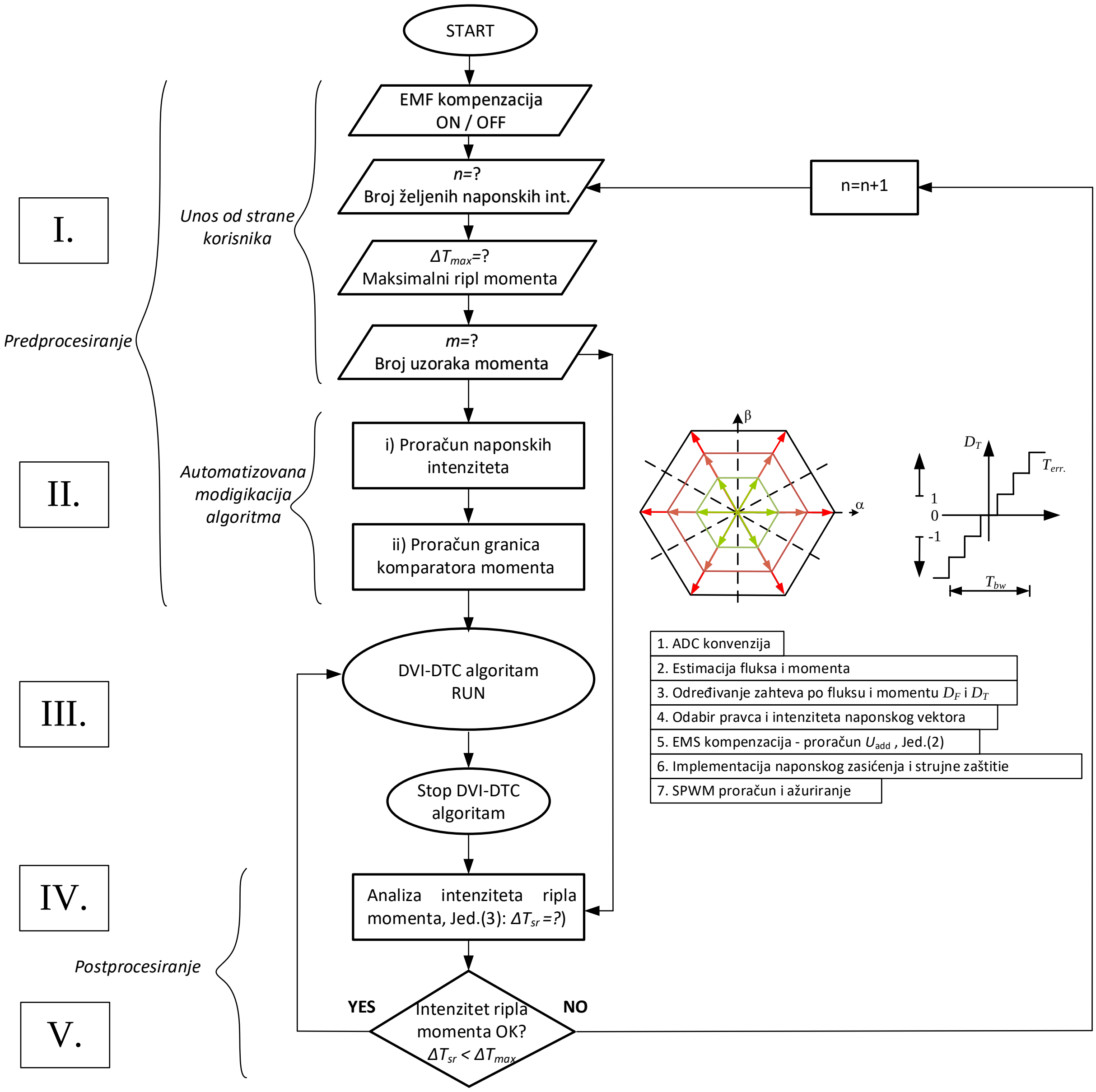

Sl. 3. Inteligentni DVI-DTC algoritam

Predefinisanje odgovarajućih naponskih intenziteta podrazumeva podelu punog opsega SVPWM generisanog naponskog vektora na jednake delove. Izuzimajući oblast nadmodulacije i negativan efekat mrtvog vremena, maksimalni intenzitet naponskog vektora generisanog uz SVPWM ograničen je radijusom upisanog kruga u heksagon koga formiraju šest aktivnih naponskih vektora (Sl.1), što predstavlja 86.7% od intenziteta maksimalnog naponskog vektora. Dalje se ovaj intenzitet deli na jednake delove na osnovu čega se definišu odgovarajuća vremena vođenja prekidačkih elemenata kod SVPWM. Odgovarajući komparator momenta i njegove granice određene su prema (1) ravnomernom raspodelom nivoa komparatora i odgovarajućih naponskih intenziteta u okviru širine komparatora T_{ba}.

Kako se opisane sekcije algoritma I i II izvršavaju pre starta glavnog dela DVI-DTC algoritma definisani su kao predpocesiranje. Ovo omogućava da glavni deo algoritma (sekcija III) zadrži proračunsku jednostavnost sličnu kao kod cDTC. Glavni deo DVI-DTC algoritma startuje sa ADC konverzijom statorskih struja i prikazan je na slici 3 koracima od 1 do 7.

Postprocesiranje odnosi se na sekcije IV i V koji se realizuju nakon zaustavljanja glavnog dela DVI-DTC algoritma. Ovaj deo zadužen je za analizu rezultata (ripla momenta) i odgovarajuće donošenje odluka u sekciji V. Ukoliko je rezultujući ripl momenta u okviru definisanih granica DVI-DTC algoritam može biti startovan opet. U suprotnom, broj definisanih naponskih intenziteta će biti uvećan u okviru sekcije I. Ova petlja (od sekcije V do sekcije I) omogućava uvećanje broja predefinisanih naponskih vektora za jedan nakon čega se na odgovarajući način algoritam automatski modifikuje u sekciji II. Odluka da li trenutna vrednost ripla momenta zadovoljava maksimalno definisanu vrednost ΔT_{max} (definisanu od strane korisnika u sekciji I) donosi se na osnovu proračuna procentualne srednje vrednosti ripla momenta ΔT_{sr} u odnosu na nominalnu vrednost momenta motora T_n prema (3).

$$\Delta T_{sr} = \frac{\sqrt{\frac{1}{m}\sum_{x=1}^{m}\left(T_x - T_{ref.}\right)^2}}{T_n} \cdot 100 \quad [\%] \tag{3}$$

Gde je m broj semplova estimiranog momenta prikupljenih u cilju analize ripla momenta T_x, a $T_{ref.}$ predstavlja aktuelnu referentnu vrednost momenta. U cilju što objektivnije ocene srednje vrednosti ripla momenta $\Delta T_{sr.}$, i odabira odgovarajućeg broja potrebnih naponskih intenziteta, potrebno je da budu ispunjeni sledeći uslovi:

- kompenzacija EMS mora biti uključena (ON)
- broj semplova estimiranog momenta m treba da obuhvata vrednosti momenta pri konstantnoj referentnoj vrednosti momenta.

Ova dva uslova obezbeđuju eliminisanje greške momenta kao posledice uticaja EMF (naročito pri visokim brzinama) i trenutne greške momenta koja se javlja kao posledica nagle promene referentne vrednosti i kašnjenja usled ograničene dinamike odziva momenta kao i kašnjenja usled digitalne implementacije.

Očigledno, ova petlja zahteva da DVI-DTC algoritam najpre bude stopiran sa svakom novom iteracijom sve dok uslov maksimalnog ripla momenta ne bude ispunjen (sekcija V). Razlog ovome leži u činjenici što su delovi algoritma koji nisu prioritetni izmešteni u predprocesiranje i postprocesiranje i kao takvi pogodni su za implementaciju zajedno sa drugim *self-tuning* algoritmima opisanim u uvodu. Sa druge strane, ovim je omogućeno očuvanje jednostavnosti glavnog dela DVI-DTC algoritma.

Automatska regulacija ripla momenta moguća je i bez zaustavljanja DVI-DTC pogona u slučaju kada se sekcije I, II, IV i V izvršavaju paralelno sa sekcijom III. Ovo bi zahtevalo implementaciju ovih delova koda koji se izvršavaju sa manjom frekvencijom kao što su poziciona ili brzinska petlja. Drugi način odnosi se na implementaciju ovih delova u posebne delove koji se izvršavaju na zahtev korisnika ili nadređene upravljačke strukture.

DVI-DTC algoritam pretenduje da pokaže svoj pun potencijal sa višefaznim mašinama i odgovarajućim višefaznim pretvaračima gde mogu biti implementirani ne narušavajući originalnu jednostavnost. Prirodno veća prostorna rezolucija naponskog vektora kod višefaznih pretvarača može biti dalje umnožena uvođenjem diskretizovanih naponskih intenziteta što bi dovelo većeg stepena redukcije ripla momenta. Takođe implementacija DVI-DTC algoritma sa višefaznim mašinama bi omogućila unapređenje robusnosti i otpornosti sistema (eng. *fault tolerant*) na potencijalne kvarove na pojedinačnim fazama.

IV. EKSPERIMENTALNI REZULTATI

DVI-DTC algoritam implementiran je i testiran na MSK28335 DSP digitalnoj platformi u EMPA laboratoriji Fakulteta tehničkih nauka u Čačku. DSP platforma sastoji se od TMS320F28335 procesora sa pokretnom tačkom, 150 MHz, konvencionalnog naponskih invertora sa 6 IGBT 750 W i 310 V DC kolom. Eksperimentalna platforma je prikazana na slici 4 dok su podaci motora dati u prilozima.

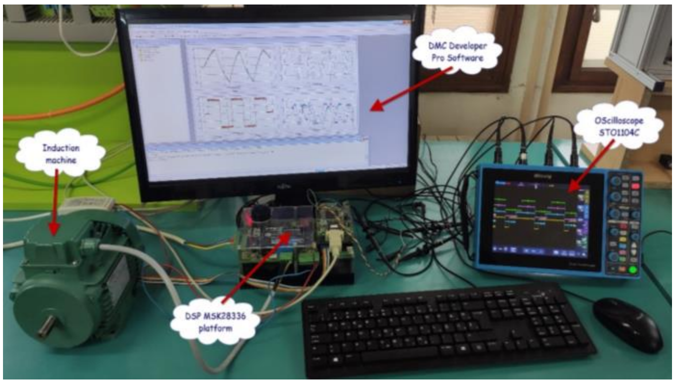

Sl. 4. Eksperimentalna postavka sa merenjem vremena izvršavanja

Prekidačka frekvencija je definisana na 20kHz, ostavljajući na raspolaganju T_s=50 µs za izvršenje DTC algoritma.

Estimacija fluksa realizovana je sa *Gopinath* fluks opserverom [12] koji kombinuje strujni i naponski model mašine. Osciloskop STO1104C je korišćen za snimanje vremena izvršavanja pojedinih DVI-DTC algoritma praćenjem digitalnog izlaza procesora koji pri startu praćenog dela algoritma daje logičku nulu a pri završetku se opet vraća na nivo logičke jedinice. Vremena trajanja cDTC i DVI-DTC su snimljena i prikazana na slici 5.

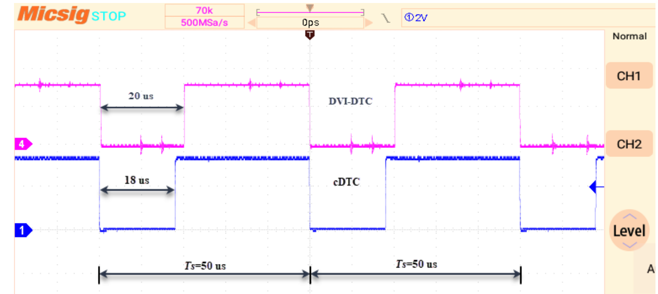

Sl. 5. Vremena izvršavanja DVI-DTC (gore) i cDTC algoritama (dole)

Slika 5 potvrđuje da glavni deo DVI-DTC algoritma zahvaljujući svojoj jednostavnosti ima oko 2 µs (≈10%) duže vreme izvršavanja u poređenju sa cDTC. Pri aktiviranju kompenzacije EMS (ON), ovo vreme izvršavanja DVI-DTC produžava se oko 7 µs kao što je prikazano na slici 6.

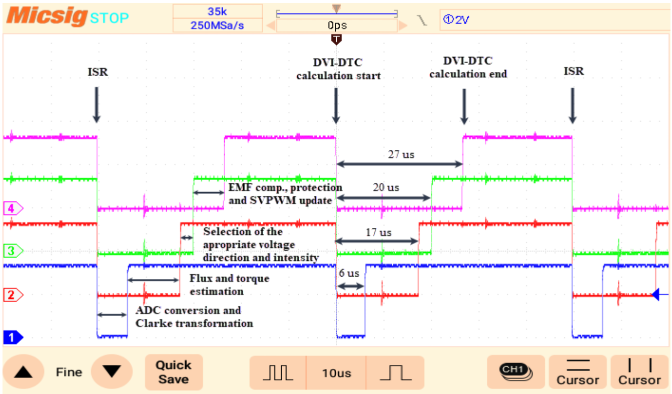

Sl. 6. Vremena izvršavanja delova DVI-DTC algoritma (sekcija III) sa uključenom kompenzacijom EMS

Eksperimentalni rezultati DVI-DTC sa 3, 4, 5 i 6 naponskih intenzitete sa ili bez kompenzacije indukovane EMS prikazani su na slici 7. Vremenska osa odgovara uzorkovanju rezultata na 1 ms. Na brzinskoj osi 15 pulseva odgovara brzini od 900 min^{-1} dok je osa momenta izražena u Nm. Rezultati prikazani na slici 7 potvrđuju da se ripl momenta značajno smanjuje sa rastom broja definisanih naponskih intenziteta.

V. ZAKLJUČAK

Ovaj rad prezentuje inteligentni DTC algoritam baziran na diskretizovanim naponskim intenzitetima koji ima mogućnost se automatske adaptacije u zavisnosti od intenziteta ripla momenta. Odgovarajući broj naponskih intenziteta može biti definisan od strane korisnika ili automatski kroz iterativni postupak u cilju zadovoljenja definisanom maksimalnog ripla momenta u pogonu. Originalna jednostavnost i dobre dinamičke osobine koje karakterišu cDTC su zadržane kod DVI-DTC. Dobijeni eksperimentalni rezultati potvrđuju proračunsku jednostavnost DVI-DTC algoritma u poređenju sa konvencionalnom DTC i značajno smanjenje ripla momenta sa porastom broja predefinisanih diskretizovanih naponskih intenziteta. Navedene karakteristike DVI-DTC sa mogućnošću automatske modifikacije u cilju redukcije ripla momenta čine ovaj metod kontrole pogodan za implementaciju u pametnim pogonima sledeće generacije.

DODATAK

TABELA II - PARAMETRI ASINHRONOG MOTORA SIEBER LS71

U_n [V]	400	R_s [Ω]	24.6
I_n [A]	0.95	R_r [Ω]	16.1
P_n [W]	370	L_m [H]	1.46
n_n [min^{-1}]	2860	L_s [H]	1.48
p [p.p.]	1	L_r [H]	1.48

ZAHVALNICA

Prikazani rezultati predstavljaju deo aktivnosti u okviru projekta pod ugovornim br. 451-03-68/2022-14/200132 zaključenog između Ministarstva prosvete nauke i tehnološkog razvoja Republike Srbije i Fakulteta tehničkih nauka u Čačku, Univerzitet u Kragujevcu.

LITERATURA

[1] D. Mohan, X. Zhang, and G. H. Beng Foo, “Generalized DTC Strategy for Multilevel Inverter Fed IPMSMs with Constant Inverter Switching Frequency and Reduced Torque Ripples”, *IEEE Trans. on Ener. Conv.* vol. 32, no. 3, pp. 1031–1041, 2017.

[2] Casadei D, Serra G, Tani A., “Implementation of a direct control algorithm for induction motors based on discrete space vector modulation”, *IEEE Trans. on .P. Elec.*, vol. 15, no. 4, pp.769-777, 2012.

[3] M. Holakooie, M. Ojaghi, A. Taheri, “Direct Torque Control of Six-Phase Induction Motor with a Novel MRAS-Based Stator Resistance Estimator”, *IEEE Trans. on Ind. El.*, vol. 65, no.10, pp.7685-7696, 2018

[4] M. N. Uddin, M. Hafeez and N. A. Rahim, “Self-tuned NFC and adaptive torque hysteresis-based DTC scheme for IM Drive”, *Proc. of the IEEE Industry Applications Society Annual Meeting*, pp. 1-8, 2011.

[5] L. Q. Zhou, “A new dead-time compensation method on direct torque control system based on DSP”, *Proc. of the 4th IEEE Conference on Industrial Electronics and Applications*, pp. 2359-2362, 2009.

[6] M. N. S. K. Shabbir, X. Liang and S. Chakrabarti, “An ANOVA-Based Fault Diagnosis Approach for Variable Frequency Drive-Fed Induction Motors”, *IEEE Trans. on Ener. Conv.*, vol. 36, no. 1, pp. 500-512, 2021.

[7] S. Shi, Y., et al., “Moving Integration Filter-Based Open-Switch Fault-Diagnosis Method for Three-Phase Induction Motor Drive Systems”, *IEEE Trans. on Tr. Electr.*, vol. 6, no. 3, pp. 1093-1103, 2020.

[8] S. Suresh and R. P. P., “Virtual Space Vector-Based Direct Torque Control Schemes for Induction Motor Drives”, *IEEE Transactions on Industry Applications*, vol. 56, no. 3, pp. 2719-2728, 2020.

[9] M. Rosic, M. Bjekic, M. Bebic and B. Jeftenic, “Electromotive force compensation in direct torque control with discretized voltage intensities”, *Proc. of the 4th International Symposium on Environmental Friendly Energies and Applications (EFEA)*, pp. 1-6, 2016

[10] M. Rosić, S. Antić, M. Bebić, “Improvements of torque ripple reduction in DTC IM drive with arbitrary number of voltage intensities and automatic algorithm modification”, *Turk. Jour. of El. Eng.&Comp. Sci.*, vol. 29, no.2, pp. 687-703, 2021.

[11] Arumugam S, Thathan M., “Novel switching table for direct torque controlled permanent magnet synchronous motors to reduce torque ripple”, *Jour. of Power Electr.*, vol. 13 no. 6, pp. 939-954, 2013.

[12] West, N. T., and Lorenz, R. D., “Digital Implementation of Stator and Rotor Flux-Linkage Observers and a Stator-Current Observer for Deadbeat Direct Torque Control of Induction Machines”, *IEEE Transactions on Industry Applications*, vol. 45, no. 2, pp.729-736, 2009.

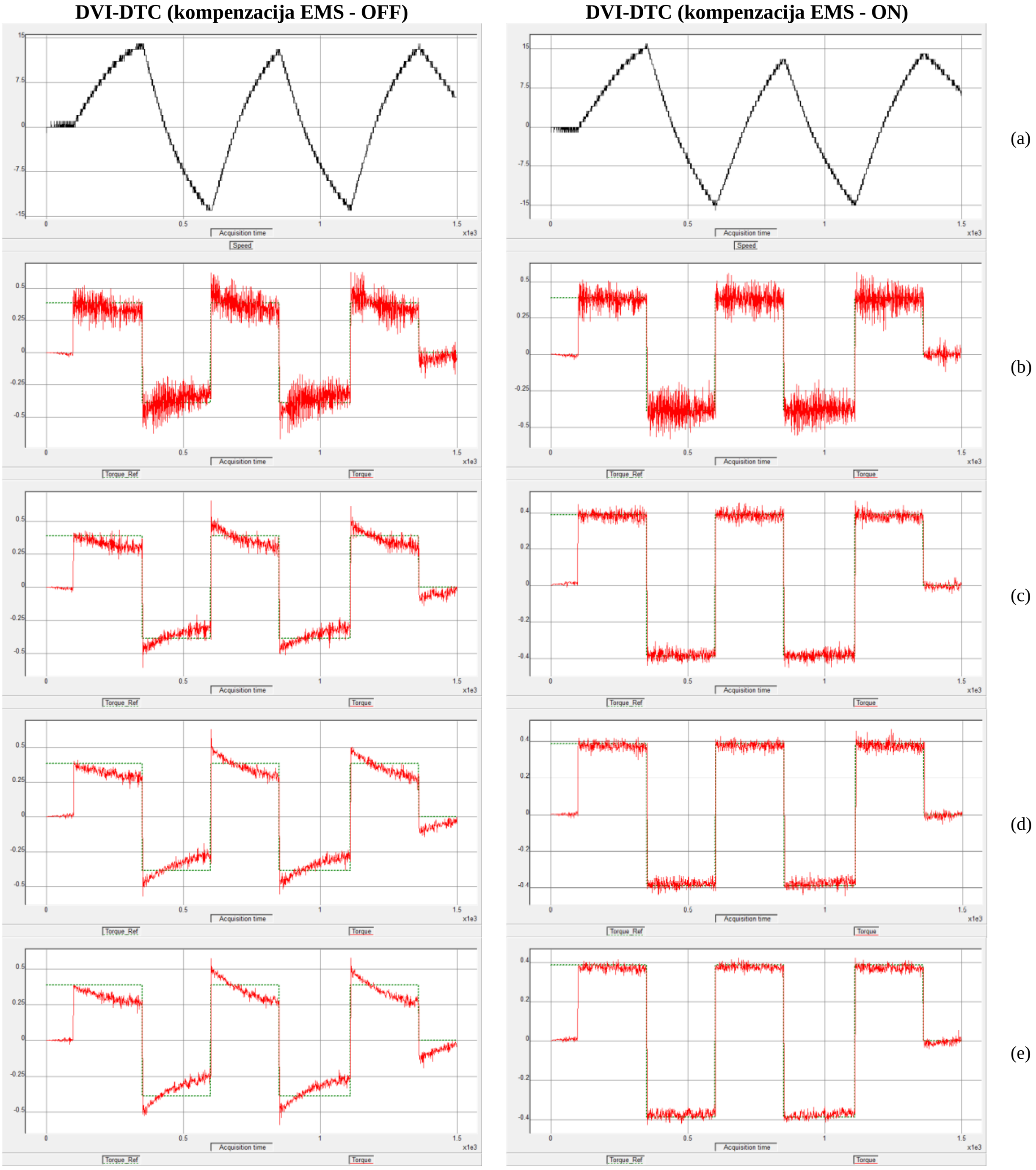
DVI-DTC (kompenzacija EMS - OFF) **DVI-DTC (kompenzacija EMS - ON)**

Sl. 7. Brzina (a) i estimirani moment (b) kod DVI-DTC sa 3 (b), 4 (c), 5 (d) i 6 (e) naponskih intenziteta sa i bez kompenzacije indukovane EMS

ABSTRACT

The paper presents characteristic of direct torque control method based on discretised voltage intensities with possibilities of automatic algorithm modification in terms of torque ripple reduction. The algorithm uses the conventional switching table with an arbitrary number of discretized voltage intensities allowing higher space-voltage resolution and consequently lower torque ripple. The number of available voltage intensities can be easily changed without the need to modify the conventional switching table. Depending on the number of defined, discretized voltage intensities corresponding algorithm structures are automatized, making this kind of control method simple, effective, and suitable for upcoming smart drives in the rapidly growing industry 4.0. Experimental validation presented in the paper confirms improvements in torque ripple reduction retaining the simple and time-effective control structure of the induction machine DTC drive.

Intelligent DTC algorithm with automatic reorganisation based on the torque ripple intensity

Marko Rosić

Primjena električnih vozila za smanjenje deficita snage u sistemu

Uroš Ognjenović[1], Saša Mujović[1], Lazar Šćekić[1]
[1]*Univerzitet Crne Gore, Elektrotehnički fakultet, Bulevar Dž. Vašingtona bb, Podgorica, Crna Gora*

Apstrakt—**Električna vozila (EVs – electric vehicles) su jedan od vodećih trendova u svijetu kada je u pitanju održivi razvoj i smanjenje emisije štetnih gasova. Prodor električnih vozila u elektroenergetski sistem znači povećano opterećenje, ali i omogućava plansko punjenje i pražnjenje ovih vozila uz benefit po sistem i korisnike električnih vozila. U ovom radu analizirana je primjena planskog punjenja i pražnjenja električnih vozila zasnovana na metodi igara na sreću, u cilju smanjenja deficita snage u sistemu.**

Ključne riječi—**električna vozila; agregator; plansko pražnjenje; plansko punjenje**

I. UVOD

Električna vozila cjelokupnu snagu ili jedan njen dio obezbjeđuju iz električne mreže i dijele se na potpuno električna vozila (AEVs – all-electric vehicles) i hibridna vozila (PHEVs – plug-in hybrid electric vehicles). Potpuno električna vozila su pokretana od strane jednog ili više električnih motora. Energiju obezbjeđuju punjenjem sa električne mreže i njenim čuvanjem u baterijama. Ne troše fosilna goriva i ne proizvode toksične gasove niti gasove sa efektom staklene bašte. Hibridna vozila koriste baterije za napajanje električnog motora, ali pored toga posjeduju i motor sa unutrašnjim sagorijevanjem (ICE – internal combustion engine).

Nagli rast interesovanja za razvoj električnih vozila je dobrim dijelom rezultat negativnog uticaja na životnu sredinu usljed industrijskog razvoja, konflikta u zemljama izvoznicama nafte na Bliskom Istoku i sa tim u vezi visokom cijenom nafte. Finansijska ulaganja i podsticaji za razvoj i posjedovanje električnih vozila su zasnovani na percepciji da su električna vozila ekološki prihvatljiv vid transporta u budućnosti.

Električna vozila su tek na početku svog ubrzanog razvoja i prodora na tržište (iako je prvo električno vozilo proizvedeno davne 1832.) što znači da će međusobni uticaj električnih vozila i EES-a (elektroenergetskog sistema) da raste u narednom periodu što potvrđuju sledeće zanimljivosti:

- 2,6% prodatih automobila u svijetu u 2019. su bila električna vozila, što predstavlja značajan porast u odnosu na 2017. kada je taj udio bio 1%.
- Norveška planira da u potpunosti izbaci iz upotrebe vozila sa motorom sa unutrašnjim sagorijevanjem do 2025., dok Francuska i Velika Britanija to planiraju da urade do 2040.
- Broj stanica za punjenje u Holandiji je u februaru 2020. iznosio nešto više od 37.000 (jedna stanica na 459 stanovnika) što Holandiju pozicionira na prvo mjesto u svijetu.
- Od ukupne potrošnje energije u Sjedinjenim Američkim Državama u 2005. u iznosu od 29.000 TWh, 28% odnosno 4.953 TWh je utrošeno u sektoru transporta. Ukoliko se pretpostavi da je ova energija utrošena isključivo u automobilima, dolazi se do zaključka da bi SAD trebalo da obezbijede energiju koja je veća od njene ukupne godišnje proizvodnje električne energije u istoj godini (4.055 TWh) za potpuni prelazak na električna vozila.

Imajući u vidu mogućnost kontrolisanog punjenja i pražnjenja, električna vozila se mogu posmatrati kao pokretni upravljivi sistemi za skladištenje električne energije. Interes korisnika električnih vozila je razlika između cijene električne energije predate u mrežu i cijene električne energije za punjenje. Kao rezultat učešća u V2G, dolazi do degradacije baterije tako da novčane naknade korisnicima moraju biti veće od troškova usljed degradacije baterije.

Ostatak rada je organizovan na sledeći način. U drugom poglavlju je objašnjen problem planskog pražnjenja vozila. Metod igara na sreću, proces aukcije i benefit korisnika su opisani u trećem poglavlju. Rezultati proračuna potencijala upotrebe električnih vozila za smanjenje deficita snage u primorskoj regiji Crne Gore su dati u poglavlju broj četiri. Peto poglavlje sumira ovaj rad. Na kraju rada je dat spisak korišćene literature.

II. ELEKTRIČNA VOZILA U ELEKTROENERGETSKOM SISTEMU

Istraživanja pokazuju da su špic sati za dolazak na posao električnim vozilom između 7:00 i 8:00 i da je vrijeme punjenja tokom radnih sati. Špic sati za povratak sa posla električnim vozilom su između 17:00 i 19:00 i vrijeme punjenja je između 19:00 i 6:00 narednog dana. Dakle, električno vozilo se može povezati na mrežu dva puta dnevno [1]. Pored toga, više od 90% vozila je parkirano negdje i 50% kod kuće tokom dana, što otvara mogućnost za ispomoć električnoj mreži ukoliko postoji odgovarajući stimulans [2]. Konkretno, zabrana prodaje automobila na benzin i dizel koja je predložena u nekim zemljama će promovisati prodor električnih vozila, tako da imaju veliki potencijal kao kontrolisano opterećenje [3].

Obzirom da se električna vozila mogu posmatrati kao distribuirani izvor energije i kao opterećenje koje može biti planirano, stvorena je ideja o sistemu vozilo-ka-mreži (V2G –

Uroš Ognjenović – Elektrotehnički fakultet, Univerzitet Crne Gore, Džordža Vašingtona bb, 81000 Podgorica, Crna Gora (e-mail: urosognjenovic@gmail.com).

Saša Mujović – Elektrotehnički fakultet, Univerzitet Crne Gore, Džordža Vašingtona bb, 81000 Podgorica, Crna Gora (e-mail: sasam@ucg.ac.me).

Lazar Šćekić – Elektrotehnički fakultet, Univerzitet Crne Gore, Džordža Vašingtona bb, 81000 Podgorica, Crna Gora (e-mail: slazar@ucg.ac.me).

vehicle-to-grid). U V2G sistemu, energija može da teče između električne mreže i električnog vozila [1].

Za koordinaciju punjenja i pražnjenja električnih vozila se koristi agregator. Agregator je centralni entitet koji koordiniše i planira status električnih vozila. Očekuje se da će u budućnosti većina električnih vozila biti povezana na Internet preko VANET-a (Vehicular ad hoc network – Bežična ad-hok mreža), Wi-Fi-ja ili mobilne mreže. Električna vozila mogu da prenose informacije kao što je tip vozila, kapacitet baterije, neophodno punjenje, ruta, itd. agregatoru [4]. Sva električna vozila karakteriše i status napunjenosti (SoC – State of Charge) koji je nivo napunjenosti u odnosu na kapacitet baterije (između 0% i 100%).

Za određivanje uticaja električnih vozila na elektroenergetski sistem neophodno je razumjeti različite statuse koje električna vozila mogu imati u bilo kom trenutku. Razlikuje se 5 statusa [5]:

- Električna vozila na punjenju: Električna vozila su priključena na mrežu i preuzimaju energiju za punjenje njihovih baterija.
- Električna vozila u V2G sistemu: Električna vozila predaju energiju mreži.
- Električna vozila kao eksplicitna rezerva: Električna vozila su priključena na mrežu, ali ne preuzimaju niti injektiraju energiju u mrežu. U ovom slučaju, električna vozila mogu započeti proces punjenja ili pražnjenja na zahtjev agregatora, uzimajući u obzir trenutno stanje baterije.
- Električna vozila koja se koriste za transport. U ovom modu električna vozila nijesu priključena na mrežu, već se koriste za transport i troše energiju skladištenu u baterijama.
- Neiskorištena električna vozila: Električna vozila su priključena na mrežu, ali agregator odlučuje da ne koristi ova vozila za punjenje, V2G niti kao rezervu.

III. METOD IGARA NA SREĆU

Za učešće u V2G sistemu se primjenjuje mehanizam aukcije po prvoj cijeni (first-price auction). Pobjednici aukcije su učesnici koji su dali najviše ponude i oni plaćaju iznose koje su ponudili. Kao benefit ostvaruju razliku između cijene električne energije za punjenje električnih vozila i ponude, sa jedne strane, i cijene električne energije predate u mrežu, sa druge strane. Učesnici aukcije nisu upoznati sa ponudama drugih učesnika (sealed-bid auction – aukcija sa zatvorenim ponudama). Potrošači, odnosno učesnici aukcije koji ne žele da pobijede na aukciji i time učestvuju u V2G sistemu, mogu da daju ponudu za koju vjeruju da neće biti najviša. Time se obezbjeđuje autonomija – potrošači bi trebalo da sami odlučuju da li da učestvuju u V2G poređenjem benefita V2G i mobilnosti [3].

Aukcija se vrši za svaki 60-minutni interval pojedinačno za naredni dan. Na osnovu prognoze proizvodnje i potrošnje za naredni dan, $P_{pro}(t)$ i $P_{pot}(t)$, se određuje deficit snage po satima $P_{def}(t)$, gdje je t indeks intervala ($t \in \{1,2,...,T\}$, gdje je T poslednji interval). Ovaj podatak se koristi za dobijanje podataka o idealnom broju idealnih vozila (idealna vozila su vozila čiji status baterije omogućava predaju određene količine energije mreži tokom odgovarajućeg intervala pri određenoj snazi) $N_{ide}(t)$ koja bi predala električnu energiju sistemu. Ukoliko su sva električna vozila istih karakteristika, $N_{ide}(t)$ se dobija po formuli:

$$N_{ide}(t) = floor(\frac{P_{def}(t)}{P_{pra}}), t = 1,2,..., T, \qquad (1)$$

gdje je P_{pra} snaga kojom električna vozila predaju električnu energiju mreži [kW]. Floor($P_{def}(t)/P_{pra}$) označava prvu manju cijelu vrijednost količnika $P_{def}(t)/P_{pra}$ – zaokruženu vrijednost.

V2G se realizuje kada se, na osnovu prognoze proizvodnje i potrošnje električne energije za naredni dan ustanovi da se makar u jednom od intervala javlja deficit snage $P_{def}(t)$ i kada je taj deficit veći od P_{pra}. Ovaj uslov se može predstaviti relacijom:

$$\sum_{t=1}^{T} N_{id}(t) \geq 1. \qquad (2)$$

Neka se u nekom EES-u nalazi N električnih vozila. Broj vozila $N_{ide}(t)$ za određeni interval može biti veći, jednak, ili manji od stvarnog broja vozila u sistemu. U slučaju da je $N_{ide}(t)$ veće od ili jednako N, svi korisnici električnih vozila mogu da učestvuju u V2G, čime se gubi potreba za održavanjem aukcije u odgovarajućem intervalu. U ovoj situaciji, agregator određuje vrijednost po kojoj se električna energija otkupljuje od korisnika električnih vozila. Ova vrijednost se određuje po relaciji:

$$C_{otk} = k_1 C_{maks}, \qquad (3)$$

gdje je:

C_{otk} – cijena otkupljene električne energije od potrošača [EUR/kWh]

k_1 – koeficijent kojim se obezbjeđuje benefit potrošaču u najnepovoljnijem slučaju kada je električno vozilo punjeno tokom perioda maksimalne cijene električne energije i koji je veći od 1 (npr. 1,1), za slučaj kada je $N_{ide}(t)$ veće od jednako N.

C_{maks} – maksimalna cijena električne energije tokom dana [EUR/kWh]

Kada je $N_{ide}(t)$ manje od N, odnosno kada je deficit u sistemu moguće pokriti sa brojem vozila koji je manji od stvarnog broja vozila u sistemu, održava se aukcija kako bi se odredio broj korisnika električnih vozila koji žele da učestvuju u V2G. Da bi korisnici električnih vozila ostvarili benefit pri učestvovanju u aukciji, moraju biti upoznati sa cijenom otkupa električne energije koja se može razlikovati od slučaja kada je $N_{ide}(t)$ veće od ili jednako N. Na osnovu ovog podatka, određuje se maksimalna moguća ponuda korisnika *maksPonuda* [EUR] koja donosi benefit po relaciji:

$$maksPonuda = floor(P_{pra}(k_2 - 1)C_{maks}), \qquad (4)$$

gdje je k_2 koeficijent kojim se obezbjeđuje benefit potrošaču, za slučaj kada je $N_{ide}(t)$ manje od N.

U realnosti, električna vozila nisu idealna, već ih karakteriše SoC između 0% i 100% što direktno utiče na mogućnosti isporuke električne energije mreži. Štaviše, usljed degradacije baterije, ne preporučuje se punjenje iznad 80% za model Nissan Leaf. Uvodi se i zahtjev da baterija nijednog električnog vozila ni u jednom trenutku ne smije da dostigne status napunjenosti manji od b kapaciteta baterije [r.j. – relativne jedinice] čime jedan dio korisnika automatski gubi mogućnost za učešće u V2G, a koji je rezultat upotrebe električnih vozila u prethodnom periodu (ovaj uslov se može eliminisati ako se uzme da je b jednako nuli što znači da se električna vozila mogu potpuno isprazniti ako se koriste za ispomoć mreži). Ovaj uslov se uvodi usljed činjenice da je glavna uloga električnih vozila transport pa se podrazumijeva da se baterija ne smije potpuno isprazniti. Neka je EV niz kapaciteta baterija svih električnih vozila u sistemu. Uslov za određivanje niza potencijalnih električnih vozila EV_{pot}, dužine N_{pot}, od svih vozila u sistemu, za učešće u planskom pražnjenju je sledeći:

$$EV(n) \geq bE_{bat} + P_{pra}, n = 1,2,\ldots,N \qquad (5)$$

gdje je E_{bat} kapacitet baterije [kWh].

Dakle, električna vozila koja mogu da učestvuju u V2G su ona vozila koja imaju skladištenu minimalnu količinu energije plus količinu energiju koju mogu predati mreži tokom jednog sata pri snazi pražnjenja P_{pra}. Od niza svih električnih vozila u sistemu se dobija niz potencijalnih vozila EV_{pot} čija je dužina N_{pot} manja od ili jednaka N. Ovaj niz sadrži podatke o vozilima u sistemu koja zadovoljavaju (5).

Treba imati u vidu da vozila $EV_{pot}(j)$ (j=1,2,...,N_{pot}) zadovoljavaju (5) samo za prvi interval posmatranog dana. Na kraju tog intervala, a u zavisnosti od upotrebe električnog vozila (punjenje, plansko pražnjenje, vožnja, itd.), električna vozila karakteriše SoC koji se razlikuje od SoC na početku intervala. Dakle, (5) je neophodno provjeriti za svaki od intervala za posmatrani dan.

Obzirom da se aukcija održava za naredni dan, tačni SoC električnih vozila u t-om intervalu nije poznat ni agregatoru ni korisniku. Međutim, SoC na početku dana se za proračune može opisati normalnom raspodjelom $N(0{,}6,\ 0{,}01)$ [1].

Iz niza EV_{pot}, na osnovu ponuda učesnika aukcije za učešće u V2G za odgovarajući interval, agregator određuje niz dobitnika aukcije EV_{dob}. Ovi korisnici su dužni da u datom intervalu obezbijede dogovorenu količinu energije mreži. U slučaju da korisnik, koji je pobijedio na aukciji za određeni interval, odluči da isključi vozilo sa mreže tokom tog istog intervala, što se u praksi može desiti, dužan je da plaća penale čiji iznos određuje sistem operator i čiji detalji su precizirani u ugovoru između ove dvije strane.

Obzirom na ograničeni kapacitet baterije, korisnici električnih vozila nisu u mogućnosti da učestvuju u V2G u svim mogućim intervalima. Za svakog pobjednika agregator vrši proračun dostupnog kapaciteta kako bi se odredio zahtijevani plan pražnjenja. Ukoliko agregator odredi da u k-tom (k=1,2,...,T) intervalu dobitnik aukcije nije u mogućnosti da učestvuje u V2G, provjerava se da li je u t-im (t=1,2,...,k-1) intervalima moguće dopuniti električno vozilo energijom neophodnom za učešće u planskom pražnjenju u k-tom intervalu. Opcije su sledeće:

- Ukoliko to jeste moguće, korisnik donosi odluku da priključi vozilo na mrežu u zahtijevanom intervalu ili da se povuče iz aukcije. U slučaju da odluči da se povuče iz aukcije, prvi gubitnik aukcije dobija priliku da učestvuje V2G.
- Ukoliko to nije moguće, prvi gubitnik aukcije dobija priliku da učestvuje u V2G.
- Agregator automatski isključuje datog korisnika iz planskog pražnjenja za posmatrani interval i prvi gubitnik aukcije dobija priliku da učestvuje u V2G.

Pored određivanja plana pražnjenja, agregator može kao izlazni podatak da daje i dostupni kapacitet baterije u nekom trenutku, što bi korisnicima olakšalo planiranje upotrebe električnog vozila.

Za interakciju između agregatora (sistema) i korisnika električnih vozila je neophodno izgraditi odgovarajuću komunikacionu infrastrukturu.

IV. NUMERIČKI REZULTATI

Posmatra se EES Crne Gore. Elektrane od velikog značaja za EES Crne Gore i njihove karakteristike su prikazane u tabeli I.

TABELA I
Velike elektrane u EES-u Crne Gore

Elektrana	Tip	Instalisana snaga [MW]
HE Piva	Akumulaciona hidroelektrana	342
HE Perućica	Protočna hidroelektrana	307
TE Pljevlja	Termoelektrana na ugalj	210
VE Krnovo	Vjetroelektrana	72
VE Možura	Vjetroelektrana	46

EES Crne Gore je pretežno hidro sistem sa instalisanom snagom velikih hidroagregata od 649 MW što predstavlja 66,43%, odnosno približno dvije trećine ukupnih kapaciteta (nisu uračunate male hidroelektrane).

Ljetnje mjesece u EES-u Crne Gore karakteriše naročito povećanje opterećenja u južnoj regiji kao rezultat izraženih turističkih aktivnosti. Na slici 1 je dat dijagram opterećenja konzuma, a na slici 2 proizvodnja proizvodnih jedinica Crne Gore na dan 27.07.2020.

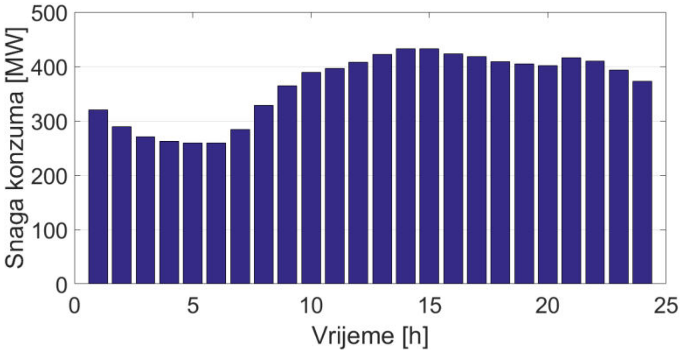

Sl. 1. Konzum Crne Gore na dan 27.07.2020. (izvor ENTSO-E Transparency)

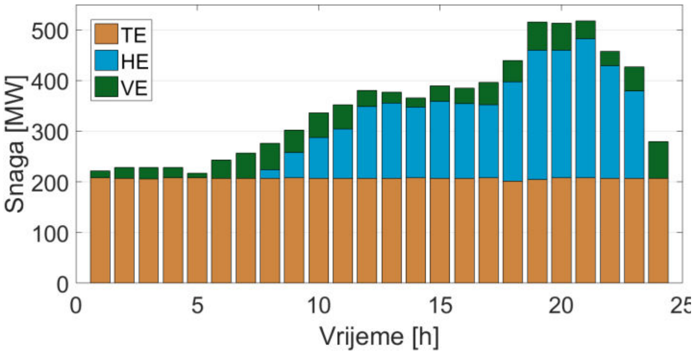

Sl. 2. Proizvodnja na dan 27.07.2020. (izvor ENTSO-E Transparency)

Na osnovu podataka sa slike 1 i 2 se zaključuje sledeće:

- TE Pljevlja tokom cijelog 24-časovnog perioda radi sa snagom koja je približno jednaka njenoj instalisanoj snazi od 210 MW i ta snaga se kreće u opsegu od 201 MW do 208 MW. Maksimalno se koristi raspoloživa snaga TE i tokom cijelog dana se javlja opterećenje koje je veće od tehničkog minimuma TE Pljevlja pa se ne javlja potreba za isključenje date elektrane sa mreže.
- Energija vjetra se koristi u onoj mjeri u kojoj je to moguće – teži se što boljem iskorišćenju raspoložive energije.

Na slici 3 dat je bilans snaga u EES-u Crne Gore na dan 27.07.2020.

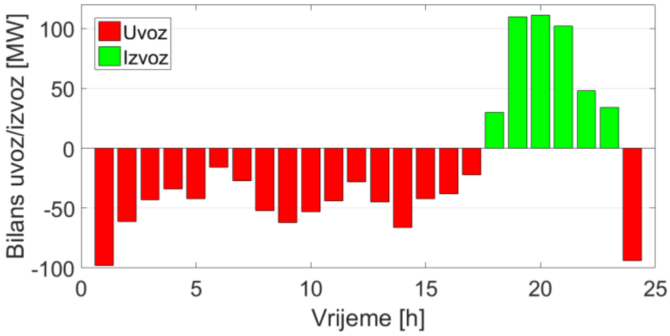

Sl. 3. Bilans snaga uvoz/izvoz na dan 27.07.2020.

Električna energija se uvozi u periodu između 00:00 i 17:00, kao i između 23:00 i 00:00, dok se izvozi u periodu između 17:00 i 23:00 časa. Višak proizvodnje u sistemu tokom ovog perioda se može iskoristiti za punjenje električnih vozila, koja se u preostalim intervalima (kada se javlja manjak snage) mogu ponašati kao generatori električne energije. Izvezena količina električne energije tokom posmatranog dana iznosi 435 MWh, dok je uvezena količina približno dva puta veća i iznosi 867 MWh.

Ukoliko se uvede pretpostavka da, od ukupne nedostajuće količine energije, odnosno snage, 30% otpada na južnu regiju, dolazi se do podataka o deficitu snage prikazanih na slici 4.

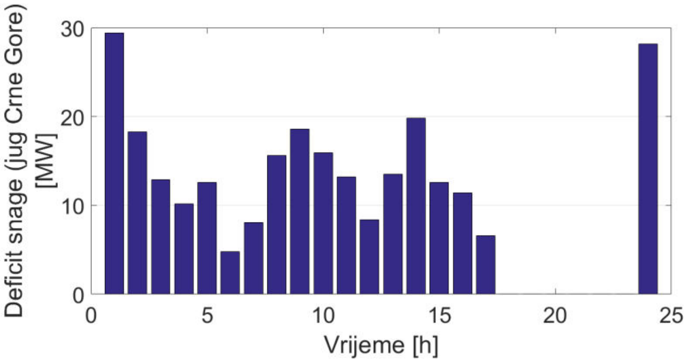

Sl. 4. Nedostajuća snaga u južnoj regiji Crne Gore na dan 27.07.2020. (aproksimacija od 30% ukupne nedostajuće snage u EES-u)

Na osnovu ovih podataka, ukupna nedostajuća količina energije u južnoj regiji Crne Gore na dan 27.07.2020. je 260,1 MWh (približno 260 MWh), a prosječna nedostajuća snaga je 14,45 MW. Nedostajuća količina energije bi mogla biti nadoknađena iz baterija električnih vozila za šta bi bilo neophodno priključiti na mrežu 5.200 vozila sa kapacitetom baterija 50 kWh i potpuno ih isprazniti. Međutim, električna vozila se koriste za transport tako da se uzima u obzir da ni u jednom trenutku ni jedno električno vozilo ne smije biti u potpunosti ispražnjeno. Time se zaključuje da u EES-u Crne Gore, tj u južnoj regiji, treba da postoji 6.500 električnih vozila sa baterijama kapaciteta 50 kWh koje ni u jednom trenutku ne padaju ispod stanja napunjenosti od 20%, odnosno 10 kWh, kako bi se pokrio deficit električne energije. U 2019. je u gradovima južne regije Crne Gore registrovano ukupno 66.410 vozila (Bar 17.232; Budva 11.922; Kotor 9.961; Tivat 7.397; Ulcinj 7.781; Herceg Novi 12.117) tako da se zaključuje da svako deseto vozilo treba da bude električno sa odgovarajućim karakteristikama.

U proračunu potencijala upotrebe električnih vozila u V2G sistemu u EES-u Crne Gore posmatraju se četiri stepena prisustva električnih vozila u južnoj regiji i to: 1.000 vozila, 5.000 vozila, 10.000 vozila i 20.000 vozila. Smatra se da su sva vozila istih karakteristika i to:

- Baterije su kapaciteta 50 kWh
- Snaga punjenja je 10 kW
- Snaga pražnjenja je 5 kW

Koeficijenti k_1 i k_2 su 1,1 i 1,2, respektivno. Na osnovu (5), minimalna količina energije neophodne za učešće u V2G, sa koeficijentom b=0,2, je 15 kWh.

SoC na početku dana se opisuje normalnom raspodjelom sa koeficijentima μ=0,6 i σ=0,1. Zaključuje se da 99,87% vozila ispunjava (5), što nema značajniji uticaj na sistem (u odnosu na slučaj kada bi 100% vozila ispunjavala dati uslov), ali je poželjno voditi računa o pomenutom uslovu radi maksimalne udobnosti korisnika koji električno vozilo koriste prije svega za transport.

Po dvotarifnom modelu u Crnoj Gori, maksimalna cijena električne energije je jednaka cijeni električne energije tokom perioda visoke tarife i iznosi približno 0,103 EUR/kWh.

Električna vozila nijesu generatori električne energije, već pokretne baterije za njeno skladištenje. Dakle, pored V2G sistema, mora se uzeti u obzir i pitanje punjenja električnih vozila tokom posmatranog dana sa ciljem bolje procjene njihovog uticaja na sistem. Iz ovog razloga, za svaki stepen prisustva električnih vozila se posmatraju dva podslučaja:

1. Kada korisnici električna vozila pune onda kada žele.
2. Kada korisnici električna vozila pune u periodu viška snage u sistemu.

Svi proračuni koji zavise od odluka potrošača koje imaju dva ishoda su izvedeni upotrebom funkcije koja nasumično generiše date odluke (npr. da li napuniti vozilo u posmatranom intervalu ili ne).

U tabelama II i III prikazani su rezultati proračuna za 8 posmatranih slučajeva. Date veličine su sledeće:

- Deficit energije u sistemu sa električnim vozilima [MWh] i u odnosu na deficit energije u originalnom sistemu [%]
- Suficit energije u sistemu sa električnim vozilima [MWh] i u odnosu na suficit energije u originalnom sistemu [%]
- Prosječna zarada planskog pražnjenja [EUR/kWh]
- Prosječna energija vozila na kraju dana [kWh]
- Prosječno pokrivanje deficita snage po satima [%] daje podatak o učešću električnih vozila u pokrivanju nedostatka snage u sistemu. Negativna vrijednost označava povećanje prosječnog pokrivanja deficita i javlja se isključivo kada korisnici vozila pune kada žele
- Prosječno pokrivanje suficita snage po satima [%] daje podatak o učešću električnih vozila (punjenju) u preuzimanju viška snage u sistemu

TABELA II
Rezultati proračuna (prvi dio)

Broj vozila	Deficit energije [MWh] ([%])	Suficit energije [MWh] ([%])	Prosječna zarada pražnjenja [EUR]
1.000 (1.)	258,62 (99,43)	425,39 (97,79)	0,0103
1.000 (2.)	239,64 (92,14)	416,6 (95,77)	0,0102
5.000 (1.)	259,03 (99,59)	390,50 (89,77)	0,0097
5.000 (2.)	158,30 (60,86)	338,24 (77,75)	0,0098
10.000 (1.)	305,88 (117,60)	378,82 (87,08)	0,0097
10.000 (2.)	61,325 (23,57)	254,97 (58,61)	0,0096
20.000 (1.)	444,45 (170,87)	374,50 (86,09)	0,0096
20.000 (2.)	0,025 (0,0096)	141,33 (32,49)	0,0097

TABELA III
Rezultati proračuna (drugi dio)

Broj vozila	Prosječna energija vozila na kraju dana [kWh]	Prosječno pokrivanje deficita snage po satima [%]	Prosječno pokrivanje suficita snage po satima [%]
1.000 (1.)	38,13	-0,15	3,03
1.000 (2.)	27,94	9	6
5.000 (1.)	38,6690	-9,58	13,84
5.000 (2.)	28,9750	34,79	31,05
10.000 (1.)	40,1900	-43,62	17,58
10.000 (2.)	28,1195	65,06	42,86
20.000 (1.)	42,2390	-106,37	18,71
20.000 (2.)	31,6760	99,95	66,27

Na osnovu podataka iz tabela II i III se zaključuje sledeće:

- Uvođenjem električnih vozila u sistem se povećava deficit snage u sistemu kada korisnici električna vozila pune onda kada to smatraju za shodno (slučajevi 1.), a pritom ne dolazi do značajnijeg smanjenja suficita što je rezultat ravnomjernog punjenja vozila tokom cijelog dana.
- Kada se V2G kombinuje sa planskim punjenjem (slučajevi 2.), dolazi do znatnog smanjenja deficita snage sa povećanjem prisustva električnih vozila u sistemu.
- Prosječna energija skladištena u baterijama električnih vozila na kraju dana u slučajevima 2. iznosi u prosjeku 29,21 kWh, odnosno 97,37% prosječnog kapaciteta energije na početku dana, što govori da je V2G sistem u kombinaciji sa planskim punjenjem održiv i kada se primijeni na periode duže od jednog dana. U proračunima međutim nije uzeto u obzir korišćenje električnih vozila za prevoz, odnosno smanjenje dostupne energije u baterijama električnih vozila tokom dana.
- Kombinovanje V2G sistema i planskog punjenja pozitivno utiče na sistem, jer u suprotnom električna vozila praktično međusobno izmjenjuju električnu energiju (kada jedno električno vozilo predaje energiju mreži, drugo se puni, pa je uticaj na sistem manji nego kada bi se punjenje električnih vozila prebacilo u interval viška snage u sistemu).

Na slici 5 dat je prikaz deficita snage na jugu Crne Gore po satima i ukupan deficit u sistemu sa 10.000 električnih vozila koja se pune tokom perioda viška snage (slučaj 2.).

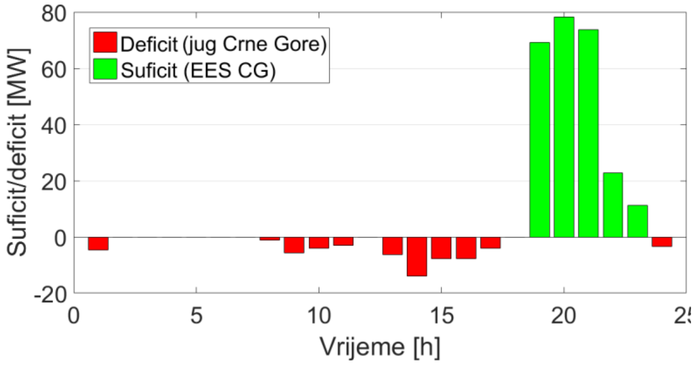

Sl. 5. Deficit snage na jugu Crne Gore i ukupni suficit u sistemu sa 10,000 (2.) električnih vozila na dan 27.07.2020.

Poredeći podatke sa slike 5 i podatke sa slike 3 i 4, zaključuje se da je deficit snage na jugu Crne Gore (pretpostavka o 30% deficita snage na nivou EES-a) značajno smanjen uvođenjem plana planskog pražnjenja vozila. U periodu između 1 i 6 časova u jutarnjim satima bilans snaga je jednak nuli. Primjećuje se i da je uticaj električnih vozila manji u kasnijim satima usljed pretpostavke da se električna vozila tokom posmatranog dana pune isključivo tokom perioda viška snage u sistemu, kada opet dostižu minimalnu količinu energije za učešće u V2G. Suficit snage u sistemu u periodu između 17 i 23 časa je takođe smanjen planskim punjenjem vozila. U intervalu između 17 i 18 časova se u potpunosti absorbuje višak proizvodne snage.

U proračunima o mogućem učešću električnih vozila u EES-u Crne Gore je zanemareno postojeće stanje. Naime, u 2018. godini je, od ukupnog broja registrovanih vozila od oko 235.000, registrovano tek nešto više od 100 električnih vozila, odnosno približno 0,043 %. Poredeći ovaj podatak i podatak o neophodnom broju vozila za pokrivanje nedostajuće snage u južnoj regiji Crne Gore, zaključuje se da se broj električnih vozila u ovoj regiji mora uvećati više od 300 puta.

Glavni uslov za prodor električnih vozila na tržište Crne Gore je uvođenje podsticajnih mjera za njihovu kupovinu i posjedovanje poput ukidanja poreza pri kupovini, besplatne registracije i parkinga, kao i izgradnje mreže stanica za punjenje. Pritom treba imati u vidu da su električna vozila još uvijek znatno skuplja od tradicionalnih vozila sa motorom sa unutrašnjim sagorijevanjem i da je kupovna moć građana Crne Gore znatno manja od kupovne moći zemalja koje su lideri u prelasku na električna vozila.

V. ZAKLJUČAK

U ovom radu je obrađen problem primjene električnih vozila kao pokretnih upravljivih sistema za skladištenje električne energije i predaju energije mreži (V2G sistem) sa osvrtom i na pitanje planskog punjenja električnih vozila, a sa ciljem smanjenja deficita snage u sistemu. Izvedeni su proračuni za različite nivoe prisustva električnih vozila u elektroenergetskom sistemu Crne Gore za tipičan ljetnji dan koji karakteriše relativno visoko opterećenje tokom cijelog dana i smjena intervala manjka i viška proizvodne snage u sistemu.

Iako V2G sistem dobija puni smisao kada se električna vozila pune tokom perioda niskih opterećenja i predaju energiju mreži tokom vrhova opterećenja, ovaj rad tretira pitanje upotrebe električnih vozila za davanje ispomoći sistemu onda kada mu je to potrebno, nezavisno od doba dana i trenutnog opterećenja. Za primjenu V2G sistema za pokrivanje deficita snage u realnim uslovima je neophodno uzeti u obzir brojne faktore koji utiču na stepen ispomoći mreži kao što su: prisustvo vozila u EES-u i očekivani udio ovih vozila u budućnosti, upotreba električnih vozila za transport i matematički modeli koji opisuju ovaj mod, održivost, odnosno ekonomska isplativost otkupa električne energije od korisnika električnih vozila, itd.

LITERATURA

[1] H. Fu, Y. Han, J. Wang, Q. Zhao, "A Novel Optimization of Plug-In Electric Vehicles Charging and Discharging Behaviors in Electrical Distribution Grid", *J. Electr. Compute. Eng.*, vol. *2018*, no *1-9*, Aug., 2018.

[2] D. Wu, D. C. Aliprantis, K. Gritza, "Electric Energy and Power Consumption by Light-Duty Plug-in Electric Vehicles", *IEEE Trans. Power Syst.: A Publication of the Power Engineering Society*, vol. *26*, no *2*, pp. *738-746*, Jun., 2011.

[3] H. Kikusato, Y. Fujimoto, S.-I. Hanada, D. Isogawa, S. Yoshizawa, H. Ohashi, Y. Hayashi, "Electric Vehicle Charging Management Using Auction Mechanism for Reducing PV Curtailment in Distribution Systems", *IEEE Trans. Sustain. Energy*, vol. *11*, no. *3*, pp. *1394-1403*, Jul., 2019.

[4] J. C. Mukherjee, A. Gupta, "Distributed Charge Scheduling of Plug-In Electric Vehicles Using Inter-Aggregator Collaboration", *IEEE Trans. Smart Grid*, vol. *8*, no. *1*, pp. 331-341, Jan., 2016.

[5] M. A. Ortega-Vazquez, F. Bouffard, V. Silva, "Electric Vehicle Aggregator/System Operator Coordination for Charging Scheduling and Services Procurement", *IEEE Trans. Power Syst.: A Publication of the Power Engineering Society*, vol. *28*, no. *2*, pp. *1806-1815*, May, 2013.

ABSTRACT

EVs (electric vehicles) are one of the leading trends in the world when it comes to sustainable growth and reducing impact on the environment. EV penetration in power systems means an increased load, but it allows for planned charging and discharging which benefit both the system and the owners of EVs. This paper proposes the use of planned charging and discharging of EVs based on game theory, with the aim to reduce the power deficit in a system.

Index terms—electric vehicles; aggregator; planned discharging; planned charging

Use of Electric Vehicles for Reduction of Power Deficit in System

Uroš Ognjenović, Saša Mujović, Lazar Šćekić

Realizacija laboratorijskog sistema za bežični prenos energije

Dejan Janjić, Alenka Milovanović i Branko Koprivica

***Apstrakt*—Cilj ovog rada je prikaz teorijskih osnova i realizacije laboratorijskog sistema za bežični prenos električne energije. Na početku će biti razmotreni osnovni principi induktivnog i rezonantnog bežičnog prenosa energije i biće navedene njihove osnovne prednosti i mane. Dalje, biće detaljnije opisana rezonantna metoda realizovanog sistema, uključujući: šemu veza i opis principa rada predajnog i prijemnog dela sistema, tehničke podatke, prikaz realizovanog laboratorijskog sistema, kao i rezultate merenja i odgovarajuću analizu.**

***Ključne reči*—Bežični prenos energije; rezonantna metoda; rezonantna frekvencija, redno-paralelna kompenzacija.**

I. UVOD

Metodologiju za bežični prenos električne energije je predložio Nikola Tesla, krajem 19. veka [1, 2]. Prve realizacije takvih sistema se javljaju na početku 21. veka, kada MIT realizuje prenos električne energije na rastojanje od 2 m za napajanje sijalice [3], kao i INTEL [4], a SONY predstavlja prvi bežični televizor [5]. Bežični prenos energije je sada već realnost koja se dalje razvija kroz različite primene, u medicini, robotici, za napajanje kućnih uređaja ili punjenje baterija prenosnih uređaja, električnih bicikli i mopeda, a očekuje se da će uskoro ući u primenu i bežični sistemi za punjenje električnih automobila.

Dosadašnja istraživanja u Srbiji u oblasti bežičnog prenosa električne energije (koliko je autorima poznato) odnose se na analizu i izradu Teslinog transformatora, ali ne i na realizacije sistema za napajanje uređaja [6, 7].

U ovom radu će biti date osnove teorije bežičnog prenosa energije bazirane na induktivnoj i rezonantnoj metodi i biće analizirane njihove prednosti i nedostaci. Zatim će biti analizirana rezonantna metoda sa redno-paralelnom kompenzacijom, koja se dobija dodavanjem kondenzatora [8]. Biće prikazana i praktična realizacija sistema, kao i rezultati merenja dobijeni u toku testiranja sistema.

II. OSNOVI BEŽIČNOG PRENOSA ENERGIJE

Postoje dve glavne tehnologije koje se trenutno koriste za implementaciju bežičnog prenosa energije:

- induktivna i
- rezonantna.

Obe tehnologije rade po principu sprezanja predajnog i prijemnog namotaja u bliskom elektromagnetskom polju i koriste magnetsku spregu da prenesu električnu energiju. Glavna razlika je u tome koliko su namotaji međusobno udaljeni i da li su izrađeni tako da se javlja rezonancija ili ne, kao što je prikazano na Slici 1.

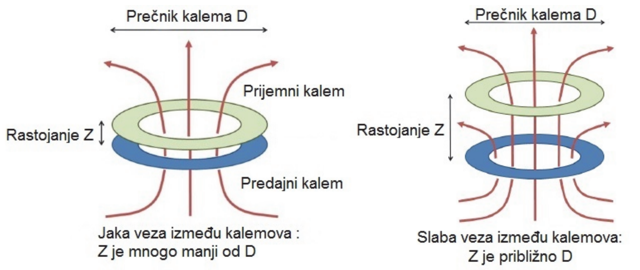

a) *b*)

Sl. 1. Ilustracija položaja kalemova za *a*) induktivnu i *b*) rezonantnu metodu.

Induktivni prenos energije podrazumeva blisku magnetsku spregu između predajnog kalema i prijemnog kalema na relativno malom rastojanju, reda nekoliko milimetara ili centimetara. Ovaj prenos energije se naziva i prenos energije sa jakom spregom. Predajni kalem je povezan na izvor naizmeničnog napona (najčešće u opsegu 100-400 kHz) koji generiše naizmeničnu struju kroz kalem i tako stvara magnetsko polje. Promenljivo magnetsko polje predajnog kalema se obuhvata prijemnim kalemom u kojem se indukuje naizmenični napon po Faradejevom zakonu, a samim tim i struja prijemnika. Količina prenete energije/snage se kontroliše promenom frekvencije napona u predajnom kalemu. Ova vrsta prenosa električne energije se može uporediti sa prenosom energije pomoću transformatora sa magnetskim jezgrom.

Rezonantna metoda prenosa električne energije se zasniva na magnetskoj rezonanciji između predajnog i prijemnog kalema. Predajni i prijemni kalem mogu biti i više desetina puta udaljeniji nego kod induktivnog prenosa, što karakteriše slabo spregnute kalemove za bežični prenos energije. Ova vrsta prenosa električne energije se može uporediti sa radio prenosom.

Rezonantni bežični prenos energije ima brojne prednosti u odnosu na induktivni, kao što su:

1. veće rastojanje između predajnog i prijemnog kalema,
2. veće osno odstupanje između predajnog i prijemnog kalema koji ne moraju biti postavljeni u osi, kao što je slučaj sa induktivnim prenosom,

Dejan Janjić – Tehnički remontni zavod Čačak, Dr Dragiše Mišovića 167, 32000 Čačak, Srbija (e-mail: dzandz@gmail.com).

Alenka Milovanović – Univerzitet u Kragujevcu, Fakultet tehničkih nauka u Čačku, Svetog Save 65, 32000 Čačak, Srbija (e-mail: alenka.milovanovic@ftn.kg.ac.rs).

Branko Koprivica – Univerzitet u Kragujevcu, Fakultet tehničkih nauka u Čačku, Svetog Save 65, 32000 Čačak, Srbija (e-mail: branko.koprivica@ftn.kg.ac.rs).

3. jedan predajni kalem može preneti energiju/snagu na više prijemnih kalemova, dok induktivni prenos zahteva više predajnih kalemova, što omogućava prenos snage na više uređaja sa različitim opterećenjima (uređaji sa različitom snagom).

Nedostatak rezonantnog prenosa u nekim slučajevima je niža efikasnost u poređenju sa induktivnim prenosom. Razlog je to što se veći deo polja rasipa oko prijemnog kalema, zbog povećane udaljenosti, što nije slučaj kod induktivne metode.

III. REZONANTNA METODA SA KOMPENZACIJOM

Za razliku od induktivne metode, rezonantna metoda se zasniva na postojanju reaktivnih (induktivnih i kapacitivnih) delova u predajnom i prijemnom kalema, kako bi sistem radio u rezonantnim uslovima. Zbog dimenzija kalemova, parazitna kapacitivnost nije dovoljna da obezbedi rezonanciju u radnom opsegu frekvencija, određenog primenom sistema za bežični prenos. U skladu sa tim, za postizanje rezonancije u željenom opsegu frekvencija potrebno je na predajnoj i prijemnoj strani dodati reaktivne elemente (najčešće kondenzatore), što se karakteriše kao dodatna kompenzaciona mreža. Tako se mogu realizovati redno-redna, redno-paralelna, paralelno-redna i paralelno-paralelna kompenzaciona metoda.

Šema veza rezonantnog kola sa redno-paralelnom kompenzacijom je prikazan na Slici 2.

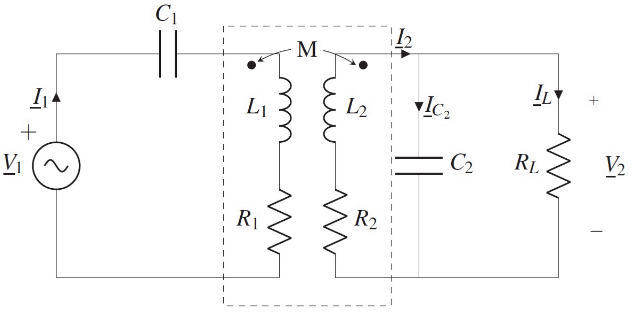

Sl. 2. Šema veza rezonantnog kola sa redno-paralelnom kompenzacijom.

Za spregnuto kolo sa Slike 2 se mogu napisati sledeće jednačine po I i II Kirhofovom zakonu i to:

$$\underline{V}_1 = \left(R_1 + \mathrm{j}\omega L_1 + \frac{1}{\mathrm{j}\omega C_1}\right)\underline{I}_1 - \mathrm{j}\omega M\underline{I}_2 , \tag{1}$$

$$\underline{V}_2 = -\left(R_2 + \mathrm{j}\omega L_2\right)\underline{I}_2 + \mathrm{j}\omega M\underline{I}_1 = R_L\underline{I}_L = \frac{\underline{I}_{C_2}}{\mathrm{j}\omega C_2} , \tag{2}$$

$$\underline{I}_2 = \underline{I}_{C2} + \underline{I}_L , \tag{3}$$

$$\underline{I}_2 = \mathrm{j}\omega R_L C_2 \underline{I}_L , \tag{4}$$

gde je ω kružna učestanost i $\mathrm{j}^2 = -1$.

Izjednačavanjem imaginarnog dela ulazne impedanse:

$$\begin{aligned}\underline{Z}_{ul} = \frac{\underline{V}_1}{\underline{I}_1} = \left(R_1 + \mathrm{j}\omega L_1 + \frac{1}{\mathrm{j}\omega C_1}\right) + \\ + \frac{\omega^2 M^2\left(\mathrm{j}\omega C_2 R_L + 1\right)}{R_L + \left(R_2 + \mathrm{j}\omega L_2\right)\left(\mathrm{j}\omega C_2 R_L + 1\right)}\end{aligned} , \tag{5}$$

sa nulom, može se odrediti rezonantna učestanost kola ω_r.

Međutim, u praksi se rezonantna učestanost podešava pomoću parametara prijemnog kola (induktivnosti L_2 prijemnog kalema i kompenzacione kapacitivnosti C_2) tako da ona bude jednaka:

$$\omega_r = \frac{1}{\sqrt{L_2 C_2}} . \tag{6}$$

Kada kolo radi u režimu rezonancije važe sledeći izrazi [8]:

$$\omega_r L_1 - \frac{1}{\omega_r C_1} \approx \frac{\omega_r M^2}{L_2} , \tag{7}$$

$$C_1 \approx \frac{L_2^2 C_2}{L_1 L_2 - M^2} . \tag{8}$$

Izrazom (8) je približno određena vrednost kompenzacione kapacitivnosti C_1 za odabranu induktivnost predajnog kalema L_1. U slučaju kada je međusobna induktivnost M mnogo manja od induktivnosti kalemova, odnos kapacitivnosti C_1 i C_2 će biti približno srazmeran odnosu induktivnosti L_2 i L_1.

IV. REALIZACIJA LABORATORIJSKOG SISTEMA

Sistem za bežični prenos energije rezonantnom metodom sa redno-paralelnom kompenzacijom (Slika 1) je realizovan u laboratorijskim uslovima. Sistem se sastoji od: 1) ispravljača naizmeničnog napona 230 V, 50 Hz, 2) pretvarača stalnog napona u naizmenični napon više frekvencije realizovan kao mostni invertor sa MOSFET tranzistorima [9], 3) predajnog kalema sa kompenzacionim kondenzatorom, 4) prijemnog kalema sa kompenzacionim kondenzatorom, 5) ispravljača naizmeničnog napona više frekvencije realizovanog kao Grecov spoj sa brzim diodama i kondenzatorom [9] i 6) aktivnog opterećenja (sijalica sa užarenim vlaknom). Blok šema ovog sistema je prikazana na Slici 3, a odgovarajuće fotografije na Slici 4.

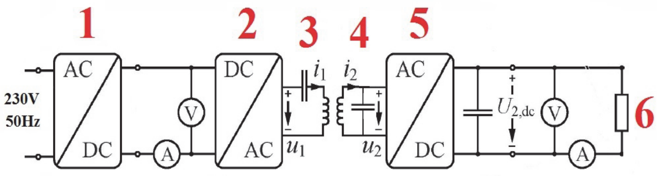

Sl. 3. Blok šema sistema za bežični prenos energije.

Sistem radi tako što se priključni napon od 230 V, 50 Hz ispravlja pomoću ispravljača 1 i na njegovom izlazu podešava na nivo od 30 V do 50 V, a zatim se taj stalni napon dovodi na ulaz DC u AC pretvarača 2 koji na svom izlazu generiše pravougaoni impulsni napon u_1 amplitude 30-50 V u opsegu frekvencija od 15 kHz do 120 kHz. Tako generisani napon se dovodi na rednu vezu predajnog kalema i kompenzacionog kondenzatora 3. Na izlazu prijemnog kalema 4 se indukuje naizmenični napon u_2 maksimalne amplitude 250-300 V za odabrano opterećenje, frekvencije jednake frekvenciji napona priključenog na predajni kalem 3. Indukovani naizmenični napon se ispravlja pomoću ispravljača 5 i priključuje na prijemnik 6. Ispravljanje napona u_2 je potrebno za većinu praktičnih primena, kao što su napajanje elektronskih uređaja ili punjenje njihovih baterija.

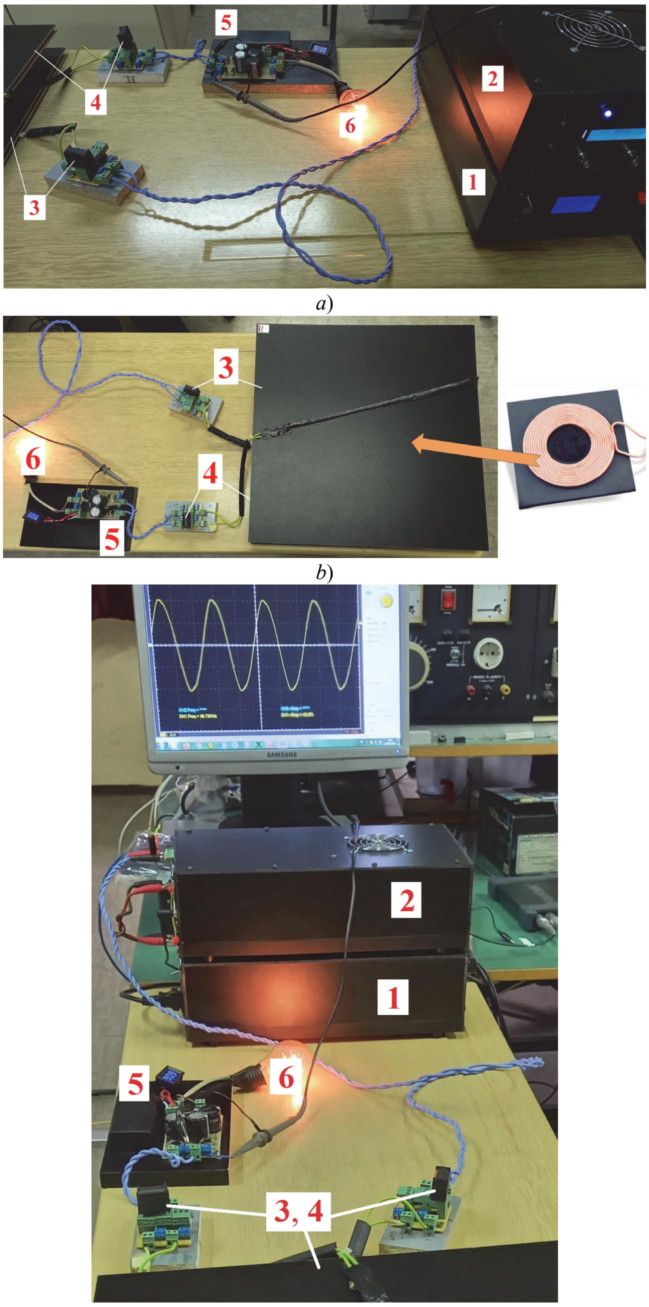

a)

b)

c)

Sl. 4. Fotografije realizovanog laboratorijskog sistema i kalema.

Predajni i prijemni kalem su namotani tako da imaju iste dimenzije i induktivnost, pa su i kompenzacioni kondenzatori izabrani tako da imaju istu kapacitivnost (zanemarujući uticaj međusobne induktivnosti). Podaci o dimenzijama i električnim parametrima sistema su date u Tabeli I.

TABELA I
PARAMETRI SISTEMA

Unutrašnji prečnik kalemova	375 mm
Spoljašnji prečnik kalemova	440 mm
L_1, L_2	100 µH
C_1, C_2	300 nF

Na osnovu izraza (6) i vrednosti parametara L_2 i C_2 datih u Tabeli 1 određena je rezonantna frekvencija sistema, koja iznosi približno 29,06 kHz.

V. REZULTATI ISPITIVANJA SISTEMA

Ispitivanje rada realizovanog sistema za bežični prenos energije je urađeno sa aktivnim opterećenjem, sa jednom ili dve redno vezane sijalice sa užarenim vlaknom od po 100 W. Kalemovi su bili postavljeni na međusobnom rastojanjima od 7 cm do 23 cm.

Merenja napona su vršena pomoću četvorokanalnog USB osciloskopa Hantek 6074 DB. Mereni su stalni naponi na izlazu ispravljača 1, pravougaoni impulsni napon u_1 na izlazu pretvarača 2 i naizmenični napon u_2 na krajevima prijemnog kalema 4. Dodatno, digitalnim voltmetrom je meren stalni napon na izlazu ispravljača 5, što je i napon prijemnika 6.

Na Slici 5 su prikazani snimci ekrana pri merenju napona na pretvaraču 2 i prijemnom kalemu 4.

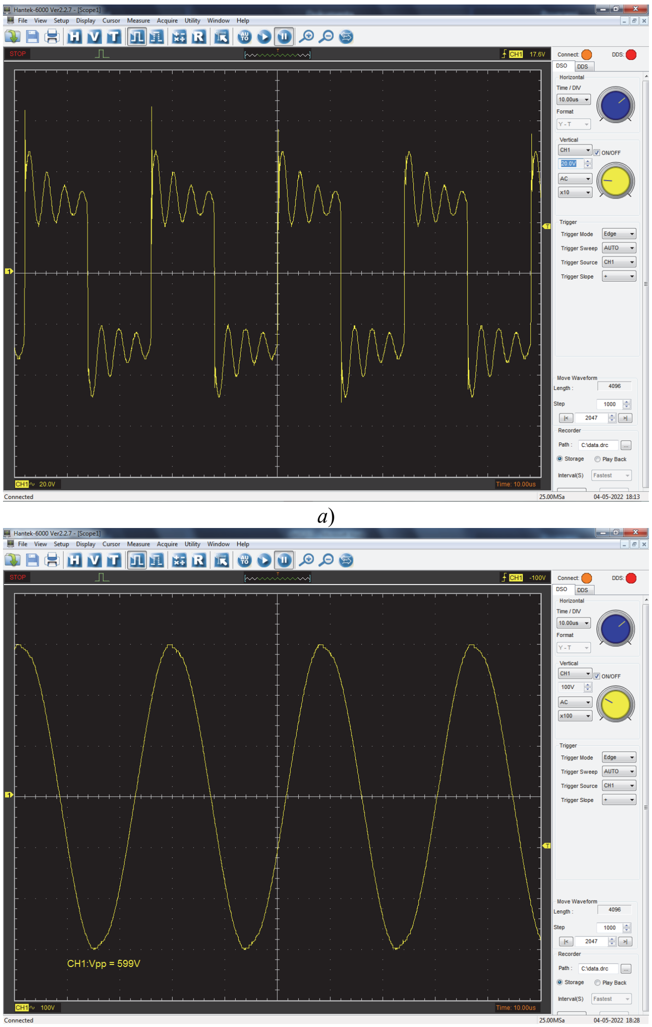

a)

b)

Sl. 5. Snimci ekrana pri merenju osciloskopom: *a*) napon u_1 na pretvaraču 2 i *b*) napon u_2 na prijemnom kalemu 4.

Uočava se da napon u_1 nema sasvim pravougaoni oblik, što je posledica oscilatornog karaktera struje kroz kalem L_1 i kondenzator C_1 koji su priključeni na taj napon. Sa druge strane napon u_2 ima skoro pravilan sinusoidalan oblik, a frekvencija mu je jednaka frekvenciji napona u_1.

U Tabeli 2 su dati rezultati merenja stalnog napona U_2 i struje I_2 prijemnika, kao i ostvarene aktivne snage P_2. Prijemnik je realizovan rednom vezom dve sijalice sa užarenim vlaknom naznačene snage od 100 W.

TABELA II
REZULTATI MERENJA

I_2 [A]	U_2 [V]	P_2 [W]
0,1	14,8	1,48
0,2	82,0	16,4
0,3	193,0	57,9
0,4	334,0	155,6

Detaljnije ispitivanje rada sistema su izvršena sa ciljem određivanja rezonantne učestanosti sistema merenjem napona na prijemniku za različite frekvencije izlaznog napona pretvarača 2. U toku ovakvog merenja se može očekivati da će se najveći napon izmeriti onda kada frekvencija napona pretvarača 2 odgovara rezonantnoj učestanosti sistema. S obzirom na to da je izračunata rezonantna frekvencija približno jednaka 29 kHz, ispitivanja su vršena u frekventnom opsegu od 25 kHz do 35 kHz.

Promena izmerenog napona sa frekvencijom za tri međusobna rastojanja između kalemova je prikazana na Slici 6. Strelicom je označen vrh rezonantne krive, na frekvenciji od 29,57 kHz, dobijene za najveće rastojanje između kalemova. Dobijena vrednost rezonantne frekvencije je veoma bliska proračunatoj vrednosti (29,06 kHz). Na manjim rastojanjima dolazi do razdvajanja maksimuma, koji se postižu za dve frekvencije, jednoj manjoj i jednoj većoj od proračunate. Razlika frekvencija za koje se postižu maksimumi se povećava sa smanjenjem rastojanja između kalemova. Ova pojava je povezana sa vrednošću međusobne induktivnosti M, koja se povećava sa smanjenjem rastojanja, pa se povećava i njen uticaj na vrednost rezonantne frekvencije, odnosno učestanosti ω_r, približno određenu izrazom (7).

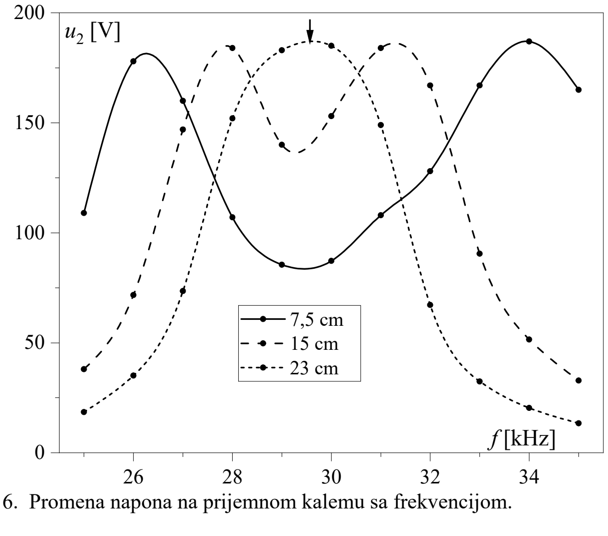

Sl. 6. Promena napona na prijemnom kalemu sa frekvencijom.

VI. ZAKLJUČAK

U ovom radu su dati osnovi metodologije bežičnog prenosa električne energije pomoću spregnutih kalemova i pri tome su ukratko analizirane prednosti i nedostaci induktivne i rezonantne metode. Detaljnije je analiziran slučaj rezonantnog kola sa redno-paralelnom kompenzacijom i određena je rezonantna učestanost kola za poznate parametre kalemova i kompenzacionih kondenzatora. Proračunom je utvrđeno da rezonantna frekvencija iznosi približno 29 kHz.

U radu je prikazana i realizacija laboratorijskog sistema za bežični prenos energije rezonantnim kolom sa redno-paralelnom kompenzacijom. Sistem je testiran u frekventnom opsegu 25-35 kHz, bliskim proračunatoj rezonantnoj frekvenciji. Pri tome su mereni naponi na predajnom i prijemnom kalemu. Rad sistema na frekvencijama od 15 kHz do 120 kHz omogućava njegovo ispitivanje u skladu sa međunarodnim standardima (IEC, ISO, SAE i drugi) u oblasti bežičnog prenosa energije.

Detaljnije ispitivanje sistema je izvršeno za tri međusobna rastojanja između kalemova, pri čemu je meren napon na prijemnom kalemu u odabranom frekventnom opsegu. Pokazana je promena tog napona sa frekvencijom za tri slučaja i utvrđeno je da se maksimum može postići za dve frekvencije kada je rastojanje relativno malo i kada je uticaj međusobne induktivnosti značajan. Sa povećanjem rastojanja se smanjuje uticaj međusobne induktivnosti, pa se maksimum napona dobija na frekvenciji vrlo bliskoj proračunatoj rezonantnoj frekvenciji.

Realizovani laboratorijski sistem za bežični prenos energije će poslužiti kao osnova za nova istraživanja u oblasti koja je veoma aktuelna u svetu, a koja je još uvek nedovoljno istražena. Cilje daljih istraživanja će biti nalaženja novih praktičnih primena bežičnog prenosa energije u elektroenergetici.

ZAHVALNICA

Istraživanja prezentovana u ovom radu su delimično finansirana sredstvima Ministarstva prosvete, nauke i tehnološkog razvoja RS, ugovor br.451-03-68/2022-14/200132 čiji je realizator Fakultet tehničkih nauka u Čačku - Univerziteta u Kragujevcu.

LITERATURA

[1] N. Tesla, “System of Transmission of Electrical Energy,” Patent No. 645,576, March 1900.

[2] A. Marinčić, Z. Civrić, B. Milovanović, “Nikola Tesla’s Contributions to Radio Developments,” *Serb. J. Electr. Eng.*, vol. *3*, no. *2*, pp. *131-148*, Nov. 2006.

[3] https://news.mit.edu/2007/wireless-0607.

[4] https://geekologie.com/2008/08/intel-demonstates-wireless-pow.php.

[5] https://www.sony.com/en/SonyInfo/News/Press/200910/09-119E/.

[6] R. Radetić, *Teslin transformator: teorija i praksa,* Niš, Srbija: Agencija Eho, 2019.

[7] J. M. Cvetić, “Tesla’s High Voltage and High Frequency Generators with Oscillatory Circuits,” *Serb. J. Electr. Eng.*, vol. *13,* no. *3*, pp. *301-333,* Oct. 2016.

[8] A. Triviño-Cabrera, J. M. González-González, J. A. Aguado, *Wireless Power Transfer for Electric Vehicles: Foundations and Design Approach,* Cham, Switzerland: Springer Nature, 2020.

[9] R. Radetić, *Tranzistorski pretvarači,* Bor, Srbija: Grafomed, 2006.

ABSTRACT

The aim of this paper is to present the theoretical foundations and realization of the laboratory system for wireless transfer of electric energy. At the beginning, the basic principles of inductive and resonant wireless energy transfer will be considered and their basic advantages and disadvantages will be stated. Further, the resonant method of the implemented system will be described in more details, including the connection scheme and description of the principles of operation of the transmitting and receiving part of the system, its technical data, presentation of the implemented laboratory system, as well as measurement results and appropriate analysis.

Realization of laboratory system for wireless energy transmission

Dejan Janjić, Alenka Milovanović i Branko Koprivic

ISBN 978-86-7466-930-3

ZBORNIK RADOVA, LXVI KONFERENCIJA ETRAN, Novi Pazar 6 - 9. juna 2022.

Pravci istraživanja u elektroenergetici kroz tematsku orijentaciju radova sa skupova CIRED Srbija i ETRAN/IcETRAN

Zoran J. Simendić i Vladimir A. Katić, *Senior Member, IEEE*

***Apstrakt*—U radu su razmatrani pravci istraživanja kroz radove na dva značajna naučno-stručna skupa, koja se održavaju u Srbiji, savetovanje CIRED Srbija i konferencije ETRAN/IcETRAN. Detaljnije je predstavljena struktura oba skupa, kao i ključne teme, koje se na njima razmatraju. Kod savetovanja CIRED Srbije teme su vezane za problematiku elektrodistribucije, preko stalnih studijskih komiteta i njihovih preferencijalnih tema, dok su kod konferencija ETRAN/IcETRAN one vezane i pokrivaju kompletnu oblast elektroenergetike. Na bazi toga razmatrana je zainteresovanost učesnika ovih skupova za predstavljanje svojih rezultata kroz brojnost prezentovanih naučno-stručnih radova u odgovarajućim tematskim oblastima. Zaključeno je da su najzastupljenije teme iz oblasti generisanja električne energije, distribuirane proizvodnje, primene obnovljivih izvora energije, priključenja električnih vozila, te upravljanja takvom proizvodnjom i pridruženim merenjima. Ovo ukazuje da istraživači u Srbiji obrađuju najnovije prodore u nauci i struci, te da razmatrani skupovi daju adekvatan prikaz o najnovijim dostignućima iz ovih oblasti.**

***Ključne reči*—Pravci istraživanja, Naučno-stručni radovi, Savetovanje CIRED Srbija, Konferencije ETRAN/IcETRAN.**

I. UVOD

Elektroenergetski sistem u Srbiji je obuhvaćen delovanjem tri velika državna preduzeća, Elektroprivreda Srbije (EPS), Elektromreže Srbije (EMS) i Elektrodistribucija Srbije (ODS), koja su proistekla i ranijeg centralizovanog sistema EPS-a. Pored toga niz privatnih domaćih i stranih kompanija se bavi proizvodnjom električne energije uglavnom na bazi obnovljivih izvora, kao i proizvodnjom i ugradnjom elektroenergetske opreme. Takođe, niz firmi se bavi projektovanjem i izgradnjom elektroenergetskih objekata i mreže. U svim ovim preduzećima radi impozantan broj inženjera i tehničara, kao i veći broj magistara i doktora nauka. S druge strane, rad i tehnički napredak ovih firmi neraskidivo su vezani za usvajanje i primenu novih tehničkih i tehnoloških rešenja, stručnih inovacija i originalnih tehničkih unapređenja i patenata. Sve to motiviše zaposlene, odnosno pruža dobru osnovu za prikazivanje postignutog na redovnim dvogodišnjim savetovanjima sa regionalnim učešćem CIRED Srbije. Na njima se uglavnom prikazuju radovi iz oblasti elektrodistribucije, odnosno vezani za rad, planiranje i održavanje elektrodistributivnih mreža. Ova savetovanja organizuje udruženje CIRED Srbije, koje je nacionalni komitet u sklopu međunarodnog udruženja CIRED sa sedištem u Liježu (*Liege*), Belgija [1].

Društvo za elektroniku, telekomunikacije, računarstvo, automatiku i nuklearnu tehniku (Društvo za ETRAN), kao jedno od najstarijih društava iz oblasti elektrotehnike u Srbiji, koje ove godine organizuje svoju LXVI konferenciju, od 1994. godine neguje sekciju Elektroenergetika [2]. U njoj se uglavnom prezentuju radovi iz akademskog okruženja, odnosno od strane autora sa univerziteta u Beogradu, Novom Sadu, Nišu i Kragujevcu. Od 2014. god. ETRAN ima i svoje međunarodno izdanje, IcETRAN (International Conference on ETRAN), na kom se predstavljaju radovi na engleskom jeziku. Na obe konferencije se prikazuju radovi iz svih oblasti elektroenergetike, ali je najčešća tematika vezana za elektroenergetske mreže, industrijsku elektroenergetiku i električne potrošače.

Cilj ovog rada je da predstavi pregled stručne problematike i glavnih tema istraživanja iz oblasti elektroenergetike u Srbiji u poslednjih sedam godina (2014. – 2021. god.) čiji rezultati su predstavljeni na savetovanjima CIRED Srbije, odnosno konferencijama ETRAN/IcETRAN. Na taj način autori žele da ukažu na moguću spregu istraživača sa univerziteta i iz privrede u formulisanju najboljih rešenja za rad elektrodistributivnog sistema.

II. SAVETOVANJA CIRED SRBIJA

Savetovanje CIRED Srbija održavaju se dvogodišnje, svake parne godine i na njima se okupi oko 500 učesnika iz zemlje i regiona. Pored naučno-stručnog dela u kom se izlaži prijavljeni radovi, organizuje se i velika izložba kompanija i preduzeća iz oblasti, kao i tematski okrugli stolovi. Tako struktuirano, savetovanje je pre svega namenjeno stručnjacima iz privrede, koji na njemu mogu da vide najnovija tehnička i tehnološka dostignuća, kao i da dobiju pregled naučnih istraživanja u oblasti. Pored toga, značajno je prisustvo i prezentacije istraživača sa univerziteta i naučnih instituta, kroz koje se mogu videti i pravci istraživanja i moguće primeene u praksi.

Rezultati istraživanja prikazani u naučnim ili stručnim radovima (referatima ili informacijama) svrstani su tematski

---

Zoran J. Simendić – Predsednik CIRED Srbija, Elektrodistribucija Srbije d.o.o. Beograd, Ogranak Elektrodistribucija Sombor, Apatinski put bb, 25101 Sombor, Srbija (e-mail: Zoran.Simendic@epsdistribucija.rs)

Vladimir A. Katić – Predsednik Društva za ETRAN, Univerzitet u Novom Sadu, Fakultet tehničkih nauka, Trg Dositeja Obradovića 6, 21000 Novi Sad, Srbija (e-mail: katav@uns.ac.rs)

prema preferencijalnim temama. Ove teme za svako savetovanje definišu odgovarajući studijski komiteti CIRED Srbije. Postoji šest stalnih studijskih komiteta (STK), čije delovanje obuhvata najaktuelnije teme vezane za savremene elektrodistributivne sisteme. To su:

STK 1 – Komponente mreža,

STK 2 – Kvalitet električne energije u elektrodistributivnim sistemima,

STK 3 – Zaštita i upravljanje elektroenergetskim mrežama,

STK 4 – Distribuirana proizvodnja i efikasno korišćenje električne energije,

STK 5 – Planiranje distributivnih sistema, i

STK 6 – Tržište električne energije i deregulacija.

A. Preferencijalne teme CIDER Srbija 2022

Preferencijalne teme (PFT) daju bliže odrednice tematike referata i definišu se u skladu sa razvojem nauke i struke. Za ovogodišnje savetovanje CIRED Srbija 2022 predložene preferencijalne teme obuhvataju sledeće problematike navedenih studijskih komiteta (ovde su teme navedene u skraćenom obliku, a kompletne se mogu naći u [1]):

STK 1:
- PFT 1.1 - Savremene konstrukcije, primena novih tehničkih rešenja i održavanje komponenti elektrodistributivnih mreža;
- PFT 1.2 - Testiranje, monitoring, dijagnostika i strategija održavanja komponenti elektrodistributivnih mreža;
- PFT 1.3 - Modelovanje i primena savremenih softverskih alata za analizu komponenti elektrodistributivnih mreža;
- PFT 1.4 - Uticaj komponenti elektrodistributivnih mreža na životnu i radnu sredinu;
- PFT 1.5 - Tehnička regulativa iz domena komponenti elektro-distributivnih mreža.

STK 2:
- PFT 2.1 - Kvalitet isporuke i kvalitet isporučene električne energije – uzroci, prostiranje, imunitet, eliminisanje, analize, iskustva;
- PFT 2.2 - Uređaji i metode za merenje i praćenje parametara kvaliteta električne energije (dijagnostičke metode, oprema, postupci i sl.);
- PFT 2.3 - Domaća i evropska tehnička regulativa o kvalitetu električne energije (standardizacija, tehnički propisi i postupci);
- PFT 2.4 - Uticaj distribuiranih generatora na kvalitet električne energije (naponski nivoi, struje kratkih spojeva, harmonici, podrška mreži – LVRT i sl.);
- PFT 2.5 - Uslovi priključenja nelinearnih potrošača i distribuiranih generatora, elektromagnetna kompatibilnost, bezbednost i interferencija;
- PFT 2.6 - Uticaj nedovoljnog kvaliteta u mreži na rad potrošača ili distribuiranih generatora (tehnički problemi, energetska efikasnost, pouzdanost, finansijski efekti, odnosi sa potrošačima...);
- PFT 2.7 - Prenaponi i zaštita od prenapona u distributivnim mrežama, poremećaji u uzemljenju i uticaj na kvalitet električne energije i druge povezane teme.

STK 3:
- PFT 3.1 - Ekploatacija (Strategije održavanja i procena stanja, tehnike i alati za upravljanje radnom snagom, zahtevi u pogledu upravljanja podacima, strategije upravljanja kriznim situacijama, eksploatacija industrijskih mreža);
- PFT 3.2 - Zaštita (Strategije pri zameni i rekonstrukciji zaštite, sistemi za nadzor i upravljanje u transformatorskim stanicama, uticaj distribuirane proizvodnje, nove zaštitne šeme i funkcije, simulacioni modeli, alati i nove funkcije, aspekti pouzdanosti, ispitivanje relejne zaštite, funkcija i sistema, analiza pojave kvarova i registrovanih zapisa);
- PFT 3.3 - Upravljanje i komunikacije (Automatizacija ED mreža, upravljanje u tržišnim uslovima, primena energetskih aplikacija, uvođenje sistemskih usluga, regulacija napona u SN i NN mrežama, primena komunikacionih sistema, sigurnosni aspekti pristupa informacijama, komunikacione tehnike i protokoli za realizaciju inteligentnih mreža, međusobna zavisnost).

STK 4:
- PFT 4.1 - Integracija i upravljanje distribuiranih izvora električne energije (DER) u distributivnim mrežama (Aktivno upravljanje sa distribuiranim izvorima električne energije, Upravljački algoritmi i filozofije, Prognoza proizvodnje iz obnovljivih izvora, Analiza mogućnosti priključenja distribuiranih izvora, Mikro-mreže, Električna vozila);
- PFT 4.2 - Uloga DER u poslovnim procesima u distributivnim sistemima (Koordinacija i upravljanje DER, Dobiti od skladišta električne energije i različitih strategija upravljanja, aktivno upravljanje DER u cilju optimizacije rada, uloga u unapređenju otpornosti distributivnih mreža, upravljanje opterećenjem);
- PFT 4.3 - Efikasno korišćenje električne energije (Smanjenje gubitaka, unapređenje efikasnosti distributivnih sistema, isporuka održive energije sa niskom emisijom gasova staklene bašte);
- PFT 4.4 - Pametna brojila i sistemi za daljinsko očitavanje i upravljanje brojilima (Korišćenje informacija sa pametnih brojila, analitika i studije slučaja, analiza troškova i dobiti).

STK 5:
- PFT 5.1 - Predviđanje potrošnje i proizvodnje distribuiranih izvora;
- PFT 5.2 - Pokazatelji kvaliteta mreža: zahtevi, rezultati i poređenje;
- PFT 5.3 - Strukture mreža i kriterijumi za planiranje mreža;
- PFT 5.4 - Metode za planiranje;
- PFT 5.5 - Strategije za investiranje.

STK 6:
- PFT 6.1 - Otvaranje tržišta električne energije i restrukturiranje elektroprivrede u regionu, praksa i iskustva;
- PFT 6.2 - Regulacija, modeli regulacije, uloga regulatora, izmene i unapređenja;
- PFT 6.3 - Učesnici tržišta električne energije, modeli

snabdevanja i modeli tržišta;

PFT 6.4 - Distribuirani izvori energije u konkurentnim uslovima otvorenog tržišta.

B. Tematska struktura naučnih radova

CIRED savetovanja održavaju se od 1998. god., a ove 2022. god. se proslavlja 25 godina. U tom periodu održano je 12 savetovanja i predstavljeno 1449 radova u formi referata i stručnih informacija, odnosno u proseku po 121 rad po savetovanju [1, 3]. Na slici 1 prikazan je pregled prikazanih radova po godinama u kojima su održana savetovanja. Može se videti da broj radova se polako menja (opada), ali da se na poslednjih nekoliko savetovanja ustalio na oko 110 radova, što ukazuje na promenu aktivnosti istraživača u ovoj oblasti. Interesantno je uočiti da pandemija Korona-19 virusa nije ostavila posledice na broj radova, ali da je usled nje 12. savetovanje iz 2020. god. pomereno u 2021. god.

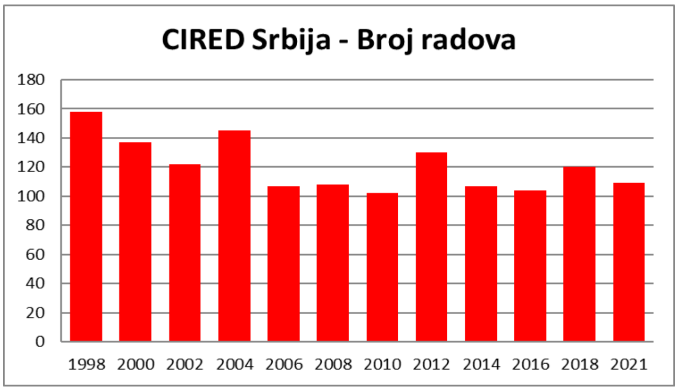

Sl. 1. Pregled broja radova na savetovanjima CIRED Srbija (ranije JUKO CIRED) od 1998. – 2021. god.

Međutim, da bi se dobila adekvatna slika tematske orijentacije istraživača u Srbiji kroz prezentovane radove na savetovanju CIRED Srbija, koja bi pravilno odslikavala postojeće stanje istraživanja u Srbiji, sužen je obim posmatranja. U obzir je uzet period poslednjih sedam godina (2014. god. – 2021. god.) u kom su održana četiri savetovanja na kojima je ukupno referisano 440 radova, informacija i referata na forumu „Smart grids“. U tom periodu su predstavljeni radovi razvrstani po studijskim komitetima, da bi se uočili dominantni pravci istraživanja. Na slici dva prikazan je broj radova po studijskom komitetu na poslednja četiri savetovanja. Može se uočiti da su najviše bile zastupljeni radovi iz tematike STK 1 (ukupno 100 rada), pa onda STK 3 (82 rada) i STK 4 (74 rada), dok su manje zastupljeni radovi iz oblasti STK 5 (59 radova), STK 2 (58 radova) i STK 6 (45 radova), dok je forum „Smart grids“ okupio još 22 rada.

III. KONFERENCIJE ETRAN/ICETRAN

Društvo za ETRAN se sastoji od 16 tematskih sekcija, koje pokrivaju kompletnu oblast elektrotehnike i to: Akustika (AK), Antene i prostiranja (AP), Automatika (AU), Biomedicinska tehnika (BT), Električna kola, električni sistemi i obrada signala (EK), Elektroenergetika (EE), Elektronika (EL), Metrologija (ML), Mikroelektronika i optoelektronika (MO), Mikrotalasna tehnika, tehnologije i sistemi (MT), Novi materijali (NM), Nuklearna tehnika (NT), Računarstvo (RA), Robotika i fleksibilna automatizacija (RO), Telekomunikacije (TE), Veštačka inteligencija (VI). Društvo svake godine organizuje dve paralelne konferencije (nacionalnu ETRAN i međunarodnu IcETRAN), a prosečan broj radova je oko 200. Na ovim konferencijama autori uglavnom dolaze sa naučno-obrazovnih (univerziteta, fakulteta) i naučno-istraživačkih (instituta) institucija, odnosno iz akademskog okruženja, dok je prisustvo i doprinosi učesnika iz privrede znatno ređe.

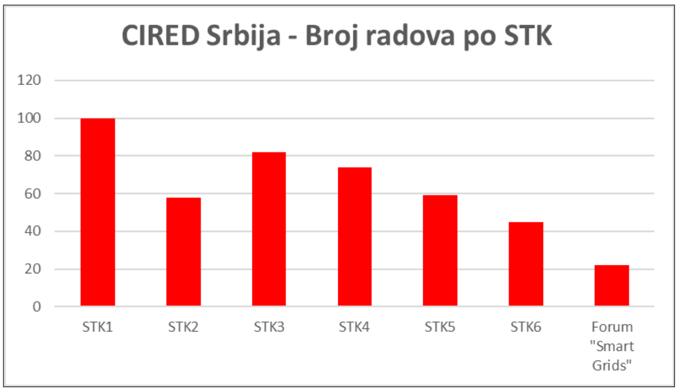

Sl. 2. Pregled ukupnog broja radova po studijskim komitetima (tematskim celinama) u periodu 2014.-2021. god.

Dok su savetovanja CIRED Srbija u celosti posvećena elektroenergetici, konferencije ETRAN/IcETRAN tek u jednom segmentu, kroz aktivnost sekcije Elektroenergetika pokrivaju ovu oblast. Međutim, konferencije se odvijaju svake godine, pa se u poređenju sa savetovanjima CIRED Srbija mogu predstaviti nešto aktuelniji radovi. Do sada je na sekciji prezentovano 456 radova, s tim da je na konferencijama ETRAN bilo 414 radova, a na IcETRAN 42 rada. Na slici 3 prikazan je pregled broja radova u periodu od formiranja sekcije 1994. god. do 2021. god. [2, 4]. Može se uočiti sličan opadajući trend, kao i kod CIRED Srbija savetovanja, s tim da se ovde prosečan broj radova 16,3, ali se poslednjih godina ustalio (spustio) na oko 10.

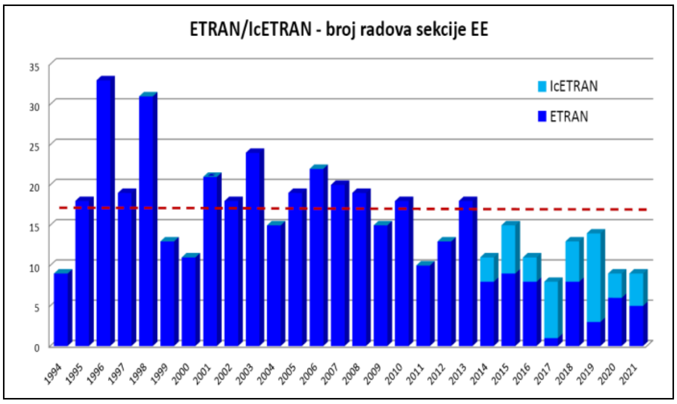

Sl. 3. Pregled broja radova na sekciji Elektroenergetika na konferencijama ETRAN i IcETRAN od 1994. – 2021. god.

Iz razloga aktuelnosti i ovde će se posebno analizirati period 2014. – 2021. god. Karakteristika tog perioda je da se u njemu javlja IcETRAN konferencija (počinje od 2014. god.), kao međunarodna konferencija i ETRAN, kao nacionalna. To daje mogućnost autorima da svoje radove predstave na jednoj od ove dve paralelne konferencije u zavisnosti kom auditorijumu žele da predstave svoje rezultate. Na slici 3 se može videti odnos radova na ove dve konferencije, koji se kreće u proseku 1,14:1 (53,3% i 46,7%).

Radovi na sekciji EE konferencija ETRAN/IcETRAN uglavnom su deljeni u dve oblasti: elektroenergetski sistemi i industrijska elektroenergetika. Međutim, da bi se bolje sagledala njihova tematska orijentacija i uskladila sa onom sa savetovanja CIRED Srbija, urađena je detaljnija klasifikacija. Kriterijum je bila uža tematika rada utvrđena kroz naslov, ključne reči i abstrakt. Sad su radovi svrstani su u osam tematskih oblasti:

EE-T1: Električne mreže (prenosne i distributivne), mikromreže i pametne mreže (smart grids);
EE-T2: Kvalitet električne energije, prenaponi i kompenzacija;
EE-T3: Elektroenergetska oprema, zaštita i informacioni sistemi;
EE-T4: Generatori, obnovljivi izvori energije (DER), električna vozila, te upravljanje proizvodnjom i merenje;
EE-T5: Električne mašine i transformatori (modelovanje, kvarovi, gubici, održavanje i sl.);
EE-T6: Elektromotorni pogoni (modelovanje, regulacija brzine, dinamika i sl.);
EE-T7: Energetska elektronika (energetski elektronski pretvarači, filteri, upravljački sklopovi i sl.);
EE-T8: Edukacija i ostalo.

Može se uočiti da se prve četiri oblasti (EE-T1 – EE-T4) više-manje poklapaju sa oblastima delovanja studijskih komiteta STK 1 – STK 4, dok su ostale van toga. Isto tako, radovi iz oblasti preostalih studijskih komiteta (STK 5 i STK 6) generalno nisu zastupljeni na konferencijama ETRAN/IcETRAN, pa su u slučaju eventualnog pojavljivanja svrstani pod ostalo, odnosno u EE-T8.

Na slici 4 prikazan je pregled broja radova na konferencijama ETRAN/IcETRAN svrstanih u skladu sa gornjom listom tematskih oblasti. Može se primetiti da su po broju radova tematske oblasti EE-T4 i EE-T5 dominantne, da su izražene teme iz oblasti EE-T7, EE-T1 i EE-T2, dok su oblasti EE-T6 i EE-T3 manje zastupljene. Dakle, na ovim konferencijama najčešće su bili izlagani radovi vezani za električne generatore, obnovljive izvore energije (DER), električna vozila, upravljanje proizvodnjom i merenjem, kao i vezane za električne mašine i transformatore, pa i energetsku elektroniku (energetske elektronske pretvarače) i filtere.

IV. PRAVCI ISTRAŽIVANJA U SRBIJI

Na osnovu podataka sa slika 2 i 4 može se videti da su istraživači u Srbiji najviše bili zaokupljeni temama iz oblasti STK 1 (Komponente mreža), STK 3 (Zaštita i upravljanje elektroenergetskim mrežama) i STK 4 (Distribuirana proizvodnja i efikasno korišćenje električne energije), odnosno EE-T4 (Generatori, obnovljivi izvori energije (DER), električna vozila, te upravljanje proizvodnjom i merenje), EE-T5 (Električne mašine i transformatori) i EE-T7 (Energetska elektronika, energetski elektronski pretvarači i filteri). U tim oblastima, ukupno je prikazano 58,2% radova savetovanja CIRED Srbija, odnosno 62,1% radova sa konferencija ETRAN/IcETRAN. S obzirom na datu tematiku i pomenuto preklapanje tema, može se zaključiti da je fokus autora na obe konferencije u periodu 2014. god. – 2021. god. bio usmeren na različite teme, osim u slučaju problematike izučavane u STK 4, odnosno EE-T4. To opravdava organizaciju oba skupa, ali i ukazuje na zone daljeg profilisanja.

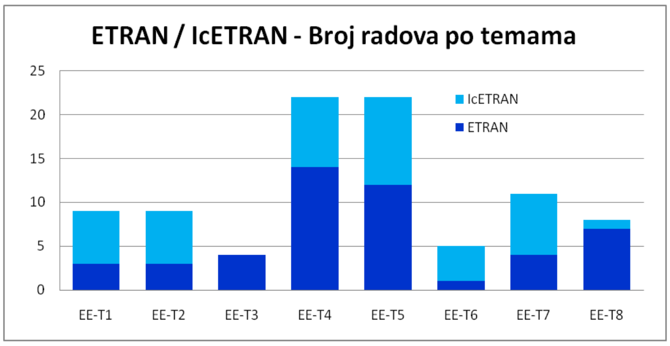

Sl. 4. Pregled broja radova sekcije Elektroenergetika na ETRAN/IcETRAN konferencijama u periodu 2014.-2021. god. svrstanih po oblastima

Dublja analiza radova iz tih oblasti može ukazati na specifičnu tematiku, kao i njenu moguću tehnološku vrednost i aplikativnost u srpskoj industriji.

A. Pravci istraživanja i broj radova

U skladu sa gornjim zaključkom, dublje je analizirana produkcija po preferencijalnim temama pojedinih STK sa savetovanja CIRED Srbija, odnosno subtemama tematskih oblasti na konferencijama ETRAN/IcETRAN.

U studijskim komitetima STK 1, STK3 i STK4 na savetovanjima CIRED Srbija ponuđeno je ukupno 12 preferencijalnih tema (STK1=5, STK3=3 i STK4=4), s tim što je kod STK3 za savetovanje 2022. god. njihov broj znatno uvećan, pa su ovde one agregirane pod tri glavne. Na slici 5 prikazano je ukupno učešće radova po PFT za pomenuta tri STK u periodu 2014.-2021. god. Može se videti da su najistaknutije preferencijalne teme PFT 4.1, PFT 1.2 i PFT 3.3. Pored toga, istaknute su (sa više od 25 radova) teme PFT 4.2 i PFT 3.1.

Na osnovu toga može se zaključiti da su savetovanjima CIRED Srbija najčešće prezentovani rezultati istraživanja po temama Integracija i upravljanje distribuiranih izvora električne energije (DER) u distributivnim mrežama, Testiranje, monitoring, dijagnostika i strategija održavanja komponenti elektrodistributivnih mreža, Upravljanje i komunikacije u distributivnim mrežama, kao i teme Uloga DER u poslovnim procesima u distributivnim sistemima i Ekploatacija distributivnih mreža.

Što se tiče istaknutih tema iz elektroenergetike na konferencijama ETRAN/IcETRAN, sa slike 4 vidi se da se radi o temama EE-T4, EE-T5 i EE-T7, čiji sadržaj je naveden ranije. Po broju radova, konferencije ETRAN/IcETRAN nešto su skromnije od savetovanja CIRED Srbija, pa dalja parcelizacija ne bi bila svrsishodna.

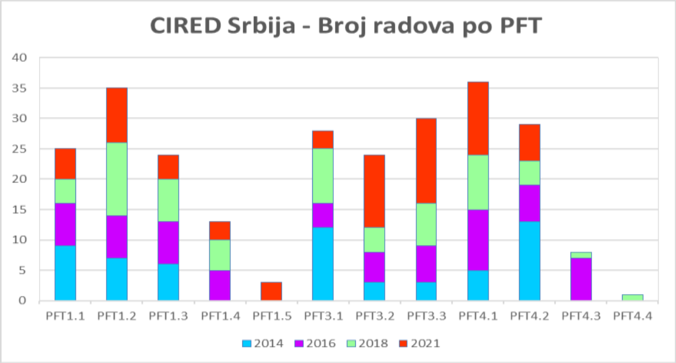

Sl. 5. Pregled broja radova sa savetovanje CIRED Srbija sortiranih po preferencijalnim temama za STK1, STK3 i STK4 u periodu 2014.-2021. god.

B. Pravci istraživanja i nagrađeni radovi

Oba skupa nagrađuju najistaknutije radove po STK-ovima, odnosno po sekcijama. Nagrade se dodeljuju i mladim autorima, kao podsticaj u njihovom razvoju. Uglavnom se radi o radovima koji su ostavili najbolji utisak, prikazuju rezultate naprednih istraživanja ili neka istaknuta tehnička rešenja. U skladu sa prethodnim posmatrane su teme nagrađenih radova iz STK1, STK3 i STK4, odnosno sa sekcije EE.

Kod savetovanja CIRED Srbija u posmatranom periodu STK1 je dodelio dve nagrade za radove u sklopu PFT1.2, a dve za PFT1.3, kod STK3 dve nagrade su bile u PFT 3.2, a po jedna PFT3.1 i PFT3.3, dok su kod STK4 tri nagrađena rada bila iz PFT4.1, a jedan iz PFT4.2. Ovo u potpunosti odgovara prethodnom zaključku o glavnim pravcima istraživanja za STK1 i STK4, dok delimično za STK3.

Kod konferencija ETRAN/IcETRAN nagrađeni radovi su bili iz tematskih oblasti EE-T5 sa pet radova, EE-T4 sa tri rada, EE-T1 i EE-T2 sa po dva rada i iz EE-T6 i EE-T7 sa po jednim nagrađenim radom. Vidi se da se ovo poklapa sa ranijim zaključkom o najpopularnijim temama.

C. Ključni pravci istraživanja

Poređenjem rezultata o najčešćim temama radova sa skupova CIRED Srbija i ETRAN/IcETRAN u periodu 2014.-2021. god., može se uočiti skoro potpuno poklapanje najpopularnije PFT 4.1 od STK4 i najzastupljenije teme EE-T4. To ukazuje da je i interesovanje akademske i stručne javnosti usmereno na istraživanja iz oblasti generisanja električne energije, distribuirane proizvodnje, primene obnovljivih izvora energije, priključenja električnih vozila, te upravljanja takvom proizvodnjom i pridruženim merenjima.

V. ZAKLJUČAK

Posmatranjem tematike radova sa dva skupa, koja prezentuju rezultate istraživanja iz oblasti elektroenergetike, savetovanje CIRED Srbija i konferencije ETRAN/IcETRAN, razmatrani su glavni pravci istraživanja u Srbiji.

Po prirodi, prvi skup je nacionalnog karaktera sa međunarodnim učešćem (radovi su na srpskom jeziku sa dodatim naslovom i abstraktom na engleskom ili kompletno na engleskom jeziku, ako se radi o nekim stranim učesnicima), konferencija ETRAN je takođe nacionalnog tipa (radovi su na srpskom jeziku sa dodatim naslovom i abstraktom na engleskom jeziku), dok je konferencija IcETRAN čisto međunarodna (radovi su na engleskom jeziku u IEEE formatu).

Po svojoj naučno-stručnoj orijentaciji, koncepciji i strukturi, prvi skup je u potpunosti orijentisan na oblasti elektroenergetike, odnosno preciznije na oblast elektrodistributivnih sistema, dok se na druga dva razmatraju rezultati iz kompletne elektrotehnike, pa je tek u jednom segmentu posvećen elektroenergetici, u sklopu istoimene sekcije.

Po svojoj nameni i učesnicima, prvi je generalno namenjen stručnoj i akademskoj javnosti, dok je druga dva u najvećem broju okuplja učesnike sa univerziteta i naučnih instituta. Pored toga, gro autora je iz Srbije, ali je značajno i učešće autora iz inostranstva.

Na bazi ove komparacije, može se zaključiti da su ova dva skupa kompatibilna i da mogu poslužiti za dobijanje predstave o glavnim pravcima istraživanja.

U posmatranom periodu od 2014. god. do 2021. god. u kom su održana četiri savetovanja i osam konferencija uočeno je da postoji odgovarajuća bliža tematika, koja je najzastupljenija na oba skupa i koja ukazuje na glavni pravac istraživanja u Srbiji. Ona se odnosi, odnosno upravljena je na istraživanja iz oblasti generisanja električne energije, distribuirane proizvodnje, primene obnovljivih izvora energije, priključenja električnih vozila, te upravljanja takvom proizvodnjom i pridruženim merenjima.

Autori su uvereni da bi se slični zaključci mogli doneti i za druge (slične) konferencije u Srbiji i svetu. Ovo ukazuje da istraživači u Srbiji tretiraju najnovije prodore u nauci i struci, te da razmatrani skupovi mogu da posluže za dobijanje dobrog uvida o najnovijim dostignućima iz oblasti elektroenergetike u svetu.

LITERATURA

[1] Simendić Z. i dr., *„Dvadeset godina rada srpskog nacionalnog komiteta CIRED Srbija“*, Monografija, Novi Sad, Srpski nacionalni komitet CIRED Srbija, 2017.

[2] Katić V., „Elektroenergetika“, u knjizi *„ET(R)AN Prvih šezdeset konferencija – Doprinos ravoju elektrotehničke struke“*, Uredili: B. Milovanović i Z. Jakšić, pp. 90-98, Beograd, Društvo za ETRAN i Akademska misao, 2016.

[3] http://www.ciredserbia.org.rs

[4] https://www.etran.rs

ABSTRACT

The paper discusses the directions of research through papers at two important scientific and professional gatherings, which are held in Serbia, the CIRED Serbia conference and the ETRAN/IcETRAN conferences. The structures of the both are presented in more detail, as well as the key topics discussed in them. At the CIRED Serbia conference, topics are related to the issue of electricity distribution, through standing study committees and their preferential topics, while at the ETRAN / IcETRAN conferences, they are related to and cover the entire field of electricity. Based on that, the interest of the participants in these gatherings was discussed through the number of presented scientific and professional papers for the relevant thematic areas. It was concluded that the most common topics are in the field of electricity generation, distributed generation, application of renewable energy sources, a connection of electric vehicles, and control of such generation and associated measurements. This indicates that researchers in Serbia are treating the latest breakthroughs in science and profession, and that the considered conferences give an adequate overview of the latest achievements in this fields.

Directions of research in electrical power engineering through thematic orientation of papers from CIRED Serbia and ETRAN/IcETRAN conferences

Zoran J. Simendić and Vladimir A. Katić